

Copyright

by

Michael James Klein

2017

**The Dissertation Committee for Michael James Klein Certifies that this is the  
approved version of the following dissertation:**

**Understanding the Electrochemistry and Reaction Mechanisms of Solid-  
State Sulfides with Application to the Lithium-Sulfur Battery System**

**Committee:**

---

Arumugam Manthiram, Supervisor

---

John B. Goodenough

---

Paulo J. Ferreira

---

Guihua Yu

---

Gyeong S. Hwang

**Understanding the Electrochemistry and Reaction Mechanisms of Solid-State Sulfides with Application to the Lithium-Sulfur Battery System**

**by**

**Michael James Klein, B.S.**

**Dissertation**

Presented to the Faculty of the Graduate School of

The University of Texas at Austin

in Partial Fulfillment

of the Requirements

for the Degree of

**Doctor of Philosophy**

**The University of Texas at Austin**

**May 2017**

## Acknowledgements

I would like to first and foremost express my deep gratitude to my advisor, Professor Arumugam Manthiram, for his support throughout my doctoral studies, from applying to graduate school all the way through preparing my dissertation. I would additionally like to thank the entirety of my committee, Professors John Goodenough, Paulo Ferreira, Guihua Yu, and Gyeong Hwang, for their time and role overseeing my doctoral studies. I would like to particularly acknowledge the invaluable support of Dr. Gabriel Veith at Oak Ridge National Lab, who hosted me in his lab for several months, and who has been a continuous source of advice and help throughout the latter portion of my studies. Additionally, my research would not have been possible without the help and support of the many members of Professor Manthiram's group, particularly Dr. Yongzhu Fu, Dr. Yu-Sheng Su, Dr. Sheng-Heng Chung, Dr. Chenxi Zu, Dr. Craig Milroy, Dr. James Knight, Dr. Veronica Augustyn, Dr. Wei Li, Dr. Sung Hoon Ahn and Lauren Murrah. Collaborators outside our group, including Dr. Karel Goossens, Prof. Chris Bielawski, Dr. Andrei Dolocan, Dr. Hugo Celio, and Dr. Karalee Jarvis were hugely supportive throughout my time at UT. I would like to thank the National Science Foundation Graduate Research Fellowship Program, the Cockrell School of Engineering, and the U. S. Department of Energy for their support funding my studies and research. Finally, I must thank my friends and family for their continual love and support, without which I never could have completed my studies.

# **Understanding the Electrochemistry and Reaction Mechanisms of Solid-State Sulfides with Application to the Lithium-Sulfur Battery System**

Michael James Klein, Ph.D.

The University of Texas at Austin, 2017

Supervisor: Arumugam Manthiram

The lithium-sulfur (Li-S) battery is a highly promising technology for next-generation high energy density storage. This high energy density has its roots in the conversion chemistry of the Li-S system, which also imparts numerous challenges to the realization of practically viable cells. This dissertation focuses on improving the performance and understanding of insulating solid-state lithium sulfides, which are the source of many of the challenges inherent to Li-S batteries.

First, a facile strategy is presented to generate a manganese sulfide surface layer on  $\text{Li}_2\text{S}$  particles, which dramatically improves cycling performance. Analysis of this reaction mechanism demonstrates how surface layers with limited conductivity but high electrochemical stability and facile charge transfer can profoundly improve the solid  $\text{Li}_2\text{S}$  charge mechanism.

The role of solid sulfur-sulfur bonding in the cycling mechanism was then analyzed by direct chemical synthesis and isolation of insoluble sulfur-sulfur bonded species (*i.e.*,  $\text{Li}_2\text{S}_2$ -type species). While these syntheses are shown not to generate  $\text{Li}_2\text{S}_2$  separate from  $\text{Li}_2\text{S}$ , the insoluble polysulfide species were isolated from the soluble polysulfides. These isolated insoluble sulfides are used to demonstrate that solid-state

sulfur-sulfur bonds can be reduced in the absence of soluble polysulfides, and the formation of  $\text{Li}_2\text{S}_2$  is thus not inherently limiting to the capacity of Li-S batteries.

To further clarify the fundamental limitation of  $\text{Li}_2\text{S}$  thickness on Li-S battery rate performance, a system was built to sputter-deposit air-sensitive lithium sulfide films of arbitrary thickness. It is shown that while the deposition initially generates a novel sulfide structure containing polymer-like  $\text{Li}_2\text{S}$  units, highly pure crystalline films of  $\text{Li}_2\text{S}$  can be generated with annealing. These  $\text{Li}_2\text{S}$  films are used to systematically determine the maximum thickness of  $\text{Li}_2\text{S}$  that can be charged at a practical rate is approximately 40 nm at a local charge density of  $1 \mu\text{A cm}^{-2}$ . This systematic approach additionally identified the appearance of the activation overpotential when charging  $\text{Li}_2\text{S}$  to be associated with the generation of soluble polysulfide species. Finally, these results are used to develop a model for the rational design of Li-S cathodes by tailoring the conductive pore structure around the local charge density and total sulfur content.

## Table of Contents

List of Tables .....	xiii
List of Figures .....	xiv
Chapter 1: Introduction .....	1
1.1. Introduction to lithium-sulfur batteries .....	1
1.1.1. Materials properties .....	2
1.1.2. Electrolytes .....	3
1.1.3. Mechanism .....	3
1.2. Challenges and approaches to Li-S batteries .....	5
1.2.1. Insulating solid materials .....	5
1.2.1.1. Conductive composites .....	6
1.2.1.2. Polysulfide catholytes .....	7
1.2.1.3. Active material loss.....	7
1.2.2. Lithium metal anodes.....	7
1.2.2.1. Li <sub>2</sub> S cathodes.....	8
1.2.2.2. Volume expansion .....	9
1.2.3. Electrolyte effects .....	9
1.2.3.1. Shuttle effect .....	9
1.2.3.2. Self-discharge .....	10
1.2.4. Cell-level energy density .....	11
1.2.5. All-solid-state cells .....	12
1.3. Conclusions and future directions.....	12
1.4. Objectives .....	13
Chapter 2: Experimental Methods .....	15
2.1. Description of synthesis techniques and apparatus.....	15
2.1.1. Drop-cast electrodes.....	15
2.1.1.1. Self-weaving carbon nanofiber paper current collectors	15
2.1.2. Chemical synthesis techniques .....	16

2.1.2.1. Direct $\text{Li}_2\text{S}_2$ synthesis in ammonia.....	16
2.1.2.2. $\text{Li}_2\text{S}_x$ filtration scheme .....	17
2.1.3. Physical vapor deposition (PVD).....	17
2.1.3.1. Basics of thermal evaporation.....	17
2.1.3.2. Basics of sputter deposition .....	17
2.1.3.3. Apparatus .....	19
2.1.3.4. Target preparation.....	22
2.1.3.5. Substrate preparation .....	23
2.2. Description of characterization techniques .....	24
2.2.1. Morphological techniques.....	24
2.2.1.1. X-ray diffraction (XRD) .....	24
2.2.1.2. Scanning electron microscopy (SEM) .....	25
2.2.1.3. Quartz crystal microbalance (QCM) thickness monitoring .....	25
2.2.2. Spectroscopic/spectrometric techniques .....	26
2.2.2.1. X-ray photoelectron spectroscopy (XPS) .....	26
2.2.2.2. Ultraviolet photoelectron spectroscopy (UPS) .....	27
2.2.2.3. Ultraviolet/visible light spectroscopy (UV/vis) .....	27
2.2.2.4. Time-of-flight - secondary ion mass spectrometry (TOF- SIMS).....	27
2.2.2.5. Raman spectroscopy .....	28
2.2.3. Electrochemical techniques .....	29
2.2.3.1. Cell fabrication.....	29
2.2.3.2. Galvanostatic cycling .....	29
2.2.3.3. Cyclic voltammetry (CV) .....	29
2.2.3.4. Electrochemical impedance spectroscopy (EIS).....	30
2.2.3.6. Open circuit analysis.....	30
Chapter 3: An effective lithium sulfide encapsulation strategy for stable lithium-sulfur batteries .....	31
3.1. Introduction.....	31
3.2. Experimental .....	33

3.2.1. Synthesis of carbon nanofiber (CNF) current collector .....	33
3.2.2. Electrochemical characterization .....	33
3.2.3. Morphology characterization .....	33
3.2.4. UPS and XPS characterization.....	34
3.2.5. TOF-SIMS characterization .....	34
3.3. Results and Discussion .....	35
3.3.1. Encapsulation Strategy.....	35
3.3.2. Electrochemical performance .....	36
3.3.2.1. Li <sub>2</sub> S/Mn performance .....	36
3.3.2.2. Electrochemical impedance spectroscopy (EIS) data ....	38
3.3.2.3. Electrochemistry of additional transition metal additives	39
3.3.3. Morphological analysis .....	40
3.3.4. Ultraviolet Photoelectron Spectroscopy (UPS) Analysis .....	42
3.3.5. X-ray Photoelectron Spectroscopy (XPS) Analysis .....	46
3.3.6. Time of Flight Secondary Ion Mass Spectroscopy (TOF-SIMS) Analysis .....	49
3.3.6.1. Metal ion yields.....	49
3.3.6.2. M <sup>+</sup> normalized profiles .....	50
3.3.6.3. Analysis of lithium gradients .....	51
3.3.6.4. Effect of cycling on ToF-SIMS profiles .....	52
3.3.6.5. LiS <sup>+</sup> /Li <sup>3+</sup> Profiles .....	54
3.4. Conclusion .....	57
Chapter 4: Elucidating the electrochemical activity of electrolyte-insoluble polysulfide species in lithium-sulfur batteries .....	58
4.1. Introduction .....	58
4.2. Experimental .....	60
4.2.1. Li <sub>2</sub> S <sub>2</sub> synthesis .....	60
4.2.2. Filtration/polysulfide extraction in DME/DOL .....	62
4.2.3. Carbon nanofiber (CNF) paper synthesis .....	63
4.2.4. Electrochemical cell fabrication and characterization .....	63

4.2.5. Ultraviolet-visible spectroscopy (UV-vis) .....	64
4.2.6. X-ray diffraction (XRD) .....	64
4.2.7. X-ray photoelectron spectroscopy (XPS) .....	64
4.3. Results and Discussion .....	65
4.3.1. Morphology.....	65
4.3.2. XPS analysis .....	66
4.3.2.1. As-synthesized $\text{Li}_2\text{S}_x$ S 2p spectrum .....	66
4.3.2.2. Elemental sulfur reference .....	68
4.3.2.3. Carbon and oxygen spectra .....	69
4.3.2.4. Peak broadening effects .....	71
4.3.2.5. Elemental quantification .....	71
4.3.3. UV/vis and filtration analysis .....	72
4.3.3.1. Filtration.....	72
4.3.3.2. UV/vis spectra.....	72
4.3.3.3. XPS of filtered samples .....	76
4.3.3.4. Effects of sputtering on XPS data .....	77
4.3.4. $\text{Li}_2\text{S}$ reference analysis .....	80
4.3.5. Analysis of potential contamination sources .....	82
4.3.6. Electrochemical analysis.....	85
4.3.7. Electrochemical background subtraction .....	87
4.3.8. Current collector size effects .....	88
4.3.9. Isolation of insoluble polysulfide electrochemistry .....	89
4.3.9.1. Electrochemically-monitored filtration.....	90
4.3.9.2. Electrochemical calculation of polysulfide concentration.....	93
4.3.9.3. Electrochemistry of soluble polysulfide-extracted $\text{Li}_2\text{S}_x$ .....	95
4.3.9.4. Effect of washing and particle size on commercial $\text{Li}_2\text{S}$ .....	98
4.4. Conclusion .....	99
Chapter 5: Chemistry of sputter-deposited lithium sulfide films.....	100
5.1. Introduction.....	100
5.2. Experimental .....	101

5.2.1. Apparatus .....	101
5.2.2. Target preparation .....	102
5.2.3. Substrate preparation .....	102
5.2.4. Deposition conditions .....	103
5.2.5. Characterization techniques .....	103
5.2.5.1. Quartz crystal microbalance .....	103
5.2.5.2. X-ray diffraction .....	104
5.2.5.3. Scanning electron microscopy .....	104
5.2.5.4. Raman spectroscopy .....	104
5.2.5.5. X-ray photoelectron spectroscopy .....	104
5.2.5.6. Ultraviolet-visible spectroscopy .....	105
5.2.5.7. Time of flight secondary ion mass spectrometry .....	105
5.2.6. Electrochemistry .....	105
5.3. Results and Discussion .....	106
5.3.1. Deposition analysis .....	106
5.3.2. Morphological analysis .....	109
5.3.3. Spectroscopic analysis .....	111
5.3.4. Electrochemistry .....	116
5.3.5. TOF-SIMS Analysis .....	120
5.3.6. Indirect deposition analysis .....	123
5.4. Conclusions .....	129
Chapter 6: Rational design of lithium-sulfur battery cathodes based on experimentally determined maximum active material thickness .....	130
6.1. Introduction .....	130
6.2. Experimental .....	131
6.2.1. Deposition parameters .....	131
6.2.2. Background electrolyte oxidation .....	133
6.2.3. Polysulfide catholyte reference preparation .....	134
6.2.4. Pore-filling model .....	134
6.3. Results and discussion .....	135

6.3.1. Open circuit analysis.....	135
6.3.2. Thick film charge behavior.....	137
6.3.3. Electrolyte stability analysis.....	138
6.3.4. Polysulfide catholyte reference.....	139
6.3.5. Determination of maximum active material thickness.....	140
6.3.6. Pore filling model.....	144
6.3.6.1. Application of pore-filling model to literature Li-S materials.....	146
6.3.6.2. Evaluation of pore-filling model assumptions.....	152
6.4. Conclusion.....	154
Chapter 7: Summary.....	155
Appendix.....	159
A.1. MATLAB pore-filling model code.....	159
References.....	165
Vita.....	172

## List of Tables

<b>Table 1.1.</b> Overview of sulfur content and performance for a variety of sulfur/graphene composites. Adapted with permission from Manthiram <i>et al.</i> <sup>12</sup> Copyright 2014. American Chemical Society.....	6
<b>Table 3.1.</b> UPS results .....	43
<b>Table 4.1.</b> Comparison of the XPS quantification for the synthesized $\text{Li}_2\text{S}_x$ sample before and after filtration from DME/DOL, and a reference commercial $\text{Li}_2\text{S}$ sample .....	80
<b>Table 4.2.</b> Efficiency of filtration scheme .....	93
<b>Table 6.1.</b> Measured and calculated $\text{Li}_2\text{S}$ film thickness, based on given pre-sputter and deposition times. The measured thicknesses are from Figure 5.4, and the calculated thicknesses were based on the deposition rates indicated in the first row of the table. ....	132
<b>Table 6.2.</b> Estimate of $\text{Li}_2\text{S}$ film resistivity and conductivity based on approximate overpotential for observed charge plateaus at given charge densities.	141
<b>Table 6.3.</b> A comparison of reported average pore sizes, pore volumes, and specific surface areas from Ding <i>et al.</i> , <sup>170</sup> for a selection of carbon materials (top) and the modeled pore structure (bottom). ....	147
<b>Table 6.4.</b> Literature carbon framework data for two Li-S cathodes exhibiting notable performance. *These values were calculated to include the CNTs added to the cathode during cell assembly according to the MWCNT pore structure reported in Ding <i>et al.</i> <sup>170</sup> .....	149

## List of Figures

**Figure 1.1.** Typical discharge and charge curve of a liquid electrolyte Li-S battery versus depth of discharge, showing the upper and lower plateaus on discharge, and the average polysulfide stoichiometry. Reproduced from Ji and Nazar<sup>14</sup> with permission of The Royal Society of Chemistry. .4

**Figure 1.2.** Activation effect over three galvanostatic charge/discharge cycles. In the first cycle, the cell must be charged over 3.5 V (vs. Li/Li<sup>+</sup>) to initiate charge. In subsequent cycles, no overpotential requirements are observed, and the Li-S cell cycles normally. Adapted with permission from Yang *et al.*<sup>63</sup> Copyright 2012. American Chemical Society. ....8

**Figure 1.3.** Surface plot of the cell-level energy density for a Li-S battery based on the sulfur content and electrolyte/sulfur (E/S) ratio. The color scale begins at 400 Wh kg<sup>-1</sup> to indicate the threshold at which the Li-S energy density can compete with high-performance lithium-ion batteries at the cell-level. The highest E/S ratio that meets this threshold at 90 wt.% sulfur content is indicated. ....11

**Figure 2.1.** Self-woven CNF paper removed from filter paper after vacuum drying. ....15

**Figure 2.2.** Photographs of the components built for the PVD synthesis of air-sensitive materials. The components with numerical annotations are described in the text. (a) The assembled chamber and processing components in the glovebox, prior to glovebox window installation. (b) The bottom (fixed) half of the deposition chamber. (c) The interior of the top half of the deposition chamber in the open position for sample loading. (d) The top of the deposition chamber in the closed position during a  $\text{Li}_2\text{S}$  sputter deposition. The intense pink ring visible in the mirror is the optical emission from the argon plasma confined above the  $\text{Li}_2\text{S}$  target. (e) The electronics cabinet with the hardware for controlling the deposition and vacuum systems.....20

**Figure 2.3.** Sputter-coated metallic species evaluated as  $\text{Li}_2\text{S}$  conductive substrates (a) after annealing but before  $\text{Li}_2\text{S}$  deposition and (b) after  $\text{Li}_2\text{S}$  deposition and subsequent annealing.....23

**Figure 3.1.** Schematic of the proposed  $\text{Li}_2\text{S}$  encapsulation with a stable surface layer. In this work, the second phase on the surface (in blue) is a transition-metal sulfide.....35

**Figure 3.2.** Electrochemical characterization: (a) CV profile, (b) voltage profile, and (c) cell cycling performance of the  $\text{Li}_2\text{S}/\text{Mn}$  and  $\text{Li}_2\text{S}$  cathodes. (d) Rate capability test. (e) Initial charging voltage profile of  $\text{Li}_2\text{S}$  as a cathode after the surface reaction with various transition-metal salts (denoted as  $\text{Li}_2\text{S}/\text{M}$ ). (f) Cell cycling performance of  $\text{Li}_2\text{S}/\text{M}$  at  $C/10$  rate. ....36

**Figure 3.3.** (a) Galvanostatic discharge curve of the Mn/Li<sub>2</sub>S cells with increasing amounts of Mn(acac)<sub>2</sub> additive. EIS spectra of the (a) freshly assembled Li<sub>2</sub>S and Mn/Li<sub>2</sub>S cells with different amounts of additive, (b) Li<sub>2</sub>S and 9% Mn/Li<sub>2</sub>S cells with increasing rest time in the as-prepared state, and (c) Mn/Li<sub>2</sub>S cells with increasing amounts of additive before (light dashed lines) and after cycling .....38

**Figure 3.4.** Morphological characterization of the cathode after cell operation. Morphologies of (a) Li<sub>2</sub>S, (d) Li<sub>2</sub>S/Mn, and (g) Li<sub>2</sub>S/Fe before cell cycling. Morphologies of (b) Li<sub>2</sub>S, (e) Li<sub>2</sub>S/Mn, and (h) Li<sub>2</sub>S/Fe (h) after the first charge. Morphologies of (c) Li<sub>2</sub>S, (f) Li<sub>2</sub>S/Mn, and (i) Li<sub>2</sub>S/Fe after the first discharge .....40

**Figure 3.5.** (a) UPS schematic showing the photoemission (PE) occurring from the polycrystalline Au, Li<sub>2</sub>S and Li<sub>2</sub>S/Fe samples before cycling. The vertical blue arrows represent the UV photon energy (21.2 eV). (b) Polycrystalline Au, Li<sub>2</sub>S, Li<sub>2</sub>S/Fe, and Li<sub>2</sub>S/Mn photoemission spectra. (c) Detailed valence band region of the spectra in (b), showing the calculation of the valence band maxima (VBM) for the Li<sub>2</sub>S and Li<sub>2</sub>S/Fe cells. (d) Energy band diagram summarizing the location of the vacuum levels and valence band maxima for the polycrystalline Au, Li<sub>2</sub>S, Li<sub>2</sub>S/Mn, and Li<sub>2</sub>S/Fe samples. The vertical gray areas highlight the pristine cells. The ionization energy (i.e., the energy required for an electron to be removed from the surface, which translates to the distance between the VBM and the vacuum level) is displayed on the right axis as the black open circles .....42

**Figure 3.6.** XPS sulfur 2p region spectra after background subtraction for (a) pristine cells, (b) cells after the first charge, and (c) cells after the first discharge. (d) Comparison of the sulfur 2p spectra for the Li<sub>2</sub>S/Mn cells in the pristine, charged, and discharged states. ....46

**Figure 3.7.** XPS of the (a) Mn 2p spectra for the Li<sub>2</sub>S/Mn cell before and after charge and (b) Fe 2p spectra of the Li<sub>2</sub>S/Fe cell before and after charge. The signals have been scaled to normalize the intensity before and after charge. The charged Fe 2p signal shown is the corresponding region from the survey spectrum.....48

**Figure 3.8.** TOF-SIMS depth profiles for the Li<sub>2</sub>S/Mn cells before charge (dashed line), after charge (solid line), and after discharge (dotted line) of the (a) Mn<sup>+</sup> secondary ion yield, (b) MnS<sup>+</sup> yield normalized to the Mn<sup>+</sup> yield, and (c) LiMnS<sup>+</sup> yield normalized to the Mn<sup>+</sup> yield. Profiles for Li<sub>2</sub>S/Fe cells before charge (dashed line), after charge (solid line), and after discharge (dotted line) of the (d) Fe<sup>+</sup> secondary ion yield, (e) FeS<sup>+</sup> yield normalized to the Fe<sup>+</sup> yield, and (f) LiFeS<sup>+</sup> yield normalized to the Fe<sup>+</sup> yield.....49

**Figure 3.9.** TOF-SIMS depth profiles normalized to the overall transition-metal secondary ion yield for (a) LiMn<sup>+</sup> in the Li<sub>2</sub>S/Mn cells and (b) LiFe<sup>+</sup> in the Li<sub>2</sub>S/Fe cells. ....51

**Figure 3.10.** TOF-SIMS depth profiles for the  $\text{Li}_2\text{S}/\text{Mn}$  cells (blue lines),  $\text{Li}_2\text{S}/\text{Fe}$  cells (black lines), unmodified  $\text{Li}_2\text{S}$  cells (red lines), and commercial  $\text{Li}_2\text{S}$  powder (green line) (a) before charge, (b) after first charge, and (c) after first discharge. (d) Schematic of the proposed reaction mechanism and resultant particle morphology for the  $\text{Li}_2\text{S}/\text{Mn}$  cell (i) before and (ii) after charge and for the  $\text{Li}_2\text{S}/\text{Fe}$  cell (iii) before and (iv) after charge. The  $\text{Li}_2\text{S}/\text{Fe}$  charged schematic represents the failure of the encapsulant layer leading to a relatively homogenous film depositing on the CNF current collector. The inset profiles in (d) represent the expected TOF-SIMS depth profiles for the ratio of  $\text{LiM}^+$  yield to  $\text{M}^+$  yield, where M stands for the transition-metal.....54

**Figure 3.11.**  $\text{LiOH}^+$  to  $\text{Li}_3^+$  ratio as a function of sputtering time (i.e., depth) for the  $\text{Li}_2\text{S}$ ,  $\text{Li}_2\text{S}/\text{Fe}$ , and  $\text{Li}_2\text{S}/\text{Mn}$  cells after the first charge and discharge. Comparison of the amounts of surface degradation products, *i.e.*  $\text{LiOH}$ , induced by the first charge and discharge processes for the 3 cells. The  $\text{Li}_2\text{S}/\text{Fe}$  and  $\text{Li}_2\text{S}/\text{Mn}$  cells show the highest and the lowest  $\text{LiOH}^+$  to  $\text{Li}_3^+$  ratio, respectively. ....56

**Figure 4.1.** XRD pattern of the synthesized  $\text{Li}_2\text{S}_x$  after initial filtration from THF. Crystalline  $\text{Li}_2\text{S}$  peaks are identified and indexed. ....65

**Figure 4.2.** XPS sulfur 2p region spectrum of the synthesized  $\text{Li}_2\text{S}_x$  after initial filtration from THF. The background-subtracted data points are indicated with triangular markers. The deconvolved  $\text{Li}_2\text{S}$ -type (red line), terminal-type (blue line), and bridging-type (green line) signals are plotted along with the fit (dashed grey line) from summing the deconvoluted signals. ....67

**Figure 4.3.** XPS sulfur 2p spectrum collected for the (a) as-synthesized  $\text{Li}_2\text{S}_x$  and (b) elemental sulfur, along with schematic illustrations of the physical interpretation of the  $\text{Li}_2\text{S}$ -type (red), terminal-type (blue), bridging-type (green), and elemental-type (orange) sulfur peaks. (c) Lithium 1s, (d) oxygen 1s, and (e) carbon 1s spectra collected for the as-synthesized  $\text{Li}_2\text{S}_x$  with two (lithium and oxygen) or three (carbon) peaks used to fit the signal. ....70

**Figure 4.4.** (a) Photograph of the observed color change with sequential filtrations, with the first filtration on the left and the 9<sup>th</sup> filtration second from the right. The rightmost vial contains the DME/DOL blank solution. (b) Linear scale and (c) log scale UV-vis spectra of the filtrate collected after selected filtrations (4<sup>th</sup> - blue, 5<sup>th</sup> - red, 8<sup>th</sup> - green, 9<sup>th</sup> - purple) of the synthesized  $\text{Li}_2\text{S}_x$ . The expanded region in (d) shows the interference patterns apparent in later filtrations. The magnified region is identified by the dashed grey rectangle in (c). ....73

**Figure 4.5.** UV-vis spectra of the filtrates collected during the filtration of the synthesized  $\text{Li}_2\text{S}_x$ . (a) Linear scale and (b) log scale spectra of the 4<sup>th</sup> and 5<sup>th</sup> filtrates; (c) linear scale and (d) log scale spectra of the 8<sup>th</sup> and 9<sup>th</sup> filtrates; and (e) linear scale and (f) log scale spectra of the 1<sup>st</sup> and 9<sup>th</sup> filtrates and a prepared  $\text{Li}_2\text{S}_6$  reference solution (black line). The peak assignments are inferred from those given by Barchasz *et al.* for lithium polysulfides in TEGDME.<sup>33</sup> ....74

**Figure 4.6.** Background-subtracted, post-sputtering XPS sulfur 2p spectra for (a) filtered, synthesized  $\text{Li}_2\text{S}_x$  and (b) commercial, reference  $\text{Li}_2\text{S}$ . The deconvolved  $\text{Li}_2\text{S}$ -type (red line), terminal-type (blue line), and bridging-type (green line) signals are plotted along with the fit (dashed grey line) from summing the deconvolved signals. The inset of each figure isolates the terminal-type and bridging-type signals. ....76

**Figure 4.7.** The XPS sulfur 2p spectra before and after sputtering are shown with deconvolved peaks for (a) synthesized  $\text{Li}_2\text{S}_x$  and (b) commercial reference  $\text{Li}_2\text{S}$ . The dashed lines are the pristine data and the solid lines are the sputtered data. Just the terminal-type (blue lines), bridging-type (green lines), and sulfite-type (purple lines) peaks are shown for (c) synthesized and (d) commercial powders. (e) Carbon 1s deconvolved peaks before (dashed lines) and after (solid lines) sputtering for the synthesized powder. (f) Lithium 1s data and two-peak fits for the synthesized powder before (dashed lines) and after (solid lines) sputtering. Arrows in the figure show changes in individual peaks with sputtering.....78

**Figure 4.8.** (a) The apparatus used to filter the as-synthesized product from THF on the Schlenk line is shown, with the collected yellow precipitate in the center. (b) The color variation in the  $\text{Li}_2\text{S}_x$  samples discharged electrochemically, with the THF-only filtered sample on the left, the  $1 \times$  DME/DOL filtered sample in the center, and the  $3 \times$  DME/DOL filtered sample on the right. (c) Comparison of the THF-only filtered powder and the filtered powder collected after electrochemical analysis verified all soluble polysulfides had been removed. (d) White color of commercial  $\text{Li}_2\text{S}$  slurry cast onto CNF current collectors. ....81

**Figure 4.9.** Comparison of the background-subtracted S 2p spectra for (a)  $\text{Li}_2\text{S}$  from Alfa Aesar stored in a glovebox used for sulfur battery research and (b)  $\text{Li}_2\text{S}$  from Aldrich tested immediately after opening in a glovebox not used for sulfur battery research. The insets show the relative ratio of terminal-type (blue lines) and bridging-type (green lines) sulfur atoms in the peak deconvolution. (c) XPS survey spectra of freshly exposed lithium metal in the glovebox used for sulfur research.....83

**Figure 4.10.** Galvanostatic discharge curves at  $50 \mu\text{A cm}^{-2}$  to 1.8 V vs.  $\text{Li/Li}^+$  for the synthesized  $\text{Li}_2\text{S}_x$  powder after only THF filtration (green line), one filtration from DME/DOL (blue line), and three filtrations from DME/DOL (red line).....85

**Figure 4.11.** Galvanostatic discharge curves at  $50 \mu\text{A cm}^{-2}$  to 1.8 V vs.  $\text{Li/Li}^+$  for different loadings, from 0 mg (control, in red) to 2.4 mg (0.3 mg - black, 0.6 mg - blue, 1.2 mg - green, 2.4 mg - orange) of commercial reference  $\text{Li}_2\text{S}$  (a) before and (b) after background subtraction. The inset of (a) shows the appearance of the  $\text{Li}_2\text{S}$ -loaded CNF paper current collectors with increasing loading (from left to right).....86

**Figure 4.12.** Galvanostatic discharge curves at  $50 \mu\text{A}$  for (a) commercial  $\text{Li}_2\text{S}$ -loaded and (b) control cells with CNF current collectors of decreasing size as seen in the photograph of each cell above the corresponding graph. (c) Raw and (d) background-subtracted galvanostatic discharge curves for commercial  $\text{Li}_2\text{S}$ -loaded CNF (red) and nickel foam (grey) current collectors.....89

**Figure 4.13.** (a) Schematic of the iterative approach to calculating the residual soluble polysulfide concentration with sequential cycling. (b) Photographs of the supernatants (top row) and filtrates (bottom row) collected for the first three electrochemically-monitored filtrations. (c) The iterative filter-free approach to extracting the remaining soluble polysulfides after the solid particles began passing through the filter. The photograph in the top right of (c) shows the supernatants collected from the first extraction (left) and second extraction (right). .....91

**Figure 4.14.** Background-subtracted galvanostatic discharge curves at  $50 \mu\text{A cm}^{-2}$  for catholytes prepared from the supernatant solution above synthesized  $\text{Li}_2\text{S}_x$  after sequential polysulfide extractions with DME/DOL. (a) Includes the capacity (black line) observed for the solution above the as-synthesized sample before any further polysulfide extraction in DME/DOL. (b) Shows an expanded view of the area indicated by the grey box in (a) and includes only the 1<sup>st</sup> (blue), 2<sup>nd</sup> (green), and 3<sup>rd</sup> (red) sequential extractions. ....94

**Figure 4.15.** (a) Raw and (b) background-subtracted galvanostatic discharge curves at  $100 \mu\text{A cm}^{-2}$  to 1.8 V vs.  $\text{Li/Li}^+$  for CNF paper control (red line), commercial  $\text{Li}_2\text{S}$  (blue line), and synthesized  $\text{Li}_2\text{S}_x$  after complete extraction of soluble polysulfides (black line). ....95

**Figure 4.16.** (a) Raw and (b) background-subtracted galvanostatic discharge capacities for cells prepared with as-received commercial  $\text{Li}_2\text{S}$  (green) and washed and nano-sized to  $< 100 \text{ nm}$  particle size (blue) commercial  $\text{Li}_2\text{S}$ . The background reference cells (dashed lines) in (a) were assembled using CNF current collectors punched from the same batch of CNF paper used for the corresponding  $\text{Li}_2\text{S}$ -loaded cell. ....98

**Figure 5.1.** Photographs of **(a)** as-prepared  $\text{Li}_2\text{S}$  target and **(b)** target after extended deposition. Photographs during X-ray excitation in XPS chamber of **(c)** unannealed sputter-deposited  $\text{Li}_2\text{S}$  film, **(d)** 600 °C annealed sputter-deposited  $\text{Li}_2\text{S}$  film, and **(e)** 600 °C annealed, compressed  $\text{Li}_2\text{S}$  powder illustrating intense violet fluorescence for annealed  $\text{Li}_2\text{S}$ . Photographs of color variation in **(f)** unannealed and **(g)** 600 °C annealed  $\text{Li}_2\text{S}$  films deposited with gradient thickness on single substrates. The indicated thicknesses are calculated for the films after annealing.....106

**Figure 5.2.** **(a)** Dependence of QCM-determined deposition rate with sputtering power at 3 mTorr. **(b)** Dependence of deposition rate on chamber pressure at 50 W power.....107

**Figure 5.3.** XRD of an  $\text{Li}_2\text{S}$  film grown on Ir-coated corundum before annealing (red curve), after annealing at 200 °C (purple curve), and after annealing at 600 °C (green curve). The insets are magnified views of the three strongest  $\text{Li}_2\text{S}$  peaks. ....109

**Figure 5.4.** SEM of the post-annealed film cross-sections after **(a)** 20 minutes and **(b)** 560 minutes of deposition. The inset in **(a)** shows the same deposition before annealing. The bright regions are sputter-deposited Ir contrast layers and the substrates are single crystal silicon. ....110

**Figure 5.5.** (a) Shirley background-subtracted XPS spectra for the S 2p sulfide region for unannealed (red curve), 500 °C annealed (blue curve), and 600 °C annealed (green curve) films. The spectra are fit with doublets for the Li<sub>2</sub>S-type (dashed lines) and terminal-type (dotted lines) sulfur atoms, and the sum of these fits are shown (solid lines). The 600 °C curve was fit with only an Li<sub>2</sub>S type doublet. The inset shows a magnified view of the polysulfide region, highlighting the fit in this region. (b) Raman spectra for a film before (red curve) and after (blue curve) annealing, with peak positions labeled. (c) UV-vis spectra of a DME/DOL solution used to solubilize polysulfides from unannealed (red curve) and 600 °C annealed (green curve) films.....112

**Figure 5.6.** Galvanostatic charge of unannealed as-deposited Li<sub>2</sub>S films (red curve), unannealed films pre-treated with DME/DOL (purple curve), and 600 °C annealed film (green curve) at 2 μA cm<sup>-2</sup> (solid line) or 1 μA cm<sup>-2</sup> (dashed line) for the unannealed films and 500 nA cm<sup>-2</sup> for the annealed film. (a) Full charge for all three cells to 3.0 V (vs. Li/Li<sup>+</sup>); the theoretical Li<sub>2</sub>S charge capacity for an annealed film after 4 h deposition at 2.2 nm min<sup>-1</sup> is indicated by the dashed grey line. (b) Immediate start of the charge process, with the open-circuit voltages (OCV) for each cell indicated. ....116

**Figure 5.7.** Galvanostatic charge and discharge curves after the first charge for DME/DOL pre-treated unannealed Li<sub>2</sub>S cells cycles at (a) 2 μA cm<sup>-2</sup> and (b) 1 μA cm<sup>-2</sup> .....119

**Figure 5.8.** Normalized TOF-SIMS depth profiles for an as-deposited thick  $\text{Li}_2\text{S}$  film on a polished tungsten-coated substrate. Profiles are shown for  $^{34}\text{S}_2^-$  (blue curve),  $^6\text{LiS}^-$  (red curve),  $^6\text{Li}^-$  (green curve), and  $\text{W}_2^-$  (black curve) molecular fragments. Below the profiles is a schematic of the different regions in the context of the proposed deposition mechanism. ....120

**Figure 5.9.** TOF-SIMS depth profiles for a ratio of the normalized  $^{34}\text{S}_2^-$  molecular fragment to the  $^6\text{LiS}^-$  fragment for unannealed (red curve) and 600 °C annealed (blue curve) films after deposition for **(a)** 15 minutes (~30 nm), **(b)** 38 minutes (~80 nm), **(c)** 71 minutes (~160 nm), and **(d)** 131 minutes (~300 nm). The dashed line at a ratio of unity represents an idealized profile for a homogenous single-component film. The substrate was Ir-coated single crystal silicon. ....122

**Figure 5.10.** **(a)** Background-subtracted S 2p XPS region spectra of the surface of unannealed sulfide films after deposition in the direct (red curve) and indirect (purple curve) configuration. Two doublets (dashed and dotted lines) are used to fit the spectra. **(b)** XRD patterns for indirect and direct depositions as well as a reference pattern for orthorhombic sulfur.124

**Figure 5.11.** (a) Deposition rate at selected deposition powers, pressures, and rate monitor positions. Green triangles are at 40 mTorr, blue squares are at 5 mTorr, and black circles are at 3 mTorr. Open markers indicate the QCM was in an indirect position and closed markers indicate the QCM was directly above the target. (b) Thickness of QCM measured deposition at 60 W and 3 mTorr as a function of time in the direct configuration after QCM had spent no time (red curve), 8 h (green curve), and 18 h (blue curve) in the indirect position. (c) Deposition rate at 50 W and 40 mTorr as a function of angle and (d) horizontal distance between the substrate the thickness monitor. The inset schematics illustrate the definition of these parameters. (e) Schematic of the various relevant processes hypothesized to lead to the observed deposition rates. (1) High-angle backscattering of Li. (2) Low-angle forward scattering of S. (3) Redeposition of Li on target. (4) Low energy thermalized deposition of S on substrate surface. (5) Resputtering of low surface binding energy sulfur from substrate. (6) Ballistic deposition of Li into substrate film. (7) Thermalized deposition of Li and S species throughout chamber. ....125

**Figure 6.1.** Calculated thickness for  $\text{Li}_2\text{S}$  films of increasing pre-sputter and deposition time vs. FWHM for the  ${}^6\text{LiS}^-$  secondary ion fragment ToF-SIMS profile. The dashed line is a linear least-squares fit passing through the origin for the data. ....133

**Figure 6.2.** Schematic illustrating the pore model used, illustrated with two populations of regular cylindrical pores, of diameters  $d_{\text{pore},1}$  and  $d_{\text{pore},2}$ .134

**Figure 6.3.** Representative OCV measured over 30 minutes for  $\text{Li}_2\text{S}$  films of increasing thickness. Additionally the OCV measured before charge is included for the  $\text{Li}_2\text{S}_4$  and  $\text{Li}_2\text{S}_8$  catholytes as well as the highly annealed  $\text{Li}_2\text{S}$  film from Figure 5.4, which was verified by XPS to contain no measurable sulfur-sulfur bonding .....136

**Figure 6.4.** Galvanostatic (a) first charge and (b) subsequent discharge for a  $3.5 \mu\text{m}$  thick  $\text{Li}_2\text{S}$  film at  $2 \mu\text{A cm}^{-2}$  (blue curve) and  $5 \mu\text{A cm}^{-2}$  (red curves). The theoretical capacity is  $530 \mu\text{Ah}$ . .....137

**Figure 6.5.** First charge at different rates of  $\text{Li}_2\text{S}$ -free iridium-coated planar current collectors with 1.2 M LiTFSI in DME/DOL electrolyte and lithium metal anodes. The inset is a magnified view of the initial charge region. The dotted lines indicate a potential of 3.4 V (vs.  $\text{Li}/\text{Li}^+$ ), below which no oxidation plateaus were observed. ....138

**Figure 6.6.** Galvanostatic charge curves for 100 nm  $\text{Li}_2\text{S}$ -equivalent (14 mM) and 50 nm  $\text{Li}_2\text{S}$ -equivalent (7 mM) of  $\text{Li}_2\text{S}_4$  catholyte at different rates with a bare planar iridium current collector. The theoretical capacities are indicated by dashed lines. ....139

**Figure 6.7.** Galvanostatic first charge and subsequent discharge curve of a 37 mM  $\text{Li}_2\text{S}_8$  catholyte containing 0.2 mg of sulfur ( $2 \mu\text{A cm}^{-2}$  rate). The equivalent thickness sulfur deposition after charge as well as the theoretical sulfur thickness assuming complete sulfur oxidation are indicated. ....140

- Figure 6.8.** Galvanostatic charge curves for films of  $\text{Li}_2\text{S}$  of approximately (a) 30 nm, (b) 40 nm, (c) 70 nm, (d) 90 nm, (e) 160 nm, (f) 290 nm, (g) 550 nm, and (h) 1100 nm. The theoretical charge capacity for each thickness is indicated by a vertical dashed line. ....142
- Figure 6.9.** Pore-filling model for a close-packed array of cylindrical pores as a function of pore diameter at (a and c)  $C/2$  and (b and d)  $C/10$  rates. (a and b) Calculated gravimetric capacity vs. local charge density and (c and d) local charge density vs. deposited  $\text{Li}_2\text{S}$  thickness. The dashed line in (c and d) represent the limiting local charge density calculated for a 0.1 V overpotential given thickness  $\text{Li}_2\text{S}$  deposit and using the least restrictive conductivity from Table 6.2. ....145
- Figure 6.10.** Modeled data for conductive carbons using the pore model parameters of Table 6.3, based on the measured pore structures in Ding *et al.*<sup>170</sup> The blue curves plot the gravimetric charge capacity versus the thickness of  $\text{Li}_2\text{S}$  deposited and the red curves plot the local charge density as a function of thickness  $\text{Li}_2\text{S}$  deposited. The dashed line represents the charge/thickness envelope beyond which the charge ceased. ....150
- Figure 6.11.** Calculated gravimetric charge capacity vs. local charge density as a function of charge rate for a model of the cathode structures in (a) Strubel *et al.*<sup>75</sup> and (b) Chung *et al.*<sup>171</sup> Calculated local charge density vs.  $\text{Li}_2\text{S}$  thickness for a model of (c) Strubel *et al.*<sup>75</sup> and (d) Chung *et al.*<sup>171</sup> The dashed line in (d) indicates the charge/thickness envelope calculated from the experimental data in Figure 6.8. ....151

**Figure 6.12.** Surface plot of the charge capacity realizable by a regular array of close-packed cylindrical pores as a function of charge rate and pore diameter.  
(b) A magnified region of the dashed region in (a). The combination of charge rate and pore diameter from Moon *et al.*<sup>43</sup> is indicated by a star.

.....152

# Chapter 1: Introduction

## 1.1. INTRODUCTION TO LITHIUM-SULFUR BATTERIES

The global demand for energy coupled with concerns for climate change have motivated a move away from fossil fuels, necessitating new energy sources and increased electrification.<sup>1-4</sup> Both of these needs have driven demand for improved energy storage, as electrification of transportation infrastructure requires high-energy density batteries,<sup>5</sup> while grid-scale storage is needed to allow intermittent green power sources (particularly wind and solar) to replace significant fractions of baseload power generation.<sup>6</sup> Both applications demand significant improvements in the cost per kilowatt-hour of storage, while vehicular batteries must simultaneously exhibit high gravimetric and volumetric energy and power densities to be practical.<sup>5-7</sup>

Currently, lithium-ion batteries are the dominant storage technology for electric vehicles, while several different technologies ranging from high-temperature metals<sup>8</sup> to aqueous systems,<sup>9</sup> as well as lithium-ion chemistries, are being explored for stationary grid-scale storage.<sup>10,11</sup>

Lithium-sulfur (Li-S) batteries and related chemistries have emerged in recent years as a leading contender for a next-generation storage technology, with promising properties from both energy density and cost perspectives.<sup>1,7,12-16</sup> The active cathode material in a simple Li-S battery is elemental sulfur, an extremely cheap bulk chemical, particularly in comparison to the transition-metal oxides generally employed in traditional lithium-ion batteries.<sup>17</sup> Additionally, Li-S is an example of a conversion chemistry, where the entire electrode volume reacts, as opposed to an intercalation chemistry wherein lithium ions shuttle in and out of relatively stable host materials. As a

result, the theoretical energy density of conversion materials on a weight or volume basis can be a full order of magnitude greater than intercalating materials.

An ideal Li-S battery in the charged state consists of sulfur as the cathode and metallic lithium as the anode. The theoretical gravimetric capacity for each electrode is 1,672 mAh g<sup>-1</sup>-sulfur and 3,860 mAh g<sup>-1</sup>-lithium. The cell in the fully discharged state is composed of lithium sulfide (Li<sub>2</sub>S), thus the theoretical gravimetric capacity for a perfectly balanced cell is 1,167 mAh g<sup>-1</sup>-Li<sub>2</sub>S. A high-performance lithium-ion battery might be comprised of a LiNi<sub>1/3</sub>Co<sub>1/3</sub>Mn<sub>1/3</sub>O<sub>2</sub> (NMC) cathode with a gravimetric capacity as high as 200 mAh g<sup>-1</sup>-NMC paired with a graphite cathode (372 mAh g<sup>-1</sup>-graphite).<sup>18,19</sup> A perfectly balanced cell with this couple would have a theoretical capacity of 130 mAh g<sup>-1</sup>. From these simple calculations, the motivation to realize practical Li-S batteries becomes abundantly clear.

### 1.1.1. Materials properties

The principal stable, equilibrium solid species of a Li-S battery are lithium, sulfur, and lithium sulfide. Lithium is an oxygen and moisture-sensitive, alkali metal. It has a room temperature density of 0.535 g cm<sup>-3</sup> and is a metallic conductor. Lithium reacts slowly with oxygen to form LiO<sub>2</sub>, and more aggressively with water to form LiOH and H<sub>2</sub>. Lithium metal melts at 180.5 °C.<sup>20</sup>

Elemental sulfur is a stable insulator. In its most stable state at room temperature, sulfur exists as cyclic S<sub>8</sub> molecules and crystallizes in an orthorhombic phase (JCPDS No. 08-0247). It has a room temperature density of 2.07 cm<sup>3</sup> g<sup>-1</sup> and a conductivity near 6.1 x 10<sup>-15</sup> S m<sup>-1</sup>.<sup>21</sup> Sulfur melts at 119.6 °C, and sublimates rapidly above 90 °C.<sup>22</sup>

Li<sub>2</sub>S is a strongly insulating, oxygen- and moisture-sensitive ionic solid. It crystallizes in an antifluorite phase (JCPDS No. 23-0369). It has a room temperature

density of  $1.66 \text{ g cm}^{-3}$  and does not melt until  $938 \text{ }^\circ\text{C}$ .<sup>23</sup> It has a bandgap between 3.5 and  $3.7 \text{ eV}$ <sup>24-26</sup> and its inherent conductivity has been calculated to be theoretically as low as  $1.9 \times 10^{-24} \text{ S m}^{-1}$ .<sup>27</sup>  $\text{Li}_2\text{S}$  reacts slowly with oxygen to form  $\text{Li}_2\text{SO}_4$ , and readily with moisture to form  $\text{LiOH}$  and evolve  $\text{H}_2\text{S}$ .

### 1.1.2. Electrolytes

Traditional organic carbonate lithium-ion battery electrolytes such as  $\text{LiPF}_6$  in ethylene carbonate and diethyl carbonate (EC/DEC)<sup>1</sup> are not suitable for battery chemistries utilizing metallic lithium.<sup>12</sup> The most common organic electrolyte for Li-S batteries is a 1 : 1 volumetric mixture of 1,3-dimethoxyethane (DME) and 1,2-dioxolane (DOL), hereafter referred to as DME/DOL. Lithium triflate ( $\text{LiTF}$ ) or lithium bis(trifluoromethanesulfonyl)imide ( $\text{LiTFSI}$ ) are the most commonly employed salts. Tetraethyleneglycol dimethylether (TEGDME) and dimethylsulfoxide (DMSO) are also relatively commonly employed organic liquids.<sup>28</sup> There has been a recent push to develop semisolid polymer electrolytes<sup>29</sup> as well as solid-state ceramics, such as thio-LISICON glasses.<sup>30,31</sup>

### 1.1.3. Mechanism

The mechanism of operation for a liquid electrolyte Li-S battery is significantly more complex than a traditional lithium-ion battery due to its conversion nature. In each full half-cycle (charge or discharge), the cathode undergoes two solid/solution phase changes.<sup>7,15</sup> On discharge, elemental sulfur is first reduced by lithium, forming a long-chain, soluble polysulfide, generally identified as  $\text{Li}_2\text{S}_8$ .<sup>32</sup> These soluble polysulfides then undergo a series of chemical disproportionation and electrochemical reduction reactions, forming a series of shorter-chain soluble polysulfides down to  $\text{Li}_2\text{S}_4$  and  $\text{Li}_2\text{S}_3$ .<sup>32,33</sup> In the final stages of discharge, solid sulfides are formed, either  $\text{Li}_2\text{S}$ , or an insoluble  $\text{Li}_2\text{S}_2$

species.<sup>24,34–37</sup> The existence and/or role of  $\text{Li}_2\text{S}_2$  has been a source of debate in the literature.<sup>32,38,39</sup> Similarly, the precise speciation, the role of radicals,<sup>40</sup> and the individual reactions among the soluble polysulfide species have been intensely studied.<sup>32,33,38–40</sup> These reactions occur in reverse during charge, though some consensus has emerged that  $\text{Li}_2\text{S}_4$  is the first soluble polysulfide observed.

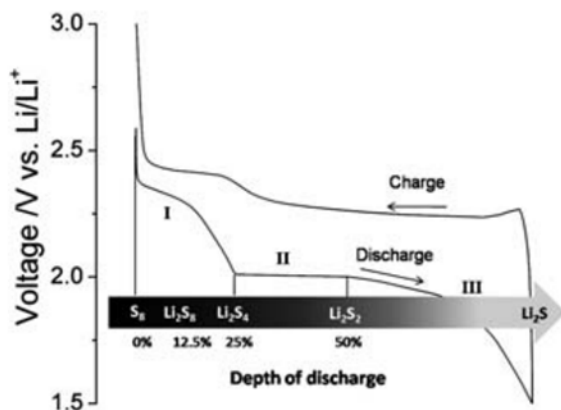


**Figure 1.1.** Typical discharge and charge curve of a liquid electrolyte Li-S battery versus depth of discharge, showing the upper and lower plateaus on discharge, and the average polysulfide stoichiometry. Reproduced from Ji and Nazar<sup>14</sup> with permission of The Royal Society of Chemistry.

The initial two-phase reduction of sulfur produces an “upper” voltage plateau during discharge around  $\sim 2.4$  V (vs.  $\text{Li}/\text{Li}^+$ ).<sup>15</sup> The series of single-phase solution reactions among the polysulfides results in a sloping voltage profile between 2.4 V and 2.0 V (vs.  $\text{Li}/\text{Li}^+$ ). Finally two-phase reactions forming  $\text{Li}_2\text{S}_2$  and  $\text{Li}_2\text{S}$  result in a long “lower” voltage plateau around 2.0 V vs.  $\text{Li}/\text{Li}^+$ . Notably, reactions associated with the formation of solid sulfides account for 75% of the theoretical capacity for Li-S batteries.<sup>12,14,15</sup> A typical galvanostatic Li-S charge and discharge cycle is shown in Figure 1.1 from Ji and Nazar.<sup>14</sup> The sloping voltage region separates into several closely spaced plateaus at low temperature, as the chemical interconversion of polysulfides slows down

relative to the rate of electrochemical reduction reactions.<sup>41,42</sup> As a result, individual polysulfide reduction reactions can be identified.

The reaction mechanism for solid-state Li-S batteries is markedly different than for liquid electrolyte cells, generally only exhibiting a single plateau.<sup>30</sup> This behavior has been associated with direct formation of  $\text{Li}_2\text{S}$  or  $\text{Li}_2\text{S}_2$  from sulfur,<sup>37</sup> and has also been identified in configurations with highly confined sulfur, which is believed to sterically hinder formation of long-chain polysulfides.<sup>43</sup>

## **1.2. CHALLENGES AND APPROACHES TO LI-S BATTERIES**

While the conversion nature of the Li-S system promises many benefits, it also is the root of many challenges preventing the realization of practical, commercial batteries. Many of the problems have their roots in the insulating nature of the active materials as well as the reactivity and mobility of the intermediates. While not a challenge, *per se*, the relatively low average discharge voltage,  $\sim 2.1$  V (vs.  $\text{Li}/\text{Li}^+$ ), of the Li/S couple relative to common lithium-ion chemistries (ranging from  $\sim 3.5$  V to as high as 5 V in some systems),<sup>1,44</sup> tempers some of its relative advantages when considering the more practical energy density as opposed to specific capacity. The NMC cathode described above, with an average discharge potential of  $\sim 3.7$  V (vs.  $\text{Li}/\text{Li}^+$ ) has an energy density of around 740  $\text{Wh kg}^{-1}$ ,<sup>17,45</sup> while the value for Li-S is about 2600  $\text{Wh kg}^{-1}$ ,<sup>12</sup> not quite a fourfold theoretical improvement.

### **1.2.1. Insulating solid materials**

Because both end members of the cycling mechanism, sulfur and  $\text{Li}_2\text{S}$ , are strong electronic insulators, they are not suitable for use in electrochemical devices at practical rates without significant modification. The most basic approach to addressing this

problem is to form a composite cathode with sulfur and a conductive material, typically carbon.

### 1.2.1.1. Conductive composites

**Table 1.1.** Overview of sulfur content and performance for a variety of sulfur/graphene composites. Adapted with permission from Manthiram *et al.*<sup>12</sup> Copyright 2014. American Chemical Society.

material	S content <sup>a</sup>	method	electrolyte (binder)	performance	ref
sulfur-graphene nanosheets	22/18	heat treatment	LiTFSI in PEGDME 500 (PVdF)	600 mA h g <sup>-1</sup> (40th cycle, 0.03C)	48
Nafion-coated FGSS	72/57	heat treatment	LiTFSI in DOL + DME (PVdF)	960 mA h g <sup>-1</sup> (100th cycle, 0.1C)	49
sulfur-polyacrylonitrile-graphene composite	47/38	heat treatment	LiPF <sub>6</sub> in EC + DMC (PTFE)	1200 mA h g <sup>-1</sup> (50th cycle, 0.1C)	50
sulfur-graphene oxide composite	66/46	heat treatment	LiTFSI in PYR14TFSI + PEGDME (-)	954 mA h g <sup>-1</sup> (50th cycle, 0.1C)	51
CTAB-coated sulfur-graphene oxide composite	80/56	heat treatment	LiTFSI in PYR14TFSI + DOL + DME (SBR/CMC)	740 mA h g <sup>-1</sup> (1500th cycle, 0.02C)	52
graphene/PEG-wrapped sulfur	70/56	solution-based method	DOL + DME (-)	550 mA h g <sup>-1</sup> (140th cycle, 0.5C)	53
graphene-enveloped sulfur	87/78	solution-based method	LiTFSI in DOL + TEGDME (-)	550 mA h g <sup>-1</sup> (50th cycle, 0.2C)	54
sulfur-hydroxylated graphene composite	50/40	solution-based method	LiCF <sub>3</sub> SO <sub>3</sub> in DOL + DME (PVdF)	1021 mA h g <sup>-1</sup> (100th cycle, 0.5C)	55

<sup>a</sup>The sulfur content is presented as S concentration in the composite/S concentration in the electrode (wt %).

Carbon is generally the conductive additive of choice, due to its low weight, ability to form a variety of porous structures with high surface area, and potentially low cost (depending on synthesis method).<sup>7,12-14,16,38</sup> The relatively recent outburst of interest in Li-S research can largely be traced to the first report of good sulfur utilization and cyclability using a carbon/sulfur composite by Ji *et al.*<sup>15</sup> Various electroactive conductive additives have been explored, including TiS<sub>2</sub> and conductive, electroactive polymers.<sup>46,47</sup> A key parameter when evaluating sulfur/carbon composites is the sulfur content—the weight percent of sulfur in the cathode. The extent of sulfur/carbon composite research can be seen by examining Table 1.1 from Manthiram *et al.*,<sup>12</sup> which summarizes sulfur content and performance from a selection of specifically sulfur/graphene composites.<sup>48-55</sup> While excellent performance can often be realized in terms of the sulfur utilization (*i.e.*,

capacity in mAh g<sup>-1</sup>-sulfur) when using low sulfur content, the specific cathode capacity (*i.e.*, capacity in mAh g<sup>-1</sup>-composite) suffers greatly.

### ***1.2.1.2. Polysulfide catholytes***

An approach that has been employed to mitigate the difficulty of working with insulating active materials is to cycle the battery as a liquid cell, utilizing only the soluble polysulfides, with their relatively high ionic mobility.<sup>56</sup> While this approach could be appealing for stationary grid-scale applications, an all-liquid cell cycling between Li<sub>2</sub>S<sub>8</sub> and Li<sub>2</sub>S<sub>4</sub> end members has a theoretical capacity of only 198 mAh g<sup>-1</sup>-Li<sub>2</sub>S<sub>8</sub>.

### ***1.2.1.3. Active material loss***

Related to the insulating nature of the solid reaction end members, the morphology of solid deposition is critically important to the long term cycling stability of a Li-S battery. If large Li<sub>2</sub>S or sulfur particles form, they may require excessive iR overpotentials to induce oxidation or reduction, leading to active material loss.<sup>57</sup> Additionally, if electrodeposition occurs on a surface other than a connected, conductive current collector, it will be electrically isolated, and generally inactive (though there are reports that electrically isolated particles can be charged through coupled chemical and redox reactions).<sup>58</sup>

## **1.2.2. Lithium metal anodes**

While lithium metal is extremely appealing as an anode due to its unparalleled gravimetric energy density, it also presents a host of problems.<sup>59</sup> Lithium metal has a tendency to plate either as a low-density mossy growth or, at higher rates, as rapidly growing dendrites.<sup>60</sup> These can lead to either problematic volume expansion and/or more significantly, shorting of the cell, leading to failure and potentially a fire. As a result, using metallic lithium is generally considered a potential safety hazard, especially when

coupled with a flammable organic electrolyte. Many schemes exist to treat the lithium metal surface to form an ideally stable, ionically-conductive solid electrolyte interphase (SEI) layer,<sup>61</sup> but no reliable method has emerged to guarantee a passively safe cell when using a lithium metal anode and a liquid organic electrolyte.

### 1.2.2.1. $\text{Li}_2\text{S}$ cathodes

A promising approach has been to design a cell assembled in the discharged state with  $\text{Li}_2\text{S}$  as the cathode and a lithium-metal free anode such as hard carbon or silicon.<sup>62</sup> There have been problems utilizing  $\text{Li}_2\text{S}$  cathodes, as their initial electrochemistry is often significantly more sluggish than a similarly prepared composite using sulfur.

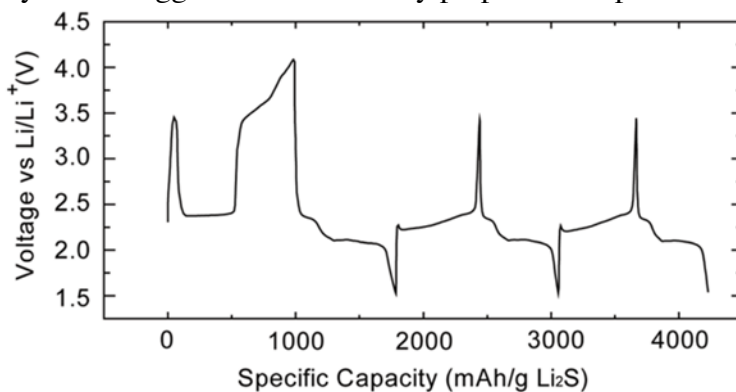


**Figure 1.2.** Activation effect over three galvanostatic charge/discharge cycles. In the first cycle, the cell must be charged over 3.5 V (vs.  $\text{Li}/\text{Li}^+$ ) to initiate charge. In subsequent cycles, no overpotential requirements are observed, and the Li-S cell cycles normally. Adapted with permission from Yang *et al.*<sup>63</sup> Copyright 2012. American Chemical Society.

Yang *et al.*<sup>63</sup> identified that large  $\text{Li}_2\text{S}$  particles could be ‘activated’ by applying a large overpotential during the first charge cycle, after which the cell would function like a typical Li-S battery, as shown in Figure 1.2. The origin of this activation effect has been the subject of some debate, with its root being ascribed to size effects, phase nucleation, surface conductivity, or poor charge transfer between  $\text{Li}_2\text{S}$  and the electrolyte.<sup>58,63–65</sup> In

each of these contexts, nano-sizing, surface treatments, and electrolyte additives have been employed to significantly reduce the activation overpotential.<sup>66</sup>

### ***1.2.2.2. Volume expansion***

The 78.7% volume expansion when going from solid sulfur to solid Li<sub>2</sub>S is an additional concern when designing a cell architecture. Without careful consideration, this large volume change during each cycle can cause pulverization of the cathode structure. Rational design of porous cathode structures must account for this effect.

### **1.2.3. Electrolyte effects**

While generally stable within the cycling window, the typically employed DME/DOL electrolytes will oxidize noticeably above 3.0 V and reduce below 1.8 V (vs. Li/Li<sup>+</sup>), which is one reason it is important to mitigate the activation effect when using Li<sub>2</sub>S as a starting material. The metallic lithium anode is generally reactive, which leads to a couple deleterious effects, namely polysulfide shuttling and self-discharge.<sup>28</sup>

#### ***1.2.3.1. Shuttle effect***

Because the Li-S charge mechanism utilizes highly mobile solution-state intermediates, unwanted transport from cathode to anode can occur, coupled with unwanted redox reactions. In this case, during charge, relatively oxidized long-chain polysulfides migrate to the lithium anode, where they react, forming two short-chain polysulfides, which must then both be oxidized to finish the charge. As a result, the coulombic efficiency of the cell is drastically impacted.<sup>67</sup>

Two primary strategies have been employed to combat the shuttle effect. The first is to add additives to the electrolyte which passivate the lithium metal surface, preventing the chemical reactions between polysulfides and lithium. The two most common approaches are to add lithium nitrate<sup>68,69</sup> (LiNO<sub>3</sub>) or very high concentrations of the salt

(e.g., 1.85 M LiTF or LiTFSI)<sup>67,70-72</sup>. There are downsides with these approaches however, as LiNO<sub>3</sub> is quite reactive, and will reduce in the cycling window around 1.8 V (vs. Li/Li<sup>+</sup>), leading to undesirable electrolyte discharge products on the cathode. High salt concentrations lead to highly viscous electrolytes, which degrades rate capability and pore-filling.

The second strategy is to trap the polysulfides on the cathode side of the cell so that they never reach the lithium metal anode. For example, an interlayer can be inserted between the separator and cathode as a polysulfide trap.<sup>73</sup> These have been shown to be very effective in improving the coulombic efficiency, but the addition of an electrochemically inactive solid layer will degrade the cell-level energy density and consume more electrolyte. The other approach here is to design a conductive framework for the composite that inherently retains generated polysulfides, either through microporous traps,<sup>74,75</sup> or surface functionalization that favors polysulfide adsorption.<sup>55,76,77</sup>

### ***1.2.3.2. Self-discharge***

Related to the shuttle effect is the self-discharge effect, whereby inactive cells will slowly lose capacity.<sup>70</sup> Sulfur is slowly solubilized by the electrolyte, where it can then migrate to the lithium anode and react, leading to capacity loss. Similar strategies to those employed to address the shuttle effect can be used to improve the self-discharge behavior.<sup>12</sup>

### 1.2.4. Cell-level energy density

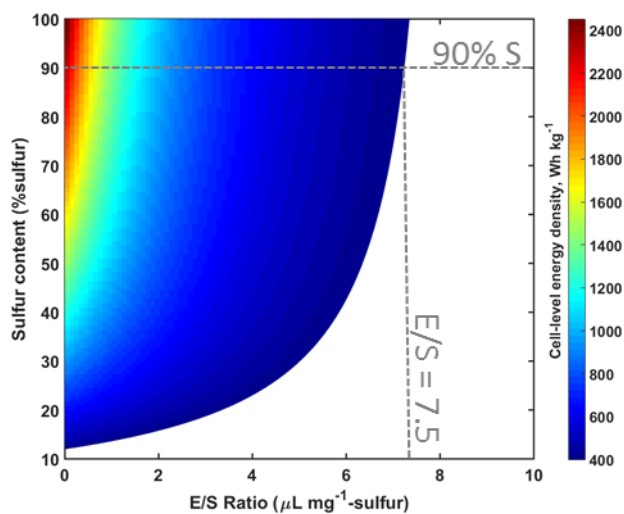


**Figure 1.3.** Surface plot of the cell-level energy density for a Li-S battery based on the sulfur content and electrolyte/sulfur (E/S) ratio. The color scale begins at  $400 \text{ Wh kg}^{-1}$  to indicate the threshold at which the Li-S energy density can compete with high-performance lithium-ion batteries at the cell-level. The highest E/S ratio that meets this threshold at 90 wt.% sulfur content is indicated.

The net result of many of the challenges discussed above is that by the time all the conductive material, binders, additives, interlayers, and electrolyte have been added to the cell to produce a Li-S battery with long cycle life and high sulfur utilization, the cell-level energy density ends up being similar to or significantly worse than existing lithium-ion batteries. As a result, there has been a recent emphasis on considering the cell-level energy density of the Li-S battery.<sup>78</sup> While increasing the sulfur content has long been an aim of the research community, decreasing the electrolyte is now emerging as the key concern on this front. The electrolyte/sulfur (E/S) ratio, defined as the volume of electrolyte per mass of sulfur is a convenient parameter to describe the electrolyte requirements for a Li-S battery.<sup>78</sup> Significant quantities of electrolyte are consumed by high-surface area carbons, reactive lithium anodes, and for solubilizing polysulfides during cell operation. The cell-level energy density as a function of sulfur content and

E/S ratio is shown in Figure 1.3. Lithium-ion batteries require comparatively low volumes of electrolyte. Even assuming an overly conservative equivalent “E/S” ratio of 0.5, the NMC/graphite cell described above would yield a cell-level energy density near 400 Wh kg<sup>-1</sup>. From Figure 1.3, we can see that even with a very high sulfur content of 90 wt% (and assuming 100% utilization), a Li-S battery must have an E/S ratio of less than 7.5 to compete favorably. There have only recently been reports of reasonable performance below this threshold. Strubel *et al.*<sup>75</sup> reported a cell with E/S of 4 that cycled well. The sulfur content and utilization (at a rate of C/10) were both ~ 60%, which would yield a cell-level energy density of ~ 360 Wh kg<sup>-1</sup>, not quite reaching the target energy density proposed above.

### **1.2.5. All-solid-state cells**

An area of increasing research is the fabrication of all-solid-state cells using a solid-state electrolyte.<sup>28,30,31,79</sup> This configuration, in theory, mitigates many of the concerns with liquid cells, including cell shorting, polysulfide shuttle, and E/S ratio. While there has been much progress, the low inherent ionic conductivity and cost associated with solid electrolytes, as well as the difficulty in maintaining good electrode/electrolyte contact in an all-solid-state cell, have limited the realization of cells with practical performance, particularly at high rates.<sup>79</sup>

## **1.3. CONCLUSIONS AND FUTURE DIRECTIONS**

While much progress has been made in overcoming some of the inherent materials challenges, particularly low conductivity, associated with Li-S batteries, as well as in understanding the relevant reaction mechanisms, a number of outstanding challenges persist before practical, commercially-viable cells can be realized. Of the utmost concern is decreasing the E/S ratio while maintaining high sulfur content and

performance to improve the cell-level energy density. To this end, improved understanding of the fundamental materials properties and chemistry of the solid-state sulfides that exist around the discharged state is of the utmost importance. The limiting behavior of these materials determines the ideal conductive composite structure to maximize utilization while minimizing carbon and electrolyte requirements.

Additionally, the development of improved cells that address the inherent problems of the lithium anode is critical, whether coupling  $\text{Li}_2\text{S}$  with a lithium metal-free anode or realizing all-solid-state cells. Again, improvement in our understanding of the properties of the solid-state sulfides is key, particularly the charge mechanism of  $\text{Li}_2\text{S}$ . For all-solid-state cells, new synthesis methods that address the inherent difficulty in assembling these cells with good electrochemical transport properties are also needed.

#### **1.4. OBJECTIVES**

The primary objective of this dissertation is to improve our understanding of the properties, limitations, and mechanisms of solid-state lithium sulfides, particularly  $\text{Li}_2\text{S}$  and any metastable electrolyte-insoluble lithium polysulfides. Through improved understanding of these materials we can enable improved, rational design of cathode structures, and ultimately all-solid-state cells. Additionally, improved understanding of these solid-state sulfides will better our ability to understand and construct lithium metal-free Li-S batteries based around  $\text{Li}_2\text{S}$  cathodes. After a brief description of key experimental techniques in Chapter 2, this dissertation will focus on a number of problems associated with the use and understanding of solid-state lithium sulfides.

After providing an introduction in Chapter 1 and describing the experimental details in Chapter 2, Chapter 3 presents a technique to modify the surface of large  $\text{Li}_2\text{S}$  particles with transition metal sulfides, delivering both improvements in the activation

behavior as well as good cycling performance. This chapter focuses on the mechanism by which the surface modification influences the cycling behavior of  $\text{Li}_2\text{S}$  and why only certain transition-metal sulfides deliver performance improvements. This mechanistic understanding serves to decouple the activation effect and surface conductivity from the cycling performance of  $\text{Li}_2\text{S}$  cathodes.

Chapter 4 directly approaches the question of the existence and electrochemical activity of  $\text{Li}_2\text{S}_2$ . A direct chemical synthesis is employed to isolate the material to the extent possible. Improving our understanding of the properties of insoluble solid polysulfides lets us consider the degree to which cell architecture and cycling parameters need to be tailored to promote electrochemical reduction of these materials.

Chapter 5 presents a new method for the preparation of thin and thick films of  $\text{Li}_2\text{S}$  via sputter deposition. This technique will allow for the fabrication of chemically and morphologically well-defined  $\text{Li}_2\text{S}$  structures so that fundamental and limiting materials properties can be probed and novel characterization techniques can be employed. The characterization of metastable and amorphous structures produced by this technique can also offer new insights into the potential to use metastable solid-state sulfides as electroactive materials. Finally, the techniques introduced can see application for the fabrication of novel all-solid-state structures.

Chapter 6 utilizes the ability to systematically synthesize  $\text{Li}_2\text{S}$  films of arbitrary thickness to determine the maximum thickness of active material that can be charged at practical rates. This determination is then used to design a model to enable rational design of composite cathodes that will maximize cell-level energy density.

Finally, Chapter 7 presents a brief summary of the research presented in this dissertation and offers prospects for future work building off these results.

## Chapter 2: Experimental Methods

### 2.1. DESCRIPTION OF SYNTHESIS TECHNIQUES AND APPARATUS

A brief overview of synthetic techniques employed in this dissertation is presented here. In every case, relevant details and specific applications will be provided in the experimental sections of individual chapters.

#### 2.1.1. Drop-cast electrodes

To introduce active material to a wide range of conductive current collectors, slurries were prepared of the active material ( $\text{Li}_2\text{S}$  or sulfur), along with any chemical additives, added into electrolyte. The slurries were magnetically stirred overnight, and then added dropwise by a micropipette into freestanding current collectors.

##### *2.1.1.1. Self-weaving carbon nanofiber paper current collectors*



**Figure 2.1.** Self-woven CNF paper removed from filter paper after vacuum drying.

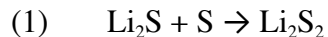
To avoid the need for a substrate current collector (such as aluminum foil) in addition to the conductive carbon employed in a cathode, carbon nanofiber (CNF) paper was prepared by a simple self-weaving technique. In a typical preparation, 175 mg of

CNFs with diameters between 100 nm and 150 nm were added to 650 mL of deionized water and 50 mL of isopropanol. This solution was ultrasonicated to disperse the CNFs, and then slowly vacuum-filtered through medium-porosity filter paper (Fisherbrand, P5). By applying only a slight vacuum, the CNFs interweave as they settle, producing a strong, flexible paper. After heating at 60 °C in a vacuum oven overnight, the CNF paper could be removed from the filter paper in a single piece, as seen in Figure 2.1.

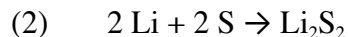
## 2.1.2. Chemical synthesis techniques

### 2.1.2.1. Direct $\text{Li}_2\text{S}_2$ synthesis in ammonia

Direct chemical synthesis of  $\text{Li}_2\text{S}_2$  was attempted via two approaches after Dubois *et al.*<sup>80</sup> In one scheme, a stoichiometric 1 : 1 molar ratio of lithium sulfide and elemental sulfur powder were added to a Schlenk (Kjeldahl) flask in an argon glovebox. This reaction follows the scheme:



In the alternative scheme, a stoichiometric 1 : 1 molar ratio of divided lithium metal and elemental sulfur were added to the Schlenk flask. This reaction follows the scheme:



The sealed flask was then transferred from the glovebox to a Schlenk line under ultra-high purity (99.999%) argon. Research-grade (99.999%) ammonia gas was flowed over divided sodium metal (to further dry the gas), then condensed in the Schlenk flask at – 78 °C using a bath of dry ice in acetone. The solution was magnetically stirred to dissolve and react the two reactants. The temperature of the ice bath was progressively raised to – 44 °C, while the ammonia was slowly evaporated under an increasing vacuum overnight.

### ***2.1.2.2. $\text{Li}_2\text{S}_x$ filtration scheme***

The nominal  $\text{Li}_2\text{S}_2$  product from these reactions was initially filtered from dry tetrahydrofuran (THF) through a glass frit filter using a rotary apparatus on the Schlenk line. This filtered product was sealed in a Schlenk flask and transferred to an argon glovebox. Further filtration from DME/DOL was then performed on a vacuum line installed in the glovebox, through filter paper with progressively smaller pore sizes, down to 100 nm nylon filters.

### **2.1.3. Physical vapor deposition (PVD)**

To deposit solid-state air-sensitive alkali sulfide films, as well as potentially sulfide glasses and all-solid-state cells, a dedicated apparatus for synthesis and processing of these materials via sputter deposition and/or thermal evaporation was built at Oak Ridge National Laboratory.

#### ***2.1.3.1. Basics of thermal evaporation***

In a typical thermal evaporation process, the material to be deposited is placed in a refractory conductive crucible, such as tantalum. High current is passed through the crucible to raise the temperature via resistive heating. The temperature is increased to near the melting or sublimation point of the material, resulting in a high vapor pressure. The vapor molecules diffuse through a small aperture after which they can condense on the relatively cool substrate. Thermal evaporation is performed under ultra-high vacuum (UHV) conditions (typically less than  $1 \times 10^{-8}$  torr), so vapor molecules exiting the aperture reach the substrate by line-of-sight transport, without being scattered by the gas.

#### ***2.1.3.2. Basics of sputter deposition***

In a simple direct current (DC) sputter deposition process, electrons are stripped from a rare gas to generate a plasma via an applied potential between two parallel

electrodes, one containing the “target” material, and the other the substrate on which the film will be deposited.<sup>81</sup> The separation of electrons and positive ion cores produces a series of regions of relatively high and low electric fields. Of particular importance is the “dark space”, a region of high potential and low ion density above the target. The high potential in this region accelerates positive ions through the dark space, where they impact the target with high energy, producing cascading collisions, which can eject (“sputter”) material with high energy. The ratio of sputtered species per incident ion is termed the “sputtering yield” for that species.<sup>82</sup>

Sputtered species are produced with much higher thermal energy than the surrounding gas. At relatively high pressure (above  $\sim 10$  mTorr), almost all of the sputtered species will be thermalized by collision with gas molecules, and the energy of most sputtered species will approach the average of the gas. At lower pressures, sputtered species can reach the substrate ballistically, *i.e.* via line-of-sight high energy deposition with no gas collisions.<sup>83</sup>

To increase the rate of ion-target collisions, and to allow lower deposition pressures, a magnetron sputter process is employed. In this technique a high-strength magnet is placed underneath the sputter target, producing crossed electric and magnetic fields, which confine positive ions near the surface of the target, drastically increasing the sputter rate. Whereas simple DC sputtering requires chamber pressures typically above 40 mTorr, a DC magnetron sputter deposition typically occurs around 10 – 15 mTorr.<sup>81</sup>

DC sputter deposition is only appropriate for conductive targets, as a large positive charge will build up on the surface of an insulator, repelling further impact by positive plasma species. To overcome this problem, radio-frequency (RF) sputter deposition is employed.<sup>81</sup> In this approach, an oscillating RF potential is supplied by a matching network to a pair of capacitively coupled electrodes (the target and substrate) to

generate an oscillating RF electric field. The low mass electrons can oscillate with the electric field, while the relatively massive positive ions cannot, allowing the electrons to compensate for charge buildup on the target surface. RF sputtering will produce an oscillating field above both electrodes, and as a result both the target and substrate will be sputtered. However, by electrically connecting the substrate to the chamber walls, the ratio of the substrate electrode area to the target electrode area becomes very large. As a result, the electric field across the target dark space is much greater, leading to preferential ion acceleration and sputtering of the target.<sup>81,82</sup> Additionally, a magnetron can be employed along with the RF field to further increase the density of positive ions sputtering the target. With this approach, lower density plasmas can be sustained (as the RF potential efficiently strips electrons from the gas), generally allowing sputtering down to 1 mTorr, where line-of-sight deposition dominates over thermalized deposition for target-substrate spacings less than 10 cm.<sup>83</sup>

### ***2.1.3.3. Apparatus***

The system centered around a custom-built (Vacuum Technologies, Inc.) stainless steel chamber integrated directly into the reinforced floor of a high-purity argon glovebox. The top half of the chamber was fitted to a manual lift to allow access to the interior of the chamber from inside the glovebox. The chamber contained a series of CF flanges to integrate all components for accomplishing and monitoring the PVD process.

The following relevant components, indicated by numbers in Figure 2.2 showing the system under construction and in operation, are described along with their function.



**Figure 2.2.** Photographs of the components built for the PVD synthesis of air-sensitive materials. The components with numerical annotations are described in the text. (a) The assembled chamber and processing components in the glovebox, prior to glovebox window installation. (b) The bottom (fixed) half of the deposition chamber. (c) The interior of the top half of the deposition chamber in the open position for sample loading. (d) The top of the deposition chamber in the closed position during a  $\text{Li}_2\text{S}$  sputter deposition. The intense pink ring visible in the mirror is the optical emission from the argon plasma confined above the  $\text{Li}_2\text{S}$  target. (e) The electronics cabinet with the hardware for controlling the deposition and vacuum systems.

- (1) Bottom-mounted sputter gun for deposition on planar substrates facing down
- (2) Top-mounted sputter gun for deposition on powders
- (3) Rotary drive for agitation of powders to promote even coating
- (4) Speaker for agitation of powders to promote even coating
- (5) High-current and thermocouple contacts for thermal evaporator to allow deposition of lithium metal for all-solid-state batteries
- (6) Rotary apparatus for positioning of substrate and quartz crystal microbalance (QCM)
- (7) QCM sensor crystal for thickness monitoring
- (8) Substrate holder
- (9) QCM oscillator and RF feedthrough
- (10) Turbomolecular pump to reach base pressure of  $1.0 \times 10^{-6}$  torr for sputter deposition
- (11) Manual gate valve to throttle vacuum to deposition pressure during deposition
- (12) Cryogenic pump to reach base pressure of  $1.0 \times 10^{-9}$  torr for evaporation
- (13) Pneumatic gate valve to regulate cryopump
- (14) Rotary vane roughing pump for initial chamber evacuation and backing of turbomolecular pump
- (15) Gas inlet from mass flow controller (MFC) for primary sputtering gas.
- (16) Manual valve regulating MFC inlet
- (17) Ionization gauge for measurement of pressures below  $1.0 \times 10^{-3}$  torr
- (18) Capacitance manometer pressure gauge for measurement of intermediate pressures during sputter deposition

- (19) Convection gauge for measuring intermediate pressures to atmospheric pressure during pump down and sputter deposition
- (20) Thermocouple gauge for measuring near atmospheric pressure during pump down
- (21) Cut-off valve to protect capacitance manometer outside pressure range.
- (22) Water chiller and cooling lines for thermal regulation of target during sputtering
- (23) Manual lift for chamber access
- (24) Hydraulic press for target preparation
- (25) 1000 °C furnace for target preparation and sample annealing
- (26) Balance for target preparation
- (27) RF matching networks and electrical bias control for RF sputter deposition
- (28) Pressure gauge controllers
- (29) Mass flow controller
- (30) Turbomolecular pump controller
- (31) High-current power supply for thermal evaporation
- (32) QCM controller
- (33) Rotary drive controller
- (34) Pneumatic gate valve controller
- (35) Thermocouple readout for evaporator

#### ***2.1.3.4. Target preparation***

To prepare the  $\text{Li}_2\text{S}$  sputtering target, 7.20 g of commercial  $\text{Li}_2\text{S}$  powder (Alfa Aesar, 99.9% trace metals basis) was loaded into the pellet die and pressure was slowly increased to 2000 psi and allowed to rest under pressure for 12 h. The pressure was then

increased to 4400 psi and held for 8 h. The compressed pellet was extracted from the die and transferred to the furnace where it was heat treated for 1 h at 200 °C, followed by 1.5 h at 450 °C, and finally 12 h at 600 °C. The resultant 1/8” thick pellet was transferred to the vacuum chamber, where a 200 nm thick chromium layer was sputter deposited on one side, followed by sputter deposition of 200 nm of nickel, and finally 200 nm of gold. A ¼” thick, 2” copper support plate likewise underwent sequential sputter deposition of 200 nm of chromium, nickel, and gold. A ca. 1.5” diameter piece of indium foil was placed between the gold-coated sides of the support plate and the Li<sub>2</sub>S target, and placed in the furnace at 200 °C for 1 h. This treatment allowed the indium to melt and alloy with the gold layers, bonding the Li<sub>2</sub>S pellet to the support plate, forming the finished target.

#### 2.1.3.5. Substrate preparation

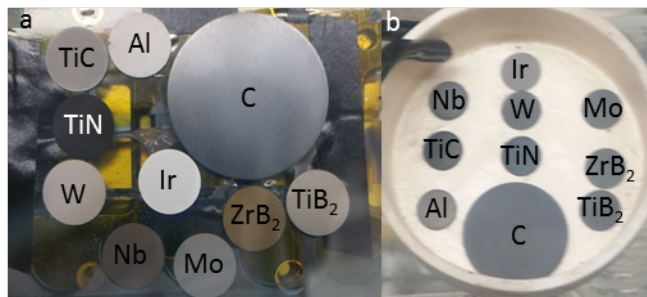


**Figure 2.3.** Sputter-coated metallic species evaluated as Li<sub>2</sub>S conductive substrates (a) after annealing but before Li<sub>2</sub>S deposition and (b) after Li<sub>2</sub>S deposition and subsequent annealing.

For most applications, 1-cm diameter lapped or polished corundum (Al<sub>2</sub>O<sub>3</sub>) was used as the base substrate. A variety of 500 nm and 1000 nm thick sputter-deposited coatings were evaluated on these substrates to serve as a conductive surface on which to deposit Li<sub>2</sub>S. Aluminum, titanium carbide, titanium nitride, titanium boride, zirconium boride, molybdenum, niobium, iridium, and tungsten, as well as a hard carbon substrate were evaluated. Coated substrates were annealed at 650 °C, sputter deposited with Li<sub>2</sub>S,

then annealed again at 500 °C, as shown in Figure 2.3. Iridium and tungsten were ultimately selected for their refractory properties and lack of reactivity toward sulfides, with iridium generally preferred for its conductivity.

For applications requiring a near atomically smooth surface, single crystal silicon was used as the substrate. Approximately 100 nm of TiO<sub>2</sub>/Ti was sputter deposited on the silicon substrate to act as a conductive surface for Li<sub>2</sub>S deposition.

## **2.2. DESCRIPTION OF CHARACTERIZATION TECHNIQUES**

Brief overviews of the principal characterization techniques employed are presented in this section. Again, specific applications of the techniques will be described in greater detail in the experimental sections of each chapter.

### **2.2.1. Morphological techniques**

#### ***2.2.1.1. X-ray diffraction (XRD)***

X-ray diffraction was used to study the crystal structure of various sulfide materials. Diffraction patterns were collected with Cu K $\alpha$  radiation ( $\lambda = 1.5148 \text{ \AA}$ ) with a Rigaku Miniflex, typically between  $2\theta = 20^\circ$  and  $80^\circ$ . Due to the air- and moisture-sensitive nature of most materials studied, one of the two following approaches was used to protect the samples from oxidation. In the first approach, a layer of 0.1-mm thick polyimide film was used to seal the material being studied against a polyimide tape. The sealed sample was then adhered to a glass slide during the XRD scan. At low angles, the X-ray beam would pass through an increasing thickness of the film, leading to an amorphous background signal. In the second approach, an air-sensitive holder with a 0.1-mm thick domed polyimide film from Rigaku was used to protect the sample during the scan. Because the domed film is always normal to the X-ray source and detector, the

thickness film the beam passes through is minimized and approximately constant, greatly reducing the background signal.

### ***2.2.1.2. Scanning electron microscopy (SEM)***

Scanning electron microscopy (SEM), wherein a condensed beam of typically 10 keV electrons is rastered over the surface of a sample under vacuum and low energy secondary electrons generated in the sample surface are collected by a detector, was used to investigate the morphology of samples at the nanoscale. JEOL JSM-5610 and Hitachi TM3030 microscopes were used. To protect particularly air-sensitive samples from oxidation during sample loading, a glovebag was affixed over the loading port of the Hitachi TM3030. The samples, loaded onto the SEM stub in an argon glovebox were sealed in a container and transferred into the glovebag. Argon was fed into the glovebag to produce an inert environment. Then the container with the pre-loaded SEM stub was opened and transferred into the analysis chamber under argon.

### ***2.2.1.3. Quartz crystal microbalance (QCM) thickness monitoring***

A QCM thickness monitor was employed during sputter deposition to monitor the rate of film growth. This technique operates by oscillating a quartz crystal of known acoustic frequency. As material is deposited onto the crystal, the oscillation frequency decreases. By measuring the change in frequency, the mass of material deposited can be calculated based on the Sauerbrey equation,<sup>84</sup> assuming a homogenous, dense film. Gold-coated AT-cut quartz crystals were utilized as the sensor crystals.

## 2.2.2. Spectroscopic/spectrometric techniques

### 2.2.2.1. X-ray photoelectron spectroscopy (XPS)

X-ray photoelectron spectroscopy (XPS) for chemical and bonding state analysis was performed with monochromated Al  $K\alpha$  radiation ( $h\nu = 1486.5$  eV) on a Kratos AXIS Ultra DLD system with a hemispherical photoelectron kinetic energy analyzer. An electron flood gun was employed to neutralize charge build-up on insulating samples. Powder samples were embedded in indium foil to enhance conductivity and to stabilize the particles. Sputtering with an  $Ar^+$  ion beam was used to probe materials underneath their surface layer.

The basic mechanism of XPS is to use X-ray photons to excite core-level electrons to the vacuum level. The energy associated with core-level excitation is generally unique to a given element and electronic orbital.<sup>85</sup> By measuring the energy of the emitted electrons, the chemical composition of a sample can be quantified. Furthermore, slight shifts to the core-level binding energy are induced by the particular bonding environment present in a molecule. As a result, shifts in the binding energy from known references can be used to characterize the bonding and oxidation state of a sample.<sup>86</sup> Orbitals with electrons in different spin states will exhibit multiplet peaks due to the slight difference in binding energy among the electrons. The splitting and relative intensity of the individual peaks are characteristic of individual elements and orbitals. The sulfur 2p orbital, for instance, exhibits doublet peaks separated by 1.18 eV for the  $2p_{3/2}$  and  $2p_{1/2}$  peaks, with the integrated intensity of the  $2p_{3/2}$  peak twice that of the  $2p_{1/2}$ .<sup>85</sup> This multiplet behavior must be considered when attempting to fit experimental XPS spectra to theory. The escape depth for core-level photoelectrons is generally less than 10 nm, making the technique quite surface sensitive.<sup>87,88</sup>

A custom stainless steel transfer capsule designed at the Texas Materials Institute was used to seal samples under argon in a glovebox and transfer them to the vacuum environment of the XPS chamber with no exposure to air or moisture.

#### ***2.2.2.2. Ultraviolet photoelectron spectroscopy (UPS)***

Ultraviolet photoelectron spectroscopy (UPS) was performed on the same system as XPS, but using a He 1 $\alpha$  ( $h\nu = 21.2$  eV) source to generate ultraviolet (UV) photons. Because the energy of UV photons is so much less than X-rays, rather than exciting tightly bound core-level electrons, UPS excites electrons located near the Fermi level.<sup>89</sup> As a result, the conduction and valence bands of a material can be probed, yielding insight into its electronic band structure and conductivity. Because the escape depth for low-energy electrons is significantly smaller than for core-level electrons, UPS only probes  $\sim 1$  nm of the surface.<sup>88</sup> As a result, it can be used to analyze surface conductivity specifically.

#### ***2.2.2.3. Ultraviolet/visible light spectroscopy (UV/vis)***

Ultraviolet/visible spectroscopy (UV/vis) was performed by shining light of wavelength varied from 225 nm to 825 nm through soluble materials dissolved in a carrier solvent, placed in transparent quartz 1-cm pathlength quartz cuvettes. By measuring the transmittance of light through the solution, specific wavelengths of light that are strongly absorbed by the sample can be detected. These characteristic wavelengths are specific to a particular molecule's bonding structure, and thus can be used to identify various species in solution.

#### ***2.2.2.4. Time-of-flight - secondary ion mass spectrometry (TOF-SIMS)***

Time-of-flight - secondary ion mass spectrometry (TOF-SIMS) is a highly elemental sensitive technique, in which a sample is sputtered with a low energy ion beam,

generating secondary ions that originate from the sample surface. These charged secondary ions can be directly by an electric field to select ions only of a given charge. By sputtering the sample with short, 20 ns pulses of known length, the time between sputtering and arrival of the secondary ion fragments can be precisely calculated, allowing determination of the mass of the secondary fragment. This technique can identify the presence of trace elements down to the ppm level.

By alternating low-energy sputtering with high-energy sputtering (ion milling) of the surface, a depth profile of the material can be generated, revealing information about the chemistry of buried layers. The sputtering yield of individual fragments is highly dependent on the local bonding and chemical matrix the sputtered species exist within. Care must thus be taken to normalize changes in sputtering yield of an individual fragment that are driven by changes in chemistry versus changes in the matrix when comparing depth profiles among different samples.<sup>90</sup> TOF-SIMS was performed in this work with an IONTOF GmbH TOF.SIMS 5 with a primary sputtering beam of either  $\text{Cs}^+$  or  $\text{O}_2^+$  and a pulsed secondary ion-generating  $\text{Bi}^+$  beam. Air-free sample transfer was accomplished with the same capsule as for XPS and UPS.

#### ***2.2.2.5. Raman spectroscopy***

Raman spectroscopy was performed using a solid-state 532-nm excitation laser on a WITec Alpha 300 confocal Raman microscope. The samples were sealed inside a hermetic capsule against a quartz window, to allow collection of Raman spectra without moisture exposure.

The Raman technique is an example of vibrational spectroscopy, where small excitations of individual bonds' bending and stretching modes are probed.<sup>91</sup> This allows specific insight into a molecule's bond structure. Raman activity is predicated on the

individual mode being excited causing a change in the polarizability of the molecule. As a result, certain modes that would otherwise be expected to exist may be forbidden by these selection rules, and will not be observed.<sup>92</sup>

### **2.2.3. Electrochemical techniques**

#### ***2.2.3.1. Cell fabrication***

Electrochemical testing was performed in CR2032 coin cells assembled in an argon-filled glovebox. In a typical assembly procedure, cathodes were loaded into one half of the cell, and an aliquot of electrolyte or catholyte, generally 20 to 30  $\mu\text{L}$ , was added via micropipette. A polypropylene/polyethylene separator (Celgard 2325) was then added, followed by another 20 to 30  $\mu\text{L}$  of electrolyte on the anode side. Finally a ca. 1  $\text{cm}^2$  lithium metal anode and nickel foam spacer were added to the cell. After closing with the anode-side cell cap, the battery was sealed using a cell crimping press.

#### ***2.2.3.2. Galvanostatic cycling***

Galvanostatic cycling was performed on Arbin BT-2000 multichannel cyclers. For typical Li-S battery operation, cells were cycled between 1.8 and 2.8 V (vs.  $\text{Li}/\text{Li}^+$ ). For investigations of the ‘activation’ effect for  $\text{Li}_2\text{S}$  cathodes, cells were charged as high as 4.0 V (vs.  $\text{Li}/\text{Li}^+$ ).

#### ***2.2.3.3. Cyclic voltammetry (CV)***

CV testing was performed on the Arbin multichannel cyclers or BioLogic VMP3 multichannel potentiostats to identify individual oxidation and reduction reactions occurring during cell operation. Cell potential was swept between 1.8 and 3.0 V (or 4.0 V for  $\text{Li}_2\text{S}$  cathodes) vs.  $\text{Li}/\text{Li}^+$ , at a typical scan rate of 0.05  $\text{mV s}^{-1}$ .

#### ***2.2.3.4. Electrochemical impedance spectroscopy (EIS)***

EIS was performed on the BioLogic potentiostat between a frequency range of  $10^2$  to  $10^6$  Hz. The application of EIS to battery cells is dependent on the mixed capacitive and resistive characteristics of the various electrode/electrolyte interfaces in the cell. As a result, by developing an appropriate equivalent circuit model for the cell, the EIS spectrum can be simulated and used to extract information on the charge transfer resistance and transport characteristics of the cell.<sup>93</sup> However, because the extracted data is dependent on an accurate equivalent circuit model, care must be taken when drawing conclusions from this technique on complex, changing systems. Given the number of chemical species and states involved in the conversion chemistry of a Li-S battery, this can be particularly problematic.<sup>94</sup>

#### ***2.2.3.6. Open circuit analysis***

Changes in cell chemistry at the open circuit voltage (OCV) were probed by measuring cells on the Arbin multichannel cycler over several hours with no applied current or potential. The OCV could also be used to estimate the chemical state of assembled Li-S batteries, particularly in relation to (poly)sulfide oxidation state.

## **Chapter 3: An effective lithium sulfide encapsulation strategy for stable lithium-sulfur batteries\***

### **3.1. INTRODUCTION**

The increasing consumption of limited fossil fuels is exerting global environmental concerns, requiring advances in alternative clean energy resources and the associated energy-storage devices.<sup>1-4,95,96</sup> Among all the viable energy-storage devices, high-energy-density lithium-ion batteries (LIBs) have been dominant for decades. Through continuous efforts, particularly with cell engineering, researchers have pushed the energy density of LIBs to the current stage. However, the cost and performance are unable to meet the requirements of the emerging markets for electrical vehicles and grid storage, demanding new battery chemistries with higher energy densities.<sup>97</sup> With a theoretical capacity an order of magnitude higher than that of LIBs, lithium-sulfur (Li-S) batteries are widely considered as a promising candidate for next-generation energy-storage devices.<sup>12,14,16,98-100</sup> Despite the promising prospects of the Li-S battery chemistry, its immediate practical realization is hindered by several fundamental concerns: (i) low sulfur utilization attributed to the insulating nature of sulfur and its discharge product,  $\text{Li}_2\text{S}$ ; (ii) fast capacity decay due to active-material loss in the form of soluble polysulfide species; and (iii) potential safety hazards arising with the use of lithium metal as an anode.

To mitigate the safety concerns of metallic lithium, one approach is to start with  $\text{Li}_2\text{S}$  and couple it with a lithium-free anode (silicon, tin, or graphite).<sup>62</sup> When employed

---

\* Portions of this chapter have been submitted for publication as [M. J. Klein](#), A. Dolocan, C. Zu, and A. Manthiram, "An effective lithium sulfide encapsulation strategy for stable lithium-sulfur batteries," submitted, 2017.

M. J. Klein and C. Zu carried out experimental work with assistance from A. Dolocan. M. J. Klein developed the mechanisms with A. Dolocan, and A. Manthiram supervised the research. All participated in manuscript preparation.

as a cathode,  $\text{Li}_2\text{S}$  encounters less volume expansion in the first cycle; however, similar to its sulfur cathode counterpart, it also requires efficient electron transport pathways around the insulating  $\text{Li}_2\text{S}$  particles and an effective encapsulation to reduce polysulfide dissolution.<sup>63</sup> In 2014, Seh *et al.* performed pioneering work that successfully encapsulated  $\text{Li}_2\text{S}$  with a nanocomposite strategy consisting of two-dimensional layered transition-metal disulfides that offered high conductivity and affinity for polysulfides.<sup>101</sup> The nanocomposite cathodes exhibited enhanced activity in Li-S batteries as revealed by a lower charging overpotential, and improved cycling stability up to 400 cycles. However, the process utilized nano-sized  $\text{Li}_2\text{S}$  particles and a complex processing scheme requiring high-temperature annealing of the reacted product, among other preparation steps. In addition, hierarchical carbon structures have also been used to encapsulate  $\text{Li}_2\text{S}$  forming nanocomposites;<sup>102,103</sup> however, their long-term cycling stability remains a concern considering the nonpolar nature of carbon and its lower affinity for polysulfide species with high polarity.<sup>104,105</sup> To date, a low-cost design of a stable, conductive encapsulation architecture for  $\text{Li}_2\text{S}$  is yet to be realized.

In this work, we build an encapsulation layer comprised of a transition-metal sulfide on the surface of  $\text{Li}_2\text{S}$  bulk particles via a facile strategy employing a surface chemical reaction between  $\text{Li}_2\text{S}$  and an electrolyte additive containing the transition-metal salt. It is demonstrated that the surface ionization energy of the encapsulation layer determines the initial charging overpotential of  $\text{Li}_2\text{S}$ . Moreover, while most additives generate encapsulation layers in the open-circuit configuration that are unstable during cycling, it is shown that at least one transition-metal additive, containing manganese, forms a stable encapsulation layer consisting of  $\text{MnS}$  via a chemical reaction with  $\text{Li}_2\text{S}$ . The stability of such an in-situ-formed encapsulation layer is a result of the  $\text{MnS}$  compound being chemically inactive within the cycling window. Through this

mechanistic analysis, we demonstrate that the long term cycling performance of the encapsulated  $\text{Li}_2\text{S}$  is not dictated primarily by the conductivity of the encapsulating layer.

## **3.2. EXPERIMENTAL**

### **3.2.1. Synthesis of carbon nanofiber (CNF) current collector**

To synthesize the CNF current collector, carbon nanofibers (150 mg, Fisher Scientific) were dispersed in deionized water (700 mL) and isopropyl alcohol (50 mL), ultrasonicated for 15 min, and vacuum filtered to produce the free-standing CNF film.

### **3.2.2. Electrochemical characterization**

$\text{LiCF}_3\text{SO}_3$  (98 %, Acros Organics, 1 M) and  $\text{LiNO}_3$  (1 M) in TEGDME constitutes the electrolyte. Commercial  $\text{Li}_2\text{S}$  powders were dispersed in TEG-DME and heated overnight at 50 °C, which is denoted as the pristine  $\text{Li}_2\text{S}$ . Metal acetylacetonate was added into the suspension of  $\text{Li}_2\text{S}$  in TEGDME and heated overnight at 50 °C, which is denoted as  $\text{Li}_2\text{S}/\text{M}$ . The weight ratio between metal acetylacetonate and  $\text{Li}_2\text{S}$  is 1 : 9. CR2032 coin cells were assembled in an argon-filled glovebox for electrochemical characterization. The suspension of  $\text{Li}_2\text{S}$  or  $\text{Li}_2\text{S}/\text{M}$  in TEGDME was drop cast onto the CNF current collector, followed by Celgard 2400 separator, electrolyte, and lithium metal anode. Galvanostatic cycling was conducted at room temperature with an Arbin battery cycler at 1.8 V – 3.4 V (vs.  $\text{Li}/\text{Li}^+$ ).

### **3.2.3. Morphology characterization**

Morphologies of the electrodes were examined by SEM (FEI Quanta 650 ESEM) equipped with a Bruker EDX system.

### 3.2.4. UPS and XPS characterization

The valence band spectra and x-ray photoelectron spectra of the samples were recorded with a Kratos AXIS Ultra DLD spectrometer that combines a monochromatic He 1 $\alpha$  ultraviolet (UV) source ( $h\nu = 21.2$  eV) for UPS, a monochromated Al K $\alpha$  X-ray source ( $h\nu = 1486.5$  eV) for XPS, hybrid optics (employing a magnetic and electrostatic lens simultaneously), and a multichannel plate coupled to a hemispherical photoelectron kinetic analyzer. The photoelectrons were recorded at normal emission with 50 meV energy resolution while the UV beam hits the sample at a 45° angle. An electron flood gun was used to prevent charging of the samples and the pressure in the analysis chamber was typically 10<sup>-9</sup> Torr during data acquisition. The Fermi level of the UPS instrument-sample setup was determined by the photoemission spectrum of a clean, Ar-sputtered Au polycrystalline sample. To avoid any spectral artifacts in the low kinetic energy region (i.e., ambiguities in determining the secondary cut-off) due to the secondary electrons produced in the analyzer, a -9 V constant bias was applied on the sample during the analysis. The XPS spectra binding energies were corrected to the adventitious carbon 1s peak at 284.6 eV.

### 3.2.5. TOF-SIMS characterization

For chemical analysis and depth profiling, we employ a TOF.SIMS 5 (ION-TOF GmbH, Germany 2010) instrument with a pulsed, Bi<sup>+</sup> analysis ion beam (20 ns pulse width, 30 keV ion energy, high current bunched mode with ~ 3.5 pA measured sample current) and an O<sub>2</sub><sup>+</sup> sputtering ion beam (1 keV ion energy, ~ 210 nA measured sample current). During depth profiling, the analysis beam was typically raster scanned over an area of 100 x 100  $\mu\text{m}^2$  that is centered within the regressing O<sub>2</sub><sup>+</sup> sputtered area (250 x 250  $\mu\text{m}^2$ ). The profiles were acquired in interlaced mode, i.e., the analysis was performed while the O<sub>2</sub><sup>+</sup> beam is sputtering the surface. All detected ions had positive polarity while

the mass resolution was  $>5000$  ( $m/\delta m$ ) for all detected secondary ion fragments of interest. The data were acquired at a base pressure of  $10^{-9}$  Torr. To reduce sample charging, a constant current electron beam (21 eV electron energy) was directed onto the sample during depth profiling. For XPS, UPS, and TOF-SIMS measurements, we used an in-house-built, air-free capsule to transfer the samples from a glove box and in-between instruments.

### 3.3. RESULTS AND DISCUSSION

#### 3.3.1. Encapsulation Strategy

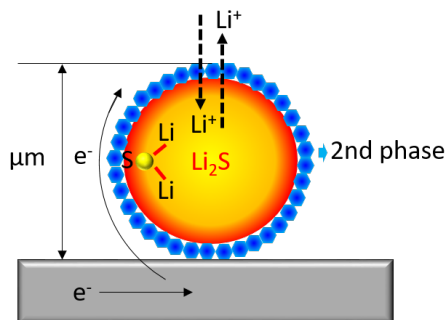


**Figure 3.1.** Schematic of the proposed  $\text{Li}_2\text{S}$  encapsulation with a stable surface layer. In this work, the second phase on the surface (in blue) is a transition-metal sulfide.

Figure 3.1 demonstrates the schematic of the encapsulation strategy. The encapsulation layer on the  $\text{Li}_2\text{S}$  bulk particles should be (i) electronically and ionically conductive; (ii) impermeable to polysulfide anions in order to mitigate material loss to the electrolyte; and (iii) robust enough to sustain repeated  $\text{Li}^+$  transport. Among several other additives containing transition metals (Cr, Fe, Ni, Co) that were tested, the manganese(II) acetylacetonate ( $\text{Mn}(\text{acac})_2$ ) additive was uniquely able to initiate surface reactions that lead to a stable a encapsulation layer during cycling. For simplicity, the

encapsulated  $\text{Li}_2\text{S}$  obtained with the addition of  $\text{Mn}(\text{acac})_2$  is hereafter referred to as  $\text{Li}_2\text{S}/\text{Mn}$  and the pristine  $\text{Li}_2\text{S}$  without such an encapsulation is referred to as  $\text{Li}_2\text{S}$ .

### 3.3.2. Electrochemical performance

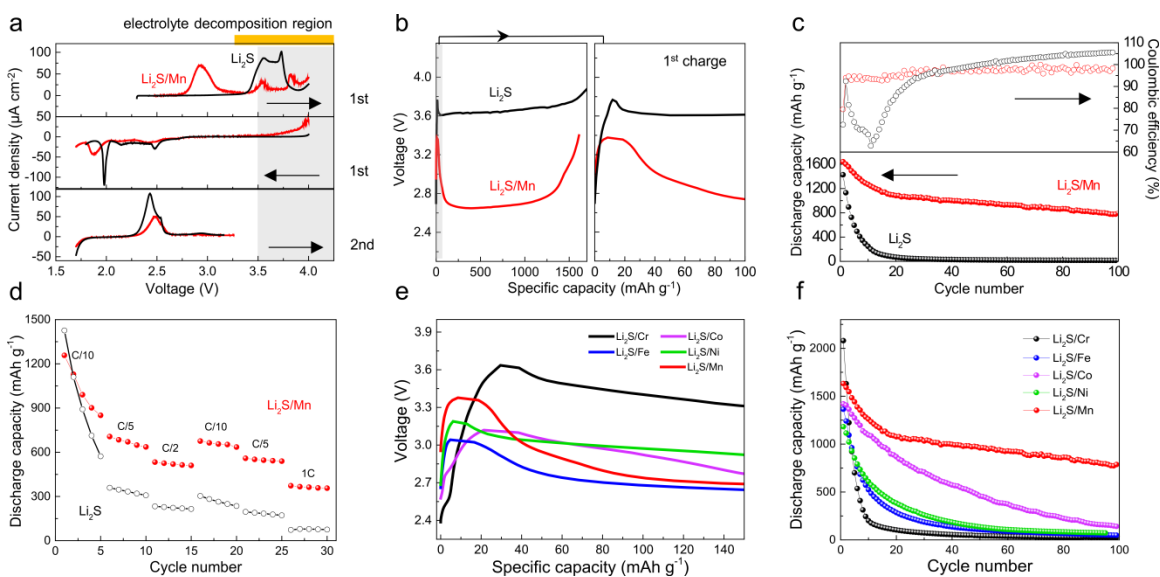


**Figure 3.2.** Electrochemical characterization: (a) CV profile, (b) voltage profile, and (c) cell cycling performance of the  $\text{Li}_2\text{S}/\text{Mn}$  and  $\text{Li}_2\text{S}$  cathodes. (d) Rate capability test. (e) Initial charging voltage profile of  $\text{Li}_2\text{S}$  as a cathode after the surface reaction with various transition-metal salts (denoted as  $\text{Li}_2\text{S}/\text{M}$ ). (f) Cell cycling performance of  $\text{Li}_2\text{S}/\text{M}$  at C/10 rate.

#### 3.3.2.1. $\text{Li}_2\text{S}/\text{Mn}$ performance

Electrochemical performance of the encapsulated  $\text{Li}_2\text{S}/\text{Mn}$  cathode was evaluated and compared with the pristine  $\text{Li}_2\text{S}$  with CR2032 coin cells (Figure 3.2). In Figure 3.2a, the cyclic voltammetry (CV) profiles of  $\text{Li}_2\text{S}/\text{Mn}$  reveal a downshifted main anodic peak centered at  $\sim 2.9$  V in the first charge compared to  $\text{Li}_2\text{S}$  with a main anodic peak above 3.5 V. Without the encapsulation layer, the  $\text{Li}_2\text{S}$  oxidation would occur concurrently with the electrolyte decomposition as indicated by the CV profile. In the subsequent discharge,

two cathodic peaks are observed at 2.4 and 1.9 V for  $\text{Li}_2\text{S}/\text{Mn}$ , indicative of the two-step conversion from sulfur to lower-order polysulfides, primarily  $\text{Li}_2\text{S}_4$ , and from lower-order polysulfides to  $\text{Li}_2\text{S}$ . There is a slight cathodic shift in the reduction peak of the  $\text{Li}_2\text{S}/\text{Mn}$  cathode, possibly due to surface reactions mediated by the sulfide encapsulant layer. During subsequent charge, both  $\text{Li}_2\text{S}$  and  $\text{Li}_2\text{S}/\text{Mn}$  exhibit anodic peaks at  $\sim 2.5$  V. The reduced charge overpotential for  $\text{Li}_2\text{S}/\text{Mn}$  was also verified with galvanostatic charge-discharge tests. As shown in Figure 3.2b, the initial charging voltage barrier is lowered from 3.8 V for  $\text{Li}_2\text{S}$  to 3.4 V for  $\text{Li}_2\text{S}/\text{Mn}$ . Moreover, the initial discharge capacity is as high as  $1142 \text{ mAh g}^{-1}$  (based on  $\text{Li}_2\text{S}$  mass) and  $1642 \text{ mAh g}^{-1}$  (based on sulfur mass) for  $\text{Li}_2\text{S}/\text{Mn}$  (Figure 3.2c). After 100 cycles,  $\text{Li}_2\text{S}/\text{Mn}$  retains reversible capacities of over  $800 \text{ mAh g}^{-1}$  (based on sulfur mass). Coulombic efficiency is stable between 96 % and 100 % for  $\text{Li}_2\text{S}/\text{Mn}$ .

Figure 3.2d demonstrates the rate capability of the  $\text{Li}_2\text{S}/\text{Mn}$  cathode, which is seen to be superior to  $\text{Li}_2\text{S}$  under various charge/discharge rates ranging from C/10 to 1C. The rate performance of the  $\text{Li}_2\text{S}/\text{Mn}$  is particularly noteworthy, given the large, micron-scale size of the  $\text{Li}_2\text{S}$  particles. The capacity up to a C/2 rate rivals that of the work of Seh et al., which used nanoscale particles and conductive coatings.<sup>[16]</sup> We believe that the initial reduction in  $\text{Li}_2\text{S}$  particle size would improve high rate performance, though at the expense of the appealing single-step procedure. This result with large particles suggests charge transfer across the MnS surface must be quite facile, with significant rate limitations appearing only at high rates (1C). Koh et al. have shown that the  $\text{Li}_2\text{S}$  charge mechanism with polysulfides in solution is dominated by redox reactions between the solid and the soluble polysulfides.<sup>58</sup>

### 3.3.2.2. Electrochemical impedance spectroscopy (EIS) data

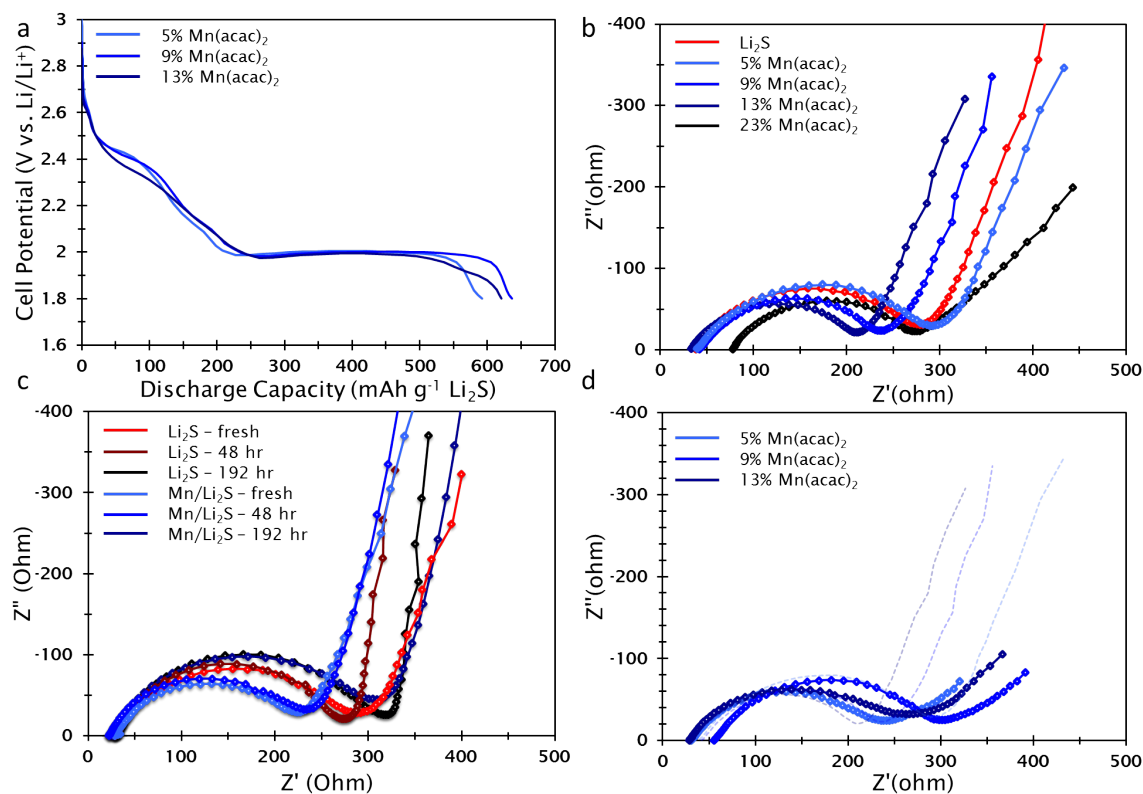


**Figure 3.3.** (a) Galvanostatic discharge curve of the Mn/Li<sub>2</sub>S cells with increasing amounts of Mn(acac)<sub>2</sub> additive. EIS spectra of the (a) freshly assembled Li<sub>2</sub>S and Mn/Li<sub>2</sub>S cells with different amounts of additive, (b) Li<sub>2</sub>S and 9% Mn/Li<sub>2</sub>S cells with increasing rest time in the as-prepared state, and (c) Mn/Li<sub>2</sub>S cells with increasing amounts of additive before (light dashed lines) and after cycling.

In light of this observation, we further conclude that the encapsulant layer readily mediates these reactions at intermediate rates. Electrochemical impedance spectroscopy (EIS) data (Figure 3.3) indicated that the charge-transfer resistance decreased for commercial Li<sub>2</sub>S modified with over 5% Mn(acac)<sub>2</sub>.

Preliminary analysis of the effect of varying the transition-metal additive amount is presented in Figure 3.3a-b for the Mn/Li<sub>2</sub>S cells. Galvanostatic discharge showed a significant increase in capacity when increasing the weight ratio of Mn(acac)<sub>2</sub> : Li<sub>2</sub>S from

1 : 20 (5 wt%) to 2 : 20 (9 wt%). Further increase saw a decrease in capacity and an increase in overpotential (reflected in lower discharge potential in the upper plateau and at the end of the lower plateau). EIS analysis showed improvement in the charge-transfer resistance of the Mn/Li<sub>2</sub>S cells up to 13 wt.% (including over the reference Li<sub>2</sub>S cell), but further increase led to a significant change in the EIS spectrum, likely reflecting excess additive remaining in the electrolyte.

Looking at the stability of the as-prepared cells with rest time (Figure 3.3c) showed almost no change for Mn-modified Li<sub>2</sub>S up to 48 h, unlike for reference Li<sub>2</sub>S, presumably reflecting excess polysulfides entering into solution. With additional rest, changes in the spectrum were apparent, confirming imperfect encapsulation of the Li<sub>2</sub>S particles by the MnS. The form of the EIS spectra after cycling are substantially modified from the as-assembled state, reflecting the many changes in the Li-S battery system with cycling, including changes in electrolyte polysulfide concentration, lithium anode surface modification, and electrolyte decomposition products on the cathode and current collector. The complexity in EIS changes and requirements for semi-empirical modeling motivated the use of UPS to directly probe changes on the cathode surface.

### ***3.3.2.3. Electrochemistry of additional transition metal additives***

Additionally, we evaluated the use of various other transition-metal salts as additives to initiate surface reaction on the Li<sub>2</sub>S surface. Cathodes composed of commercial Li<sub>2</sub>S particles were exposed to chromium (III) acetylacetonate (denoted as Li<sub>2</sub>S/Cr), iron (II) acetylacetonate (denoted as Li<sub>2</sub>S/Fe), cobalt (II) acetylacetonate (denoted as Li<sub>2</sub>S/Co) and nickel (II) acetylacetonate (denoted as Li<sub>2</sub>S/Ni) additives, and the initial charging voltage profiles are shown in Figure 3.2e. Li<sub>2</sub>S/Fe, Li<sub>2</sub>S/Co and Li<sub>2</sub>S/Ni cells exhibit less charge overpotential compared to Li<sub>2</sub>S/Mn and the pristine Li<sub>2</sub>S,

among which  $\text{Li}_2\text{S}/\text{Fe}$  displays the lowest charging barrier. However,  $\text{Li}_2\text{S}/\text{Fe}$  suffers from fast capacity decay compared to  $\text{Li}_2\text{S}/\text{Mn}$  (Figure 3.2f). Of note,  $\text{Li}_2\text{S}/\text{Cr}$  has negligible advantages compared to the pristine  $\text{Li}_2\text{S}$  in terms of initial activation, possibly due to the formation of chromium sulfide species with lower conductivity or ineffective surface reaction with transition-metal ions with higher oxidation states.

### 3.3.3. Morphological analysis

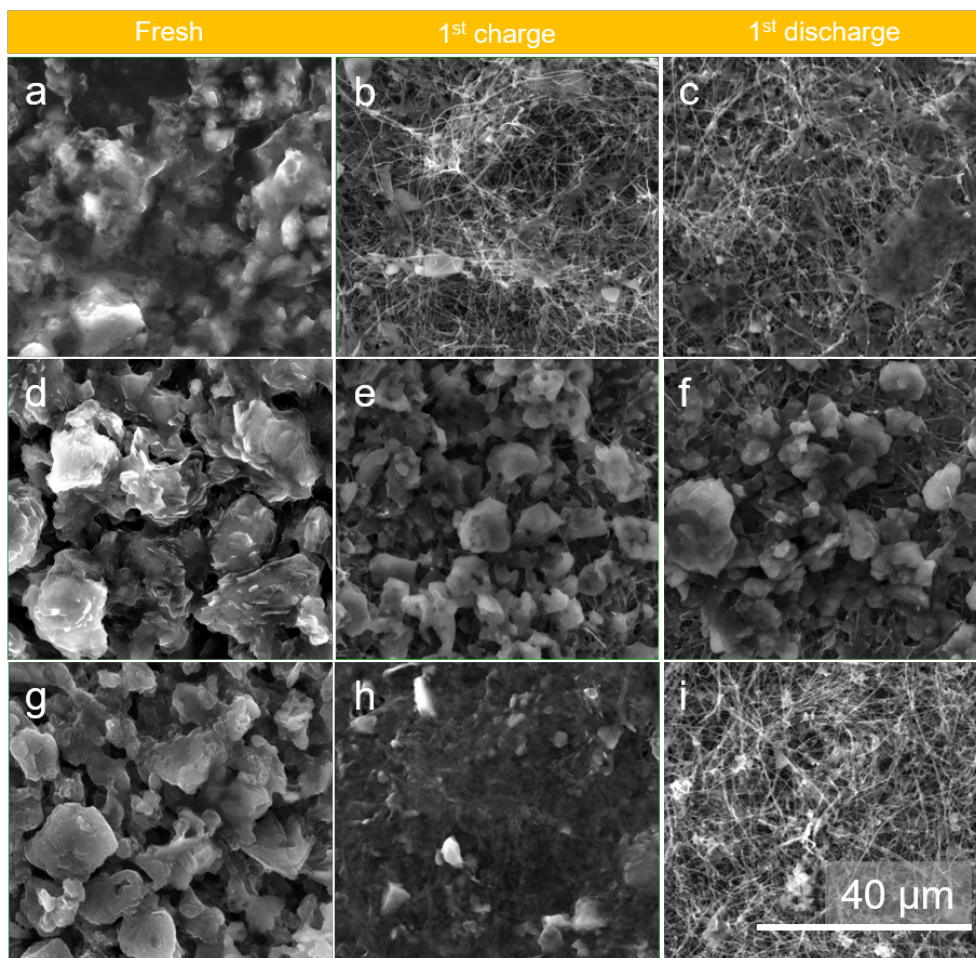


**Figure 3.4.** Morphological characterization of the cathode after cell operation. Morphologies of (a)  $\text{Li}_2\text{S}$ , (d)  $\text{Li}_2\text{S}/\text{Mn}$ , and (g)  $\text{Li}_2\text{S}/\text{Fe}$  before cell cycling. Morphologies of (b)  $\text{Li}_2\text{S}$ , (e)  $\text{Li}_2\text{S}/\text{Mn}$ , and (h)  $\text{Li}_2\text{S}/\text{Fe}$  (h) after the first charge. Morphologies of (c)  $\text{Li}_2\text{S}$ , (f)  $\text{Li}_2\text{S}/\text{Mn}$ , and (i)  $\text{Li}_2\text{S}/\text{Fe}$  after the first discharge.

To gain an understanding of the effect of the transition-metal salts on the cathode morphology with cycling, we examined the  $\text{Li}_2\text{S}/\text{Mn}$ ,  $\text{Li}_2\text{S}/\text{Fe}$ , and unmodified  $\text{Li}_2\text{S}$  cells via scanning electron microscopy (SEM) before cycling, after charge, and after discharge (Figure 3.4). We selected  $\text{Li}_2\text{S}/\text{Fe}$  as the reference case because it exhibited the best activation behavior, but significantly worse cycling performance than  $\text{Li}_2\text{S}/\text{Mn}$  (and almost identical to that of  $\text{Li}_2\text{S}/\text{Ni}$ ). A surface morphology retaining the spherical particles of the unmodified  $\text{Li}_2\text{S}$  (Figure 3.4a) persisted after reaction with manganese(II) acetylacetonate and iron (II) acetylacetonate (Figures 3.4d and 3.4g). The spherical features were retained for the  $\text{Li}_2\text{S}/\text{Mn}$  cell after charge ( $\text{Li}^+$  removal, Figure 3.4e) and discharge ( $\text{Li}^+$  incorporation, Figure 3.4f); however, the surface layer with spherical features disappeared for  $\text{Li}_2\text{S}/\text{Fe}$  during cell operation (Figures 3.4h and 3.4i). Furthermore, the morphology of the  $\text{Li}_2\text{S}/\text{Fe}$  cathode is similar to that of the pristine  $\text{Li}_2\text{S}$  after a charge and discharge.

### 3.3.4. Ultraviolet Photoelectron Spectroscopy (UPS) Analysis

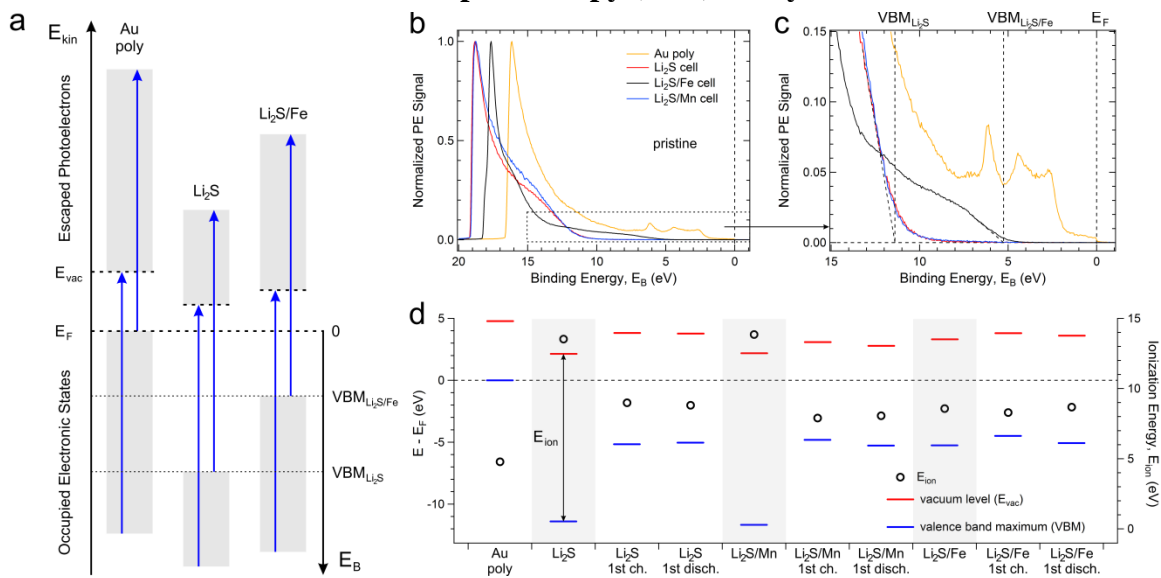


**Figure 3.5.** (a) UPS schematic showing the photoemission (PE) occurring from the polycrystalline Au, Li<sub>2</sub>S and Li<sub>2</sub>S/Fe samples before cycling. The vertical blue arrows represent the UV photon energy (21.2 eV). (b) Polycrystalline Au, Li<sub>2</sub>S, Li<sub>2</sub>S/Fe, and Li<sub>2</sub>S/Mn photoemission spectra. (c) Detailed valence band region of the spectra in (b), showing the calculation of the valence band maxima (VBM) for the Li<sub>2</sub>S and Li<sub>2</sub>S/Fe cells. (d) Energy band diagram summarizing the location of the vacuum levels and valence band maxima for the polycrystalline Au, Li<sub>2</sub>S, Li<sub>2</sub>S/Mn, and Li<sub>2</sub>S/Fe samples. The vertical gray areas highlight the pristine cells. The ionization energy (i.e., the energy required for an electron to be removed from the surface, which translates to the distance between the VBM and the vacuum level) is displayed on the right axis as the black open circles.

**Table 3.1.** UPS results

Sample	Work function, $\Phi$ (eV)	Valence band maximum, VBM (eV)	Ionization energy, $E_{\text{ion}} = \Phi - \text{VBM}$ (eV)
Au (polycrystalline)	4.78	0	4.78
Li <sub>2</sub> S washed	2.14	-11.39	13.53
Li <sub>2</sub> S 1 <sup>st</sup> charge	3.84	-5.16	8.99
Li <sub>2</sub> S 1 <sup>st</sup> discharge	3.78	-5.04	8.81
Li <sub>2</sub> S/Mn washed	2.19	-11.67	13.86
Li <sub>2</sub> S/Mn 1 <sup>st</sup> charge	3.09	-4.81	7.90
Li <sub>2</sub> S/Mn 1 <sup>st</sup> discharge	2.79	-5.27	8.06
Li <sub>2</sub> S/Fe washed	3.32	-5.26	8.57
Li <sub>2</sub> S/Fe 1 <sup>st</sup> charge	3.81	-4.49	8.30
Li <sub>2</sub> S/Fe 1 <sup>st</sup> discharge	3.61	-5.07	8.67

Although the Li<sub>2</sub>S/Fe and Li<sub>2</sub>S/Mn cells exhibit similar surface morphologies after the exposure to the transition-metal salts before charging (Figures 3.4d and 3.4g), the Li<sub>2</sub>S/Fe cell requires significantly lower activation energy compared to the Li<sub>2</sub>S and Li<sub>2</sub>S/Mn cells, as demonstrated in Figure 3.2e. It is known that the initial activation energy of a lithium sulfide cathode can be related to its initial surface conductivity,<sup>63,64,106</sup> which can be further linked to its electronic band structure in the valence band region. Ultraviolet photoelectron spectroscopy (UPS) was employed to uncover the valence band structure and work function (i.e., the difference between the vacuum and the Fermi level) of the cathode surface (refer to Figure 3.5a for a schematic). Directly connected to the surface conductivity, the ionization energy of a surface,  $E_{\text{ion}}$ , is defined as the minimum

energy required for an electron to be extracted into vacuum, i.e., the energy between the valence band maximum (VBM) and the vacuum level. As such, in most cases, a lower ionization energy translates to a higher surface conductivity, thus rendering UPS a relatively straightforward technique for surface conductivity measurements with respect to EIS, which requires complicated modeling. A comparison between the UPS spectra of the pristine  $\text{Li}_2\text{S}$ ,  $\text{Li}_2\text{S}/\text{Fe}$ , and  $\text{Li}_2\text{S}/\text{Mn}$  cells is presented in Figure 3.5b, where the secondary cut-offs (i.e., the left side onsets) give the work functions. To assess the valence band maxima (i.e., the right side onset), we look at the detailed spectral structure around the Fermi level (Figure 3.5c).<sup>89</sup> In Figure 3.5d, we summarize the valence band maxima and vacuum levels of the Au polycrystalline,  $\text{Li}_2\text{S}$ ,  $\text{Li}_2\text{S}/\text{Mn}$ , and  $\text{Li}_2\text{S}/\text{Fe}$  samples, while the ionization energy is displayed on the right axis. The numerical values extracted from the UPS spectra are listed in Table 3.1.

Interestingly, although having the lowest work functions ( $\sim 2.1$  eV) among the studied samples, the pristine  $\text{Li}_2\text{S}$  and  $\text{Li}_2\text{S}/\text{Mn}$  surfaces exhibit the highest ionization energy ( $\sim 13.5$  eV), a result of VBMs that appear at much higher binding energies than for all the other samples. In contrast, the pristine  $\text{Li}_2\text{S}/\text{Fe}$  sample shows significantly lower ionization energy ( $\sim 8.6$  eV), comparable to the ionization energies of the activated cells, which explains the lower initial activation energy requirement. Due to the large differences between the band structures of the  $\text{Li}_2\text{S}/\text{Mn}$  and  $\text{Li}_2\text{S}/\text{Fe}$  uncycled cells (after rinsing with tetraethylene glycol dimethyl ether, denoted as TEGDME – we will refer to such samples hereafter as “TEGDME-washed“ or simply “washed“), although both Mn and Fe additives reduce the activation barrier in the voltage profile (Figure 3.2e), we conclude that at open circuit,  $\text{Li}_2\text{S}/\text{Mn}$  and  $\text{Li}_2\text{S}/\text{Fe}$  cathodes possess significantly different surface layers. Moreover, the TEGDME-washed uncycled  $\text{Li}_2\text{S}/\text{Mn}$  sample appears to have electronic surface properties similar to the  $\text{Li}_2\text{S}$  uncycled cell. These

observations can be explained by considering the previously measured electrical conductivity and band gap of the likely surface layers, together with their estimated thickness.

Our working hypothesis is that  $\text{Mn}(\text{acac})_2$  reacts with  $\text{Li}_2\text{S}$  to form  $\text{MnS}$ , while  $\text{Fe}(\text{acac})_2$  generates a lithiated pyrite structure,  $\text{Li}_x\text{FeS}_2$ .  $\text{Li}_x\text{FeS}_2$  (with  $x$  between 0.5 to 2) has been identified in numerous studies using iron sulfide as a battery active material.<sup>107-112</sup> In contrast, while the synthesis of hollow  $\text{MnS}$  spheres for battery applications has been demonstrated, we are unaware of any reports of stable  $\text{Li}_x\text{MnS}_y$ -type species.<sup>108</sup> As the reaction to form  $\text{MnS}$  requires displacement of lithium from  $\text{Li}_2\text{S}$ , the resultant Li diffusion range is expected to limit surface layer formation until additional  $\text{Li}^+$  is extracted during charge. Also, since the calculated band gaps of  $\text{Li}_2\text{S}$ <sup>24</sup> and  $\text{MnS}$ <sup>113</sup> are both significantly larger than that of  $\text{Li}_x\text{FeS}_2$ , which exhibits similar conductivity as  $\text{FeS}_2$ <sup>111,114</sup>, and the initial  $\text{Li}_2\text{S}/\text{Mn}$  surface layer is hypothesized to be thinner than for  $\text{Li}_2\text{S}/\text{Fe}$ , one would expect a higher ionization energy for the pristine  $\text{Li}_2\text{S}$  and  $\text{Li}_2\text{S}/\text{Mn}$  cells compared to the pristine  $\text{Li}_2\text{S}/\text{Fe}$  cell. We will present detailed spectroscopic evidence in support of the hypothesized surface layer formation mechanism.

For the  $\text{Li}_2\text{S}$  and  $\text{Li}_2\text{S}/\text{Mn}$  cycled samples, from the electronic band structure perspective, the initial charge activation of a pristine cell produces a large reduction in the surface ionization energy by roughly 5 eV. Once activated, all cells have an ionization energy between 7.9 and 9 eV, with  $\text{Li}_2\text{S}/\text{Mn}$  exhibiting the lowest value, 7.9 eV, and  $\text{Li}_2\text{S}$  the highest, 9 eV. This most pronounced change for  $\text{Li}_2\text{S}/\text{Mn}$  is reflective of the continued formation of the  $\text{MnS}$  surface with charge. After the first discharge, the ionization energy of the  $\text{Li}_2\text{S}/\text{Fe}$  cell increases by  $\sim 0.4$  eV to 8.7 eV while that of  $\text{Li}_2\text{S}$  slightly decreases by  $\sim 0.2$  eV to 8.8 eV. On the other hand, the  $\text{Li}_2\text{S}/\text{Mn}$  cell only increases by 0.1 eV to  $\sim 8$  eV, which explains its higher electronic conductivity retention

with respect to the other cells upon cycling. The similarity between  $\text{Li}_2\text{S}/\text{Fe}$  and  $\text{Li}_2\text{S}$  after charge is likely reflective of a surface conductivity dominated by adsorbed electrolyte species, particularly lithium polysulfides. As determined spectroscopically in the ensuing section, little if any Fe is detectable on the cathode surface after charge, whereas Mn is persistently present for the  $\text{Li}_2\text{S}/\text{Mn}$  cell. The small change in the ionization energy of the  $\text{Li}_2\text{S}/\text{Mn}$  cell relative to the  $\text{Li}_2\text{S}/\text{Fe}$  cell (charge vs. discharge) is additionally consistent with a more stable Mn-derived surface encapsulant layer.

### 3.3.5. X-ray Photoelectron Spectroscopy (XPS) Analysis

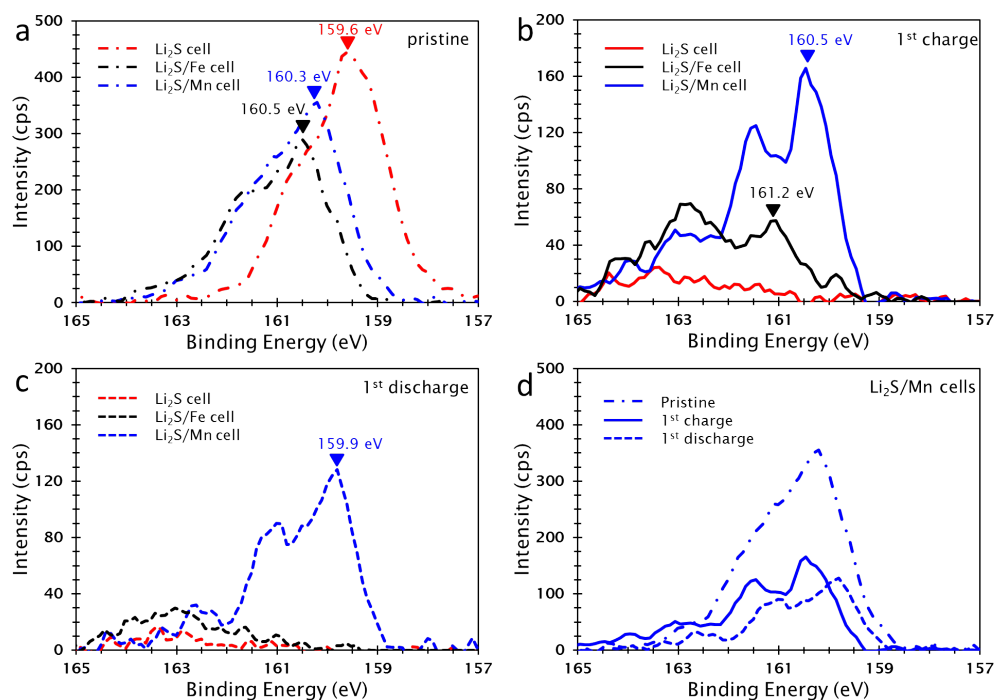


**Figure 3.6.** XPS sulfur 2p region spectra after background subtraction for (a) pristine cells, (b) cells after the first charge, and (c) cells after the first discharge. (d) Comparison of the sulfur 2p spectra for the  $\text{Li}_2\text{S}/\text{Mn}$  cells in the pristine, charged, and discharged states.

Considering the disparate effects that  $\text{Fe}(\text{acac})_2$  and  $\text{Mn}(\text{acac})_2$  additives convey upon the band structure, morphology, and electrochemical performance of the modified  $\text{Li}_2\text{S}$  cathodes, we investigated the surface chemical properties of the materials before and after cycling via X-ray photoelectron spectroscopy (XPS) to verify the proposed surface products. Figure 3.6 shows the sulfur 2p region spectra collected for the pristine  $\text{Li}_2\text{S}$ ,  $\text{Li}_2\text{S}/\text{Mn}$ , and  $\text{Li}_2\text{S}/\text{Fe}$  in the as-assembled state (after washing in TEGDME) after the first charge and first discharge. As observed in Figure 3.6a, the primary sulfide peak for the transition metal-modified surfaces is shifted to higher binding energy by  $\sim 1$  eV, consistent with the formation of a transition-metal sulfide species. The slightly less ionic character of the transition metal-sulfur bond relative to the lithium-sulfur bond in  $\text{Li}_2\text{S}$  decreases the anionic charge on sulfur, producing the binding energy shift. As seen in Figures 3.6b and 3.6c, the metal-sulfide peak was greatly reduced and shifted in the case of the  $\text{Li}_2\text{S}/\text{Fe}$  cell after the first charge, and is indistinguishable after first discharge, consistent with the electrochemical reactivity and instability of  $\text{Li}_x\text{FeS}_2$  within the cycling window.<sup>112</sup> The shift in the  $\text{Fe}/\text{Li}_2\text{S}$  sulfur signal supports the oxidation of  $\text{Li}_2\text{FeS}_2$  (nominal sulfur oxidation state of -2) toward  $\text{Li}_x\text{FeS}_2$  ( $x < 1.2$ , nominal sulfur oxidation state  $< -1.6$ ).<sup>112</sup> Changes in the Mn-S peak, on the other hand, are less pronounced after both the charge and discharge, consistent with the formation of a stable MnS surface layer in the  $\text{LiS}/\text{Mn}$  cell. The sulfur signal with binding energy above 163 eV corresponds to high-order polysulfides and elemental sulfur. Figure 3.6d shows a small shift to lower binding energy in the discharged state, which indicates the incorporation of  $\text{Li}^+$  ions during discharge as they are transported through the MnS encapsulant layer, and likely sampling of the  $\text{Li}_2\text{S}$  in contact with the encapsulant layer.

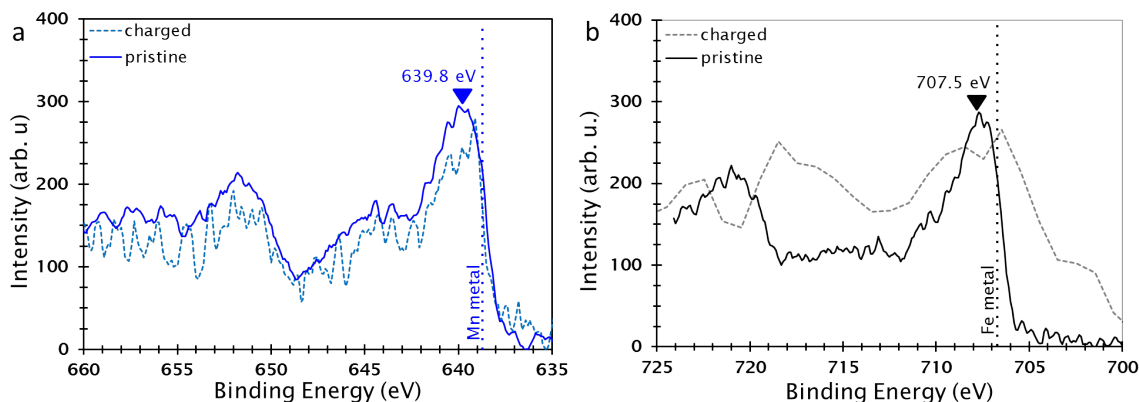


**Figure 3.7.** XPS of the (a) Mn 2p spectra for the  $\text{Li}_2\text{S}/\text{Mn}$  cell before and after charge and (b) Fe 2p spectra of the  $\text{Li}_2\text{S}/\text{Fe}$  cell before and after charge. The signals have been scaled to normalize the intensity before and after charge. The charged Fe 2p signal shown is the corresponding region from the survey spectrum.

XPS spectra collected of the transition-metal species (Figure 3.7) in the  $\text{Mn}/\text{Li}_2\text{S}$  and  $\text{Fe}/\text{Li}_2\text{S}$  cells provide some information complementary to the S 2p spectra. In both the pristine cells, the principal  $2p_{3/2}$  peak is shifted to higher binding energy relative to that of the neutral metal, consistent with the metals being oxidized. The variation in binding energy with chemical structure and not only oxidation state (*e.g.*, per the NIST XPS reference database,<sup>\*</sup> FeS and  $\text{FeS}_2$  exhibit binding energies separated by more than 3 eV, despite iron being in the 2+ state in both structures) means the oxidation state of the metals cannot be assigned from this data. We do observe that the Mn 2p peak does not shift with charge, however, consistent with that the MnS encapsulant not reacting. The Fe 2p signal after charge was not detectable above the level of noise in the survey spectrum (Figure 3.7b), so no region spectrum was collected. The lack of iron signal is consistent with a thick layer of decomposition products and lithium sulfides forming on the cathode surface after the loss of the spherical particle morphology with charge.

<sup>\*</sup> NIST X-ray Photoelectron Spectroscopy Database, NIST Standard Reference Database 20, Version 4.1, <https://srdata.nist.gov/xps/Default.aspx>, accessed 2/7/2016

### 3.3.6. Time of Flight Secondary Ion Mass Spectroscopy (TOF-SIMS) Analysis

#### 3.3.6.1. Metal ion yields

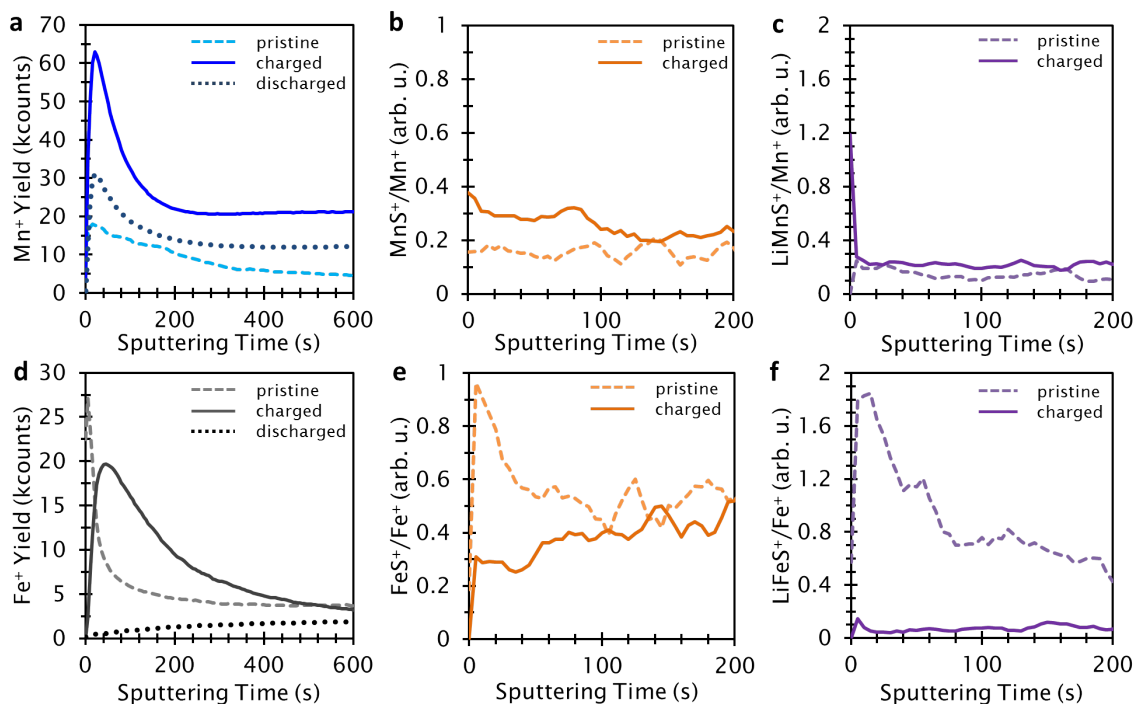


**Figure 3.8.** TOF-SIMS depth profiles for the  $\text{Li}_2\text{S}/\text{Mn}$  cells before charge (dashed line), after charge (solid line), and after discharge (dotted line) of the (a)  $\text{Mn}^+$  secondary ion yield, (b)  $\text{MnS}^+$  yield normalized to the  $\text{Mn}^+$  yield, and (c)  $\text{LiMnS}^+$  yield normalized to the  $\text{Mn}^+$  yield. Profiles for  $\text{Li}_2\text{S}/\text{Fe}$  cells before charge (dashed line), after charge (solid line), and after discharge (dotted line) of the (d)  $\text{Fe}^+$  secondary ion yield, (e)  $\text{FeS}^+$  yield normalized to the  $\text{Fe}^+$  yield, and (f)  $\text{LiFeS}^+$  yield normalized to the  $\text{Fe}^+$  yield.

Although the XPS sulfur spectrum suggests that the  $\text{MnS}$  sulfide encapsulant layer is stable, the overlap of the sulfur signal arising from a transition metal-sulfide bond and a lithium-sulfur bond in a polysulfide bond induces analytical ambiguities. Therefore, our analysis requires additional techniques to clarify the apparent mechanism. To further understand the effects of the Fe and Mn additives on the chemical composition and physical structure of the  $\text{Li}_2\text{S}$  cathodes, we employed time of flight - secondary ion mass

spectrometry (TOF-SIMS), an ultra-high elemental and surface sensitive technique.<sup>90</sup> Figure 3.8 presents several TOF-SIMS depth profiles for Fe-modified and Mn-modified cells in their uncycled, “pristine”, state (after rinsing with TEGDME), and after the first charge and discharge. The stability of the Mn encapsulation layer relative to Fe is demonstrated by comparing the overall transition-metal secondary ion yield of  $\text{Mn}^+$  and  $\text{Fe}^+$  after charge and discharge (Figures 3.8a and 3.8d). The  $\text{Mn}^+$  yield remains high (above the value in the pristine cell) after the first discharge, while the yield of  $\text{Fe}^+$  is greatly diminished, consistent with iron being lost to the cell during the cycling of the unstable  $\text{Li}_x\text{FeS}_2$  layer.

### 3.3.6.2. $M^+$ normalized profiles

Further, to properly identify the relative changes in the depth profiles of metal-containing species, independent of changes in the matrix and sputtering conditions, we analyze the yields of various sulfur-containing transition-metal fragments normalized to the overall yields of the corresponding transition metals (i.e.,  $\text{Mn}^+$  or  $\text{Fe}^+$ ). As observed from the  $\text{MnS}^+/\text{Mn}^+$  and  $\text{LiMnS}^+/\text{Mn}^+$  depth profiles for the pristine Mn/ $\text{Li}_2\text{S}$  cells (Figures 3.8b and 3.8c), the concentration gradients of both species are largely constant with depth. The existence of the  $\text{LiMnS}^+$  fragment implies that there is some degree of Li-Mn-S bonding present (i.e., trace amounts). Analysis of an additional transition-metal-containing fragment, the  $\text{LiMn}^+/\text{Mn}^+$  profile (Figure 3.9), suggests this is not a result of the formation of a  $\text{Li}_x\text{MnS}_2$ -like species, but more likely an artifact of lithium diffusion through the MnS film, as will be discussed in detail. The existence of the  $\text{LiMnS}^+$  fragment does imply some trapped  $\text{Li}^+$  in the MnS structure; therefore the average stoichiometry of the generated surface film reads  $\text{Li}_x\text{MnS}$  (with  $x \ll 1$ ). In contrast to the corresponding Mn species, the  $\text{FeS}^+/\text{Fe}^+$  and  $\text{LiFeS}^+/\text{Fe}^+$  profiles in the pristine  $\text{Li}_2\text{S}/\text{Fe}$

cell exhibit strong enhancement at the surface (Figures 3.8e and 3.8f), with the  $\text{LiFeS}^+$  signal extending deeper than  $\text{FeS}^+$ , which is consistent with the formation of  $\text{Li}_2\text{FeS}_2$  as the primary surface product.

### 3.3.6.3. Analysis of lithium gradients

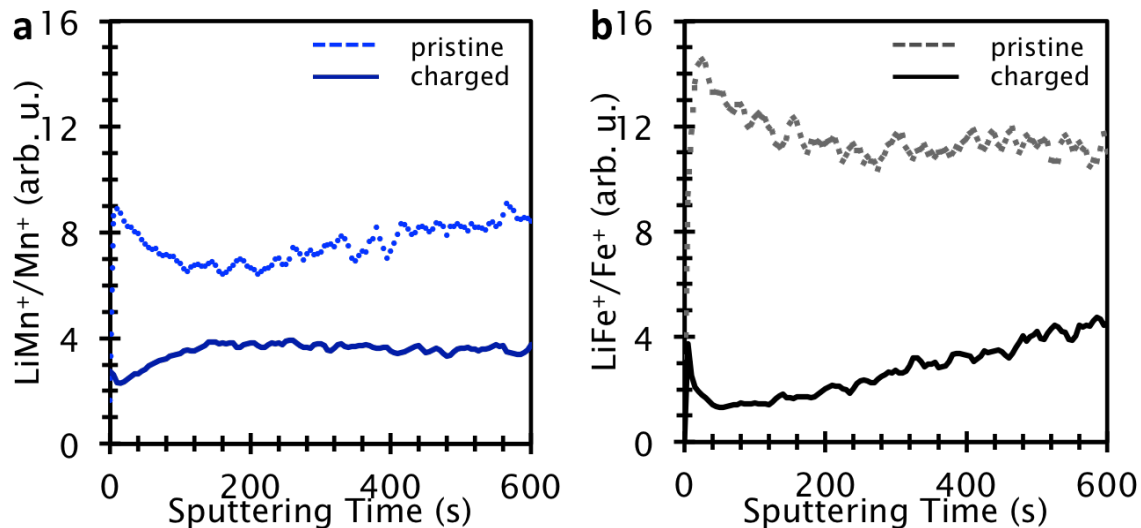


**Figure 3.9.** TOF-SIMS depth profiles normalized to the overall transition-metal secondary ion yield for (a)  $\text{LiMn}^+$  in the  $\text{Li}_2\text{S}/\text{Mn}$  cells and (b)  $\text{LiFe}^+$  in the  $\text{Li}_2\text{S}/\text{Fe}$  cells.

The  $\text{LiMn}^+/\text{Mn}^+$  profile for the pristine cell exhibits a clear minimum, corresponding to relatively low Li concentration relative to Mn, as would be the case in a (lithium-free) MnS layer. According to the proposed reaction mechanism,  $\text{Mn}(\text{acac})_2$  must react with the  $\text{Li}_2\text{S}$  particles, displacing lithium. Since the interior of the  $\text{Li}_2\text{S}$  particles cannot accommodate additional lithium ions, the displaced lithium ions must diffuse to the outside of particles away from MnS formed via surface reaction. This produced the minimum at the reaction surface (Figure 3.9a) where the ratio of Mn-Li bonds relative to Mn species (specifically Mn-S) was the lowest.

This was again consistent with a lithium gradient in the generated surface film. In the case of Fe, however, the  $\text{LiFe}^+$  fragment profile matches that of the  $\text{LiFeS}^+$  profile and

does exhibit a minimum, supporting the formation of lithium-containing  $\text{Li}_x\text{FeS}_2$  species as opposed to lithium-free  $\text{FeS}_2$ .

The  $\text{LiMn}^+/\text{Mn}^+$  ratio decreased for the charged  $\text{Li}_2\text{S}/\text{Mn}$  cell as lithium was removed out of the interior and residual  $\text{Li}^+$  trapped in the MnS layer diffused outward. The  $\text{LiMn}^+/\text{Li}^+$  gradient at the surface also switched direction in the charged cell as lithium was being removed electrochemically (with no generation via surface reaction), producing a gradient to low lithium concentration at the surface.

This was also seen in the enormous decrease in the  $\text{LiFe}^+/\text{Fe}^+$  ratio upon charge. The increase in  $\text{LiFe}^+/\text{Fe}^+$  ratio with depth was consistent with a gradient in lithium removal in the deposited solid film (as observed in the SEM images at the end of charge, Figure 3.4h).

#### ***3.3.6.4. Effect of cycling on ToF-SIMS profiles***

The stability of the generated surface layers was evaluated by comparing the TOF-SIMS profiles for the cells before and after charge (Figures 3.8b-c and 3.8e-f). The growth of the raw  $\text{Mn}^+$  surface signal after charge matches the predicted behavior, as the extraction of lithium electrochemically allows the MnS-forming surface reaction to proceed, yielding a thicker, stabilized film. While the  $\text{MnS}^+/\text{Mn}^+$  ratio for the charged cell increases, the  $\text{LiMnS}^+/\text{Mn}^+$  ratio remains virtually unchanged, corresponding to removal of  $\text{Li}^+$  from the  $\text{Li}_x\text{MnS}$  surface film. This loss of  $\text{Li}^+$  from the  $\text{Li}_x\text{MnS}$  surface is reflected in the slight shift to higher binding energy of the Mn-S bond signal in the corresponding XPS sulfur 2p spectrum. The small uptick in  $\text{LiMnS}^+/\text{Mn}^+$  at the very surface can be ascribed to adsorption of lithium polysulfides to the MnS surface, consistent with the trapping of the lithium polysulfides near the surface. Evidence for this is also seen in the XPS polysulfide signal in Figure 3.6b. In contrast, the depth profiles for the charged

Li<sub>2</sub>S/Fe cells indicate an unstable Li<sub>x</sub>FeS<sub>2</sub> surface layer, which oxidizes toward lower Li content, allowing the break-up of the encapsulant layer and the loss of the spherical morphology upon polysulfide formation. As a result, the LiFeS<sup>+</sup> signal almost completely disappears, while the FeS<sup>+</sup>/Fe<sup>+</sup> ratio becomes constant with depth (at the same level as in the bulk of the pristine cell). This is consistent with the oxidation of Li<sub>2</sub>FeS<sub>2</sub> toward Li<sub>x</sub>FeS<sub>2</sub> ( $x < 1.2$ ).

The relative stability of MnS vs. Li<sub>x</sub>FeS<sub>2</sub> can be explained via the electrochemical stability window of each sulfide. MnS has been shown not to reduce above 0.7 V vs. Li/Li<sup>+</sup> in studies of its use as battery material.<sup>115</sup> Li<sub>x</sub>FeS<sub>2</sub>, on the other hand, participates in electrochemical oxidation and reduction reactions above 1.8 V vs. Li/Li<sup>+</sup>,<sup>107-112</sup> and thus would be expected to react within the cycling window employed for the Li-S batteries in this study (1.8 – 3.4 V vs. Li/Li<sup>+</sup>).

### 3.3.6.5. $\text{LiS}^+/\text{Li}_3^+$ Profiles

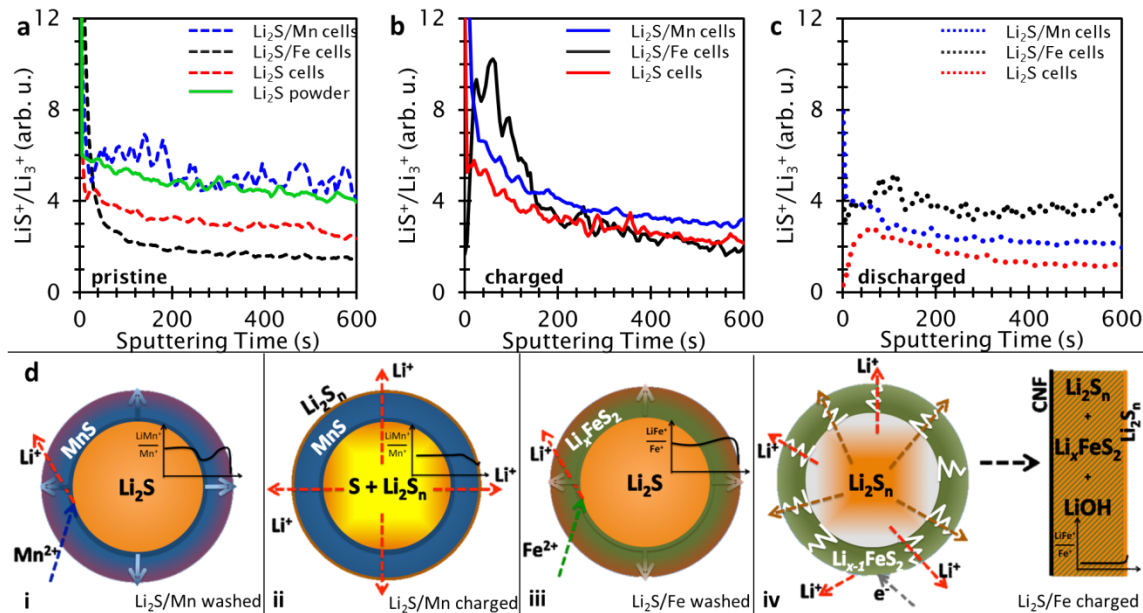


**Figure 3.10.** TOF-SIMS depth profiles for the  $\text{Li}_2\text{S}/\text{Mn}$  cells (blue lines),  $\text{Li}_2\text{S}/\text{Fe}$  cells (black lines), unmodified  $\text{Li}_2\text{S}$  cells (red lines), and commercial  $\text{Li}_2\text{S}$  powder (green line) (a) before charge, (b) after first charge, and (c) after first discharge. (d) Schematic of the proposed reaction mechanism and resultant particle morphology for the  $\text{Li}_2\text{S}/\text{Mn}$  cell (i) before and (ii) after charge and for the  $\text{Li}_2\text{S}/\text{Fe}$  cell (iii) before and (iv) after charge. The  $\text{Li}_2\text{S}/\text{Fe}$  charged schematic represents the failure of the encapsulant layer leading to a relatively homogenous film depositing on the CNF current collector. The inset profiles in (d) represent the expected TOF-SIMS depth profiles for the ratio of  $\text{LiM}^+$  yield to  $\text{M}^+$  yield, where M stands for the transition-metal.

The existence of different species generated on initial surface reaction is further supported by the profiles for  $\text{LiS}^+$  normalized to  $\text{Li}_3^+$  for the pristine  $\text{Li}_2\text{S}/\text{Mn}$  and  $\text{Li}_2\text{S}/\text{Fe}$  cells in Figure 3.10. The  $\text{LiS}^+/\text{Li}_3^+$  ratio represents the likelihood a lithium-containing species to include a lithium-sulfur bond. For species that originate from a Li-S bonding environment, this normalization additionally acts as a proxy for the sulfur : lithium elemental ratio. The profile for the pristine  $\text{Li}_2\text{S}/\text{Mn}$  cell in Figure 3.10a is relatively flat,

supporting the existence of a single dominant Li-S containing species, i.e.,  $\text{Li}_2\text{S}$ . The  $\text{LiS}^+/\text{Li}_3^+$  profile for the  $\text{Li}_2\text{S}/\text{Fe}$  cell, on the other hand, exhibits a sharp increase near the surface, which we ascribe to the existence of  $\text{Li}_2\text{FeS}_2$ , and its proportionally higher S : Li ratio than that in  $\text{Li}_2\text{S}$ . Schematics of the proposed encapsulation/degradation mechanisms for both  $\text{Li}_2\text{S}/\text{Mn}$  and  $\text{Li}_2\text{S}/\text{Fe}$  are depicted in Figure 3.10d.

Additional evidence for the encapsulation effectiveness of the MnS layer is presented in Figure 3.10a. The  $\text{LiS}^+/\text{Li}_3^+$  ratio for the  $\text{Li}_2\text{S}/\text{Mn}$  cell matches that of a commercial  $\text{Li}_2\text{S}$  powder that was never exposed to the electrolyte. The same ratio for the unmodified  $\text{Li}_2\text{S}$  electrode that was assembled into a cell, disassembled, and then washed with TEGDME was significantly less, corresponding to a lower S : Li ratio. Previous studies have noted that commercial  $\text{Li}_2\text{S}$  powders contain soluble polysulfide impurities.<sup>58,116</sup> We thus hypothesize that the soluble polysulfides are partially extracted in the uncycled  $\text{Li}_2\text{S}$  cell, while they are protected by the MnS encapsulant layer in the  $\text{Li}_2\text{S}/\text{Mn}$  cell. EIS spectra (Fig. 3.3c) show no change for the pristine  $\text{Li}_2\text{S}/\text{Mn}$  cell after 48 h, while the slope of the low frequency signal (indicative of diffusing species in the electrolyte) for the unmodified  $\text{Li}_2\text{S}$  cell increased, consistent with polysulfide formation. With additional resting time, the  $\text{Li}_2\text{S}/\text{Mn}$  EIS spectrum did change, confirming that the encapsulation effect was not perfect. Future work adapting this method to bulk cells could aim to quantify the degree of suppressed polysulfide dissolution. Additionally, the influence of the dissolved encapsulating species on the lithium anode should be considered, as a lone report by Okazaki et al. indicated that Mn deposition on lithium metal in a primary  $\text{MnO}_2/\text{Li}$  cell led to increased cell resistance.<sup>117</sup>

### 3.3.6.6. Electrolyte degradation

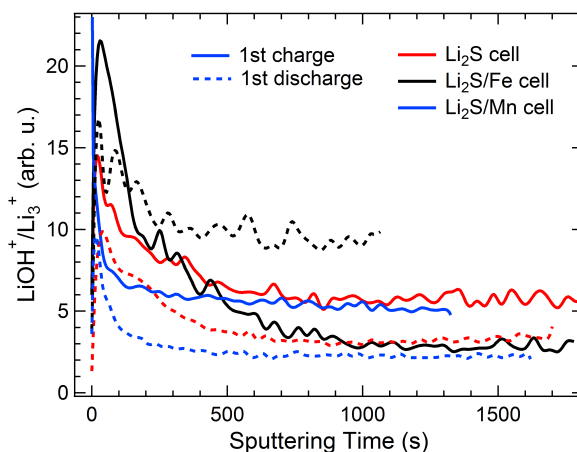


**Figure 3.11.**  $\text{LiOH}^+$  to  $\text{Li}_3^+$  ratio as a function of sputtering time (i.e., depth) for the  $\text{Li}_2\text{S}$ ,  $\text{Li}_2\text{S}/\text{Fe}$ , and  $\text{Li}_2\text{S}/\text{Mn}$  cells after the first charge and discharge. Comparison of the amounts of surface degradation products, *i.e.*  $\text{LiOH}$ , induced by the first charge and discharge processes for the 3 cells. The  $\text{Li}_2\text{S}/\text{Fe}$  and  $\text{Li}_2\text{S}/\text{Mn}$  cells show the highest and the lowest  $\text{LiOH}^+$  to  $\text{Li}_3^+$  ratio, respectively.

Finally, we note the minimal raw  $\text{Fe}^+$  (Figure 3.8d) and the high  $\text{LiOH}^+$  (Figure 3.11) yields at the surface after discharge, indicating the lack of iron species and presence of a large quantity of electrolyte discharge products after cycling the Fe-modified cell, respectively.<sup>69</sup> This also explains the lack of lithium iron sulfide signal in the XPS sulfur 2p spectrum of the  $\text{Li}_2\text{S}/\text{Fe}$  cell after discharge.

In terms of surface degradation, we look at a representative fragment,  $\text{LiOH}^+$ , which indicates the amount of oxidation products formed at the cathode surface due to side reactions with the electrolyte. For the  $\text{Li}_2\text{S}/\text{Fe}$  cell, although the intensity at the maximum of the fragment  $\text{LiOH}^+$  is  $\sim 50\%$  more, the  $\text{LiOH}^+$  to  $\text{Li}_3^+$  ratio forms a similarly wide peak at the surface as in the case of the pristine  $\text{Li}_2\text{S}$  cell, suggesting a comparable degradation depth. In contrast, the  $\text{Li}_2\text{S}/\text{Mn}$  shows  $\sim 5$  times smaller degradation depth, a result of the protective effect of the Mn incorporation into the  $\text{Li}_2\text{S}/\text{electrolyte}$  interface.

### 3.4. CONCLUSION

In conclusion, we demonstrate the use of electrolyte additives containing transition-metal salts to initiate surface reactions on  $\text{Li}_2\text{S}$  bulk particles that produce conductive and protective surface encapsulation layers for more efficient  $\text{Li}_2\text{S}$  utilization. It is identified that the electronic band structure of the as-generated encapsulation layer is critical to the initial charging resistance of the  $\text{Li}_2\text{S}$  bulk particles. Moreover, we demonstrate that stable encapsulation layers during battery operation can form at the surface of the  $\text{Li}_2\text{S}$  particles via chemical reactions that generate transition-metal sulfides electrochemically inactive within the cycling voltage window. This leads to improved material encapsulation and capacity retention. We show that by solely focusing on increasing the surface conductivity and thereby reducing the activation overpotential, one does not necessarily improve the stability of the cell. As only the manganese additive offered a viable option, further work is currently ongoing to rationally design encapsulating layers capable of providing both high conductivity and stability via specifically targeted surface reactions on  $\text{Li}_2\text{S}$  bulk particles. This work provides a strategy to overcome the major constraints in low-cost, large scale production of active  $\text{Li}_2\text{S}$  particles for battery use and opens up new prospects for tuning the properties of electrode materials by selective modifications of the surface electronic and chemical structures desired for energy-storage applications.

## Chapter 4: Elucidating the electrochemical activity of electrolyte-insoluble polysulfide species in lithium-sulfur batteries\*

### 4.1. INTRODUCTION

Lithium-sulfur (Li-S) batteries have emerged in recent years as promising next-generation energy storage devices to meet the growing need for affordable, highly energy-dense systems for electrical vehicles and grid-scale applications.<sup>7,15</sup> The high theoretical gravimetric energy density (1672 mAh g<sup>-1</sup>) of the Li-S system coupled with the low-cost and abundance of sulfur offers significant advantages over current lithium-ion batteries.<sup>7</sup> However, the conversion nature of the Li-S system leads to a complicated charge/discharge mechanism that passes through multiple soluble and insoluble species on each half-cycle.<sup>7,67</sup> This opens up a multitude of mechanisms for active material loss during long-term cycling. Additionally, the insulating nature of sulfur and lithium sulfide, the final discharge product, limits the rate capability of the system and necessitates forming composite cathodes with a conductive material such as carbon.<sup>7,15</sup>

Of particular concern to the loss of capacity with cycling is the deposition of electrochemically-inaccessible solid sulfide species (Li<sub>2</sub>S<sub>x</sub>, x < 3).<sup>34,39</sup> Multiple literature reports have reached different conclusions on the existence of the solid, electrolyte-insoluble species Li<sub>2</sub>S<sub>2</sub> and whether it forms as a solid intermediate during the discharge of Li-S batteries.<sup>24,32,33,35,38-40,118</sup> Recent studies have suggested there may be separate reaction pathways that are followed at different points during Li-S discharge: one where only Li<sub>2</sub>S is formed during reduction of soluble polysulfides (Li<sub>2</sub>S<sub>x</sub>, x > 2), and a second where both Li<sub>2</sub>S and Li<sub>2</sub>S<sub>2</sub> are formed simultaneously.<sup>35</sup> The question of whether any

---

\* Portions of this chapter have been previously published as M. J. Klein, K. Goossens, C. W. Bielawski, and A. Manthiram, "Elucidating the electrochemical activity of electrolyte insoluble polysulfide species in lithium-sulfur batteries," *Journal of the Electrochemical Society*, 2016, **163**, A2109-2116. M. J. Klein carried out the experimental work with assistance from K. Goossens. C. W. Bielawski and A. Manthiram supervised the research. All participated in manuscript preparation.

$\text{Li}_2\text{S}_2$  that forms can then be reduced is debated in the literature.<sup>38</sup> The existence and reducibility of  $\text{Li}_2\text{S}_2$  is particularly important, as the formation of any  $\text{Li}_2\text{S}_2$  during discharge that cannot be reduced to  $\text{Li}_2\text{S}$  significantly limits the theoretical capacity of the Li-S system and would cause continued capacity loss with extended cycling. It is also important to the fundamental understanding of the Li-S battery discharge mechanism whether or not  $\text{Li}_2\text{S}_2$  is the first solid species formed, as the formation of solid sulfides is involved in reactions that account for 75% of the theoretical Li-S capacity.<sup>33,35</sup>

The literature presents several chemical syntheses of  $\text{Li}_2\text{S}_2$ , notably by the stoichiometric reaction of sulfur and either lithium or  $\text{Li}_2\text{S}$  in liquid ammonia at low temperature<sup>80,119</sup> or by the reduction of sulfur with lithium triethylborohydride ( $\text{Li}(\text{C}_2\text{H}_5)_3\text{BH}$ ) in organic solvents.<sup>120</sup> However, the work first reporting that  $\text{Li}_2\text{S}_2$  was formed via  $\text{Li}(\text{C}_2\text{H}_5)_3\text{BH}$  reduction was not supported by the characterized data; rather, the product was used as an intermediate to organosulfur compounds.<sup>120</sup> Moreover, a recent study duplicated the synthetic approach and reported the product to be a stoichiometric mixture of  $\text{Li}_2\text{S}$  and amorphous  $\text{Li}_2\text{S}_6$ .<sup>32</sup>

While  $\text{Li}_2\text{S}_2$  does not appear in the phase diagram of the lithium-sulfur system at room temperature, it may form as a stable phase at low temperatures or as a metastable phase via electrochemical processes at room temperature.<sup>32,121</sup> Theoretical studies have indicated that  $\text{Li}_2\text{S}_2$  could be either slightly stable<sup>24,36</sup> or slightly unstable<sup>25</sup> to decomposition to  $\text{Li}_2\text{S}$  and sulfur at room temperature.

For a sample prepared via the low-temperature reaction in ammonia, ultraviolet-visible spectroscopy (UV-vis) on the saturated ammonia solution at room temperature showed a signal at 285 nm, which was tentatively assigned to  $\text{Li}_2\text{S}_2$ .<sup>80</sup> This signal is close to a signal at  $\sim 270$  nm reported for electrochemically-generated  $\text{Li}_2\text{S}_2$  in tetraethylene glycol dimethyl ether (TEGDME).<sup>33</sup> Additional evidence for the formation of  $\text{Li}_2\text{S}_2$  was

obtained via thermogravimetric analysis (TGA), which showed that the product started to decompose to  $\text{Li}_2\text{S}$  above  $50\text{ }^\circ\text{C}$ ,<sup>119</sup> although these data may be obfuscated by the presence of amorphous  $\text{Li}_2\text{S}_6$ .<sup>32</sup> There does not appear to be any report that unambiguously identifies  $\text{Li}_2\text{S}_2$  in the solid state.

In this work, we report that a mixture of sulfide species, including  $\text{Li}_2\text{S}_2$ , forms upon treatment of elemental lithium with sulfur in liquid ammonia. We discuss filtration schemes that effectively remove soluble higher-order polysulfides and yield a mixture of predominantly  $\text{Li}_2\text{S}_2$  and  $\text{Li}_2\text{S}$ . Finally, we examine the electrochemical activity of insoluble lithium polysulfides by demonstrating the reducibility of the  $\text{Li}_2\text{S}_2$  fraction in the synthesized sample as well as in commercial samples of  $\text{Li}_2\text{S}$  in which polysulfide-type impurities were identified.

## 4.2. EXPERIMENTAL

### 4.2.1. $\text{Li}_2\text{S}_2$ synthesis

The procedure was adapted from several literature reports.<sup>80,119,122–127</sup> Before starting the synthesis, glassware was thoroughly cleaned to minimize the decomposition of the lithium-ammonia solution prepared during synthesis.<sup>128–130</sup> The glassware was soaked for 60 min in a freshly prepared NoChromix<sup>®</sup> solution (45 g of NoChromix<sup>®</sup>, *i.e.* mainly  $(\text{NH}_4)_2\text{S}_2\text{O}_8$ , was dissolved in 2 L of concentrated sulfuric acid), after which it was rinsed with Milli-Q<sup>®</sup> water. It was then soaked for 30 min in 30%  $\text{NH}_4\text{F}$  in Milli-Q<sup>®</sup> water, rinsed again with Milli-Q<sup>®</sup> water and baked and dried for 60 min at  $120\text{ }^\circ\text{C}$  in a vacuum oven. After this treatment, the glassware was soaked for 20 min in 1 N  $\text{HNO}_3$ , rinsed with Milli-Q<sup>®</sup> water, and dried for 48 h at  $120\text{ }^\circ\text{C}$  under dynamic vacuum and then for 24 h in a gravity oven at  $200\text{ }^\circ\text{C}$ .

An argon-filled 50 mL Schlenk flask (Kjeldahl flask) charged with a glass-coated Teflon stir bar and sealed with a glass stopper, all of which were treated according to the cleaning procedure described above, was inserted into a high-purity argon-filled glovebox ( $O_2 < 1$  ppm,  $H_2O < 1$  ppm). Inside the glovebox, a stoichiometric 1 : 1 ratio of sulfur powder (Acros, 99.999%, sublimed and then kept overnight under dynamic vacuum (2.0 Pa) at room temperature; 817.8 mg, 3.188 mmol  $S_8$ ) and small, freshly cut lithium metal pieces (Aldrich, 99.9% trace metals basis; 177.0 mg, 25.504 mmol Li) were weighed and added to the Schlenk flask, which was then sealed again with a greased glass stopper. The flask was transferred to a Schlenk line and kept overnight under dynamic vacuum (2.0 Pa) at room temperature. The Schlenk line was flushed with anhydrous high-purity argon gas (Praxair, AR 5.0UH:  $O_2 < 1$  ppm,  $H_2O < 3$  ppm,  $N_2 < 4$  ppm). The next day the Schlenk flask was backfilled with argon and placed in a bath of dry ice in acetone at *ca.*  $-78$  °C. By means of chemical-resistant Tygon 2375 tubing and appropriate fittings, anhydrous ammonia gas (Praxair, AM 5.0RS:  $O_2 < 0.5$  ppm,  $H_2O < 1$  ppm,  $N_2 < 1.5$  ppm) was allowed to flow, via a drying tube filled with sodium metal, through the Schlenk flask until about 45 mL of liquid ammonia had condensed. The typical blue color resulting from the dissolution of lithium in liquid ammonia could be quickly observed. The cooling bath was changed to dry ice in a mixture of ethanol and ethylene glycol (40/60 *v/v*) to raise the temperature to *ca.*  $-41$  °C.<sup>131</sup> The reaction mixture was magnetically stirred (at 650 rpm) for 5 h under continuous cooling. During this time, the reaction mixture developed an orange-yellow color. When stirring was paused, a yellow precipitate and an orange supernatant could be observed. After 5 h, the cooling bath was changed to dry ice in a mixture of ethanol and ethylene glycol (20/80 *v/v*) to raise the temperature to *ca.*  $-28$  °C.<sup>131</sup> Under continued stirring and a flux of argon, the ammonia was expelled into a trap cooled with liquid nitrogen, and was finally completely

replaced by argon. The Schlenk flask was then removed from the cooling bath and placed under dynamic vacuum overnight. The next day the flask was connected, under a flow of argon, to a Schlenk filtration setup that was filled with argon and was equipped with an addition funnel filled with 40 mL of anhydrous, degassed THF (Note: the THF was dried over sodium-benzophenone, collected in an oven-dried Schlenk flask, subjected to five freeze-pump-thaw cycles and transferred to the addition funnel via cannula transfer). The THF was added to the yellow solid residue in the reaction flask, and the resulting suspension was magnetically stirred for 30 min at room temperature. Stirring was then ceased and the Schlenk filtration setup was rotated to separate the clear, dark-yellow to brown filtrate from the yellow powder by means of a filtration tube with frit. Finally, the Schlenk flask and the Schlenk filtration tube were decoupled from the rest of the setup under a flow of argon, and sealed. The solid residue was further dried for 16 h under dynamic vacuum at room temperature, after which the Schlenk flask was backfilled with argon and transferred into the high-purity argon-filled glovebox for all further material processing.

#### **4.2.2. Filtration/polysulfide extraction in DME/DOL**

The solid synthesis product ( $\text{Li}_2\text{S}_x$ ) was washed with ~ 20 mL of a mixture of 1,2-dimethoxyethane (DME, Sigma-Aldrich, 99.5%) and 1,3-dioxolane (DOL, Acros Organics, 99.5+%, stabilized) (50/50 v/v, “DME/DOL”). The solution was filtered through 450 nm and 200 nm pore size PTFE filters (Millipore Fluoropore) and 100 nm pore size nylon filters (Sterlitech Corporation) on a vacuum line in the glovebox. The solid powder was isolated from the filter and the liquid filtrate was collected for analysis. For initial “filter-free” polysulfide extractions, the  $\text{Li}_2\text{S}_x$  powders were mixed with 20 mL DME/DOL and magnetically stirred for several hours. The solutions were allowed to

settle overnight and the liquid supernatant was removed via micropipette and collected. For the final extractions, in place of magnetic stirring, the mixture of  $\text{Li}_2\text{S}_x$  in DME/DOL was agitated by hand to minimize any mechanical grinding action.

#### **4.2.3. Carbon nanofiber (CNF) paper synthesis**

CNF paper current collectors were fabricated as reported in the literature.<sup>64</sup> Briefly, 180 mg CNFs (Aldrich, pyrolytically stripped, > 98%) were added to 650 mL deionized water and 50 mL isopropanol (IPA, Fisher, 99.9%) and ultrasonicated. The solution was vacuum filtered and dried overnight under vacuum at 50 °C. The CNF paper was separated from the filter and punched into circular current collectors.

#### **4.2.4. Electrochemical cell fabrication and characterization**

CR2032 coin cells were fabricated to enable electrochemical characterization. Electrolyte solution was prepared by dissolving 1 M lithium bis(trifluoromethanesulfonyl)imide (LiTFSI, SynQuest Laboratories, 99.5%) in DME/DOL. For catholyte-type cells, 1 M LiTFSI was added to the solution being analyzed to form a liquid catholyte. For solid slurry-type cells, solid  $\text{Li}_2\text{S}_x$  powder was added to the electrolyte solution and magnetically stirred to form a solid slurry. To fabricate the cells, 30  $\mu\text{L}$  of the catholyte or solid slurry was deposited by micropipette on a CNF current collector. For control cells, 30  $\mu\text{L}$  of electrolyte was used in place of the catholyte or solid slurry. The cathode was covered by a polypropylene/polyethylene (Celgard 2325) separator and 20  $\mu\text{L}$  electrolyte was added to the anode side. The coin cells were sealed after addition of a 1  $\text{cm}^2$  lithium metal anode. Cells were discharged galvanostatically on an Arbin multichannel cycler to 1.8 V (vs.  $\text{Li}/\text{Li}^+$ ).

#### **4.2.5. Ultraviolet-visible spectroscopy (UV-vis)**

DME/DOL was used as a blank solution. Sample solutions were prepared by collecting 5 mL of filtrate after vacuum filtration of the  $\text{Li}_2\text{S}_x$  powder. Inside the glovebox, 3 mL of filtrate were added to 1-cm path-length quartz cuvettes with PTFE-lined caps to prevent air exposure. UV-vis absorption spectra were collected from 250 nm to 800 nm. The remaining sample solutions were then sequentially analyzed and diluted with blank solution until the absorption spectrum did not saturate the detector in the ultraviolet region. “ $\text{Li}_2\text{S}_6$ ” reference solution was prepared by mixing 5 : 1 stoichiometric amounts of sulfur powder :  $\text{Li}_2\text{S}$  powder in blank solution followed by magnetically stirring overnight at 60 °C. The reference solution was also sequentially diluted until the detector did not saturate.

#### **4.2.6. X-ray diffraction (XRD)**

$\text{Li}_2\text{S}_x$  powder was prepared for XRD by being sealed between polyimide tape and a 0.1 mm thick polyimide film to protect the sample from oxidation. Powder diffraction data were collected through the polyimide thin film using filtered Cu  $\text{K}\alpha$  radiation ( $\lambda = 1.5148 \text{ \AA}$ ), from  $2\theta = 25^\circ$  to  $2\theta = 75^\circ$ .

#### **4.2.7. X-ray photoelectron spectroscopy (XPS)**

Samples of synthesized  $\text{Li}_2\text{S}_x$  and commercial reference  $\text{Li}_2\text{S}$  from two sources (99.9% trace metals basis from Alfa Aesar and 99.98% trace metals basis from Aldrich) were embedded in indium foil (Sigma-Aldrich, 99.999%) in a glovebox and transferred immediately within an in-house designed capsule that interfaces directly with the ultra-high vacuum XPS instrument, allowing sample transport and pump-down with no exposure to the atmosphere. Surface characterization was performed with monochromated Al  $\text{K}\alpha$  radiation ( $h\nu = 1486.5 \text{ eV}$ ) at 150 W (10 mA and 15 kV). A

concentric hemispherical analyzer was used to measure electron energies. A charge neutralizer was employed with the insulating powders and the spectra were corrected with a linear offset such that the adventitious (graphite-like) carbon peak in the carbon 1s spectrum was set to 284.6 eV.<sup>132</sup> Individual region spectra were collected using a 20 eV pass energy and 0.1 eV step sizes with 800 ms dwell times. Ar<sup>+</sup> ions were used to sputter the samples to identify any bulk vs. surface effects in the powders.

XPS spectra were analyzed with CasaXPS software (Casa Software Ltd.). Spectra were fit with a Shirley-type background. Spectrum deconvolution was performed with individual peak line-shapes with 70% Gaussian and 30% Lorentzian character. S 2p signals were fit with S 2p<sub>1/2</sub> peaks offset by 1.18 eV<sup>133</sup> from the corresponding 2p<sub>3/2</sub> peaks and with equal full-width at half-maximum (FWHM) and half the integrated area of the 2p<sub>3/2</sub> peaks. For ease of discussion, all S 2p signals will be referred to by the center of their larger 2p<sub>3/2</sub> peak. Li/S stoichiometry was calculated using the standard relative sensitivity factors (RSFs) provided by CasaXPS for the Kratos XPS instrument used.

### 4.3. RESULTS AND DISCUSSION

#### 4.3.1. Morphology

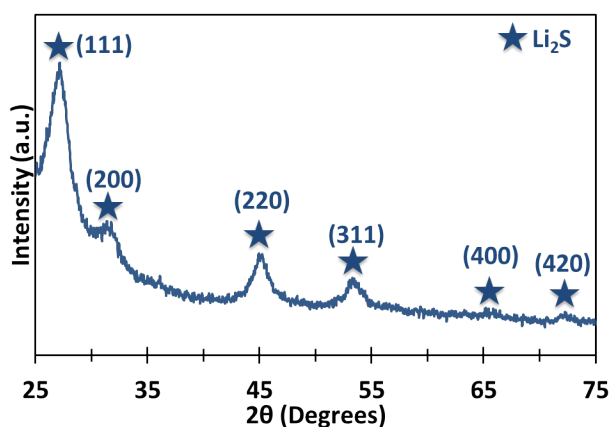


**Figure 4.1.** XRD pattern of the synthesized Li<sub>2</sub>S<sub>x</sub> after initial filtration from THF. Crystalline Li<sub>2</sub>S peaks are identified and indexed.

The air-sensitive powder obtained after the initial filtration from THF had a rich yellow color. As shown in Figure 4.1, the XRD pattern exhibited several features, notably all the observable peaks could be indexed to the antifluorite phase of  $\text{Li}_2\text{S}$  (JCPDS No. 23-0369). The peaks indexed to  $\text{Li}_2\text{S}$  were significantly broadened, consistent with the presence of sub-micron sized  $\text{Li}_2\text{S}$  particles. The broad background at  $2\theta < 40^\circ$  was attributed to the polyimide film used to protect the sample from oxidation. The pattern lacked any peaks associated with crystalline sulfur, consistent with all of the original sulfur used in the synthesis being consumed. The lack of a sulfur signal, combined with the yellow color of the powder (in contrast to the white or off-white color of  $\text{Li}_2\text{S}$  powder) suggested to us a solid polysulfide species might be present. The sodium polysulfide analogs, such as  $\text{Na}_2\text{S}_2$  and  $\text{Na}_2\text{S}_4$ , are known to be yellow.<sup>119</sup> However, the lack of any additional peaks matching simulated XRD patterns of theoretical  $\text{Li}_2\text{S}_2$  structures<sup>36</sup> suggested to us that any polysulfide species present were amorphous. Additionally, it did not rule out the product being only a mixture of  $\text{Li}_2\text{S}$  and  $\text{Li}_2\text{S}_6$  as reported for the product obtained from the above-mentioned synthetic procedure that utilized  $\text{Li}(\text{C}_2\text{H}_5)_3\text{BH}$ .<sup>32</sup>

### 4.3.2. XPS analysis

#### 4.3.2.1. As-synthesized $\text{Li}_2\text{S}_x$ S 2p spectrum

XPS spectra taken of the “as-synthesized”  $\text{Li}_2\text{S}_x$  (*i.e.*, only filtered from THF on the Schlenk line) is presented in Figure 4.2, after background subtraction. The S 2p region spectrum was deconvolved and fit with three peaks, each with clear physical interpretations for the corresponding sulfur environment. The peak at the lowest binding energy, 159.8 eV, was assigned to “ $\text{Li}_2\text{S}$ -type” sulfur atoms,<sup>69</sup> *i.e.*, sulfur atoms bonded to two lithium atoms and consistent with the anionic  $\text{S}^{2-}$  species.<sup>85,86</sup>

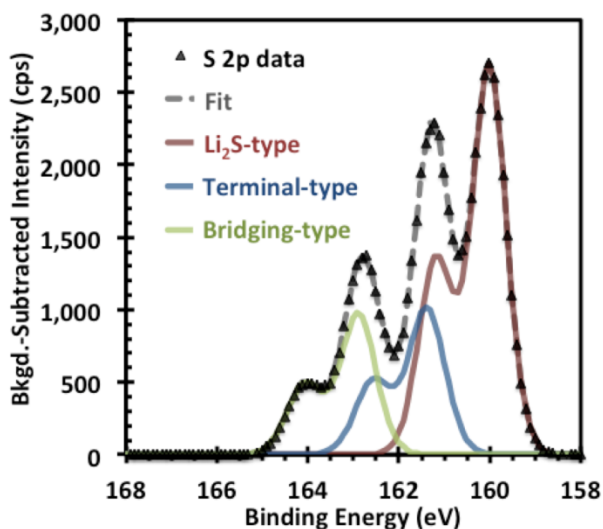


**Figure 4.2.** XPS sulfur 2p region spectrum of the synthesized  $\text{Li}_2\text{S}_x$  after initial filtration from THF. The background-subtracted data points are indicated with triangular markers. The deconvoluted  $\text{Li}_2\text{S}$ -type (red line), terminal-type (blue line), and bridging-type (green line) signals are plotted along with the fit (dashed grey line) from summing the deconvoluted signals.

The peak at slightly higher binding energy, 161.5 eV, was ascribed to “terminal” sulfur, *i.e.*, a sulfur atom that is bonded to one lithium atom and one other sulfur atom. This was the only type of sulfur atom that would be present in  $\text{Li}_2\text{S}_2$ , while all higher-order linear polysulfides would have two of these sulfurs at the termini of their polysulfide chains, regardless of chain length. The shift to higher binding energy was consistent with the intermediate anionic character of these atoms,<sup>85,86</sup> with theoretical studies putting the effective charge of terminal sulfur atoms between -0.90 (in  $\text{Li}_2\text{S}_3$ ) and -0.77 (in  $\text{Li}_2\text{S}_6$ ).<sup>134</sup> From the theoretical trend, the charge on terminal sulfur atoms in  $\text{Li}_2\text{S}_2$  can be assumed to be more negative than -0.90, though still significantly more covalent than in  $\text{Li}_2\text{S}$ .

Finally, the signal recorded at the highest binding energy, 162.9 eV, was ascribed to “bridging” sulfur, *i.e.*, a sulfur atom that is bonded to two other sulfur atoms in the

middle of a polysulfide chain. Bridging sulfurs can thus only be present in higher-order polysulfides. The higher binding energy was associated with the significant covalent character expected for bridging sulfur atoms, with theoretical studies putting the effective charge on the various bridging sulfurs in linear  $\text{Li}_2\text{S}_4$  and  $\text{Li}_2\text{S}_6$  between -0.17 and -0.11.<sup>134</sup> The distribution of some additional electron density onto the bridging sulfurs accounted for the binding energy still being significantly lower than for neutral sulfur in elemental  $\text{S}_8$  rings, for which the binding energy is above 164.0 eV.<sup>85</sup> Indeed, the lack of any spectral intensity above 165 eV confirmed that no elemental sulfur existed in the synthesized sample, as the neutral sulfur would display a S  $2p_{1/2}$  peak at  $\sim 165.3$  eV. Additionally, the lack of any signal above 166 eV confirmed there are no sulfite ( $\text{R-SO}_3^{2-}$ ) or sulfate ( $\text{R-SO}_4^{2-}$ ) species present, as these peaks appear above 166 eV and 167 eV, respectively.<sup>85</sup>

#### ***4.3.2.2. Elemental sulfur reference***

The XPS S 2p spectrum for elemental sulfur can be seen in Figure 4.3b. XPS data were collected from elemental sulfur as a reference during the analysis of the as-synthesized  $\text{Li}_2\text{S}_x$  sample. The position of the neutral  $\text{S}_8$  peak can be seen shifted to higher binding energy relative to the bridging sulfur peak in the as-synthesized sample in Figure 4.3a. Specifically, the S  $2p_{1/2}$  peak was centered at  $\sim 165$  eV, where no such spectral intensity existed in the synthesized sample. It is also useful to note here that a single instance of the modeled Lorentzian-Gaussian signal with 1.18 eV separation between  $2p_{3/2}$  and  $2p_{1/2}$ , a 2 : 1 ratio of integrated area, and a 1 : 1 ratio of FWHM fit the elemental sulfur peak well. Finally, we note that a small sulfite and sulfate impurity was observed in the sulfur sample with spectral intensity at 167 eV and 168 eV.

### ***4.3.2.3. Carbon and oxygen spectra***

The XPS spectrum for the synthesized product indicated the presence of a small quantity of carbon and oxygen, as seen in Figures 4.3d-e, consistent with a thin organic contaminant layer on the surface of the sample.<sup>85</sup> Using the standard relative sensitivity factors (RSFs), the total XPS-determined atomic concentration of carbon and oxygen was less than 20%. The formation of an organic surface contaminant layer is largely unavoidable,<sup>132</sup> and given the surface sensitivity of the XPS technique (whereby surface layers are preferentially sampled),<sup>135</sup> the degree of carbon and oxygen contamination was quite low. With increased storage time, the amount of carbon adsorbed on the surface would increase.<sup>132</sup>

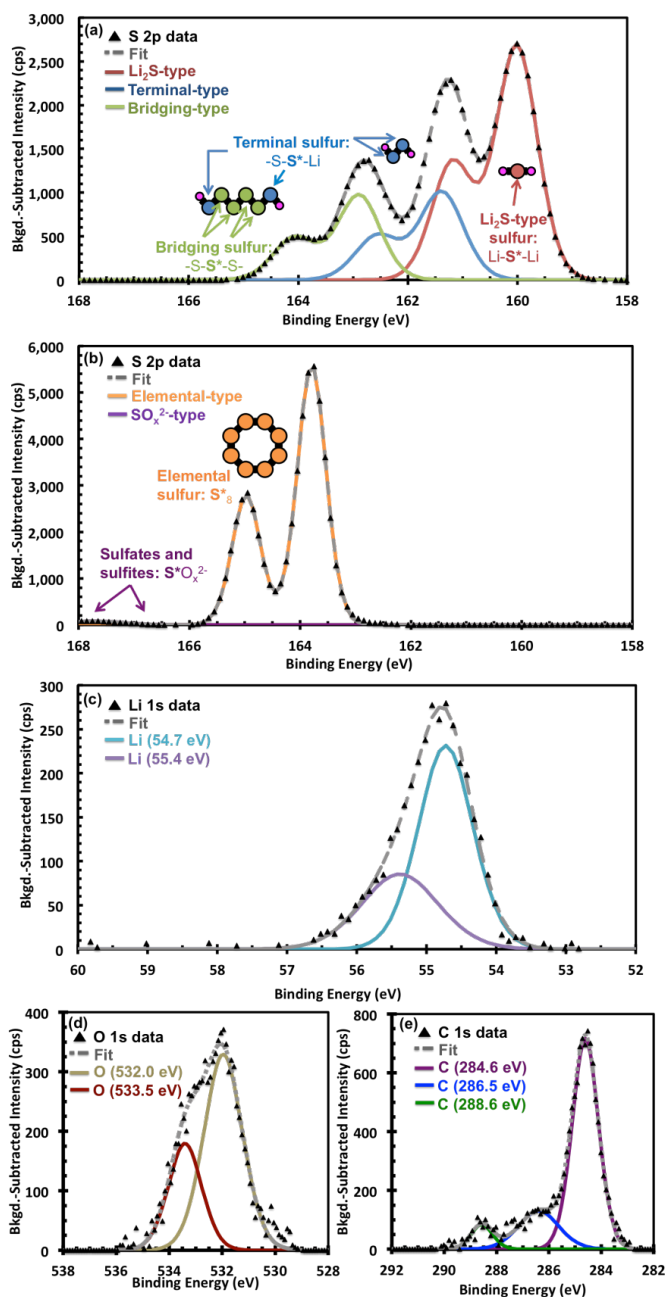


**Figure 4.3.** XPS sulfur 2p spectrum collected for the (a) as-synthesized  $\text{Li}_2\text{S}_x$  and (b) elemental sulfur, along with schematic illustrations of the physical interpretation of the  $\text{Li}_2\text{S}$ -type (red), terminal-type (blue), bridging-type (green), and elemental-type (orange) sulfur peaks. (c) Lithium 1s, (d) oxygen 1s, and (e) carbon 1s spectra collected for the as-synthesized  $\text{Li}_2\text{S}_x$  with two (lithium and oxygen) or three (carbon) peaks used to fit the signal.

#### **4.3.2.4. Peak broadening effects**

It should be noted that the ranges in effective charge on the Li<sub>2</sub>S-type, terminal-type, and bridging-type sulfur atoms can be separated into three distinct groups, corresponding to each type. Variation within a group would then manifest itself as a broadening of the FWHM for that particular signal. As there is only one specific “Li<sub>2</sub>S-type” environment, there should be the least broadening, and, as predicted, the Li<sub>2</sub>S-type peak had the smallest FWHM. Further deconvolution of the three signals to differentiate individual terminal or bridging sulfur atoms was not possible given the small predicted binding energy shifts and the resolution limits of the XPS technique.

#### **4.3.2.5. Elemental quantification**

The Li 1s spectrum presented in Figure 3.3c was fit with two arbitrary peaks to measure the integrated peak area for the purpose of elemental quantification. From the lithium and sulfur spectra, the overall stoichiometry of the product determined by XPS was Li<sub>2</sub>S<sub>1.4</sub>. This value confirmed that sulfur was preferentially lost to the synthesis and initial filtration in THF, as the initial 1 : 1 lithium : sulfur stoichiometry was not preserved. Deconvolution of the sulfur region indicated that the sulfur atoms in the synthesized sample were comprised of 56.4 atom% Li<sub>2</sub>S-type, 22.5 atom% terminal-type, and 21.2 atom% bridging-type. Using this quantification and a basis set of potential sulfide molecules, namely Li<sub>2</sub>S, Li<sub>2</sub>S<sub>2</sub>, and Li<sub>2</sub>S<sub>6</sub> (the solid polysulfide proposed by Cuisinier *et al.*),<sup>32</sup> the sulfide speciation was determined. This method identified the product as being 83.4 mol% Li<sub>2</sub>S, 8.8 mol% Li<sub>2</sub>S<sub>2</sub>, and 7.8 mol% Li<sub>2</sub>S<sub>6</sub>. The stoichiometry of this speciation, determined solely from the deconvolved sulfur signal, was Li<sub>2</sub>S<sub>1.5</sub>, in good agreement with the value calculated from the lithium and sulfur regions as a whole. The small discrepancy can be accounted for if the simple three-element basis set was expanded such that a small fraction of the bridging sulfur atoms

was ascribed to intermediate-length polysulfide-type species ( $\text{Li}_2\text{S}_3$ ,  $\text{Li}_2\text{S}_4$ , or  $\text{Li}_2\text{S}_5$ ), instead of only to  $\text{Li}_2\text{S}_6$ . The discrepancy could also arise due to systemic errors arising from the use of semi-quantitative standard elemental RSFs.

### 4.3.3. UV/vis and filtration analysis

#### 4.3.3.1. Filtration

$\text{Li}_2\text{S}_6$  and other higher-order polysulfides are known to be highly soluble in the organic solvents used as Li-S battery electrolytes.<sup>33</sup> The aim of this work was to isolate the electrochemical behavior of insoluble polysulfide-type species, so the higher order polysulfides were extracted using a filtration scheme. Figure 4.4a shows the liquid filtrates collected from nine sequential vacuum filtrations of a sample of the synthesized powder. The characteristic yellow color of polysulfide solutions was clearly visible in the initial filtrates, becoming light green, and then clear by the fifth collected filtrate.

#### 4.3.3.2. UV/vis spectra

UV-vis spectroscopy was used to track the progress of the filtration process. Several features in the absorption spectrum were seen to clearly disappear with filtration as shown in Figure 4.4b-c, including a broad peak at  $\sim 620$  nm that is characteristic of the  $\text{S}_3\bullet^-$  radical which results from dissociation of  $\text{S}_6^{2-}$ .<sup>33</sup> Other peaks were tentatively assigned based on reported absorption peaks in TEGDME, such as the peak at  $\sim 255$  nm which corresponds to the  $\text{S}_6^{2-}$  species. The absorption intensity between 360 and 530 nm was ascribed to several higher-order polysulfide species, including  $\text{S}_4^{2-}$ ,  $\text{S}_5^{2-}$ , and  $\text{S}_6^{2-}$ .<sup>33</sup>

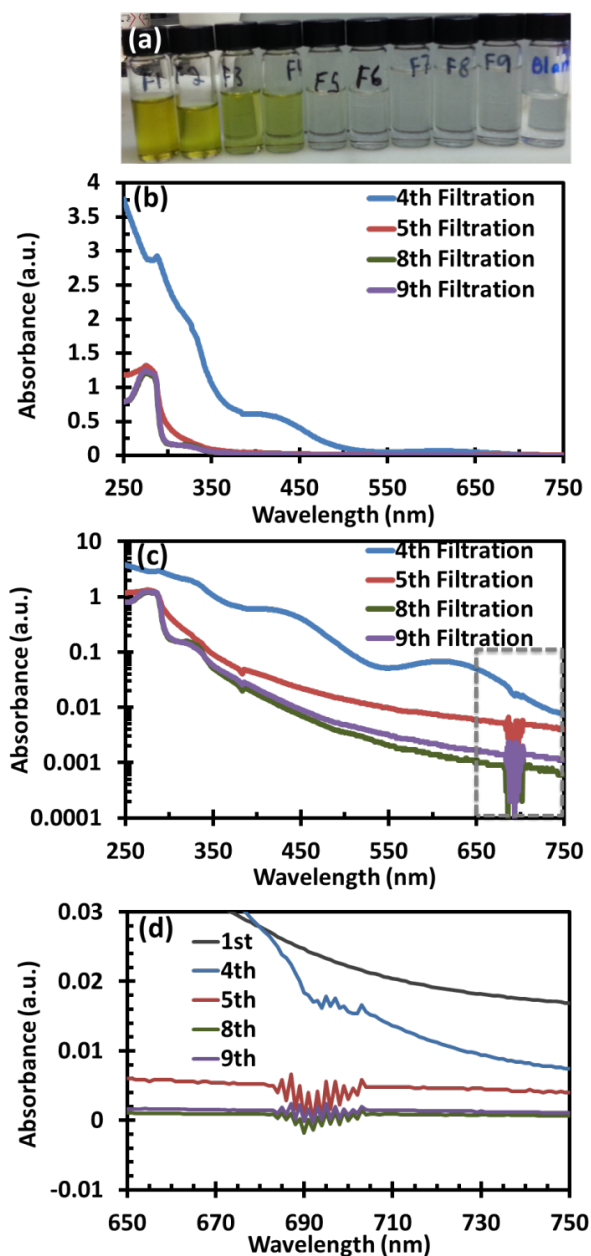


**Figure 4.4.** (a) Photograph of the observed color change with sequential filtrations, with the first filtration on the left and the 9<sup>th</sup> filtration second from the right. The rightmost vial contains the DME/DOL blank solution. (b) Linear scale and (c) log scale UV-vis spectra of the filtrate collected after selected filtrations (4<sup>th</sup> - blue, 5<sup>th</sup> - red, 8<sup>th</sup> - green, 9<sup>th</sup> - purple) of the synthesized  $\text{Li}_2\text{S}_x$ . The expanded region in (d) shows the interference patterns apparent in later filtrations. The magnified region is identified by the dashed grey rectangle in (c).

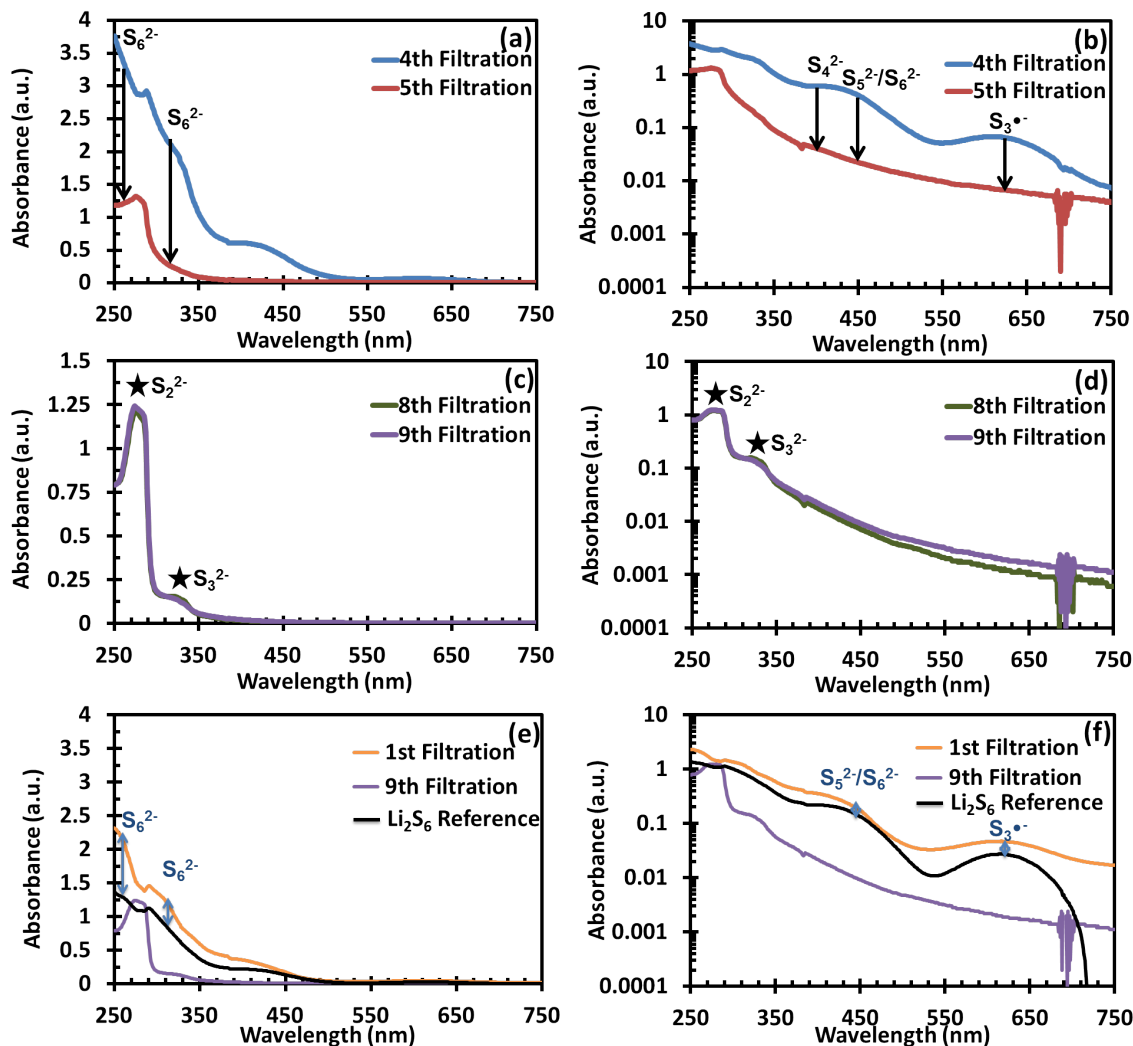


**Figure 4.5.** UV-vis spectra of the filtrates collected during the filtration of the synthesized  $\text{Li}_2\text{S}_x$ . (a) Linear scale and (b) log scale spectra of the 4<sup>th</sup> and 5<sup>th</sup> filtrates; (c) linear scale and (d) log scale spectra of the 8<sup>th</sup> and 9<sup>th</sup> filtrates; and (e) linear scale and (f) log scale spectra of the 1<sup>st</sup> and 9<sup>th</sup> filtrates and a prepared  $\text{Li}_2\text{S}_6$  reference solution (black line). The peak assignments are inferred from those given by Barchasz *et al.* for lithium polysulfides in TEGDME.<sup>33</sup>

The changes in the UV-vis absorption spectra with filtration can be seen clearly by comparing individual filtrates, as in Figure 4.5. The large color change between the 4<sup>th</sup> and 5<sup>th</sup> filtrations was apparent in the decrease in absorption intensity across all

wavelengths as seen in Figures 4.5a-b. The lack of any additional effect of further filtration past the 8<sup>th</sup> was apparent in the lack of significant changes between the 8<sup>th</sup> and 9<sup>th</sup> filtration as seen in Figures 4.5c-d. Finally, the similarity between the 1<sup>st</sup> filtrate and a “Li<sub>2</sub>S<sub>6</sub>” polysulfide reference solution (as indicated by the blue arrows) can be seen in Figures 4.5e-f. The inclusion of the 9<sup>th</sup> filtrate additionally shows the lack of correlation between the Li<sub>2</sub>S<sub>6</sub> reference and the filtrate after extended filtration, consistent with the complete removal of soluble Li<sub>2</sub>S<sub>6</sub>.

By the eighth and ninth filtration, the absorption spectra were consistent, with no observed changes with additional vacuum filtration. Two features remained, a pronounced peak at ~ 265 nm and a smaller shoulder at ~ 320 nm. These peaks were generally consistent with the peaks at ~ 270 and ~ 340 nm reported for, respectively, S<sub>2</sub><sup>2-</sup> and S<sub>3</sub><sup>2-</sup> in TEGDME.<sup>33</sup> While this result could be consistent with the sparing solubility of Li<sub>2</sub>S<sub>2</sub> and some persistent Li<sub>2</sub>S<sub>3</sub>, a third feature of the absorption spectra suggested to us that these peaks were consistent with absorption from Li<sub>2</sub>S<sub>2</sub> and Li<sub>2</sub>S<sub>3</sub>-type species in suspended sulfide particles that had passed through the filter into the filtrate. Figure 4.4d showed the appearance of an interference pattern between 686 and 706 nm that is a characteristic effect arising from forward scattering by suspended small particles.<sup>136</sup> These effects are suppressed if there is high overall absorption,<sup>136</sup> so they did not appear until later filtrations when the absorption peaks at higher wavelengths had disappeared. These results indicated that after filtration, in addition to the main Li<sub>2</sub>S portion, Li<sub>2</sub>S<sub>2</sub> and a small amount of Li<sub>2</sub>S<sub>3</sub>-type species remained in the solid state.

#### 4.3.3.3. XPS of filtered samples

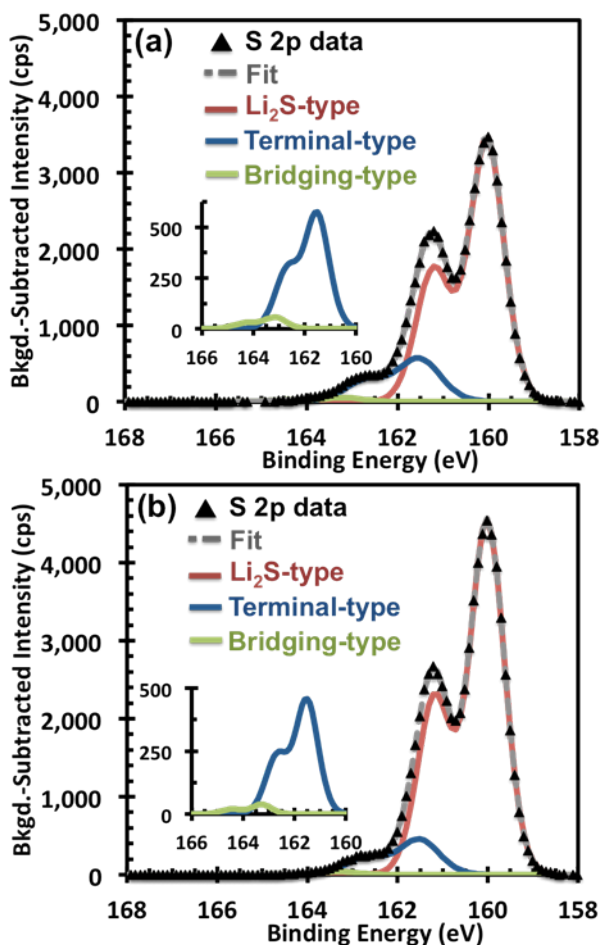


**Figure 4.6.** Background-subtracted, post-sputtering XPS sulfur 2p spectra for (a) filtered, synthesized  $\text{Li}_2\text{S}_x$  and (b) commercial, reference  $\text{Li}_2\text{S}$ . The deconvoluted  $\text{Li}_2\text{S}$ -type (red line), terminal-type (blue line), and bridging-type (green line) signals are plotted along with the fit (dashed grey line) from summing the deconvoluted signals. The inset of each figure isolates the terminal-type and bridging-type signals.

XPS spectra collected from the  $\text{Li}_2\text{S}_x$  powder obtained after extended filtration agreed with this result. Figure 4.6 shows the S 2p signal, with deconvoluted peaks for the three types of sulfur atoms identified in  $\text{Li}_2\text{S}_x$  species. The bridging-type peak had almost disappeared, while a comparatively small decrease was observed in the intensity of the terminal-type peak. The powders were sputtered to confirm that the presence of

polysulfide-type species was not confined to the immediate surface of the particles. After sputtering, quantification of the deconvolved sulfur peaks implied that the sulfur atoms were 82.0 atom%  $\text{Li}_2\text{S}$ -type, 16.5 atom% terminal-type, and 1.6 atom% bridging-type. Using the same three-species basis set as in the original XPS analysis implied sulfide speciation of 90.9 mol%  $\text{Li}_2\text{S}$ , 8.7 mol%  $\text{Li}_2\text{S}_2$ , and 0.4 mol%  $\text{Li}_2\text{S}_6$ . This result reinforced the conclusion that higher-order polysulfides were removed by filtration, while  $\text{Li}_2\text{S}_2$ -type species were insoluble and were retained. The UV-vis results implied that a better analysis of the post-filtration solid would be as a mix of  $\text{Li}_2\text{S}$ ,  $\text{Li}_2\text{S}_2$ , and  $\text{Li}_2\text{S}_3$  type species. With this alternative basis, the implied speciation was 90.9 mol%  $\text{Li}_2\text{S}$ , 7.4 mol%  $\text{Li}_2\text{S}_2$ , and 1.7 mol%  $\text{Li}_2\text{S}_3$ .

#### ***4.3.3.4. Effects of sputtering on XPS data***

The embedding of the synthesized  $\text{Li}_2\text{S}_x$  and commercial  $\text{Li}_2\text{S}$  reference powders in indium foil allowed for sputtering in the XPS. While some of the surface will always be sampled during XPS of powders, even with sputtering—unlike with a continuous film—changes in the signal could be ascribed to the increased ratio of the “bulk” powder interior to the powder surface (which was exclusively sampled in the case of powders with no sputtering). In Figure 4.7d, a sulfite impurity peak observed in the commercial  $\text{Li}_2\text{S}$  reference was seen to disappear with sputtering. In Figure 4.7e, the adventitious carbon peak at 284.6 eV can be seen to be dramatically reduced with sputtering, along with the other carbon peaks fit to the C 1s signal. Figures 4.7a-d show that the  $\text{Li}_2\text{S}$ -type and terminal-type sulfur peak was enhanced with sputtering, while little change was observed in the bridging-type sulfur peak. Some increase in the lithium signal in Figure 4.7f was also observed, comparable to the overall increase in sulfur signal in Figure 4.7a.

Some small shifts in the peak position were observed with sputtering due to imperfect charge compensation.

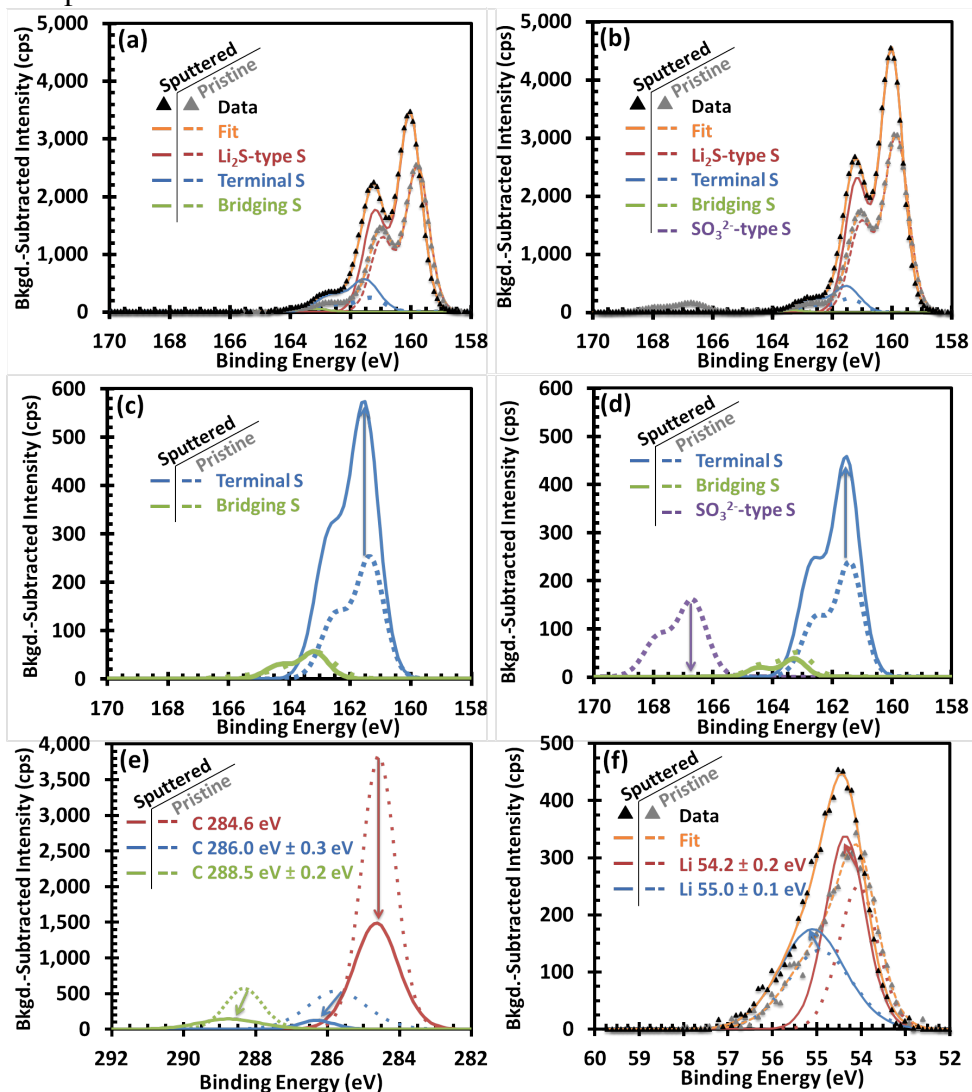


**Figure 4.7.** The XPS sulfur 2p spectra before and after sputtering are shown with deconvoluted peaks for (a) synthesized  $\text{Li}_2\text{S}_x$  and (b) commercial reference  $\text{Li}_2\text{S}$ . The dashed lines are the pristine data and the solid lines are the sputtered data. Just the terminal-type (blue lines), bridging-type (green lines), and sulfite-type (purple lines) peaks are shown for (c) synthesized and (d) commercial powders. (e) Carbon 1s deconvoluted peaks before (dashed lines) and after (solid lines) sputtering for the synthesized powder. (f) Lithium 1s data and two-peak fits for the synthesized powder before (dashed lines) and after (solid lines) sputtering. Arrows in the figure show changes in individual peaks with sputtering.

Sputtering of samples for XPS has been documented to induce damage in metal sulfide samples and to affect the relative ratios of species identified spectroscopically for some transition-metal ions.<sup>137</sup> Weakly-bound and lighter elements may be preferentially removed by sputtering. For the purposes of determining if polysulfide contamination of commercial  $\text{Li}_2\text{S}$  (and synthesized  $\text{Li}_2\text{S}_x$ ) was limited to the surface, we considered specific manifestations of sputtering damage that would lead to spurious conclusions. Particularly, the concern would be sputtering preferentially to remove lithium atoms, leading to an increase in the apparent S : Li ratio, or the ion beam driving reorganization of Li-S bonds, converting  $\text{Li}_2\text{S}$ -type bonds to terminal- or bridging-type bonds. The data indicated that neither of these effects occurred. As is apparent in Figure 4.7a-d, the strength of both the  $\text{Li}_2\text{S}$ -type and terminal-type peaks increased with sputtering, inconsistent with the conversion of  $\text{Li}_2\text{S}$  bonds to terminal- or bridging-type bonds. Likewise, the lithium signal was seen to increase approximately proportionally to the sulfur signal with sputtering (there was less than 10% change in the ratio of the integrated sulfur area to the integrated lithium area). The work of Coyle *et al*<sup>137</sup> observed reduction of metal ions under ion bombardment. As demonstrated in Figure 4.7f, the lithium spectrum did not exhibit a shift to lower binding energies, indicating the absence of the reduction of ionic  $\text{Li}^+$  to metallic  $\text{Li}^0$ . We thus conclude that the stability of the ratio of  $\text{Li}_2\text{S}$ -type sulfur to terminal-type sulfur with sputtering was not an artifact of ion beam damage.

#### 4.3.4. Li<sub>2</sub>S reference analysis

**Table 4.1.** Comparison of the XPS quantification for the synthesized Li<sub>2</sub>S<sub>x</sub> sample before and after filtration from DME/DOL, and a reference commercial Li<sub>2</sub>S sample

<i>Sulfur Species</i>	Synthesized Li <sub>2</sub> S <sub>x</sub> , THF filtration only	Synthesized Li <sub>2</sub> S <sub>x</sub> , DME/DOL filtered and sputtered	Commercial reference Li <sub>2</sub> S, sputtered
<i>Li<sub>2</sub>S-type</i>	56.4 at. %	82.0 at. %	88.8 at. %
<i>Terminal-type</i>	22.5 at. %	16.5 at. %	10.4 at. %
<i>Bridging-type</i>	21.2 at. %	1.6 at. %	0.8 at. %
<b>Li<sub>2</sub>S : Terminal Ratio</b>	<b>2.5 : 1</b>	<b>5 : 1</b>	<b>8.5 : 1</b>
<b>Discharge Capacity</b>	<b>418 mAh g<sup>-1</sup></b>	<b>116 mAh g<sup>-1</sup></b>	<b>70 mAh g<sup>-1</sup></b>

In addition, spectra collected on nominally pure Li<sub>2</sub>S obtained from commercial vendors, intended as a reference for the Li<sub>2</sub>S S 2p XPS peak, exhibited intensity in a region consistent with small amounts of polysulfide-type impurities. A previous report identified up to 2 wt% of soluble polysulfide impurities in a commercial Li<sub>2</sub>S sample.<sup>58</sup> After sputtering, which removed a sulfite surface contaminant species (cf. Figure 4.7d), the XPS S 2p data in Figure 4.6b was collected. The spectrum could be deconvolved and quantified, suggesting to us that the sulfur atoms in “reference” Li<sub>2</sub>S were 88.8 atom% Li<sub>2</sub>S-type, 10.4 atom% terminal-type, and 0.8 atom% bridging-type. Using the initial sulfide basis set, this speciation indicated that the reference Li<sub>2</sub>S sample was comprised of 94.5 mol% Li<sub>2</sub>S, 5.3 mol% Li<sub>2</sub>S<sub>2</sub>, and 0.2 mol% Li<sub>2</sub>S<sub>6</sub>. If the conclusion from the UV-vis data on the filtered, synthesized sample was applied here, the speciation was 94.5 mol% Li<sub>2</sub>S, 4.7 mol% Li<sub>2</sub>S<sub>2</sub>, and 0.8 mol% Li<sub>2</sub>S<sub>3</sub>. The atomic speciation determined by XPS for the various samples is summarized in Table 4.1.

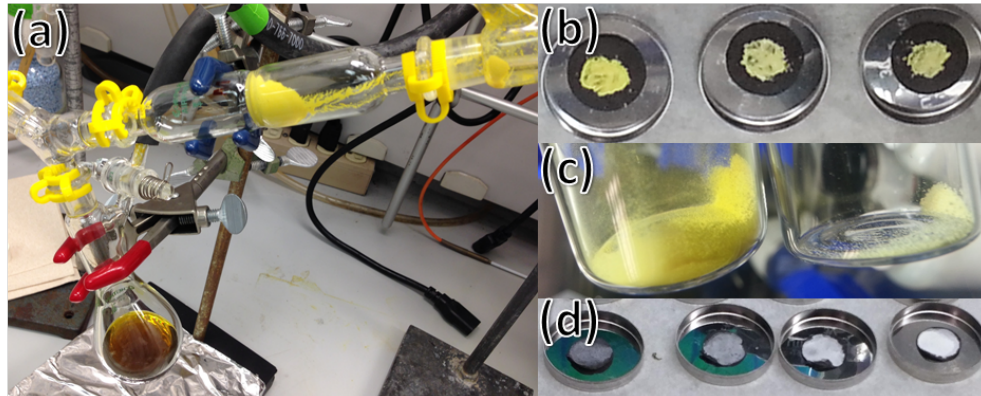


**Figure 4.8.** (a) The apparatus used to filter the as-synthesized product from THF on the Schlenk line is shown, with the collected yellow precipitate in the center. (b) The color variation in the  $\text{Li}_2\text{S}_x$  samples discharged electrochemically, with the THF-only filtered sample on the left, the  $1 \times$  DME/DOL filtered sample in the center, and the  $3 \times$  DME/DOL filtered sample on the right. (c) Comparison of the THF-only filtered powder and the filtered powder collected after electrochemical analysis verified all soluble polysulfides had been removed. (d) White color of commercial  $\text{Li}_2\text{S}$  slurry cast onto CNF current collectors.

This result indicated that nominally pure  $\text{Li}_2\text{S}$  actually had some fraction of sulfur-sulfur bonding, and could indeed be electrochemically reduced, as will be discussed in the electrochemical characterization section of this work. We note that the specification sheet for the product from Aldrich\* describes the appearance of the product as “White to Yellow” and Alfa Aesar’s safety data sheet† describes the appearance as “Yellow”, and both specify the purity only in respect to the presence of trace metals. This variation and observed yellow color was consistent with the existence of polysulfide-type impurities in the samples.

Given that the large band gap calculated<sup>24-26</sup> for  $\text{Li}_2\text{S}$ ,  $\sim 3.5 \text{ eV} - 3.7 \text{ eV}$ , would normally imply that an ionic solid would not absorb visible light and would thus be

\* Lithium Sulfide Product Specification. Sigma Aldrich. [http://www.sigmaaldrich.com/Graphics/COFAInfo/SigmaSAPQM/SPEC/21/213241/213241-BULK\\_\\_\\_\\_\\_ALDRICH\\_.pdf](http://www.sigmaaldrich.com/Graphics/COFAInfo/SigmaSAPQM/SPEC/21/213241/213241-BULK_____ALDRICH_.pdf).

† Lithium Sulfide Safety Data Sheet . Alfa Aesar. <https://www.alfa.com/en/content/msds/USA/12839.pdf>.

white, we hypothesized that existence of an off-white or yellow color in  $\text{Li}_2\text{S}$  samples was indicative of the presence of polysulfide-type impurities. Theoretical calculations suggest  $\text{Li}_2\text{S}_2$  would have an indirect band gap of  $\sim 1.8$  eV.<sup>24</sup> As can be seen in Figure 4.8, the deep yellow color of our synthesized material disappeared with filtration of the highly colored higher-order polysulfides, but a light, straw yellow color was retained. This is consistent with the presence of a greater concentration of insoluble polysulfide-type species in the synthesized sample than in reference  $\text{Li}_2\text{S}$ .

#### **4.3.5. Analysis of potential contamination sources**

The unexpected conclusion reached, that the commercial samples of  $\text{Li}_2\text{S}$  contained significant polysulfide-type impurities, necessitated an investigation of possible sources of polysulfide contamination originating from elsewhere than the samples themselves. We identified four principal possibilities to eliminate: (1) that the particular  $\text{Li}_2\text{S}$  sample received was an unrepresentative, contaminated batch; (2) that the glovebox used to store and process the  $\text{Li}_2\text{S}$  introduced contamination due to ongoing work with polysulfides and Li-S batteries; (3) that the XPS system was contaminated with polysulfide species; or (4) that the  $\text{Li}_2\text{S}$  sample had decomposed with time in the glovebox, resulting in the appearance of polysulfide species.

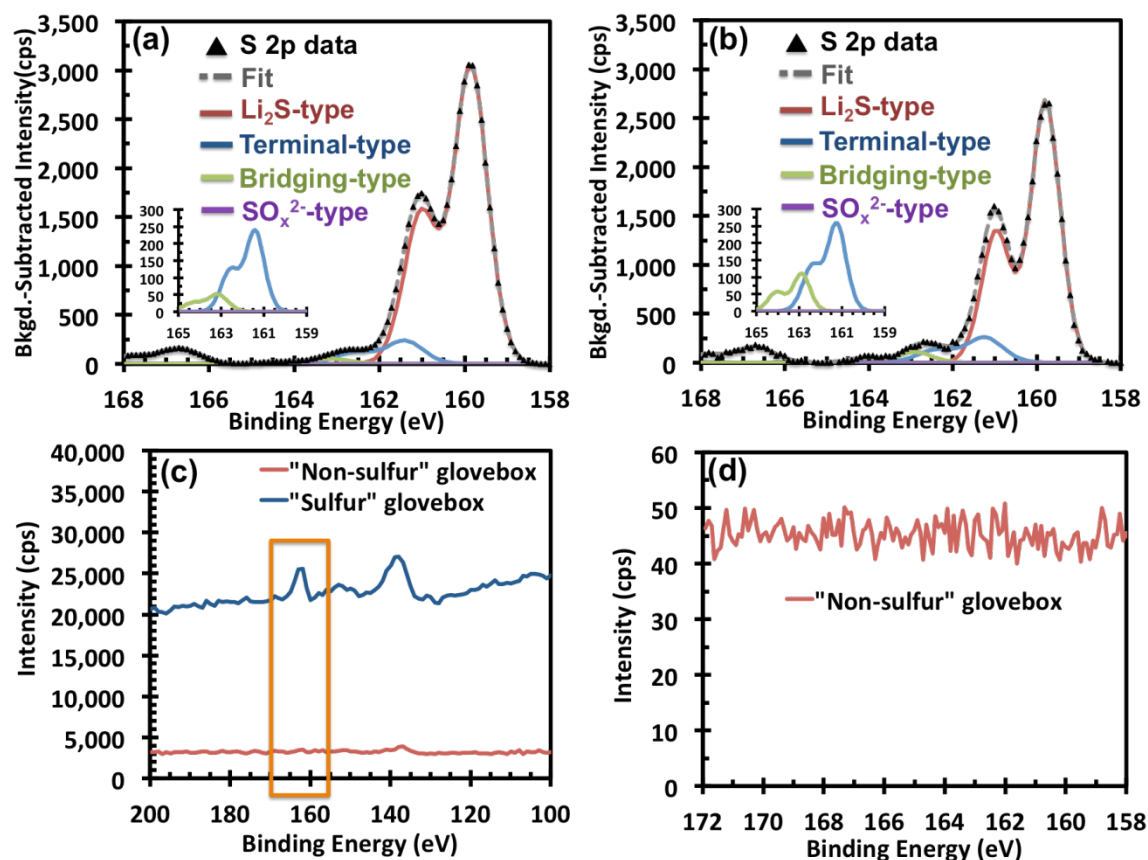


**Figure 4.9.** Comparison of the background-subtracted S 2p spectra for (a)  $\text{Li}_2\text{S}$  from Alfa Aesar stored in a glovebox used for sulfur battery research and (b)  $\text{Li}_2\text{S}$  from Aldrich tested immediately after opening in a glovebox not used for sulfur battery research. The insets show the relative ratio of terminal-type (blue lines) and bridging-type (green lines) sulfur atoms in the peak deconvolution. (c) XPS survey spectra of freshly exposed lithium metal in the glovebox used for sulfur research

We addressed these concerns with an experiment designed to eliminate all four possibilities. The original data collected for commercial  $\text{Li}_2\text{S}$ , as presented in Figure 4.3b used  $\text{Li}_2\text{S}$  purchased from Alfa Aesar (99.9% trace metals basis) stored in the laboratory's glovebox dedicated to lithium-sulfur battery research. When preparing the XPS samples in the glovebox to load into the transfer apparatus, a sample of lithium metal was scratched to expose a fresh lithium surface and included along with the sulfide samples to be transferred to the XPS. As a result, the lithium metal would react with the

glovebox and XPS environment that the sulfide samples were likewise exposed to. Indeed, the reactivity of fresh metallic lithium is expected to be much higher than that of the sulfide samples and should thus react with oxide and sulfide species in the atmosphere at a faster rate than the lithium sulfide samples.

For the new experiment, a sample of  $\text{Li}_2\text{S}$  of a nominally higher purity was purchased from Aldrich (99.98% trace metal basis). The consistency between two samples of different nominal purity purchased several months apart from two different sources would be expected to address concern (1). The newly purchased  $\text{Li}_2\text{S}$  sample was transferred into a different glovebox from the original sample, a glovebox that was not used for sulfur research in order to address concern (2). A lithium surface scratched in this glovebox was included with the  $\text{Li}_2\text{S}$  sample to address any contamination from the XPS system (as well as to confirm low sulfur levels in the glovebox) to address concern (3). Finally, the purchased sample of  $\text{Li}_2\text{S}$  was not opened from its hermetically sealed container in the glovebox for the first time until immediately before the sample was prepared and transferred to the XPS to address concern (4).

Figure 4.9 summarizes the comparison of the two samples. Figures 4.9a and 4.9b show that the ratio of the  $\text{Li}_2\text{S}$ -type sulfur to terminal-type sulfur was consistent for both samples. The inset shows that the ratio of bridging-type sulfur to terminal-type sulfur was actually higher in the nominally purer  $\text{Li}_2\text{S}$  sample prepared under conditions designed to minimize any possible external contamination. As can be seen in Figure 4.9c, lithium metal exposed in the glovebox used for sulfur research did exhibit a sulfur peak in the region of 162 eV while lithium metal exposed in the glovebox not used for sulfur research showed no such signal. The lack of a sulfur signal was further confirmed by the S 2p region spectrum in Figure 4.9d. From these results we conclude that lithium sulfide tested under ideal conditions does not show any less polysulfide-type impurities than our

original commercial sample, and that the conclusion was not an artifact due to contamination in our laboratory.

#### 4.3.6. Electrochemical analysis

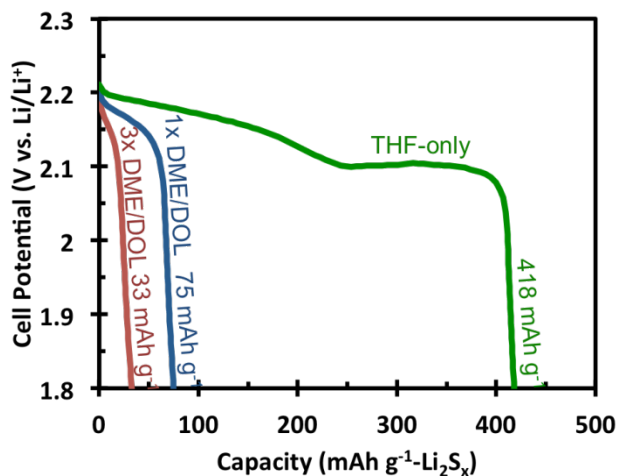


**Figure 4.10.** Galvanostatic discharge curves at  $50 \mu\text{A cm}^{-2}$  to 1.8 V vs. Li/Li<sup>+</sup> for the synthesized Li<sub>2</sub>S<sub>x</sub> powder after only THF filtration (green line), one filtration from DME/DOL (blue line), and three filtrations from DME/DOL (red line).

The quantification of polysulfide species present in a solid sample allowed for the calculation of a theoretical discharge capacity (as listed in Table 1) in an electrochemical cell if all of the polysulfides were reduced to Li<sub>2</sub>S. For the as-synthesized sample after only filtration from THF, the predicted capacity was  $\sim 418 \text{ mAh g}^{-1}$ . As can be seen in Figure 4.10, this was in excellent agreement with the capacity observed when the powder was assembled into a cell on a CNF current collector and galvanostatically discharged to 1.8 V vs. Li/Li<sup>+</sup>. This result supported the elemental quantification performed using XPS data.

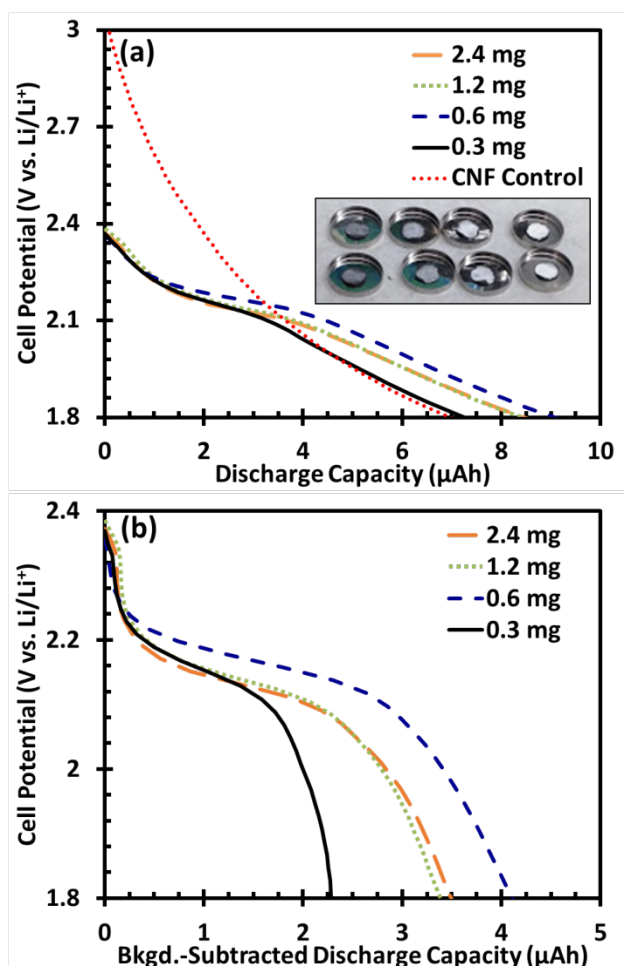


**Figure 4.11.** Galvanostatic discharge curves at  $50 \mu\text{A cm}^{-2}$  to 1.8 V vs.  $\text{Li/Li}^+$  for different loadings, from 0 mg (control, in red) to 2.4 mg (0.3 mg - black, 0.6 mg - blue, 1.2 mg - green, 2.4 mg - orange) of commercial reference  $\text{Li}_2\text{S}$  (a) before and (b) after background subtraction. The inset of (a) shows the appearance of the  $\text{Li}_2\text{S}$ -loaded CNF paper current collectors with increasing loading (from left to right).

With subsequent filtrations, the capacity can be seen to decrease in Figure 4.10, consistent with the loss of soluble, easily-reduced higher-order polysulfides. It should also be noted that the discharge curves in Figure 4.10 were at a fixed  $50 \mu\text{A cm}^{-2}$ . Thus as polysulfides were removed, at a fixed loading, the effective discharge rate for the remaining reducible species was increasing (from  $\sim C/13$  for the as-synthesized sample to  $\sim C/3$  for the filtered samples).

Figure 4.11a shows the galvanostatic discharge curves for different loadings of commercial reference  $\text{Li}_2\text{S}$  at  $50 \mu\text{A cm}^{-2}$ . As can be seen, the absolute discharge capacity of the cell saturated at a loading above  $0.6 \text{ mg cm}^{-2}$ . Indeed, the specific capacity was at a maximum for the lowest loading tested,  $0.3 \text{ mg cm}^{-2}$ , despite somewhat paradoxically, being discharged at the highest gravimetric specific rate. This result was consistent with the reduction being limited by the available surface area of the current collector.

As can also be seen in Figure 4.11a, the control cell, consisting of a CNF current collector with no sulfide loading, exhibited a discharge capacity, though no plateau. This plateau-free discharge capacity was the result of electrolyte reduction on the CNF surface. A low surface area nickel foam current collector was explored, which exhibited little background capacity. However negligible discharge capacity was also observed in cells loaded with  $\text{Li}_2\text{S}_x$  due to the lack of available surface area for polysulfide reduction.

#### **4.3.7. Electrochemical background subtraction**

In order to isolate the reduction of sulfide species from this background electrolyte reduction phenomenon, we performed a rudimentary background subtraction. For each differential voltage step in the sample discharge data, we subtracted the corresponding differential capacity for the same voltage step in the control data. The background-subtracted curves for the reference  $\text{Li}_2\text{S}$  galvanostatic discharge experiments are presented in Figure 4.11b. As can be seen, the plateaus in the background-subtracted data were significantly sharper and the long sloping tails at lower potentials due to electrolyte reduction were largely removed.

It is important to point out that this technique actually overcorrects the data due to its simplistic nature. In the control cells, the entire surface area of the CNF current collectors was available for electrolyte reduction. In the sample cells, some fraction of the

CNFs was covered with the solid slurry-cast  $\text{Li}_2\text{S}_x$  powder, and as a result, less CNF surface area was available for electrolyte reduction. The net result was that subtracting 100% of the corresponding control data actually slightly overcorrected for the background discharge capacity. This manifested itself in a very small ( $< 0.5 \mu\text{Ah}$ ) anomalous negative discharge “capacity” in very low loading cells, as seen in the background-subtracted galvanostatic discharge curves for post-filtration  $\text{Li}_2\text{S}_x$ . While a more sophisticated model can correct for this, it served to overcomplicate the analysis and the simple model was adequate for isolating the sulfide reduction plateaus in  $\text{Li}_2\text{S}_x$  samples.

#### **4.3.8. Current collector size effects**

Various effects were examined to look at their influence on the background discharge capacity exhibited by the carbon current collectors. Figure 4.12 illustrates the effect of current collector size (and thus CNF area) on the discharge capacity observed for control cells and sample cells loaded with commercial  $\text{Li}_2\text{S}$ . Figure 4.12a shows that the sample discharge capacity and plateau width increased consistently with increasing current collector size. There was a noticeable jump between the third and fourth smallest cells; we hypothesize this was the point at which the current collector was large enough that the  $\text{Li}_2\text{S}$  could be spread in an even, thin layer over the surface. Figure 4.12b shows that the background discharge capacity increased monotonically with current collector size, as was predicted for a capacity arising from electrolyte reduction on the CNF surface. Figures 4.12c-d compare the background discharge capacity and discharge capacity for commercial  $\text{Li}_2\text{S}$ -loaded cells using a low surface area nickel foam current collector versus the higher surface area CNF paper current collector. Figure 4.12c shows that the background capacity was greatly decreased for the low surface area nickel foam

current collector. However, the background-subtracted discharge curves in Figure 4.12d show that no discharge plateau was observable for the  $\text{Li}_2\text{S}$ -loaded nickel foam, consistent with the lack of surface area in contact with sulfur-sulfur bonds.

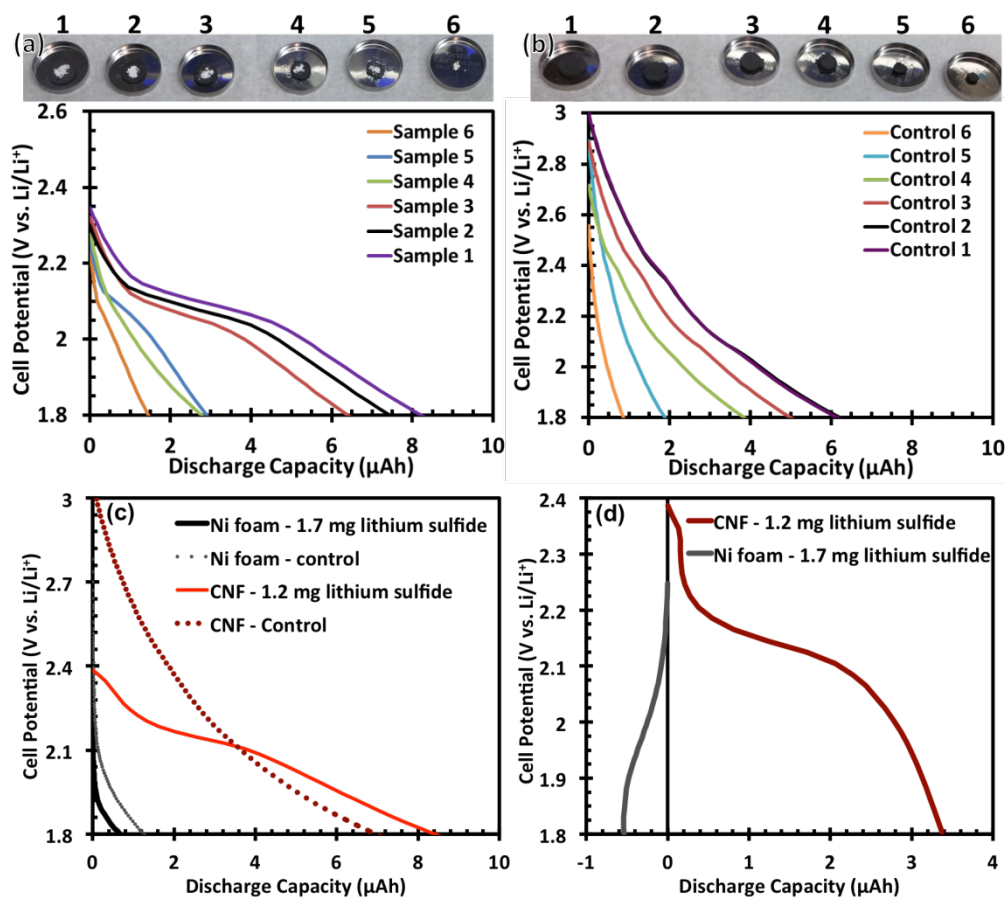


**Figure 4.12.** Galvanostatic discharge curves at  $50 \mu\text{A}$  for (a) commercial  $\text{Li}_2\text{S}$ -loaded and (b) control cells with CNF current collectors of decreasing size as seen in the photograph of each cell above the corresponding graph. (c) Raw and (d) background-subtracted galvanostatic discharge curves for commercial  $\text{Li}_2\text{S}$ -loaded CNF (red) and nickel foam (grey) current collectors.

#### 4.3.9. Isolation of insoluble polysulfide electrochemistry

The observation that commercial  $\text{Li}_2\text{S}$  samples contained polysulfide-type impurities has important implications for the analysis of Li-S cells fabricated with  $\text{Li}_2\text{S}$

cathodes as the starting material in place of sulfur. A large overpotential has been observed in the literature when first attempting to charge  $\text{Li}_2\text{S}$ .<sup>63</sup> This overpotential has been ascribed to the need to form a new polysulfide phase and has been shown to be influenced by the presence (or introduction) of sulfur-sulfur bonding in the  $\text{Li}_2\text{S}$  particle surface.<sup>63,64</sup> The prior report identifying soluble polysulfide impurities in commercial  $\text{Li}_2\text{S}$  samples suggested to the authors that they played an integral role in the oxidation mechanism of  $\text{Li}_2\text{S}$  during charge.<sup>58</sup> It is likely that the degree of sulfur-sulfur bonding already present as an impurity in  $\text{Li}_2\text{S}$  may influence this behavior, including the size of the overpotential required to charge the material. Indeed, given the mechanistic difficulty of forming  $\text{Li}_2\text{S}_4$  (the first soluble species observed when charging Li-S batteries) from  $\text{Li}_2\text{S}$ ,<sup>32,33</sup> it is worth investigating if pure  $\text{Li}_2\text{S}$  can be charged at all in the absence of polysulfide-type impurities.

#### ***4.3.9.1. Electrochemically-monitored filtration***

In order to confirm that none of the observed discharge capacity in the synthesized  $\text{Li}_2\text{S}_x$  samples was due to residual soluble higher-order polysulfides, a tailored electrochemical monitoring approach was applied to the filtration scheme. The liquid filtrate could be collected, prepared as a catholyte, and analyzed electrochemically to determine the polysulfide concentration. A schematic depiction of this approach is provided in Figure 4.13a.

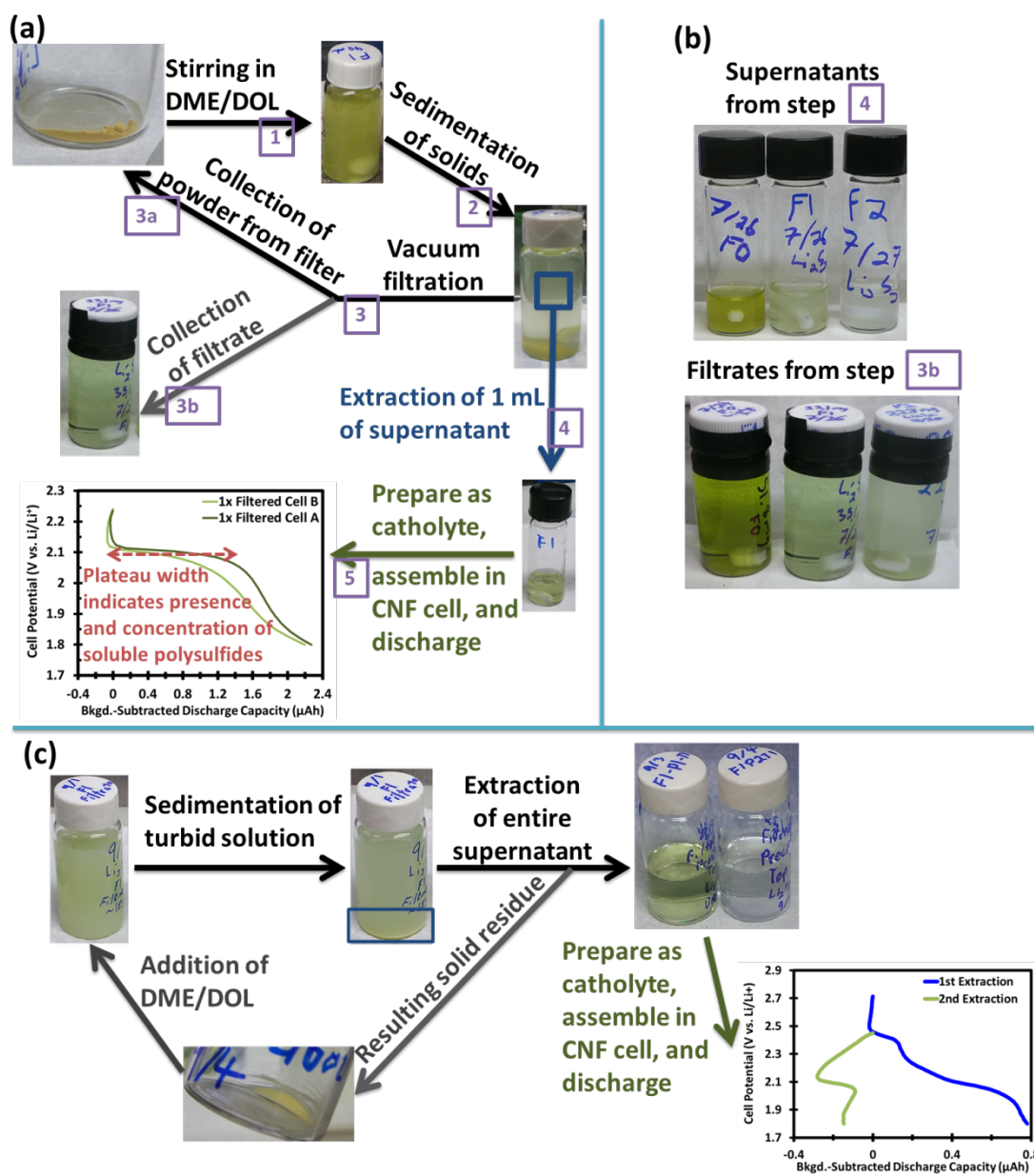


**Figure 4.13.** (a) Schematic of the iterative approach to calculating the residual soluble polysulfide concentration with sequential cycling. (b) Photographs of the supernatants (top row) and filtrates (bottom row) collected for the first three electrochemically-monitored filtrations. (c) The iterative filter-free approach to extracting the remaining soluble polysulfides after the solid particles began passing through the filter. The photograph in the top right of (c) shows the supernatants collected from the first extraction (left) and second extraction (right).

Figure 4.13b illustrates the turbidity that appeared after two such filtrations due to particles passing through the filter. The turbidity is particularly apparent in the third filtrate (bottom right vial of Figure 4.13b). Figure 4.13c illustrates the “filter-free” extraction of polysulfides from the turbid solution, resulting in the final soluble polysulfide-free  $\text{Li}_2\text{S}_x$  powder. As seen in the top right vial of Figure 4.13c, after two filter-free extractions, the supernatant above the  $\text{Li}_2\text{S}_x$  had become visibly clear.

Table 4.2 demonstrates how the electrochemically-monitored scheme was consistent with the XPS-predicted concentration of soluble polysulfides for the first two filtrations before particles passing through the filter invalidated that quantitative aspect of the technique as illustrated by the electrochemically-derived efficiency exceeding the total amount of available polysulfides.

The initial solid mass represents the mass of solid  $\text{Li}_2\text{S}_x$  powder that was mixed with DME/DOL prior to filtration or collected after a filtration. The  $\text{Li}_2\text{S}_6$  mass predicted for the 0<sup>th</sup> filtration is based on XPS-derived speciation (*i.e.*, 7.8 mol%). For subsequent filtrations, this value was calculated by subtracting the electrochemically derived  $\text{Li}_2\text{S}_x$  mass for the prior filtration, and accounting for material lost during the filtration process. The electrochemically-derived  $\text{Li}_2\text{S}_x$  mass for each filtration was the amount of  $\text{Li}_2\text{S}_x$  in solution calculated based on the width of the background-subtracted discharge curves presented in 4.13a. The implied  $\text{Li}_2\text{S}_6$  filtration efficiency was calculated by dividing the actual solid mass collected after a filtration by the amount of material that would be predicted to have been collected if material was only lost to reducible, soluble  $\text{Li}_2\text{S}_6$ . For the first row in the Table,

$$\text{Efficiency} = (33.1 \text{ mg collected}) / [(51.8 \text{ mg initial}) - (12.0 \text{ mg reducible})].$$

**Table 4.2.** Efficiency of filtration scheme

Filtration	Initial solid mass	Li <sub>2</sub> S <sub>6</sub> mass from XPS/theory	Electrochemically-derived Li <sub>2</sub> S <sub>x</sub> mass	Implied Li <sub>2</sub> S <sub>6</sub> filtration efficiency
0 <sup>th</sup>	51.8 mg	13.6 mg	12.0 mg	83 %
1 <sup>st</sup>	33.1 mg	1.4 mg	1.2 mg	71 %
2 <sup>nd</sup>	22.7 mg	0.2 mg	0.9 mg	>> 100 %
3 <sup>rd</sup>	3.2 mg	---	---	---

#### *4.3.9.2. Electrochemical calculation of polysulfide concentration*

Any soluble higher-order polysulfides in the solid powder went into solution when mixed with DME/DOL and could thus be reduced when the solution was discharged. For typical vacuum filtrations with a fixed amount of solution and no particle pass-through, this approach was quantitative and the amount of polysulfides extracted via filtration could be calculated for the starting solid powder. As is presented in Table 4.2 of, these values agreed well with the Li<sub>2</sub>S<sub>6</sub> concentration predicted by XPS for the first two filtrations. After two filtrations, the grinding action of the magnetic stir bar acted to reduce the particle size below 100 nm and solid particles passed through the filter, adding to the observed discharge capacity of the filtrate.

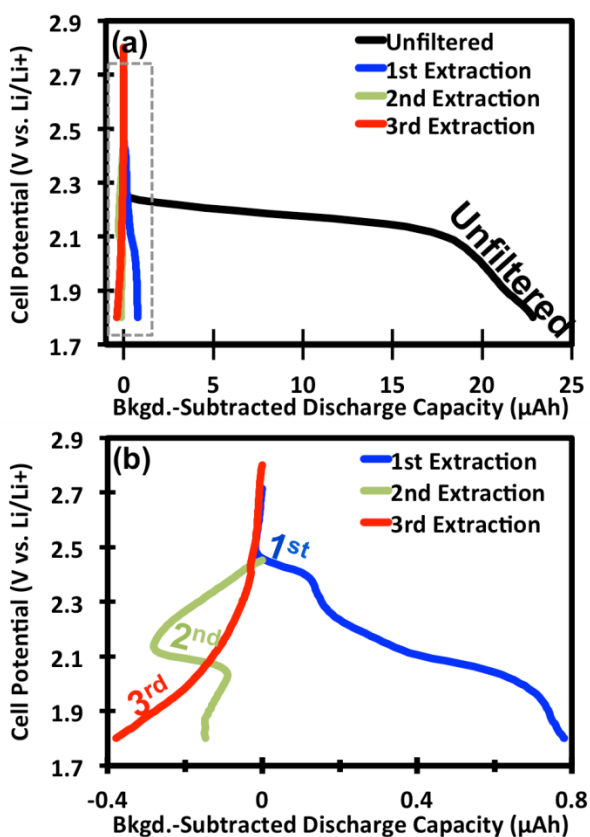


**Figure 4.14.** Background-subtracted galvanostatic discharge curves at  $50 \mu\text{A cm}^{-2}$  for catholytes prepared from the supernatant solution above synthesized  $\text{Li}_2\text{S}_x$  after sequential polysulfide extractions with DME/DOL. (a) Includes the capacity (black line) observed for the solution above the as-synthesized sample before any further polysulfide extraction in DME/DOL. (b) Shows an expanded view of the area indicated by the grey box in (a) and includes only the 1<sup>st</sup> (blue), 2<sup>nd</sup> (green), and 3<sup>rd</sup> (red) sequential extractions.

Beyond this point, sequential polysulfide extractions proceeded simply by mixing the powder with a volume of DME/DOL and allowing the solid to sediment with no filtration. The supernatant extracted after sedimentation was analyzed for residual reducible polysulfides. As can be seen in Figure 4.14, the size of the reduction plateaus decreased with each subsequent polysulfide extraction. After the third “filter-free” extraction, no plateaus existed in the discharge curve, confirming that all soluble polysulfides had been removed from the solid powder.

#### 4.3.9.3. Electrochemistry of soluble polysulfide-extracted $\text{Li}_2\text{S}_x$

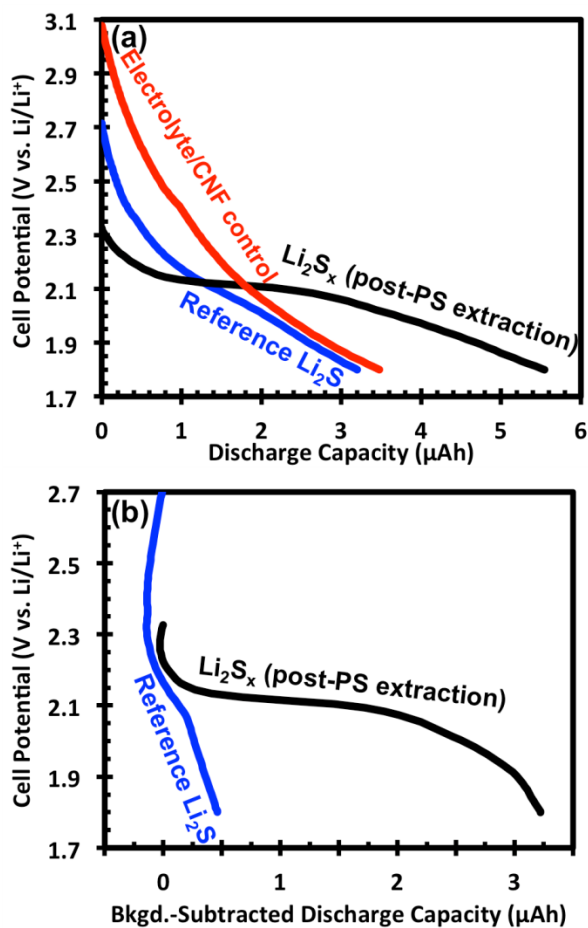


**Figure 4.15.** (a) Raw and (b) background-subtracted galvanostatic discharge curves at  $100 \mu\text{A cm}^{-2}$  to 1.8 V vs.  $\text{Li}/\text{Li}^+$  for CNF paper control (red line), commercial  $\text{Li}_2\text{S}$  (blue line), and synthesized  $\text{Li}_2\text{S}_x$  after complete extraction of soluble polysulfides (black line).

After all the soluble polysulfides were confirmed to be removed, the remaining solid  $\text{Li}_2\text{S}_x$  powder ( $0.2 \text{ mg cm}^{-2}$  nominal loading) was discharged galvanostatically at  $100 \mu\text{A cm}^{-2}$  along with a commercial  $\text{Li}_2\text{S}$  reference (also  $0.2 \text{ mg cm}^{-2}$  nominal loading) and a CNF control. The commercial  $\text{Li}_2\text{S}$  reference was first magnetically stirred in DME/DOL to both wash the material and grind down the particle size. The solution was then vacuum-filtered through a 100 nm nylon filter and the particles that passed through the filter were collected from the liquid filtrate after sedimentation. The commercial  $\text{Li}_2\text{S}$

reference was thus washed and nano-sized in an analogous fashion to the synthesized, polysulfide-extracted  $\text{Li}_2\text{S}_x$  powder. The raw and background-subtracted discharge curves are presented in Figure 4.15. At this rate, only a small sloping discharge plateau ( $\sim 0.3$   $\mu\text{Ah}$  wide) was observable in the  $\text{Li}_2\text{S}$  reference cell. The  $3.3$   $\mu\text{Ah}$  discharge plateau at  $\sim 2.1$  V vs.  $\text{Li}/\text{Li}^+$  for the synthesized  $\text{Li}_2\text{S}_x$  sample corresponded to  $16$   $\text{mAh g}^{-1}\text{-Li}_2\text{S}_x$ , approximately 14% of the capacity predicted by XPS (cf. Table 4.1). However, the discharge rate, chosen to limit the degree of background electrolyte reduction, translated to an effective rate of  $> 2\text{C}$  based on the XPS-determined concentration of polysulfides in the synthesized powder. That any sulfide reduction was observed at this high a rate was strong evidence that solid polysulfides were indeed reducible in the absence of electrolyte solubility. This result, in combination with the surface area limitation for sulfide loading observed in Figure 4.11, suggested to us that the reduction was confined to regions where the sulfur-sulfur bonds were in intimate contact with the conductive current collector.

The significantly smaller discharge plateau observed in the commercial  $\text{Li}_2\text{S}$  was consistent with this result, as the lower concentration of polysulfide-species in the commercial reference would result in more blocking of the sulfur-sulfur bonds by non-reducible  $\text{Li}_2\text{S}$  species. We hypothesize that this effect could be amplified by increased electronic conductivity and/or atomic mobility in samples with higher polysulfide concentrations. Higher mobility could increase the effective distance from the current collector for which sulfur-sulfur bonds are reducible at a given rate. These effects could account for the significant difference in the size of the reduction plateau for the synthesized sample versus the commercial  $\text{Li}_2\text{S}$ . There could additionally be a difference in particle size between the commercial  $\text{Li}_2\text{S}$  and synthesized samples. While both samples passed through  $100$  nm pore size filters, the multiple filtration/extraction cycles for the synthesized sample may have reduced the particle size further, resulting in a

greater specific surface area than the commercial  $\text{Li}_2\text{S}$ . This would increase the contact area between the sample and the current collector for polysulfide reduction. As shown in Figure 4.16, the discharge plateau for a cell prepared with commercial  $\text{Li}_2\text{S}$  that had not been rinsed or nano-sized was significantly smaller ( $\sim 0.1 \mu\text{Ah}$ ), consistent with these surface area effects.

This result has an important implication for the possible reaction mechanisms that have been proposed for Li-S batteries. While these experiments cannot prove that  $\text{Li}_2\text{S}_2$  forms during discharge of a Li-S battery, they do show that if it does form, provided it does so on a conductive surface, it can be readily reduced to  $\text{Li}_2\text{S}$ . Thus reduction pathways that form  $\text{Li}_2\text{S}_2$  as the first solid product are not inherently limited from reaching the full  $1672 \text{ mAh g}^{-1}$  theoretical capacity. Our results also emphasize the importance of solid sulfide deposition morphology, as formation of  $\text{Li}_2\text{S}_2$  at any significant distance from the current collector would not be electrochemically accessible and would thus contribute to capacity loss.

#### 4.3.9.4. Effect of washing and particle size on commercial $\text{Li}_2\text{S}$

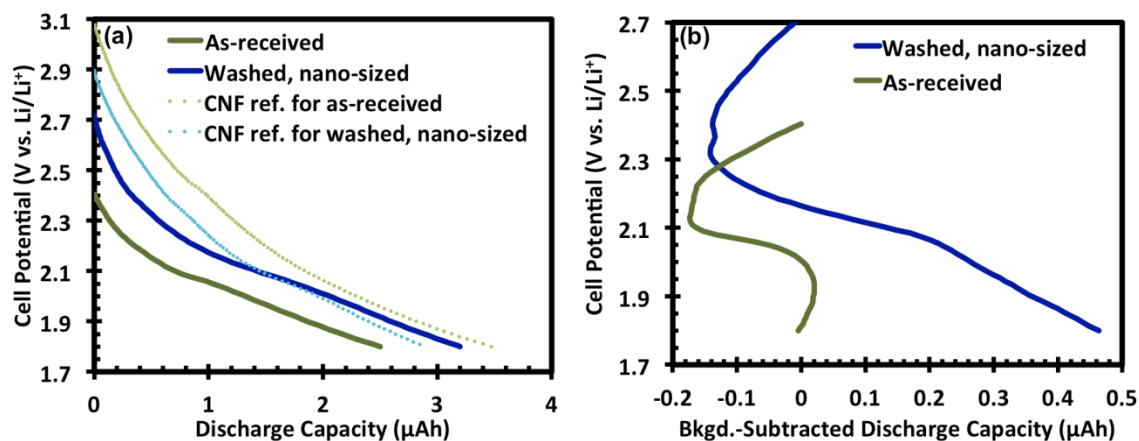


**Figure 4.16.** (a) Raw and (b) background-subtracted galvanostatic discharge capacities for cells prepared with as-received commercial  $\text{Li}_2\text{S}$  (green) and washed and nano-sized to  $< 100$  nm particle size (blue) commercial  $\text{Li}_2\text{S}$ . The background reference cells (dashed lines) in (a) were assembled using CNF current collectors punched from the same batch of CNF paper used for the corresponding  $\text{Li}_2\text{S}$ -loaded cell.

The hypothesized surface area-limited reducibility of solid polysulfides suggested that the particle size would influence the size of the observed reduction plateau for a given insoluble  $\text{Li}_2\text{S}_x$  stoichiometry. Two commercial  $\text{Li}_2\text{S}$  samples were prepared to confirm this behavior. The first sample was prepared as a catholyte as-received. The second sample was first rinsed in DME/DOL and magnetically stirred to reduce the particle size. The sample was then filtered from DME/DOL through a 100 nm pore size filter and the particles that passed through the filter were then collected from the liquid filtrate after sedimentation. Figure 4.16 compares the galvanostatic discharge at  $100 \mu\text{A cm}^{-2}$ , before and after background subtraction for the two samples. The nano-sized sample, despite being washed in DME/DOL before being prepared as a catholyte, exhibited a discharge plateau approximately three times larger than the cell prepared with as-received commercial  $\text{Li}_2\text{S}$ . This was consistent with the greater specific surface area of

the nano-sized sample increasing the amount of reducible polysulfides in contact with the current collector.

#### 4.4. CONCLUSION

We have demonstrated through spectroscopic and electrochemical means that the direct reaction of lithium and sulfur in liquid ammonia at low temperature produces a product that, while predominantly  $\text{Li}_2\text{S}$ , is enriched in solid polysulfide species. Additionally, we have shown that higher-order electrolyte-soluble polysulfide species can be extracted, while retaining lower-order ( $\text{Li}_2\text{S}_x$ ,  $x \leq 3$ ) insoluble polysulfide species. A filtered product that was  $\sim 91$  mol%  $\text{Li}_2\text{S}$  and  $\sim 9$  mol% insoluble polysulfide-type species was obtained. It was shown that these insoluble polysulfide species could be electrochemically reduced in a typical lithium-sulfur battery environment. The reduction of insoluble polysulfides appeared to be limited to sulfur-sulfur bonds that were in intimate contact with a conductive current collector. Finally, we demonstrated that nominally pure  $\text{Li}_2\text{S}$  samples obtained commercially contain small fractions (up to 5 mol%) of polysulfide-type impurities, which were confirmed to be electrochemically reducible.

## Chapter 5: Chemistry of sputter-deposited lithium sulfide films\*

### 5.1. INTRODUCTION

Alkali metal sulfides ( $M_2S$ ,  $M = Li, Na$ ) are attracting considerable research interest in the field of energy storage as cathodes for low-cost, high energy density storage systems.<sup>7,15,44,138</sup> Lithium sulfide ( $Li_2S$ ) in particular is being investigated both as the discharge product of lithium-sulfur (Li-S) batteries and as a cathode to be paired with a lithium metal-free anode.<sup>63,64</sup> Additionally, solid polysulfide species, such as  $Li_2S_2$ , are intermediate products that appear to participate in the charge/discharge mechanism.<sup>35,38,116</sup> Most of these materials are prepared electrochemically, making evaluation of their intrinsic properties challenging due to passivation reactions with the solvents. Films of these materials represent a useful form factor for analyzing their fundamental properties and forming novel all-solid-state structures and batteries. Furthermore, much of the literature characterizing  $Li_2S$  for battery applications has made use of commercially available samples that contain significant polysulfide impurities.<sup>58,116</sup>

The highly ionic nature of the Li-S bond and the disparity in the physical properties of the lithium and sulfur atoms (*e.g.* their vapor pressures) limits the number of available techniques for vapor-phase deposition of  $Li_2S$  thin films. Any deposition strategy should ideally guarantee that the Li : S stoichiometry is preserved or obtained. Additionally, the oxygen and moisture sensitivity of  $Li_2S$  requires the deposition and all subsequent materials handling to be performed in an inert environment. To date, only atomic layer deposition (ALD) has been employed to fabricate  $Li_2S$  films on textured Si

---

\* Portions of this chapter have been submitted for publication as M. J. Klein, G. M. Veith, and A. Manthiram, "Chemistry of sputter-deposited lithium sulfide films," submitted, 2017. M. J. Klein carried out the experimental work with assistance from G. M. Veith, A. Manthiram and G. M. Veith supervised the research. All participated in manuscript preparation.

and carbon powders up to  $\sim 140$  nm thick.<sup>139</sup> The generated films were determined to be amorphous, even after annealing at 500 °C. The system used required use of a glovebag for sample transfer or alternatively deposition of capping layers to prevent oxidation of the sample during air exposure and the deposition process was relatively slow and involved toxic chemicals like lithium tert-butoxide and hydrogen sulfide.

Sputter deposition represents an appealing approach to vapor phase deposition of  $\text{Li}_2\text{S}$  as it is well suited to deposit physically disparate elements with a final stoichiometry matching that of the target. Several research groups have co-sputtered  $\text{Li}_2\text{S}$  with other sulfides in order to synthesize solid electrolyte glasses.<sup>140,141</sup> There is additionally a single report analyzing the sputtering yield of  $\text{Na}_2\text{S}$ , but which did not consider deposition.<sup>142</sup> In this work, we report the sputter deposition of lithium sulfide films ranging in thickness from several nanometers to several microns using a laboratory-built deposition chamber integrated into an inert atmosphere glovebox. We analyze the novel sulfide structures and inhomogeneity in the as-deposited films, including from apparent positional variation in the plasma chemistry. Additionally, we demonstrate how annealing of the films can produce a highly pure, crystalline thin film, and characterize spectroscopic changes in the film before and after heat treatment. Finally, we demonstrate the unique electrochemistry that arises in the sputter-deposited sulfide structure as well as the crystalline annealed films.

## **5.2. EXPERIMENTAL**

### **5.2.1. Apparatus**

All equipment for preparing the sputtering targets, performing sputter deposition, and processing deposited films was integrated into a high-purity argon-filled glovebox (Inert PureLab HE). Powders were pressed into sputtering targets with a 15-ton hydraulic

press (MTI YLJ-15) using a custom fabricated 2” stainless steel pellet die. Heat treatments of the sputtering targets and deposited films were performed in a muffle furnace (Thermo Scientific). A custom built stainless vacuum steel chamber (Vacuum Technology Incorporated, Oak Ridge, TN, USA) was installed on the reinforced floor of the glovebox, with a manual lift to allow access to the interior of the chamber from inside the glovebox. A 2” radio frequency (RF) water-cooled magnetron sputter source (Kurt J. Lesker TORUS) was mounted vertically in the base of the chamber so that films were sputtered up. A rotating fixture was installed in the top of chamber to allow mounting of the substrate and a quartz crystal microbalance (QCM) thickness monitor such that either could be positioned above the sputter source or at various distances and angles away from the center of the source. Research grade (99.9997%) argon gas was fed into an external port through a mass flow controller (MFC) to sustain the plasma for sputtering.

### **5.2.2. Target preparation**

To prepare the  $\text{Li}_2\text{S}$  sputtering target, 7.20 g of commercial  $\text{Li}_2\text{S}$  powder (Alfa Aesar, 99.9% trace metals basis) was loaded into the pellet die and pressure was slowly increased to 4400 psi. The compressed pellet was heated to 600 °C for 12 h. The resultant 1/8” thick pellet was transferred to the vacuum chamber, where it was bonded to a 1/4” thick, 2” diameter copper plate with indium foil heated at 200 °C for 1 h.

### **5.2.3. Substrate preparation**

Spectroscopic evaluation of the  $\text{Li}_2\text{S}$  films was performed on aluminum oxide (corundum) substrates, which were sputter-deposited with 1000 nm of iridium or tungsten on both sides and annealed at 650 °C in argon prior to  $\text{Li}_2\text{S}$  deposition. Iridium and tungsten were selected for their refractory properties and limited reactivity toward sulfides. For time-of-flight secondary ion mass spectrometry (TOF-SIMS) and scanning

electron microscopy (SEM) analysis, the substrates were single-crystal silicon wafers which were coated with a sputter-deposited titanium/titanium dioxide bonding layer followed by ca. 100 nm of sputter-deposited iridium.

#### **5.2.4. Deposition conditions**

Substrates were mounted 5 cm above the sputter target and rotated to a shielded position away from the source. The chamber was pumped down to a base pressure below  $1.5 \times 10^{-6}$  Torr prior to deposition. Argon was fed into the chamber at 20 s.c.c.m. through the MFC and the chamber pressure was adjusted to ca. 40 mTorr via the gate valve regulating the turbo pump. The RF source was turned on at the deposition power (ranging from 30 W to 110 W) to strike the plasma, after which the pressure was immediately adjusted via gate valve to the deposition condition (ranging from 1 to 60 mTorr).

#### **5.2.5. Characterization techniques**

##### ***5.2.5.1. Quartz crystal microbalance***

The deposition rate in the chamber was analyzed with a QCM thickness monitor. The QCM used 5 Mhz AT-cut quartz sensor crystals with gold-coated electrodes. The reported thickness was measured using the literature density of  $\text{Li}_2\text{S}$  ( $1.66 \text{ g cm}^{-3}$ ) and the acoustic impedance of quartz ( $8.25 \times 10^5 \text{ g cm}^{-2} \text{ s}^{-1}$ ) typically used for films of unknown acoustic impedance. QCM crystals were only used with relatively little cumulative deposition (sensor crystal frequency greater than 90% of its pristine value) to minimize any influence of the unknown impedance value for the deposited sulfide films.

### ***5.2.5.2. X-ray diffraction***

Thin film samples were transferred to a sealed holder with a domed 0.1 mm thick polyimide window to protect the sulfides from oxidation during the scan. Diffraction data was collected using filtered Cu K $\alpha$  radiation ( $\lambda = 1.5148 \text{ \AA}$ ), from  $2\theta = 20^\circ$  to  $75^\circ$ .

### ***5.2.5.3. Scanning electron microscopy***

A ca. 100 nm layer of iridium was sputter deposited on top of the sulfide films on silicon substrates to act as a contrast layer and to protect the film from oxidation. The substrates were cleaved and mounted on the SEM stub to allow imaging of the film cross section. Samples were transferred in sealed containers into an argon-filled glovebag affixed to the exterior of the SEM. The samples were thereby transferred into the SEM under argon.

### ***5.2.5.4. Raman spectroscopy***

Deposited films were sealed within a Raman cell with a quartz window to allow for the collection of spectra under air- and moisture-free conditions. Raman spectra were acquired with an Alpha 300 confocal Raman microscope (WITec, GmbH) using a solid-state 532 nm excitation laser and a  $20\times$  objective. The laser spot size is approximately  $1 \mu\text{m}$  and was focused on the surface with a power of ca. 1 mW. Two gratings ( $600 \text{ mm}^{-1}$  and  $1800 \text{ mm}^{-1}$ ) were used to collect spectra from 0 to  $1200 \text{ cm}^{-1}$  or from 0 to  $4000 \text{ cm}^{-1}$ .

### ***5.2.5.5. X-ray photoelectron spectroscopy***

Samples were transferred from the glovebox to the XPS under argon via a custom designed stainless steel transfer capsule which interfaces directly with the instrument, allowing air- and moisture-free transfers. Photoelectron spectra were collected using a monochromated Al K $\alpha$  source ( $h\nu = 1468.5 \text{ eV}$ ) at 150 W (10 mA and 15 kV) with pass energies of 20 eV and 0.05 eV step sizes. A flood gun was utilized to minimize charge

buildup on the insulating samples and spectra were corrected to the adventitious carbon 1s peak at 284.6 eV. Shirley-type backgrounds were used to fit spectra. Sulfur peaks were modeled with two mixed Gaussian-Lorentzian functions such that the  $2p_{1/2}$  and  $2p_{3/2}$  were offset by 1.18 eV and the  $2p_{1/2}$  peak had an identical full-width at half-maximum (FWHM) and half the integrated intensity of the  $2p_{3/2}$  peak. All data processing and peak fitting were performed with CasaXPS software.

#### ***5.2.5.6. Ultraviolet-visible spectroscopy***

Deposited films were placed in 3.0 mL of a 1 : 1 mixture of dimethoxyethane (DME) and dioxolane (DOL) by volume (“DME/DOL”) for 18 h to allow the soluble sulfide species to dissolve. An aliquot of the solution was transferred to a 1-cm path length quartz cuvette and analyzed via a UV/vis spectrometer (Ocean Optics Jaz Spectrometer) located in an argon glovebox. Spectra were collected from 225 to 825 nm. DME/DOL served as the reference blank solution.

#### ***5.2.5.7. Time of flight secondary ion mass spectrometry***

Samples were transferred to the TOF-SIMS instrument via the same air-free technique as with the XPS. Samples were sputtered with a  $\text{Cs}^+$  ion beam at 500 eV or 2 keV that was rastered over an area of  $250\ \mu\text{m} \times 250\ \mu\text{m}$ . Secondary ions were generated with a pulsed 30 keV  $\text{Bi}^+$  analysis beam with 20 ns pulses which was scanned over a  $100\ \mu\text{m} \times 100\ \mu\text{m}$  area centered within the larger primary sputtered region. Mass spectra were collected in negative polarity mode (to collect negatively charged ion fragments).

### **5.2.6. Electrochemistry**

To investigate the electrochemistry of the films, iridium-coated substrates after 4 h of  $\text{Li}_2\text{S}$  deposition, before or after annealing, were assembled into CR2032 coin cells in an argon glovebox. DME/DOL (50  $\mu\text{L}$  total) with 1.2 M lithium

bis(trifluoromethanesulfonyl)imide (LiTFSI) salt added was employed as the electrolyte, with a polypropylene/polyethylene separator (Celgard 2325) and lithium metal as the anode. In order to characterize the as-deposited films without the influence of soluble species, unannealed substrates were placed in 10 mL of DME/DOL for 18 h. After dissolution, the substrates were removed and rinsed in an additional 10 mL of fresh DME/DOL prior to assembly into cells. The assembled cells were allowed to rest for at least 6 h while the open-circuit voltage (OCV) stabilized, then were galvanostatically charged on an Arbin multichannel cycler to 3.0 V (vs. Li/Li<sup>+</sup>).

### 5.3. RESULTS AND DISCUSSION

#### 5.3.1. Deposition analysis

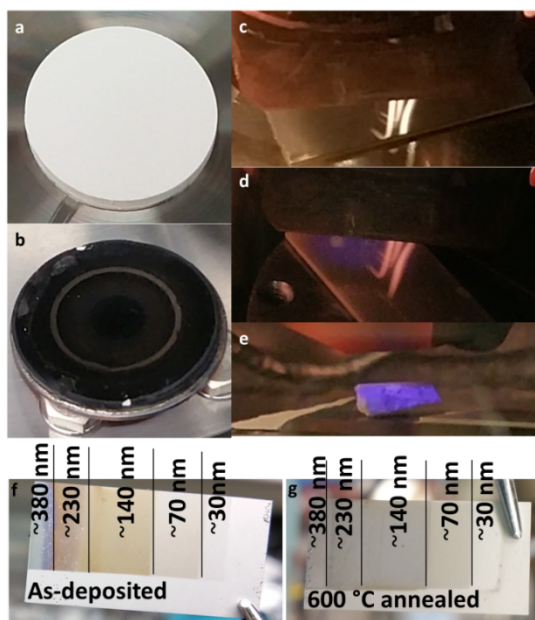


**Figure 5.1.** Photographs of (a) as-prepared Li<sub>2</sub>S target and (b) target after extended deposition. Photographs during X-ray excitation in XPS chamber of (c) unannealed sputter-deposited Li<sub>2</sub>S film, (d) 600 °C annealed sputter-deposited Li<sub>2</sub>S film, and (e) 600 °C annealed, compressed Li<sub>2</sub>S powder illustrating intense violet fluorescence for annealed Li<sub>2</sub>S. Photographs of color variation in (f) unannealed and (g) 600 °C annealed Li<sub>2</sub>S films deposited with gradient thickness on single substrates. The indicated thicknesses are calculated for the films after annealing.

Preparation of the target with the commercial  $\text{Li}_2\text{S}$  provided clear visual evidence for the polysulfide impurities present in the starting material. There was a pronounced change in color of the target before and after heating at  $600\text{ }^\circ\text{C}$ , going from beige to pure white. These off-white impurities have been associated with the presence of polysulfides,<sup>116</sup> and we concluded that heat treatment of the starting material induced evaporation of the excess sulfur, resulting in a lithium : sulfur stoichiometry close to the theoretical 2 : 1. The as-prepared target is shown in Figure 5.1a.

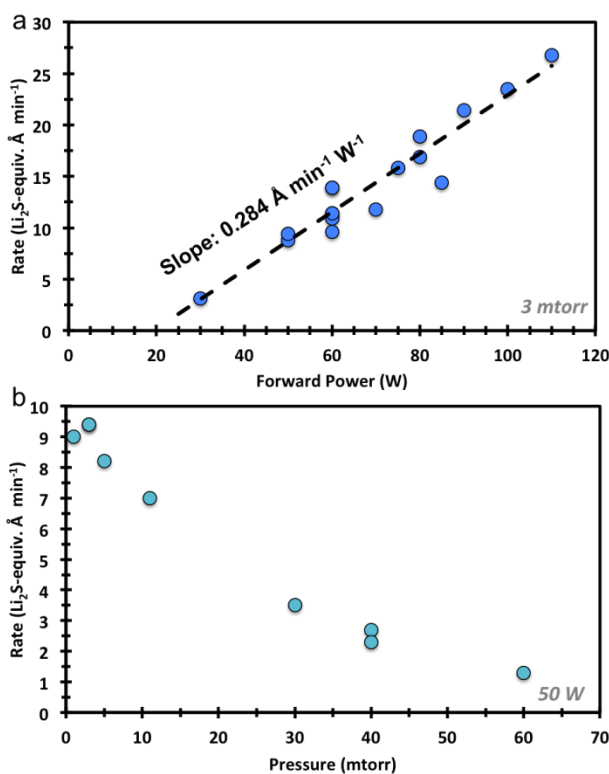


**Figure 5.2.** (a) Dependence of QCM-determined deposition rate with sputtering power at 3 mTorr. (b) Dependence of deposition rate on chamber pressure at 50 W power.

The growth rate and quality of the RF sputter-deposited films is dependent on a multitude of factors. For our system, we are primarily concerned with the chamber

pressure, RF power, and geometric relationship of the target and substrate. These factors influence the rate of primary sputtering of the target, the energy with which sputtered species are ejected, the degree to which sputtered species are thermalized by inelastic collisions with plasma species (or alternatively reach the substrate ballistically with little or no decrease in energy), the fraction of sputtered species that reach the substrate, and the rate at which deposited species are resputtered from the substrate surface. The net deposition rate is determined by the rate of primary sputtering, the fraction of sputtered species that reach the substrate and deposit, and the rate of resputtering of deposited species.

The deposition of  $\text{Li}_2\text{S}$  was monitored via QCM. The deposition rate increased approximately linearly with the forward power of the deposition between 30 and 110 W as shown in Figure 5.2a. Lithium migration and redeposition on the surface of the target during sputtering was visually apparent, as a black metallic surface developed on the target surface surrounding a yellow, sulfur-rich erosion track from the magnetron sputtering process (Figure 5.1b). The lithium migration was exacerbated at high deposition power, causing the formation of metal deposits and ultimately arcing. As such, the deposition power was generally limited to 60 W.

The influence of chamber pressure on the deposition rate (at 50 W forward power) is shown in Figure 5.2b between 1 and 60 mTorr. The net deposition rate generally increased with decreasing pressure, as the loss of deposited material to resputtering at the substrate surface is limited at low pressure and the number of sputtered species reaching the substrate ballistically without thermalizing increases.<sup>82</sup> The deposition rate reached a maximum at 3 mTorr, below which the rate decreased due to the lack of sputtering at very low pressures. Below 1 mTorr, there was insufficient ion density to maintain a plasma and deposition ceased. We grew films at 60 W forward

power and 3 mTorr to maximize the deposition rate, while limiting lithium migration at the target surface.

### 5.3.2. Morphological analysis

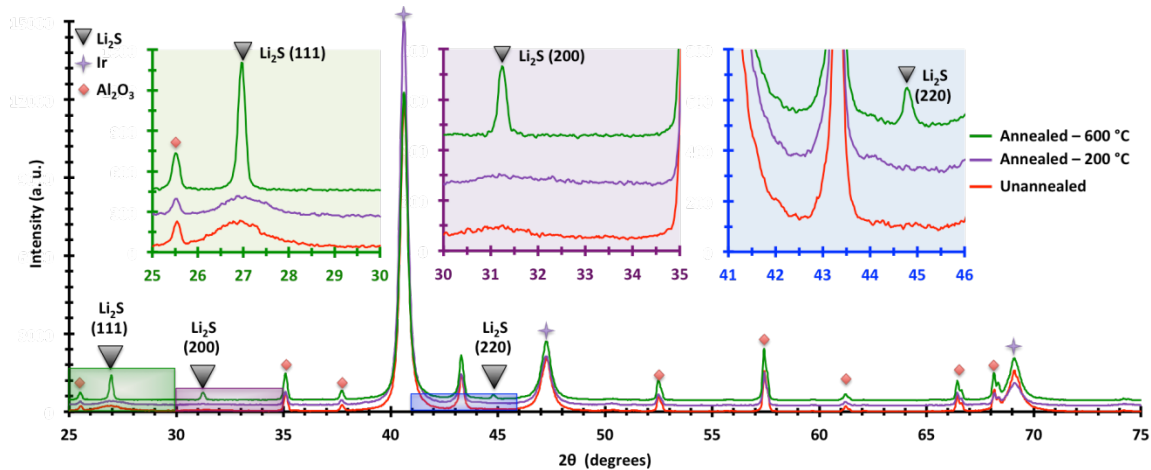


**Figure 5.3.** XRD of an Li<sub>2</sub>S film grown on Ir-coated corundum before annealing (red curve), after annealing at 200 °C (purple curve), and after annealing at 600 °C (green curve). The insets are magnified views of the three strongest Li<sub>2</sub>S peaks.

The as-deposited films were analyzed by XRD (Figure 5.3) and found to exhibit very broad peaks around  $2\theta = 27.0^\circ$  and  $2\theta = 31.2^\circ$ , which would correspond to the (111) and (200) reflections for antifluorite phase Li<sub>2</sub>S (JCPDS No. 23-0369). The peak breadths are characteristic of an amorphous or nanocrystalline material, and little change is observed after heat treatment at 200 °C. After heat treatment to 600 °C, however, the (111) and (200) reflections become sharp and additional antifluorite peaks appear, confirming the formation of crystalline Li<sub>2</sub>S. To our knowledge, this is the first report of the synthesis of crystalline Li<sub>2</sub>S thin films.

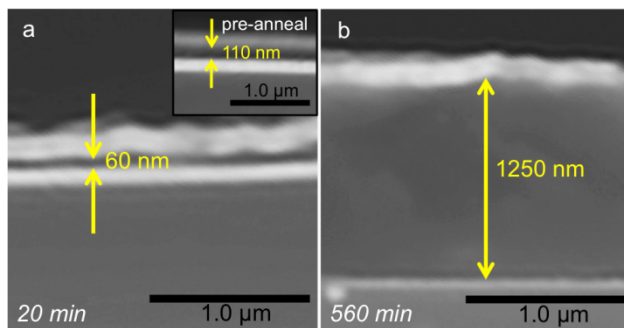


**Figure 5.4.** SEM of the post-annealed film cross-sections after **(a)** 20 minutes and **(b)** 560 minutes of deposition. The inset in **(a)** shows the same deposition before annealing. The bright regions are sputter-deposited Ir contrast layers and the substrates are single crystal silicon.

The morphology and thickness of the deposited  $\text{Li}_2\text{S}$  were analyzed by an SEM cross-section analysis of  $\text{Li}_2\text{S}$  between sputter-deposited iridium contrast layers on cleaved single crystal silicon substrates. A thin film sample after a 20 minute deposition is shown in Figure 5.4a before and after annealing, while a thick film sample after a 560 minute deposition is shown in Figure 5.4b after annealing. The decrease in film thickness after annealing demonstrates that the film densified and/or that weakly bound species evaporated. The average deposition rate for crystalline  $\text{Li}_2\text{S}$  after annealing (*i.e.*, accounting for any material loss and densification) implied by the cross-section analysis was ca.  $22 \text{ \AA min}^{-1}$ . This value is  $\sim 50 \%$  higher than the QCM-determined rate under the same deposition conditions. This could be either an indication that the annealed film is not fully densified (if the mass deposition rate determined by QCM was accurate) and/or that the QCM is underestimating the mass of lithium sulfide deposited. Particularly, if the deposition produces a very loosely adhered, acoustically lossy film, it would be expected to induce a smaller frequency change in the quartz crystal than ideally predicted by the Sauerbrey equation for a rigid film with the same total mass.<sup>84,143</sup> The thickness of the Ir contrast layer (with known acoustic properties) measured via SEM matched that

determined by QCM, confirming that the measured discrepancy in the  $\text{Li}_2\text{S}$  deposition rate is not due to hardware setup.

### 5.3.3. Spectroscopic analysis

We employed several spectroscopic techniques to characterize the chemical purity and composition of the deposited films before and after annealing as presented in Figure 5.5. The XPS sulfur 2p region spectra for an unannealed sulfide film, a film annealed for 2 h at 500 °C, and a film annealed for 18 h at 600 °C (Figure 5.5a) support several conclusions about the chemical environment and purity of the synthesized sulfides. The S 2p XPS binding energy for lithium/sulfur compounds reflects the chemical environment, and particularly the effective oxidation state of the sulfur atoms present in the sample. Elemental, neutral sulfur exhibits an S  $2p_{3/2}$  peak centered at 163.8 eV,<sup>116,144</sup> while  $\text{Li}_2\text{S}$ , with a nominal -2 sulfur oxidation state, has a S  $2p_{3/2}$  peak centered at 159.8 eV.<sup>69,116</sup> In between these two extremes exists the range of polysulfides, with lower binding energies generally reflective of increased lithium bonding to the sulfur (yielding more reduced sulfur), and higher binding energies indicating more sulfur-sulfur bonding (corresponding to less reduced sulfur).

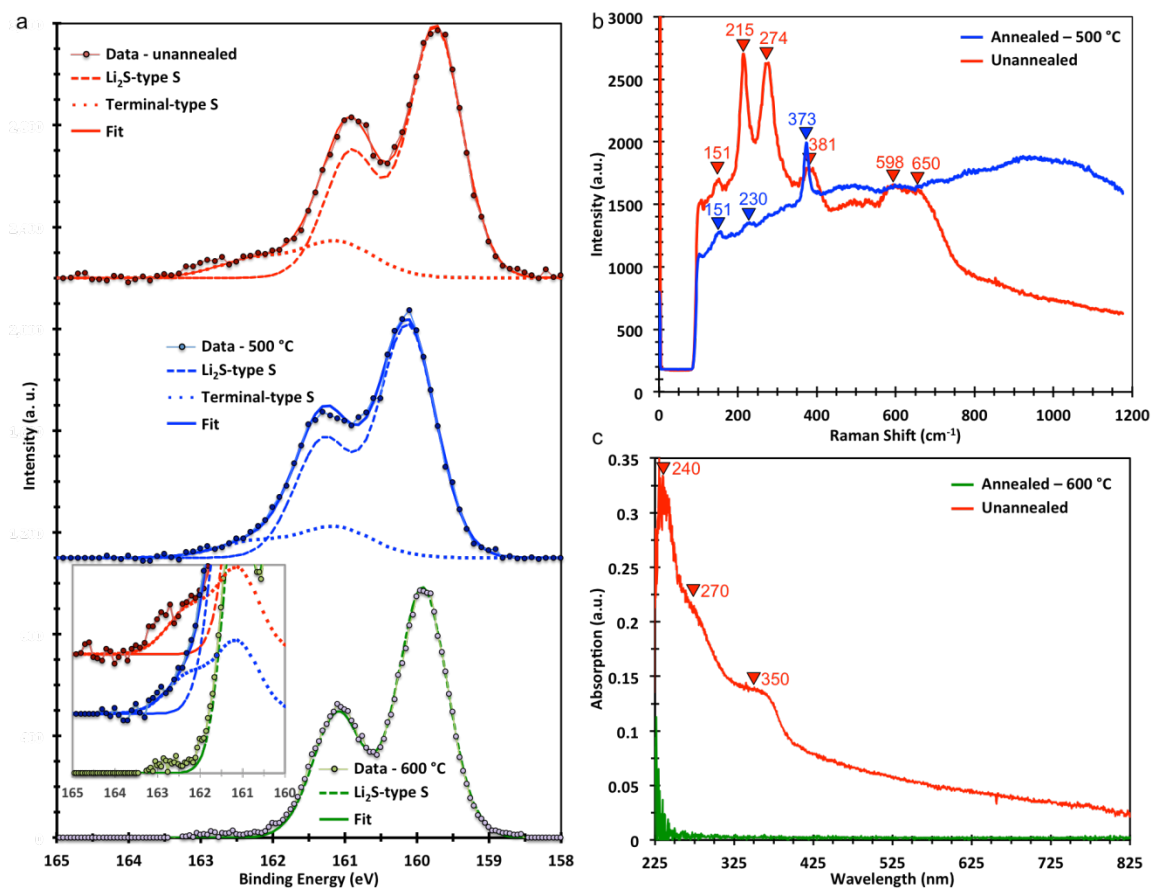


**Figure 5.5.** (a) Shirley background-subtracted XPS spectra for the S 2p sulfide region for unannealed (red curve), 500 °C annealed (blue curve), and 600 °C annealed (green curve) films. The spectra are fit with doublets for the Li<sub>2</sub>S-type (dashed lines) and terminal-type (dotted lines) sulfur atoms, and the sum of these fits are shown (solid lines). The 600 °C curve was fit with only an Li<sub>2</sub>S type doublet. The inset shows a magnified view of the polysulfide region, highlighting the fit in this region. (b) Raman spectra for a film before (red curve) and after (blue curve) annealing, with peak positions labeled. (c) UV-vis spectra of a DME/DOL solution used to solubilize polysulfides from unannealed (red curve) and 600 °C annealed (green curve) films.

Regardless of the annealing condition, there was no photoelectron intensity above 163.5 eV, confirming there was no elemental (neutral) sulfur at the surface of the films. However, the terminal-type sulfur signal with S 2p<sub>3/2</sub> peak centered around 161.2 eV showed persistence up to 500 °C. This sulfur environment is characteristic of a sulfur

atom bonded to a lithium atom and to another sulfur atom and is the sole environment associated with  $\text{Li}_2\text{S}_2$ .<sup>116</sup> As the magnified region in Figure 5.5a shows, this terminal-type peak was no longer visible after extended annealing at 600 °C. This result confirmed that the films annealed to higher temperature were chemically pure  $\text{Li}_2\text{S}$ . To our knowledge, this is the first reported high-resolution XPS spectrum (*i.e.*, with resolved sulfur doublets) for  $\text{Li}_2\text{S}$  to exhibit no apparent terminal sulfur signal under close examination. The remarkable persistence of the terminal sulfur intensity up to 500 °C implies that sulfur-sulfur bonding in lithium sulfides may be far more stable than theoretical studies have suggested.<sup>25,36,145</sup> This stability may also be an artifact of the unique sulfide structure the sputter deposition process appears to have generated.

Annealing to 500 °C did diminish the small apparent intensity around 162.7 eV that is associated with bridging sulfur, which is present only in higher-order polysulfides ( $\text{Li}_2\text{S}_n$ ,  $n > 2$ ). The low intensity of this signal for the unannealed sample suggested any polysulfides were still short-chain, particularly  $\text{Li}_2\text{S}_3$ -type, as indicated by the UV-vis spectra in Figure 5.5b.

The UV-vis spectrum supports the existence of sulfur-sulfur bonding in the unannealed film, though in the form of short chain or “lower order” polysulfides ( $\text{Li}_2\text{S}_x$ ,  $x < 4$ ). The unannealed sample exhibited an absorption peak at 250 nm with shoulders at ca. 270 nm and ca. 360 nm. The lack of absorption above 360 nm confirms that no polysulfides,  $\text{Li}_2\text{S}_n$ , with  $n > 3$  exist, as they absorb at higher wavelength, particularly at 620 nm for the  $\text{S}_3^{\bullet-}$  radical that reliably forms from the dissociation of  $\text{Li}_2\text{S}_6$ . Peaks at 265 and 340 nm have been tentatively ascribed to, respectively,  $\text{Li}_2\text{S}_2$  and  $\text{Li}_2\text{S}_3$  dissolved in TEGDME<sup>33</sup> and similar peaks have been identified for short-chain polysulfides in DME/DOL.<sup>116</sup> The UV-vis spectrum thus appears to support the existence of  $\text{Li}_2\text{S}_2^-$  and  $\text{Li}_2\text{S}_3$ -type species within the as-deposited film, which can be extracted with at least

sparing solubility by DME/DOL. After annealing to 600 °C, the UV-vis spectrum exhibits no features, consistent with the formation of crystalline Li<sub>2</sub>S and the elimination of any soluble sulfur-sulfur bonding.

The Raman spectrum in Figure 5.5c for the annealed specimen features one sharp peak at 373 cm<sup>-1</sup>, characteristic of the symmetric T<sub>2g</sub> mode for crystalline Li<sub>2</sub>S at room temperature.<sup>146</sup> The spectrum for the unannealed sample exhibited strong sharp peaks at 215 cm<sup>-1</sup> and 274 cm<sup>-1</sup> and a moderately sharp peak at 381 cm<sup>-1</sup>. We assign the peak at 381 cm<sup>-1</sup> to the Li-S bond in the largely amorphous unannealed structure, as it matches the peak observed in disordered or higher temperature samples of Li<sub>2</sub>S.<sup>146</sup> The unannealed sample additionally possessed broad intensity around 625 cm<sup>-1</sup> that appeared to be composed of two broad peaks centered near 600 and 650 cm<sup>-1</sup>. The relative intensity of this feature varied significantly between measurements, suggesting it is likely an artifact of fluorescence. Both the annealed and unannealed sample appeared to exhibit a weak feature at 151 cm<sup>-1</sup>. A very weak peak around 230 cm<sup>-1</sup> is observable after annealing at 500 °C. Identification of the weak peaks in the Raman spectra is complicated as the samples strongly fluoresced under laser illumination. The fluorescence was more pronounced in the annealed sample, whereas the background intensity of the unannealed sample tapered off considerably above approximately 700 cm<sup>-1</sup>. We also visibly observed intense violet fluorescence of annealed Li<sub>2</sub>S samples upon exposure to X-rays in the XPS as shown in Figure 5.1c-e. Unannealed and as-deposited samples did not fluoresce significantly, suggesting the presence of sulfur-sulfur bonds may quench this behavior.

The relative intensities of the peaks in the unannealed spectrum are of particular interest, notably the strong peak at 274 cm<sup>-1</sup> and the lack of peaks in the region corresponding to sulfur stretching modes between 400 and 500 cm<sup>-1</sup>. A broad range of molecules containing sulfur-sulfur bonds including various allotropes of sulfur<sup>22,147,148</sup>,

polysulfanes<sup>149,150</sup>, organic polysulfides<sup>148</sup>, and inorganic polysulfides<sup>151–154</sup> all possess a sulfur-sulfur stretching mode between 450 and 480  $\text{cm}^{-1}$  as their strongest Raman-active peak. A symmetric bending mode reliably appears in sulfur and polysulfide spectra between 200 and 230  $\text{cm}^{-1}$ . Additionally, a number of polysulfide species and long-chain neutral sulfur species exhibit a Raman asymmetric bending mode in the range of 260 – 290  $\text{cm}^{-1}$ .<sup>80,127,148,153–156</sup>

However, an extensive review of the sulfur literature found few instances where this peak was strong, particularly in comparison to the peaks around 150 and 220  $\text{cm}^{-1}$ .<sup>22,147,157,158</sup> The closest analogs were polymeric sulfurs,<sup>147</sup> particularly an example of “crystex” sulfur, a long-chain polymeric neutral sulfur allotrope with stabilizing organic constituents.<sup>159</sup> Additionally,  $\text{S}_6$  molecules are known to have a peak around 264  $\text{cm}^{-1}$  of similar strength to a peak at 202  $\text{cm}^{-1}$ ,<sup>148,160</sup> and  $\beta\text{-Na}_2\text{S}_5$  has modes of similar strength around 280 and 209  $\text{cm}^{-1}$ .<sup>152,161</sup> Again, in all cases, the stretching modes in the region of 450  $\text{cm}^{-1}$  exhibited much stronger Raman peaks.

XPS analysis of the unannealed film (Figure 5.5a) does not support the presence of neutral sulfur, so we believe this spectrum represents a previously unreported sulfide structure. The lack of crystallinity (per XRD), highly reduced sulfur (per XPS),  $\text{Li}_2\text{S}$  type bonding (per XRD, XPS, and the Raman peak at 381  $\text{cm}^{-1}$ ), and analogy to a polymeric-type sulfur in the Raman spectrum suggest the unannealed films are composed of an unusual structure containing chains of  $\text{Li}_2\text{S}$  units (with a slightly sulfur-rich average stoichiometry). The relative sharpness of the Raman peaks confirms there must be at least medium-range order to the structure of these films and that it is not a disordered, truly amorphous  $\text{Li}_2\text{S}$  as, for instance, is observed for  $\text{Li}_2\text{S}$  near its melting point.<sup>146</sup> The presence of this new phase is not too surprising given the known propensity of sputtering techniques to create new metastable structures.<sup>162–165</sup>

### 5.3.4. Electrochemistry

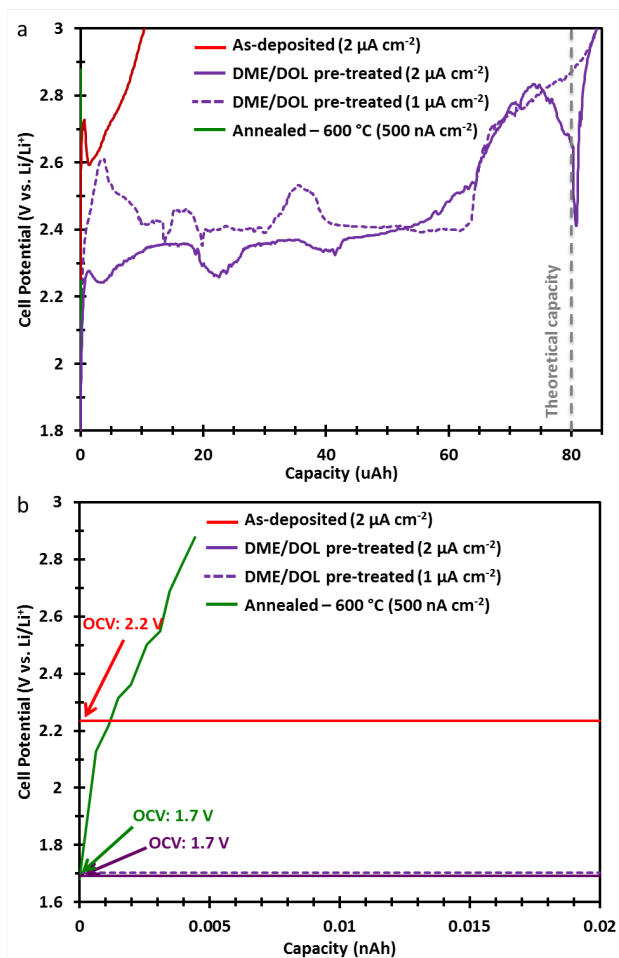


**Figure 5.6.** Galvanostatic charge of unannealed as-deposited  $\text{Li}_2\text{S}$  films (red curve), unannealed films pre-treated with DME/DOL (purple curve), and  $600\text{ }^\circ\text{C}$  annealed film (green curve) at  $2\text{ }\mu\text{A cm}^{-2}$  (solid line) or  $1\text{ }\mu\text{A cm}^{-2}$  (dashed line) for the unannealed films and  $500\text{ nA cm}^{-2}$  for the annealed film. **(a)** Full charge for all three cells to  $3.0\text{ V}$  (vs.  $\text{Li/Li}^+$ ); the theoretical  $\text{Li}_2\text{S}$  charge capacity for an annealed film after  $4\text{ h}$  deposition at  $2.2\text{ nm min}^{-1}$  is indicated by the dashed grey line. **(b)** Immediate start of the charge process, with the open-circuit voltages (OCV) for each cell indicated.

Electrochemical evaluation of lithium sulfide films with three different post-deposition treatments is presented in Figure 5.6. The dissolution of soluble polysulfides observed by UV/vis spectroscopy is clearly reflected in the OCV of the films. The OCV of the as-deposited films assembled into cells with no further treatment gradually

increased above 2.2 V (vs. Li/Li<sup>+</sup>), as the excess sulfur in the film formed lithium polysulfides in solution. Conversely, films that had the soluble components removed, either by annealing at 600 °C or pre-treatment with DME/DOL, settled near 1.7 V (vs. Li/Li<sup>+</sup>) with resting time. This value represents a useful parameter to establish the chemical purity of a Li<sub>2</sub>S cathode with respect to soluble polysulfides.

The observed galvanostatic charge behavior for the different post-deposition treatments was of interest on several fronts. Based on the post-annealing SEM-determined deposition rate of 2.2 nm Li<sub>2</sub>S min<sup>-1</sup>, the theoretical charge capacity for the insoluble Li<sub>2</sub>S in these cells is 80 μAh (corresponding to a ca. 500 nm thick film). This value is in good agreement with the observed charge capacity for the DME/DOL pre-treated film, while greatly exceeding that of the as-deposited film (ca. 10 μAh). The 600 °C annealed film was so strongly insulating that the iR overpotential at the initially employed 2 μA cm<sup>-2</sup> charge rate did not allow collection of a single data point before exceeding the 3.0 V charging cut-off voltage (the potential exceeded 6 V vs. Li/Li<sup>+</sup> upon application of current). At a reduced charging rate of 500 nA cm<sup>-2</sup>, there was still effectively no charge capacity, as shown in Figure 5.6b. This result demonstrates that thick crystalline Li<sub>2</sub>S deposits are effectively electrochemically inactive in the absence of soluble polysulfides and/or exposed current collector area. Placing this result in the context of studies analyzing the ‘activation’ of Li<sub>2</sub>S particles emphasized that any proposed mechanism for crystalline Li<sub>2</sub>S activation must account for the presence of sulfur-sulfur bonding in the starting solid and/or soluble polysulfides in the electrolyte, as *in situ* generation of a polysulfide phase via applied potential from a pure crystalline Li<sub>2</sub>S starting material may not be realistic.<sup>58,63</sup>

The comparison of the unannealed films with or without DME/DOL pre-treatment reflects the facile electrochemistry of the unique lithium sulfide structure generated by

sputter deposition. The as-deposited film without pre-treatment generated soluble polysulfides upon exposure to electrolyte. These polysulfides preferentially oxidize relative to the solid sulfide species, resulting in formation of insulating, solid sulfur on the cathode surface. The deposition of sulfur leads to a large  $iR$  overpotential, causing the charging cut-off voltage to be reached well before all the solid sulfides are oxidized.

With DME/DOL pre-treatment, however, the full theoretical charge capacity was realized. The implication of the limited charge capacity for the polysulfide-generating cell—that polysulfides are oxidized preferentially, passivating the cathode with solid sulfur—suggests that the pre-treated cells do not form polysulfides early in the charge process. The increase in potential above 60  $\mu\text{Ah}$  would then correspond to the initiation of polysulfide dissolution and oxidation and deposition of sulfur. The sharp decrease in potential below 2.4 V (vs.  $\text{Li}/\text{Li}^+$ ) near the theoretical capacity is explained by near complete oxidation and dissolution of the original solid sulfide material, exposing the bare Ir electrode surface. The cell then rapidly charges to the cut-off voltage as polysulfides are oxidized to solid, insulating sulfur. Subsequent cycling (Figure 5.7) is limited to below 12  $\mu\text{Ah}$  due to electrodeposition of insulating  $\text{Li}_2\text{S}$  or S on the cathode surface. The sharp drop in voltage is not observed at the lower charging rate of  $1 \mu\text{A cm}^{-2}$ , presumably due to complete formation of soluble polysulfides before the initiation of sulfur electrodeposition. The total charge capacity at both rates (84  $\mu\text{Ah}$ ) was identical, and corresponds to the complete oxidation of 550 nm of  $\text{Li}_2\text{S}$  to sulfur, for a back-calculated deposition rate of  $2.3 \text{ nm min}^{-1}$ .

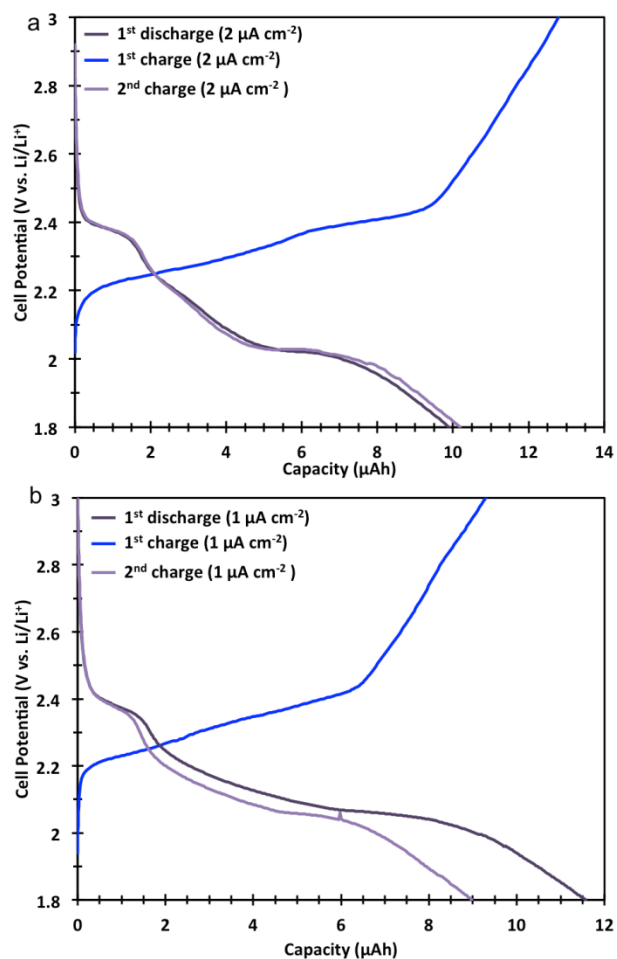


**Figure 5.7.** Galvanostatic charge and discharge curves after the first charge for DME/DOL pre-treated unannealed Li<sub>2</sub>S cells cycles at **(a)** 2 μA cm<sup>-2</sup> and **(b)** 1 μA cm<sup>-2</sup>

The markedly different electrochemistry for the polysulfide-extracted, as-deposited Li<sub>2</sub>S structure warrants further exploration as a potential active material. While we must consider the role porosity plays in films that have not been densified by annealing, the improvement in charge behavior over the annealed, crystalline film is remarkable and suggests that the sputter-deposited structure is far less insulating than crystalline Li<sub>2</sub>S. Linear (neutral) sulfur chains are known to be conductive.<sup>166</sup> Any application would require the potential solid-state charging mechanism could be utilized

without the loss of the original sulfide structure up to 50 – 75% of the theoretical capacity.

### 5.3.5. TOF-SIMS Analysis

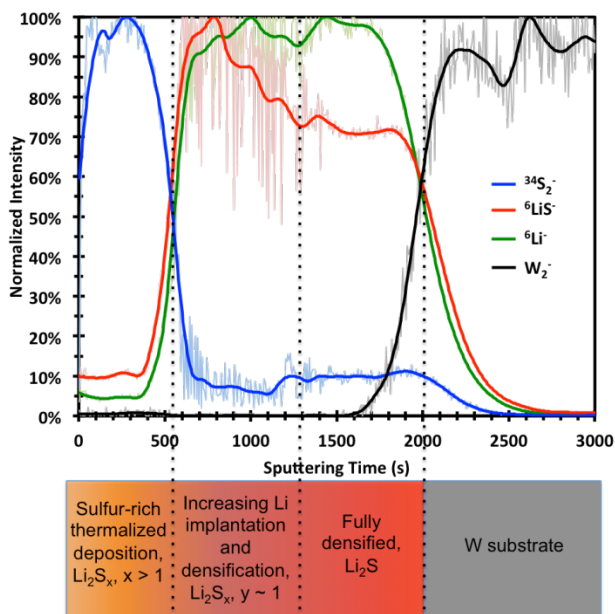


**Figure 5.8.** Normalized TOF-SIMS depth profiles for an as-deposited thick  $\text{Li}_2\text{S}$  film on a polished tungsten-coated substrate. Profiles are shown for  $^{34}\text{S}_2^-$  (blue curve),  $^6\text{LiS}^-$  (red curve),  $^6\text{Li}^-$  (green curve), and  $\text{W}_2^-$  (black curve) molecular fragments. Below the profiles is a schematic of the different regions in the context of the proposed deposition mechanism.

The chemical uniformity of the as-deposited films was analyzed by TOF-SIMS for a thick film sample, as presented in Figure 5.8. Comparing the normalized profile for a pure sulfur fragment,  $^{34}\text{S}_2^-$ , with that of the  $^6\text{Li}^-$  and  $^6\text{LiS}^-$  fragments, we see the surface of the as-deposited film is strongly enriched in sulfur relative to lithium and lithium-sulfur bonding. The pure sulfur signal appears to suggest a relatively distinct interface between the comparatively sulfur-rich and lithium-rich regions. Furthermore, comparison of the  $^6\text{Li}^-$  and  $^6\text{LiS}^-$  fragments shows some attenuation of the  $^6\text{LiS}^-$  signal relative to the

${}^6\text{Li}^-$  signal (while the  ${}^{34}\text{S}_2^-$  likewise remains approximately constant), suggesting the film become progressively more lithium-rich (relative to sulfur) with depth.

Sputtering of compounds with elements of disparate atomic weights such as  $\text{LaB}_6$  (and by analogy,  $\text{Li}_2\text{S}$ ) is known to result in a loss of stoichiometry as the low atomic weight atom is backscattered by argon at a much higher rate.<sup>167,168</sup> This results in preferential redeposition of low atomic weight B at the target (analogous to Li in this system) and corresponding stoichiometric richness of the heavier La (analogous to S in this system) in the film.<sup>167,168</sup> As a result of this discrepancy in scattering angle, it is also expected that Li atoms which reach the substrate are more likely to have experienced no or few scattering events, particularly at intermediate pressure. Therefore, the proportion of Li atoms depositing at the substrate with high energy will be greater than for S.

We hypothesize here a hybrid deposition mechanism dominated by two distinct processes to explain this profile: (1) low energy thermalized deposition of a low-density sulfur-rich flux and (2) high energy implantation of sputtered lithium atoms that experienced few or no scattering events. The high-energy implantation drives the growth of a densified layer of  $\text{Li}_2\text{S}$  underneath the surface as shown in the schematic of Figure 5.8. The plasma physics driving this mechanism are explored in greater depth in the final section of this chapter analyzing geometric variations in the deposition process. This complex depth profile reinforces the need for annealing to form a homogenous film for analysis of fundamental  $\text{Li}_2\text{S}$  properties.

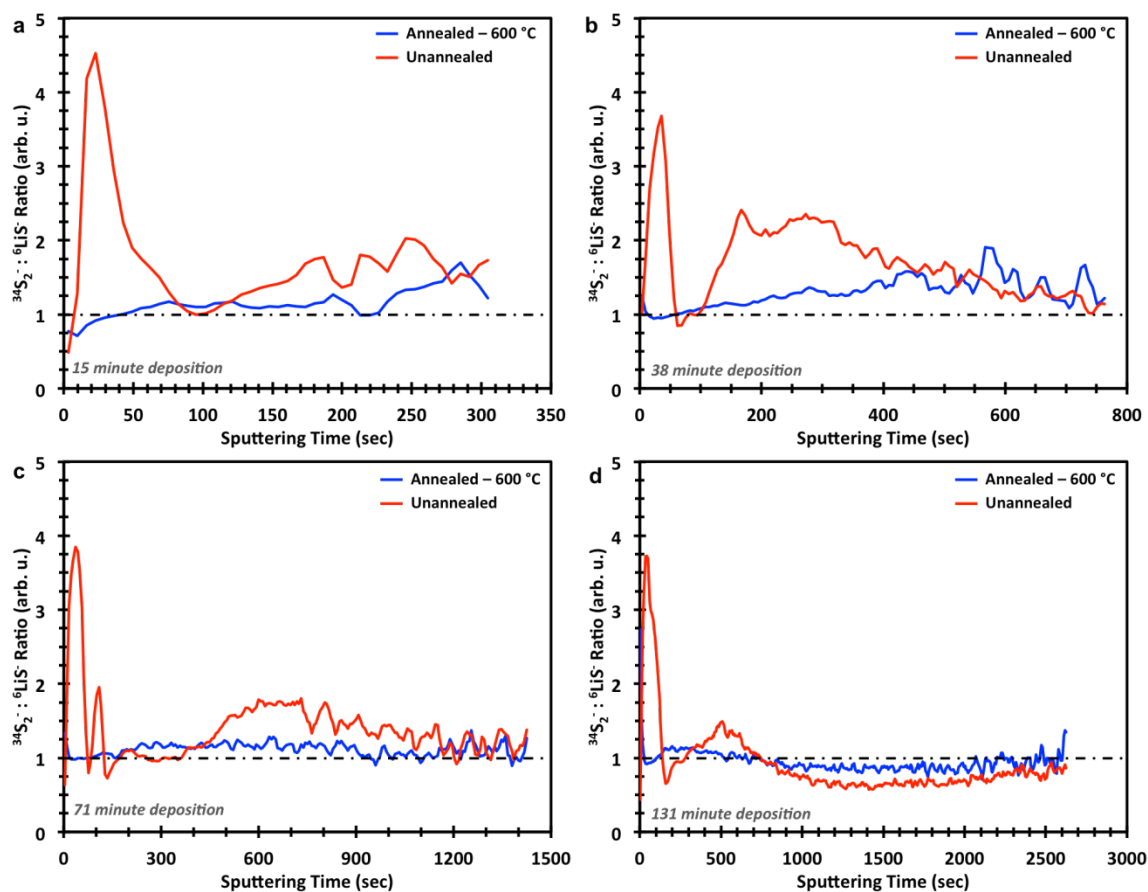


**Figure 5.9.** TOF-SIMS depth profiles for a ratio of the normalized  $^{34}\text{S}_2^-$  molecular fragment to the  $^6\text{LiS}^-$  fragment for unannealed (red curve) and 600 °C annealed (blue curve) films after deposition for **(a)** 15 minutes (~30 nm), **(b)** 38 minutes (~80 nm), **(c)** 71 minutes (~160 nm), and **(d)** 131 minutes (~300 nm). The dashed line at a ratio of unity represents an idealized profile for a homogenous single-component film. The substrate was Ir-coated single crystal silicon.

The effect of annealing on the homogeneity of the sulfur and lithium distribution was analyzed by TOF-SIMS as presented in Figure 5.9. The profiles represent the ratio of the  $^{34}\text{S}_2^-$  secondary ion fragment to the  $^6\text{LiS}^-$  fragment after both have been normalized to their respective maxima. For a homogenous film of single chemical composition, this treatment would yield a flat profile at a ratio of unity. As observed for all four depositions (of increasing time), the annealed films exhibit the expected flat profile very close to the

theoretical value of one, consistent with a homogenous lithium sulfide film. The as-deposited films, however, show strong enhancement of the sulfur film at the surface as seen in the thick film profile in Figure 5.8. Color variation in these films with thickness and annealing is shown in Figure 5.1f-g.

### 5.3.6. Indirect deposition analysis

The depth inhomogeneity observed via SIMS motivated further analysis of the plasma chemistry and deposition mechanism(s) leading to film growth. The energetics of particle impingement on the substrate—whether the sputtered particles reach the substrate ballistically (*i.e.*, line-of-sight deposition with no atomic collisions) at high energy or if they are thermalized by multiple atomic collisions in the plasma and diffuse to the substrate with the average energy of the particles in the gas—significantly affect the resulting deposition morphology. To analyze these effects, we characterized films grown via “direct deposition”, where the substrate was located directly above the target, and those grown via “indirect deposition”, where the substrate was rotated a horizontal distance of 12 cm away from the substrate (an angle from the center of the target to the center of the substrate of  $68^\circ$ ). With greater target-to-substrate distance and a correspondingly small solid angle from the substrate to target, thermalized deposition can be expected to dominate over high-energy ballistic line-of-sight deposition in the indirect configuration. Intentional positioning of the substrate in an off-axis configuration has been employed in the synthesis of  $\text{YBa}_2\text{Cu}_3\text{O}_7$  films to eliminate non-stoichiometry arising from variation in the rate of high-energy line-of-sight deposition among the constituent elements.<sup>169</sup>

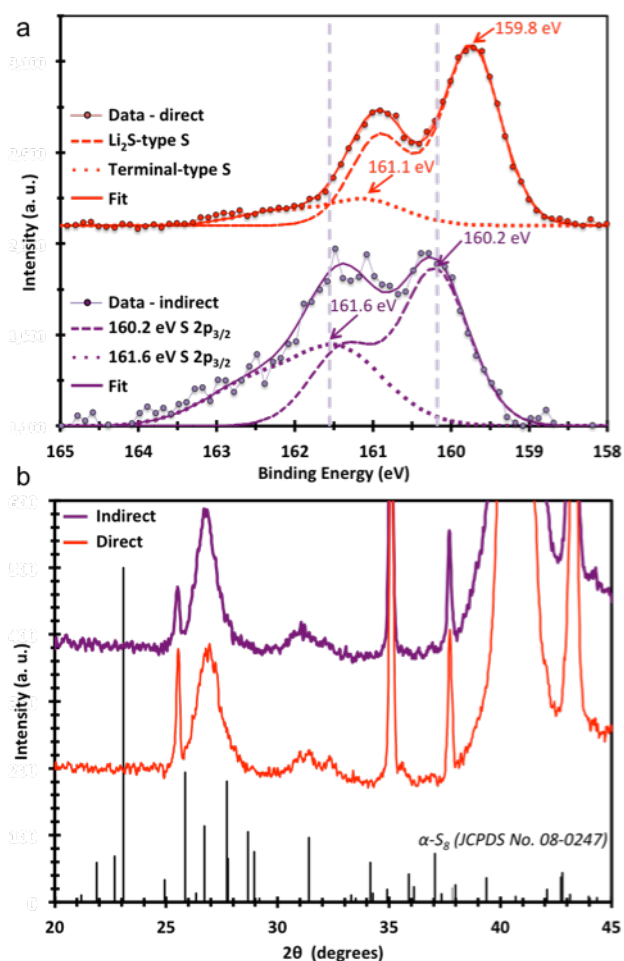


**Figure 5.10. (a)** Background-subtracted S 2p XPS region spectra of the surface of unannealed sulfide films after deposition in the direct (red curve) and indirect (purple curve) configuration. Two doublets (dashed and dotted lines) are used to fit the spectra. **(b)** XRD patterns for indirect and direct depositions as well as a reference pattern for orthorhombic sulfur.

The surface film originating from indirect deposition was compared to that from direct deposition via XPS in Figure 5.10a. The intensity of the sulfur 2p signal at binding energies greater than 161 eV, corresponding to sulfur-sulfur bonding, was much stronger for the indirect deposition, confirming the thermalized flux was sulfur-rich. Additionally, the whole spectrum appears shifted to higher binding energy by 0.4 eV for the indirect deposition, suggesting the sulfur is less oxidized than in a true Li<sub>2</sub>S bonding environment.

However, there remains no intensity at binding energies greater than 163.5 eV, indicating no neutral sulfur is at the surface.

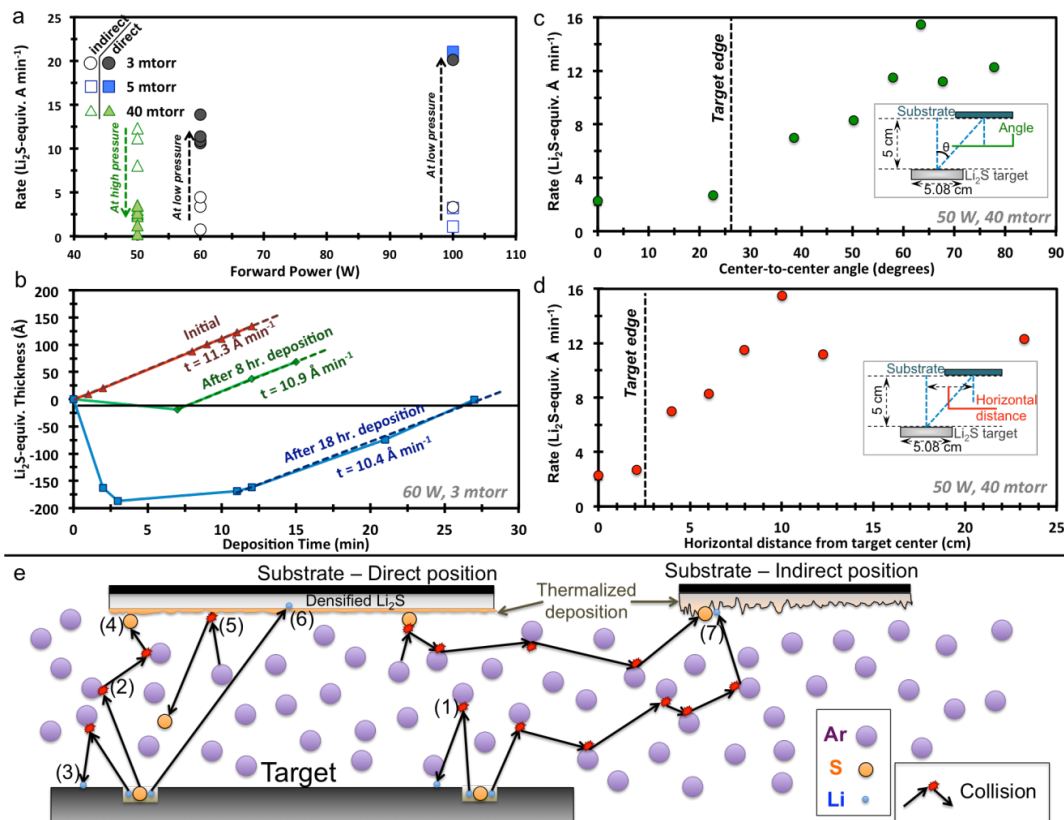


**Figure 5.11.** (a) Deposition rate at selected deposition powers, pressures, and rate monitor positions. Green triangles are at 40 mTorr, blue squares are at 5 mTorr, and black circles are at 3 mTorr. Open markers indicate the QCM was in an indirect position and closed markers indicate the QCM was directly above the target. (b) Thickness of QCM measured deposition at 60 W and 3 mTorr as a function of time in the direct configuration after QCM had spent no time (red curve), 8 h (green curve), and 18 h (blue curve) in the indirect position. (c) Deposition rate at 50 W and 40 mTorr as a function of angle and (d) horizontal distance between the substrate the thickness monitor. The inset schematics illustrate the definition of these parameters. (e) Schematic of the various relevant processes hypothesized to lead to the observed deposition rates. (1) High-angle backscattering of Li. (2) Low-angle forward scattering of S. (3) Redeposition of Li on target. (4) Low energy thermalized deposition of S on substrate surface. (5) Resputtering of low surface binding energy sulfur from substrate. (6) Ballistic deposition of Li into substrate film. (7) Thermalized deposition of Li and S species throughout chamber.

The XRD pattern for the indirect deposition is shown in Figure 5.10b and is functionally identical to the XRD pattern for the direct deposition, showing the same broad amorphous  $\text{Li}_2\text{S}$ -type reflections at  $2\theta = 27.0^\circ$  and  $31.2^\circ$ . Notably, no elemental sulfur peaks appear, such as for orthorhombic  $\alpha\text{-S}_8$ , whose powder pattern is shown for reference. We conclude from this result and the XPS that the indirect deposition is not the result of a pure evaporative sulfur flux, but instead is a relatively sulfur-rich mix of lithium sulfide species.

The angular dependence of the deposition rate at different chamber pressures, as shown in Figure 5.11a, reflects typical sputtering deposition behavior at low pressure, but deviates at high pressure. At 5 mTorr and below, the deposition rate decreased significantly, from ca.  $12 \text{ \AA min}^{-1}$  to ca.  $3 \text{ \AA min}^{-1}$  (at 50 W forward power), when the thickness monitor was rotated from the direct position over the target to the indirect position. The rate did not drop to zero, reflecting uniform deposition throughout the chamber of thermalized sputtered species. The relatively stable indirect deposition rates at low pressures and high powers reflect the fixed gas density of thermalized species at fixed pressure and independence of the energy of the thermalized species with power. As a result, there is no increase in indirect deposition rate at fixed pressure with increased RF power.

In contrast, at a higher chamber pressure of 40 mTorr, the net deposition rate dramatically increased in the indirect configuration ( $10 \text{ \AA min}^{-1}$ ). The measured net deposition rate was at a minimum when the QCM was directly above the  $\text{Li}_2\text{S}$  target ( $2 \text{ \AA min}^{-1}$ ), which we can define as the limit of direct deposition. This unexpected result was further probed by analyzing the measured deposition rate as the QCM was rotated away from target, as shown in Figure 5.11c-d. As the QCM is rotated beyond the edge of the target, the deposition rate steadily increases until the QCM has been rotated  $> 60^\circ$  ( $> 10$

cm) from the target center. Beyond this distance, the deposition rate is relatively stable (approx.  $11 \text{ \AA min}^{-1}$ ).

Two important factors to consider are that at high pressure, the rate of resputtering of deposited atoms at the substrate will be higher and/or that species with low surface binding energy, such as elemental sulfur (as evidenced by its high vapor pressure<sup>22</sup>), will be easily lost.<sup>82</sup> This is because there is less material depositing on the previously added adatoms which would normally trap the species. Consequently, the deposited species will be readily evaporated or resputtered in the direct configuration. Additionally, higher pressures lead to more collisions at the substrate and thus more substrate heating, which will further enable loss of surface species to resputtering, decomposition and/or evaporation.

The envisioned scattering and deposition processes involved, illustrated schematically in Figure 5.11e, provide a framework to understand the anomalous dependence of deposition rate with substrate position and pressure. In the indirect configuration, the QCM is exposed predominantly to a flux of low-energy thermalized species, both from the target and resputtered from the weakly adhered surface layer of the substrate, leading to a high deposition rate. As the QCM is rotated to the direct position, it begins to be exposed to high-energy particles (Li, S,  $\text{Li}_x\text{S}_y$ , Ar) in the plasma, which lowers the net deposition rate due to resputtering/evaporation.

We further note that after initially rotating the thickness monitor into the plasma over the target, the frequency of the QCM crystal would change unpredictably for several minutes, reflecting instantaneous thickness changes that would oscillate from negative values (net loss of material from the crystal surface) to extremely high values (corresponding to deposition rates  $> 10 \text{ \AA sec}^{-1}$ ). We explain this response in the context of the proposed deposition mechanism. The more thermalized flux forms a lower density,

weakly adhered sulfur-rich film on all surfaces within the deposition chamber, including the surface of the thickness monitor crystal. This is because the depositing species do not have enough energy to evaporate the sulfur. When the QCM is then rotated into the plasma above the target, initial exposure to high-energy ballistic ions alternately sputters off loosely adhered material and/or promotes evaporation of sulfur (leading to negative instantaneous deposition rates) or leads to efficient capture of sputtered ions and deposition (leading to highly positive instantaneous deposition rates). This oscillation continues until a steady state is reached (and the film is densified), after which only positive net deposition occurs. A weakly adhered sulfur-rich film also explains the underestimation of deposition rate observed earlier by QCM, as it is expected to be acoustically lossy.

Figure 5.11d shows evidence for this process behavior. The QCM initially records a stable positive deposition rate ( $11.3 \text{ \AA min}^{-1}$ ). The thickness monitor is then rotated to the indirect deposition position, while sputter deposition proceeds for 8 h on a substrate. When the crystal is then rotated back to the direct deposition position, the rate is initially negative (as a result of the loosely adhered indirect deposition being ejected by direct sputtering) before stabilizing after  $\sim 8$  min. near the initially measured deposition rate ( $10.9 \text{ \AA min}^{-1}$ ). After the QCM is again rotated away for 18 h of indirect deposition and then returned to the direct position, the deposition rate goes much more negative and takes longer to stabilize near the original rate ( $10.4 \text{ \AA min}^{-1}$ ). This is consistent with a thicker low-density film being formed with extended indirect deposition, allowing for more loosely adhered material to be resputtered and taking longer to densify and reach a stable net deposition rate upon reintroduction to the plasma.

The complexities identified in the sputter deposition process for  $\text{Li}_2\text{S}$  emphasize the need for careful consideration of the process parameters for a given application.

Relatively high growth rates can be achieved at the employed conditions (60 W and 3 mTorr), but with some sulfur richness and two distinct film regions. This is acceptable for subsequent generation of high-purity crystalline  $\text{Li}_2\text{S}$  with annealing, but to generate a stoichiometric, homogenous film with the as-deposited structure, higher deposition pressures or modified target-substrate geometries/compositions would be required.

#### **5.4. CONCLUSIONS**

We have demonstrated an apparatus for the sputter deposition and processing of air-sensitive lithium sulfide films. The sputtering of  $\text{Li}_2\text{S}$  is shown to result in a complex deposition mechanism, with nonstoichiometry and depth inhomogeneity driven by the large difference between the component atoms. This mechanism and the corresponding anomalous position- and pressure-dependent sputtering rates should provide significant understanding of nonstoichiometry arising during sputter deposition of many related sulfide materials. We observe that sulfide films generated by this process, while only slightly sulfur-rich relative to the ideal  $\text{Li}_2\text{S}$  stoichiometry, appear to form a previously unobserved polymeric-type structure. This structure is shown to exhibit promising electrochemistry, indicative of a solid-state charge process. The sulfur-sulfur bonding produced in this process was shown to possess remarkable stability up to 500 °C and extended annealing at 600 °C was ultimately required to obtain pure, crystalline films of  $\text{Li}_2\text{S}$ . Fully annealed, crystalline 500 nm thick  $\text{Li}_2\text{S}$  films were shown to be electrochemically inactive in a typical lithium-sulfur battery environment. This method provides a useful route to obtaining films of alkaline sulfide materials for sulfur battery applications, particularly the analysis of their fundamental and limiting material properties.

## Chapter 6: Rational design of lithium-sulfur battery cathodes based on experimentally determined maximum active material thickness\*

### 6.1. INTRODUCTION

Lithium-sulfur (Li-S) batteries have attracted intense research scrutiny over the last decade as a next-generation conversion battery chemistry, owing to its extremely high theoretical gravimetric energy density ( $1,672 \text{ mAh g}^{-1}$ ) relative to traditional intercalation lithium-ion battery chemistries.<sup>13,15</sup> Much progress has been made in overcoming the inherent problems associated with the use of insulating active materials, both sulfur and the final discharge product, lithium sulfide ( $\text{Li}_2\text{S}$ ). The dominant approach in this regard has been the development of nanostructured carbon/sulfur or carbon/ $\text{Li}_2\text{S}$  composites to realize sufficient conductivity and cycling rate performance. Several reviews have summarized the current landscape for these composites.<sup>13,16</sup>

While the effective utilization ( $> 75\%$  theoretical) of sulfur has been largely realized, it has become apparent the volume of electrolyte and carbon required is highly problematic. Most studies specifying the electrolyte : sulfur (E/S) ratio use at least 10 mL electrolyte per 1 g sulfur, or do not specify the electrolyte volume at all, implying it was used in excess. Recent reports have demonstrated reasonable performance down to an E/S ratio as low as 4 : 1.<sup>75</sup> Significant volumes of liquid electrolyte are required for two primary reasons: (1) liquid electrolytes are required to generate soluble polysulfides that participate in the typical Li-S charge/discharge mechanism and (2) electrolyte is required to fill the pore structure of the sulfur or  $\text{Li}_2\text{S}$  conductive host in order to provide contact between the active material and the electrolyte. The emergence of the E/S ratio as a

---

\* Portions of this chapter have been submitted for publication as, [M. J. Klein](#), G. M. Veith, A. M. Manthiram, "Rational design of lithium-sulfur battery cathodes based on experimentally determined maximum active material thickness," submitted, 2017. M. J. Klein carried out the experimental work. G. M. Veith and A. Manthiram supervised the research. All participated in manuscript preparation.

critical parameter for Li-S cells has motivated the question of what realistic energy densities are obtainable for a Li-S sulfur battery at the cell-level. In this chapter, we combine new experimental work on the limiting thickness of solid  $\text{Li}_2\text{S}$  that can be charged with a simple model for pore filling of hypothetical carbon structures to approach this problem.

## **6.2. EXPERIMENTAL**

### **6.2.1. Deposition parameters**

Films of lithium sulfide were grown on iridium metal-coated substrates by RF magnetron sputter deposition in a lab-designed chamber interfaced directly into an argon-filled glovebox to enable synthesis and processing under inert conditions. The deposition chamber was integrated directly into an argon glovebox to enable all synthesis and processing steps to occur under an inert atmosphere. The deposition set-up utilized a water-cooled toroidal RF magnetron sputter gun (Kurt J. Lesker TORUS). Substrates were rotated to a position 5 cm above the sputter target during deposition. The 2-inch diameter sputter target was prepared by compressing  $\text{Li}_2\text{S}$  powder at 4400 psi, and then heat treating at 600 °C under argon to densify the target and evaporate excess sulfur. The solid  $\text{Li}_2\text{S}$  was indium-bonded to a copper backing plate to enable good thermal contact with the sputter gun.

The chamber was evacuated by a turbomolecular pump to a base pressure below  $1.5 \times 10^{-6}$  torr prior to deposition. During deposition, 14 s.c.c.m of research-grade (99.9997 %) argon was fed into the chamber through a mass flow controller and the chamber pressure was regulated to 3 mTorr by adjusting the gate valve throttling the pump. After striking the plasma, the deposition was performed at 60 W RF power. The substrate was rotated away from the target to a shielded position for a typically 30-minute

pre-sputter period prior to deposition. After deposition, the films were annealed at 600 °C for ~ 6 h in a box furnace located in the same argon glovebox as the deposition chamber under argon to densify and crystallize the Li<sub>2</sub>S.

**Table 6.1.** Measured and calculated Li<sub>2</sub>S film thickness, based on given pre-sputter and deposition times. The measured thicknesses are from Figure 5.4, and the calculated thicknesses were based on the deposition rates indicated in the first row of the table.

<i>Deposition rate: 2.22 nm min<sup>-1</sup></i>		<i>Pre-sputter rate: 0.75 nm min<sup>-1</sup></i>	
<b>Deposition Time (min)</b>	<b>Pre-sputter time (min)</b>	<b>Measured thickness (nm)</b>	<b>Calculated thickness (nm)</b>
<b>20</b>	<b>20</b>	60	59.3
<b>240</b>	<b>30</b>	550	554.1
<b>561</b>	<b>10</b>	1250	1250.1

We determined the steady-state deposition rate for Li<sub>2</sub>S (after annealing) via SEM to be 2.2 nm min<sup>-1</sup> from Figure 5.4. For thin depositions, the final thickness was greater than predicted by the steady-state rate, which we determined was the result of imperfect shielding of the substrates during the pre-sputter period. We calculated the rate of deposition during the pre-sputter period to be 7.5 Å s<sup>-1</sup> by analyzing the measured thickness of films with different deposition and pre-sputter times (Table 6.1). We verified these values for thin films by analyzing the full-width at half-maximum (FWHM) of time-of-flight secondary ion mass spectrometry (ToF-SIMS) profiles of a <sup>6</sup>LiS<sup>-</sup> fragment—corresponding to the lithium sulfide layer—for a series of films grown with progressively longer total pre-sputter and deposition times. A plot of the calculated thickness vs. FWHM (Figure 6.1) could be fit with a linear trend line passing through the origin.

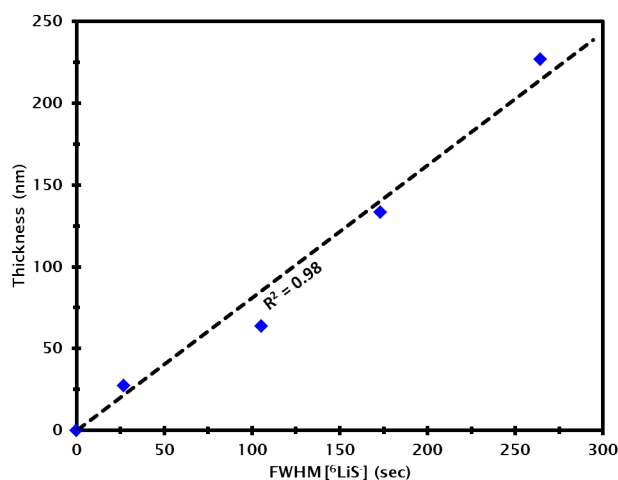


**Figure 6.1.** Calculated thickness for  $\text{Li}_2\text{S}$  films of increasing pre-sputter and deposition time vs. FWHM for the  $^6\text{LiS}^-$  secondary ion fragment ToF-SIMS profile. The dashed line is a linear least-squares fit passing through the origin for the data.

For electrochemical testing, 1-cm diameter lapped corundum substrates were sputter deposited with 1,000 nm of iridium metal on both sides to serve as a conductive current collector. Iridium was selected for its chemical stability toward sulfides and refractory properties during annealing. CR2032 coin cells were assembled to evaluate the electrochemistry of the films of different thickness. A total of 50  $\mu\text{L}$  (30  $\mu\text{L}$  on cathode side and 20  $\mu\text{L}$  on anode side) of 1.2 M lithium bis(trifluoromethanesulfonyl)imide (LiTFSI) in a 1 : 1 volumetric mixture of 1,2-dimethoxyethane (DME) and 1,3-dioxolane (DOL) was employed as the electrolyte. The anode was lithium metal and the separator was polypropylene/polyethylene sandwich (Celgard 2325). Cells were charged galvanostatically on an Arbin multichannel cycler.

### 6.2.2. Background electrolyte oxidation

Iridium-coated substrates with no  $\text{Li}_2\text{S}$  deposition were assembled in coin cells with 1.2 M LiTFSI in DME/DOL and lithium metal anodes and charged to 3.6 V vs.  $\text{Li/Li}^+$ .

### 6.2.3. Polysulfide catholyte reference preparation

Polysulfide catholytes with average stoichiometry  $\text{Li}_2\text{S}_x$  were prepared by stirring 1 : ( $x - 1$ ) molar ratio mixtures of sulfur and  $\text{Li}_2\text{S}$  in DME/DOL at 60 °C overnight, then adding 1.2 M LiTFSI salt. Cells were prepared with 20  $\mu\text{L}$  of the catholyte on the cathode side and 30  $\mu\text{L}$  of polysulfide-free 1.2 M LiTFSI in DME/DOL on the lithium anode side.

### 6.2.4. Pore-filling model

We can create a simple model for the carbon framework by considering it to be made up of cylindrical pores of a finite number of distinct average pore diameters (*cf.* Figure 6.2 with two pore size populations) with associated specific pore volumes. The surface area of these pores must necessarily be less than the specific surface area of the overall carbon structure. The excess specific surface area can be considered to make up the external surface area of the carbon, which can be considered to be effectively flat (*i.e.*, a “pore” with infinite diameter).

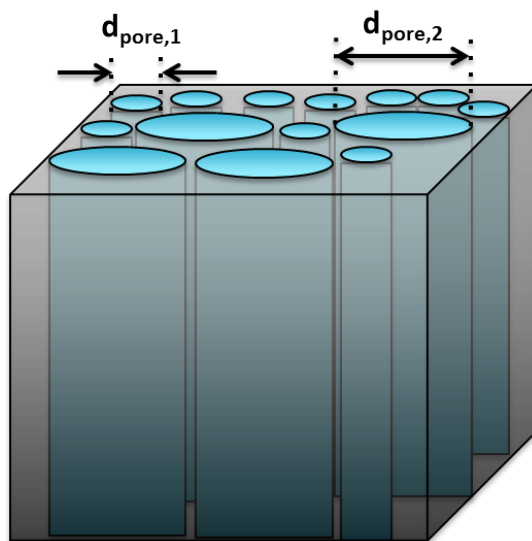


**Figure 6.2.** Schematic illustrating the pore model used, illustrated with two populations of regular cylindrical pores, of diameters  $d_{\text{pore},1}$  and  $d_{\text{pore},2}$ .

The charge density will initially be divided by the total accessible surface area, and we will consider the  $\text{Li}_2\text{S}$  to grow uniformly over the surface area. As the pores are filled, the surface area decreases, leading to an increase in the local charge density over the remainder of the unfilled pore area. Eventually, either the  $\text{Li}_2\text{S}$  will completely fill the pores without exceeding the maximum combination of average thickness and local charge density, or charge will end before all the  $\text{Li}_2\text{S}$  can deposit (leading to capacity loss).

We have developed a model in MATLAB for this pore-filling process (all code used is available as a single M-file in the Appendix, with in-line annotations). The conductive structure is described by a pore distribution (specifically the gravimetric specific pore volume for a finite distribution of average pore sizes) and total specific surface area (which, by definition, must be larger than the sum of the pore surface areas). The composite is then described by the weight percent of sulfur and the areal loading of sulfur. Given a bulk rate, the model can simulate the filling of the pore structure with active material, and calculate the local current density as a function of  $\text{Li}_2\text{S}$  thickness

To approximate a best-case pore structure, we simulated a conductive carbon host with a close-packed array of pores of homogenous thickness. The void fraction in this hypothetical carbon framework is 90.9 %, and we assume the  $\text{Li}_2\text{S}$  loading and carbon : sulfur ratio are matched perfectly to the total pore volume.

## **6.3. RESULTS AND DISCUSSION**

### **6.3.1. Open circuit analysis**

As shown in Figure 6.3, the open-circuit voltage (OCV) for the annealed films generally increased with increasing thickness, from  $\sim 1.8$  V (vs.  $\text{Li}/\text{Li}^+$ ) for the 30 nm film to  $\sim 2.4$  V (vs.  $\text{Li}/\text{Li}^+$ ) for the 1,100 nm film. The  $\text{Li}_2\text{S}_4$  and  $\text{Li}_2\text{S}_8$  references

investigated in this work had OCVs of  $\sim 2.2$  V and  $\sim 2.4$  V (vs Li/Li<sup>+</sup>), respectively. In contrast, a Li<sub>2</sub>S sample annealed for over 18 h, verified by XPS to contain no detectable sulfur-sulfur bonding in Figure 5.5a, exhibited an OCV of  $\sim 1.7$  V.

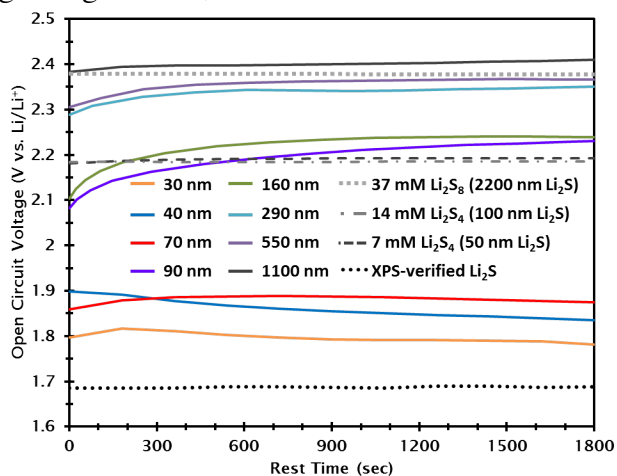


**Figure 6.3.** Representative OCV measured over 30 minutes for Li<sub>2</sub>S films of increasing thickness. Additionally the OCV measured before charge is included for the Li<sub>2</sub>S<sub>4</sub> and Li<sub>2</sub>S<sub>8</sub> catholytes as well as the highly annealed Li<sub>2</sub>S film from Figure 5.4, which was verified by XPS to contain no measurable sulfur-sulfur bonding

Commercial Li<sub>2</sub>S samples are known to contain significant polysulfide impurities.<sup>58,116</sup> To generate an equivalent reference, the Li<sub>2</sub>S films used were annealed at 600 °C for  $\sim 6$  h to crystallize and densify the Li<sub>2</sub>S, while preserving some excess sulfur, which can be readily identified by the OCV of the films). Films with small quantities of soluble sulfur-sulfur species will form polysulfides in solution and the OCV will be in the range of  $2.2 \pm 0.2$  V, as observed for the films in this work over 70 nm thick. The higher OCV (between 1.8 and 1.9 V) for the thin ( $< 90$  nm) films than the pure, crystalline Li<sub>2</sub>S reference likely reflect insoluble (Li<sub>2</sub>S<sub>2</sub>-type) solid polysulfides.<sup>116</sup>

### 6.3.2. Thick film charge behavior

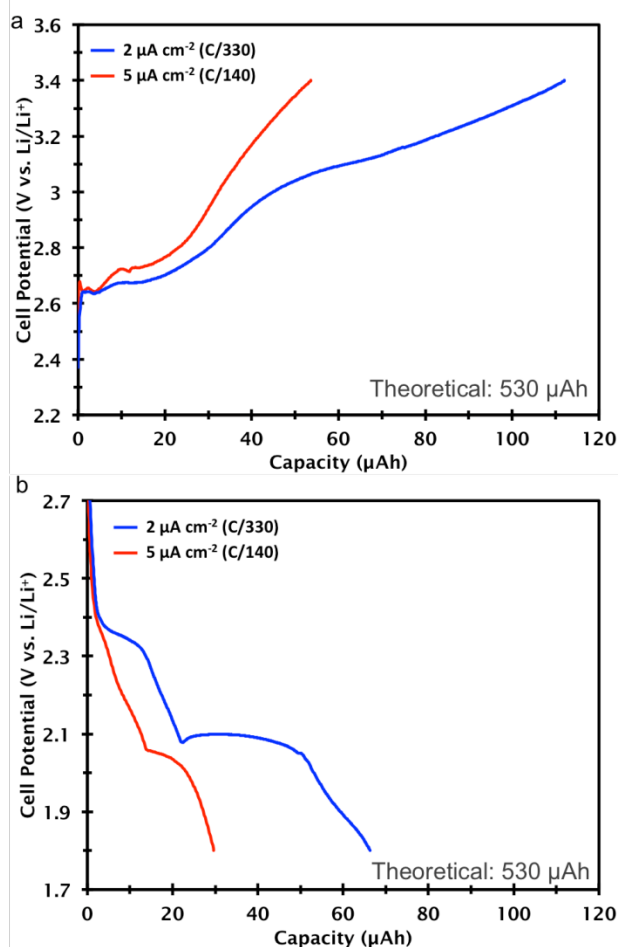


**Figure 6.4.** Galvanostatic (a) first charge and (b) subsequent discharge for a 3.5 μm thick Li<sub>2</sub>S film at 2 μA cm<sup>-2</sup> (blue curve) and 5 μA cm<sup>-2</sup> (red curves). The theoretical capacity is 530 μAh.

The initial analysis of the thick-film charge capability was performed on a 3.5 μm thick annealed Li<sub>2</sub>S film as shown in Figure 6.4. At a current density of 5 μA cm<sup>-2</sup>, a discharge rate slower than C/100, only 10 % of the theoretical capacity (ca. 530 μAh) for the cell was realized. At an even lower current density, 2 μA cm<sup>-2</sup> (less than C/300), still less than 20 % of the capacity was realizable, mostly above 3.0 V (vs. Li/Li<sup>+</sup>). Notably, a 3.5 μm thick layer of Li<sub>2</sub>S corresponds to a sulfur loading of only 0.4 mg cm<sup>-2</sup>. The

subsequent capacities on discharge are even smaller, reflective of the persistent insulating  $\text{Li}_2\text{S}$  layer on the surface of the cathode due to incomplete charge. It is explicit from this result that the limiting average film thickness for a given surface area must be significantly less to enable complete utilization of the active mass.

### 6.3.3. Electrolyte stability analysis

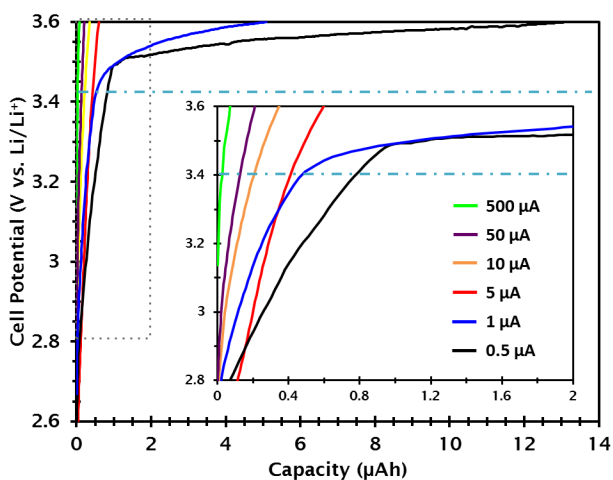


**Figure 6.5.** First charge at different rates of  $\text{Li}_2\text{S}$ -free iridium-coated planar current collectors with 1.2 M LiTFSI in DME/DOL electrolyte and lithium metal anodes. The inset is a magnified view of the initial charge region. The dotted lines indicate a potential of 3.4 V (vs.  $\text{Li}/\text{Li}^+$ ), below which no oxidation plateaus were observed.

The significant charge capacity above 3.0 V (vs.  $\text{Li}/\text{Li}^+$ ) warranted a brief look at the stability of the electrolyte to oxidation at these potentials, as electrolyte stability is known to be a concern when ‘activating’  $\text{Li}_2\text{S}$  cathodes by charging to an overpotential significantly above 3.0 V. As shown in Figure 6.5, the electrolyte is relatively stable to 3.4 V down to a rate of 500 nA. However, background charge capacities, while less than 0.4  $\mu\text{Ah}$  for all measured charge rates up to 3.0 V, do begin to appear, particularly at low rates.

### 6.3.4. Polysulfide catholyte reference

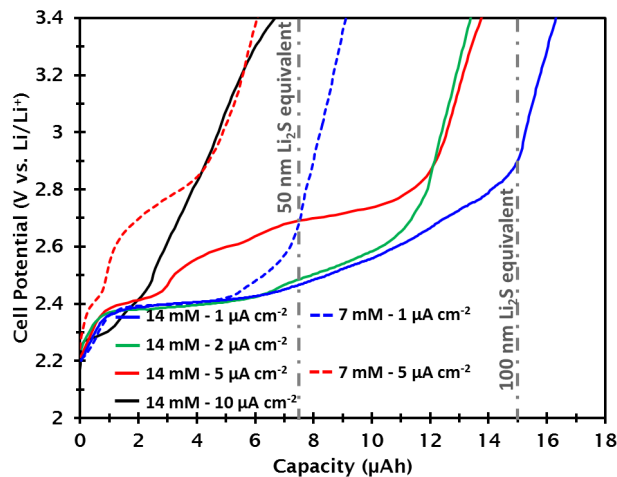


**Figure 6.6.** Galvanostatic charge curves for 100 nm  $\text{Li}_2\text{S}$ -equivalent (14 mM) and 50 nm  $\text{Li}_2\text{S}$ -equivalent (7 mM) of  $\text{Li}_2\text{S}_4$  catholyte at different rates with a bare planar iridium current collector. The theoretical capacities are indicated by dashed lines.

To verify the suitability of the cell architecture to measure the charge capacity of a Li-S cell with small quantities of significantly reduced active material, we prepared cells with uncoated iridium current collectors and 20  $\mu\text{L}$  of 7 mM and 14 mM  $\text{Li}_2\text{S}_4$  catholytes, containing an active mass equivalent to 50 nm (7.5  $\mu\text{Ah}$ ) and 100 nm (15  $\mu\text{Ah}$ ) of  $\text{Li}_2\text{S}$ , respectively.  $\text{Li}_2\text{S}_4$  was chosen as the reference polysulfide as it is routinely identified as the first species to appear in solution upon charge (*i.e.*, the least oxidized participating polysulfide).<sup>32</sup> As can be seen in Figure 6.6, 100 % of the theoretical charge capacity was realized at 1  $\mu\text{A cm}^{-2}$  for both cells. For the 100 nm cells, there is a slight decrease in capacity at 2  $\mu\text{A cm}^{-2}$  and 5  $\mu\text{A cm}^{-2}$ , with a significant charge overpotential appearing at 5  $\mu\text{A cm}^{-2}$ . At 10  $\mu\text{A cm}^{-2}$ , less than half the theoretical capacity is realized. These results point to the rapid inactivation of the active surface by deposition of insulating sulfur with charge.

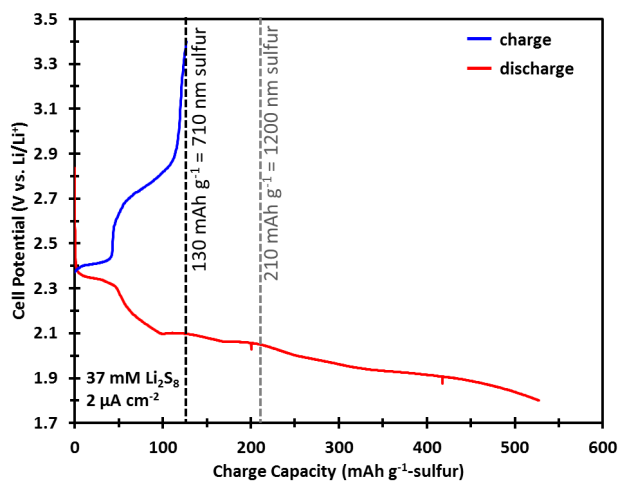


**Figure 6.7.** Galvanostatic first charge and subsequent discharge curve of a 37 mM  $\text{Li}_2\text{S}_8$  catholyte containing 0.2 mg of sulfur ( $2 \mu\text{A cm}^{-2}$  rate). The equivalent thickness sulfur deposition after charge as well as the theoretical sulfur thickness assuming complete sulfur oxidation are indicated.

We additionally evaluated the thickness of sulfur that could be deposited, given a significantly more concentrated 37 mM  $\text{Li}_2\text{S}_8$  (the most oxidized participating polysulfide) catholyte. The estimated sulfur thickness of the film, based on the charge capacity exceeded 700 nm at  $2 \mu\text{A cm}^{-2}$  as seen in Figure 6.7.

### 6.3.5. Determination of maximum active material thickness

We systematically approached the limiting capacity for  $\text{Li}_2\text{S}$ , investigating a range of thickness films down to  $\sim 30$  nm. The substrate shielding system in the deposition was imperfect, leading to a small amount of deposition ( $\sim 20$  nm) during the 30-minute pre-sputter period, limiting the minimum film thickness that could be probed under the fully-characterized deposition scheme. Figure 6.8 presents the resulting first charge capacity for  $\text{Li}_2\text{S}$  films between  $\sim 30$  nm and  $\sim 1,100$  nm, with the theoretical capacity indicated.

It is apparent that two separate trends exist. The first trend, at low thickness, shows decreasing charge capability from 30 to 70 nm. For a  $\sim 30$  nm film (Figure 6.8a)

charged at  $1 \mu\text{A cm}^{-2}$  ( $\sim C/6$  rate), the full theoretical capacity is realized with a charge plateau at  $\sim 2.5 \text{ V}$  (vs.  $\text{Li/Li}^+$ ). This plateau is within  $0.1 \text{ V}$  of the  $\text{Li}_2\text{S}_4$  polysulfide charge plateau at the same rate in Figure 6.6, indicating little  $iR$  overpotential was generated by  $30 \text{ nm}$  of  $\text{Li}_2\text{S}$  at this rate. A small plateau around  $2.9 \text{ V}$  (vs.  $\text{Li/Li}^+$ ) appeared at  $2 \mu\text{A cm}^{-2}$  ( $\sim C/3$  rate), but less than half of the theoretical capacity was realized. We see that  $2 \mu\text{A cm}^{-2}$  is already too high a specific charge density for a  $30 \text{ nm}$  film.

For a  $40 \text{ nm}$  film (Figure 6.8b), the full capacity can again be realized at  $1 \mu\text{A cm}^{-2}$  ( $\sim C/7$  rate). In this case however, the charge plateau is at  $\sim 2.8 \text{ V}$  (vs.  $\text{Li/Li}^+$ ), representing a  $\sim 0.4 \text{ V}$  overpotential relative to the  $\text{Li}_2\text{S}_4$  catholyte reference. For this slightly thicker film,  $2 \mu\text{A cm}^{-2}$  ( $\sim C/4$  rate) is not realizable, and no charge plateau is present. Indeed, a  $70 \text{ nm}$   $\text{Li}_2\text{S}$  film (Figure 6.8c) could not be charged even at  $1 \mu\text{A cm}^{-2}$  ( $\sim C/13$  rate).

**Table 6.2.** Estimate of  $\text{Li}_2\text{S}$  film resistivity and conductivity based on approximate overpotential for observed charge plateaus at given charge densities.

Thickness (nm)	Overpotential (V)	$I$ ( $\mu\text{A cm}^{-2}$ )	$\rho$ ( $\text{M}\Omega \text{ m}$ )	$\sigma$ ( $\text{S m}^{-1}$ )
30	0.1	1	300	$3.3 \times 10^{-9}$
30	0.5	2	740	$1.2 \times 10^{-9}$
40	0.4	1	1100	$0.9 \times 10^{-9}$
40	> 1.0	2	> 1300	< $0.8 \times 10^{-9}$
70	> 1.0	1	> 1400	< $0.7 \times 10^{-9}$

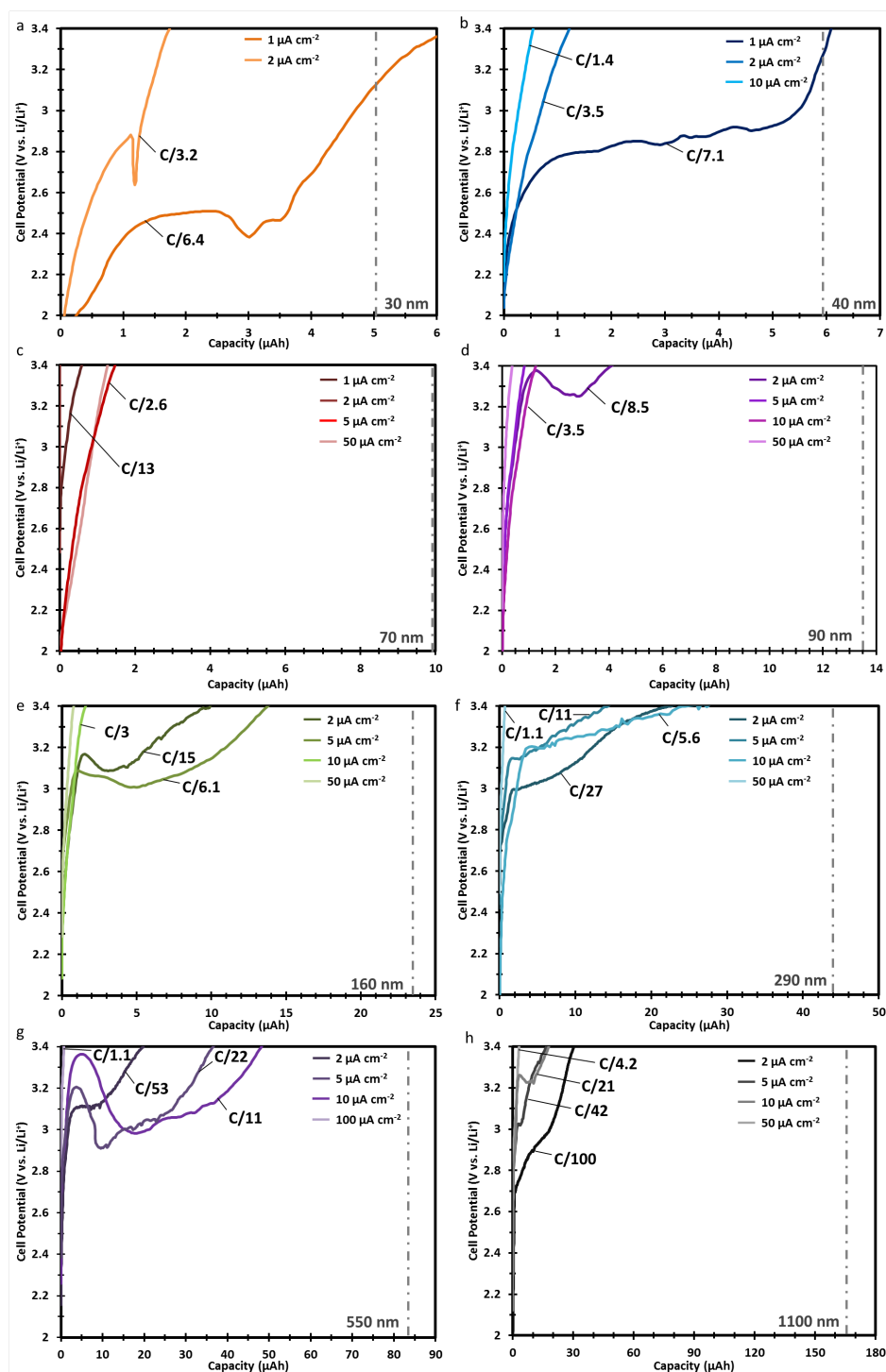


**Figure 6.8.** Galvanostatic charge curves for films of  $\text{Li}_2\text{S}$  of approximately (a) 30 nm, (b) 40 nm, (c) 70 nm, (d) 90 nm, (e) 160 nm, (f) 290 nm, (g) 550 nm, and (h) 1100 nm. The theoretical charge capacity for each thickness is indicated by a vertical dashed line.

From these results, we quickly arrive at a maximum thickness  $\text{Li}_2\text{S}$  that can be charged at a practical rate. A  $C/12$  rate can be taken as the minimum feasible cycling rate (one charge/discharge cycle per day), though  $C/8$  is in practice a more realistic minimum. Based on these conditions, we see that full utilization of the active material is only possible for  $\text{Li}_2\text{S}$  below 70 nm. Given the 0.4 V overpotential when increasing the film thickness from 30 to 40 nm, the maximum thickness given a standard Li-S charge cut-off voltage of 3.0 V must be very close to 40 nm. To realize a full charge with no significant overpotential, we see the maximum must lie close to 30 nm. Additionally, given the large decrease in capacity for a 30 nm film when increasing the charge rate to  $2 \mu\text{A cm}^{-2}$  ( $\sim C/3$  rate), we see that the maximum thickness  $\text{Li}_2\text{S}$  deposition for a high-rate application must be significantly less than 30 nm.

A rough estimate of the effective conductivity of the films based on the observed overpotentials for the charge plateaus are presented in Table 6.2, under the assumption that the overpotential arises solely from an  $iR$  drop across the film. There is a trend toward decreasing conductivity with thickness, suggesting increased current collector exposure may exist for the thinner films, but the calculated values are on the order of  $1 \times 10^{-9} \text{ S m}^{-1}$ . This value is notably 15 orders of magnitude higher than the inherent  $\text{Li}_2\text{S}$  conductivity calculated theoretically for pristine  $\text{Li}_2\text{S}$  based on ionic lithium conductivity.<sup>27</sup> Once again, this result demonstrates the importance of polysulfides in the solid and/or electrolyte to enable charging of the active material.

The second trend observed in Figure 6.8 occurred for thicker  $\text{Li}_2\text{S}$  films (Figures 6.8d-h). With increasing film thickness the “activation overpotential” that is commonly identified in Li-S batteries assembled with  $\text{Li}_2\text{S}$  cathodes appears. We hypothesize a minimum concentration of polysulfides in the electrolyte are needed to initiate chemical solvation of the  $\text{Li}_2\text{S}$  material, as demonstrated by Koh *et al.*<sup>58</sup> As the concentration of

polysulfides produced for a given volume electrolyte increases for thicker films (assuming fixed chemical composition), the activation behavior begins to appear above a critical thickness (between 70 and 90 nm at the rates studied). This behavior is reflected in the OCV of the films presented in Figure 6.3, where there is a significant increase from  $\sim 1.9$  to  $\sim 2.2$  V (vs. Li/Li<sup>+</sup>), when going from the 70 nm to the 90 nm film. The 90 nm film was the thinnest film to exhibit an OCV exceeding that of the Li<sub>2</sub>S<sub>4</sub> reference solution, consistent with the formation of this soluble polysulfide above a critical thickness between 70 and 90 nm.

We note from the successful charge of greater than 50 nm-equivalent Li<sub>2</sub>S when starting from the Li<sub>2</sub>S<sub>4</sub> catholyte (or Li<sub>2</sub>S<sub>8</sub> as in Figure 6.7), that the thickness of the sulfur deposition is not limiting in the absence of pre-existing Li<sub>2</sub>S deposits. Thick-film Li<sub>2</sub>S cathodes which are successfully “activated” via polysulfide generation thus must suffer capacity loss when the preferential oxidation of polysulfides to sulfur forms a combined solid insulating Li<sub>2</sub>S/sulfur layer too thick to continue charging. Given the limiting Li<sub>2</sub>S thickness is shown to be less than the limiting sulfur thickness, we can consider the limiting Li<sub>2</sub>S thickness to approximate the maximum combined solid deposit that can be charged.

### **6.3.6. Pore filling model**

From these results, we then want to examine the implications on the pore structure and by extension the electrolyte requirements for a given cell architecture, and ultimately the limiting rate capability of a Li-S cell. The developed model uses the maximum electroactive Li<sub>2</sub>S thickness at a given overpotential and most favorable conductivity ( $3.3 \times 10^{-9}$  S cm<sup>-1</sup>) calculated from Figure 6.8 to define an envelope of film thicknesses and local current density after which charge will cease. Figure 6.9a-b illustrates the maximum

charge capacity of an idealized close-packed array of cylindrical pores (with perfectly matched  $\text{Li}_2\text{S}$  loading) as a function of pore diameter at a charge rate of  $C/2$  and  $C/10$ . The intersection of the rate-thickness envelope is shown in Figure 6.9c-d at the same rates.

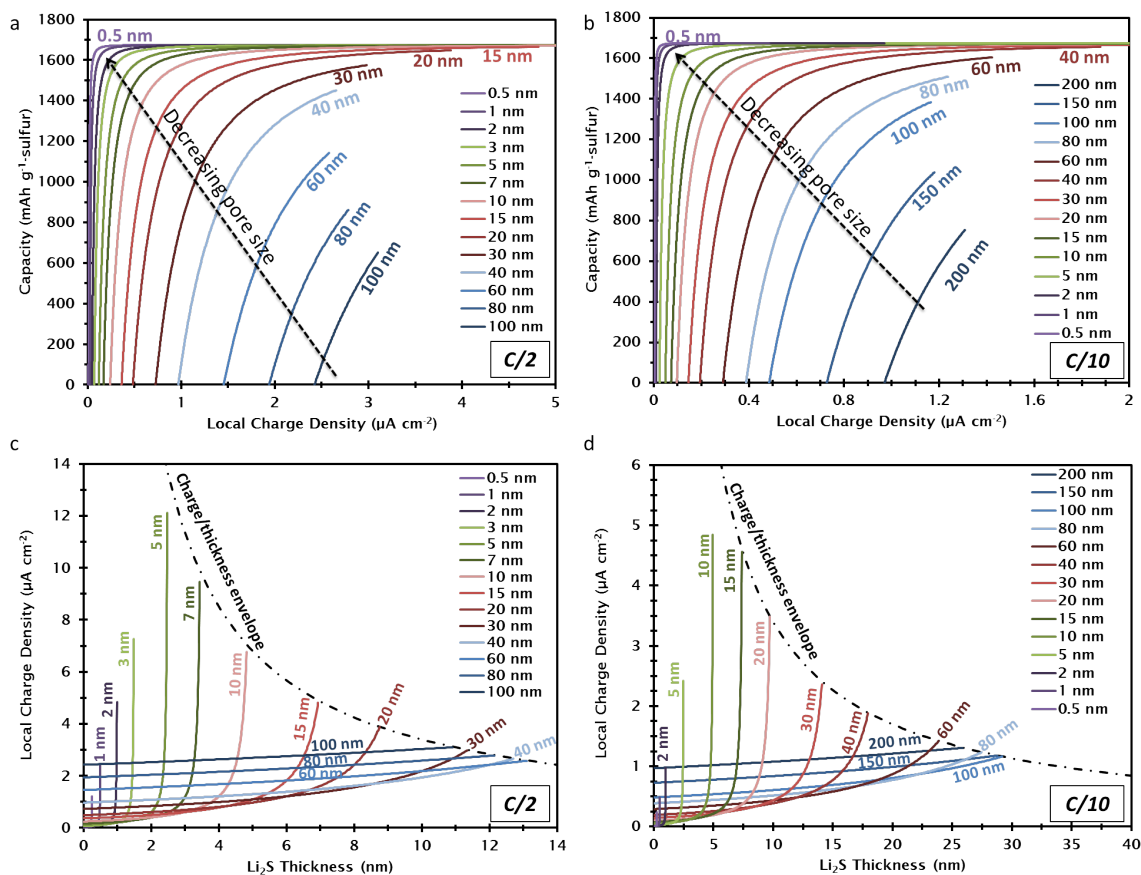


**Figure 6.9.** Pore-filling model for a close-packed array of cylindrical pores as a function of pore diameter at (a and c)  $C/2$  and (b and d)  $C/10$  rates. (a and b) Calculated gravimetric capacity vs. local charge density and (c and d) local charge density vs. deposited  $\text{Li}_2\text{S}$  thickness. The dashed line in (c and d) represent the limiting local charge density calculated for a 0.1 V overpotential given thickness  $\text{Li}_2\text{S}$  deposit and using the least restrictive conductivity from Table 6.2.

From this model, we can draw several important conclusions on the ideal pore structure of a conductive sulfur host employed in lithium-sulfur batteries. Any pore volume contained in pores with diameters of  $\sim 60$  nm or larger will lead to significant ( $> 10\%$ ) loss of theoretical capacity, even at a C/10 rate. From Figure 6.9c-d, we see that it is not until the pore size is 10 nm (5 nm at C/2) or less that 100 % of the theoretical capacity can be obtained without reaching a critical combination of  $\text{Li}_2\text{S}$  thickness and local charge density. Increasing the pore volume relative to the sulfur loading can improve this utilization, but excess pore volume will require filling by electrolyte, decreasing the E/S ratio and therefore the cell-level energy density. Relatedly, all macropores greater than 60 nm will not be fully utilized, resulting in a decrease of cell-level energy density with significant macroporosity due to electrolyte filling. Additionally, we see that smaller pore sizes yield improved rate performance and active material utilization. However, failure to match microporosity to the overall  $\text{Li}_2\text{S}$  loading, leads to rapid pore filling with corresponding increase in local charge density and ultimately poor utilization (cf. Figure 6.10). A final implication of Figure 6.9 is that limiting the charging rate at the beginning of charge and end of discharge could improve utilization by enabling filling of larger pores.

#### ***6.3.6.1. Application of pore-filling model to literature Li-S materials***

Ding, *et al.* reported average pore diameter and pore volume for a variety of conductive carbons used in battery cathodes.<sup>170</sup> We use these values to simulate the limiting sulfur content and performance for several of these carbon materials. The literature data and the modeled data are presented in Table 6.3. When the theoretical surface area based on the reported average pore diameter and pore volume was significantly larger than the reported specific surface area, we assigned a fraction of the

pore volume to a macropore until the calculated and measured surface area matched. If the theoretical surface area was lower than the reported value, we assigned a fraction of the pore volume to a population of pores with one half the reported pore diameter until the surface areas matched.

**Table 6.3.** A comparison of reported average pore sizes, pore volumes, and specific surface areas from Ding *et al.*,<sup>170</sup> for a selection of carbon materials (top) and the modeled pore structure (bottom).

Literature data from reference Ding <i>et al.</i> <sup>170</sup>					
Carbon type	Lit. average pore size(s) (nm)		Lit. specific pore volume(s) (cm <sup>3</sup> g <sup>-1</sup> )		Lit. surface area (m <sup>2</sup> g <sup>-1</sup> )
MWCNT	7		1.64		929
Ordered mesoporous	5.2		1.14		863
Activated carbon	4.7		1.07		1230
Ketjen black	7.7		1.17		818
Super P	11.9		0.32		62
Acetylene black	11.4		0.16		56
Inverse opal	16		3.17		794
Reduced graphene oxide	17.5		1.58		361
Modeled pore structure					
Carbon type	Pore 1 diam. (nm)	Pore 1 vol. (cm <sup>3</sup> g <sup>-1</sup> )	Pore 2 diam. (nm)	Pore 2 vol. (cm <sup>3</sup> g <sup>-1</sup> )	Calc. surface area (m <sup>2</sup> g <sup>-1</sup> )
MWCNT	7	1.62	30	0.02	928.4
Ordered mesoporous	5.2	1.12	90	0.02	862.4
Activated carbon	4.7	0.7	2.35	0.37	1225.5
Ketjen black	7.7	0.77	3.85	0.4	815.6
Super P	11.9	0.16	80	0.16	61.8
Acetylene black	11.4	0.159	-	-	55.8
Inverse opal	16	3.17	-	-	792.5
Reduced graphene oxide	17.5	1.579	-	-	360.9

The importance of matching microporosity with sulfur loading is apparent from comparing the pore-filling behavior for the different carbons in Figure 6.10 (at C/10 rate).

Activated carbon (Figure 6.10a), with the largest surface area exhibited the best charging performance (lowest local charge density) for low loadings (sulfur content < 40 wt.%). However, for greater sulfur content—which requires complete filling of the micropores—the capacity rapidly fades with increasing sulfur content. The inverse opal carbon structure, with approximately twice the specific pore volume of the next closest example, demonstrated the best performance at high sulfur content, exhibiting > 90% theoretical capacity up to 80 wt% sulfur content. Low surface area carbons such as Super P (Figure 6.10g) and acetylene black (Figure 6.10h) are particularly poor choices for conductive carbon hosts as their surfaces are rapidly inactivated by thick  $\text{Li}_2\text{S}$  deposits. The key conclusion from this model is that small pore diameters and high specific surface areas are ideal for charging performance, but only if the micropore volume exceeds the volume of  $\text{Li}_2\text{S}$  loading.

We can compare our model to relatively exceptional examples of reported Li-S batteries for which specific surface area and pore volume are reported. For example, the relevant reported parameters are shown in Table 6.4 for a demonstration of extremely high sulfur loading<sup>171</sup> (30.7 – 61.4 mg  $\text{cm}^{-2}$ ) and low E/S ratio<sup>75</sup> (4 : 1). The ultrahigh loading and low E/S ratio reports demonstrated stable cycling capacity above 900 mAh  $\text{g}^{-1}$ -sulfur up to C/5, and 1C rates, respectively, and above 500 mAh  $\text{g}^{-1}$ -sulfur up to C/2 and 2C, respectively.<sup>75,171</sup>

In Figure 6.11 we see the pore-filling model applied to both literature carbons. The low E/S ratio cell is noteworthy in that there do not appear to be any charge limitations up to a rate of at least 2C. The cell clearly has excess micropore volume, as the  $\text{Li}_2\text{S}$  deposition thickness does not exceed 1 nm. This implies the E/S ratio could be further decreased by modifying the pore structure to contain less mesopore volume. Additionally, given that the charge/thickness envelope is not reached (Figure 6.11c), the

relatively low overall sulfur content (and thus sulfur : carbon ratio) could safely be increased without decreasing the charge capability.

The ultra-high loading cell, in contrast, does reach the charge-voltage envelope at a rate of 1C and higher, suggesting the useful pore volume in the structure is almost fully utilized. The significant increase in local charge density above C/5 (Figure 6.11b) matches a reported decrease in the cell capacity during rate testing, indicating performance limitations appear in this cell above  $\sim 1 \mu\text{A cm}^{-2}$ . From these results, the ultra-high loading cells would benefit from a conductive carbon host with greater microporosity and micropore surface area.

**Table 6.4.** Literature carbon framework data for two Li-S cathodes exhibiting notable performance. \*These values were calculated to include the CNTs added to the cathode during cell assembly according to the MWCNT pore structure reported in Ding *et al.*<sup>170</sup>

Carbon type	Surface area (m <sup>2</sup> g <sup>-1</sup> )	Total pore volume (cm <sup>3</sup> g <sup>-1</sup> )	Micropore volume (cm <sup>3</sup> g <sup>-1</sup> )	Sulfur content (wt.%)	Ref.
Carbonized cotton	805	0.65	0.31	80.0%	Chung <sup>171</sup>
Zinc-salt templated carbon	2165*	2.32*	0.43*	58.7%*	Strubel <sup>75</sup>

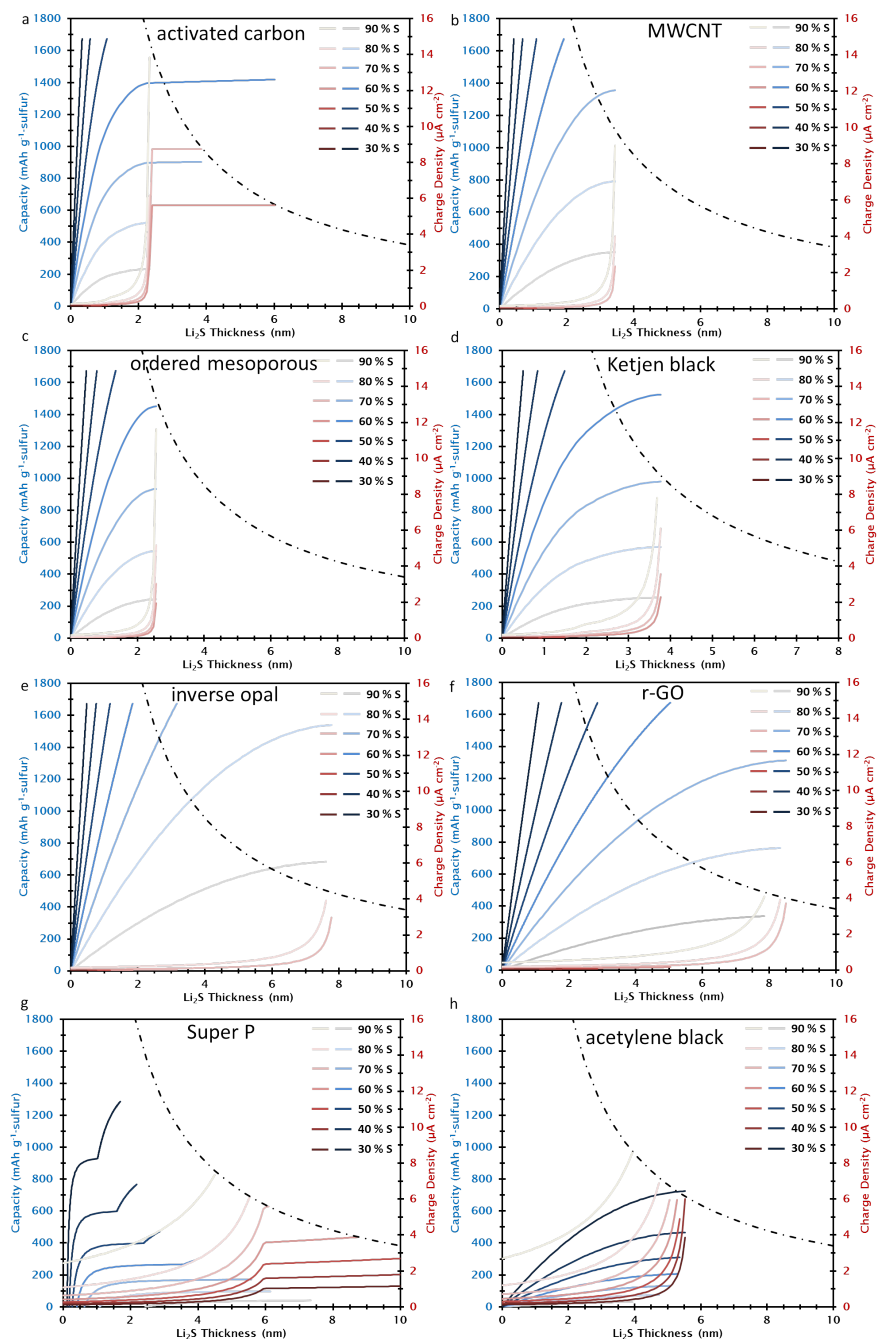


**Figure 6.10.** Modeled data for conductive carbons using the pore model parameters of Table 6.3, based on the measured pore structures in Ding *et al.*<sup>170</sup> The blue curves plot the gravimetric charge capacity versus the thickness of Li<sub>2</sub>S deposited and the red curves plot the local charge density as a function of thickness Li<sub>2</sub>S deposited. The dashed line represents the charge/thickness P envelope beyond which the charge ceased

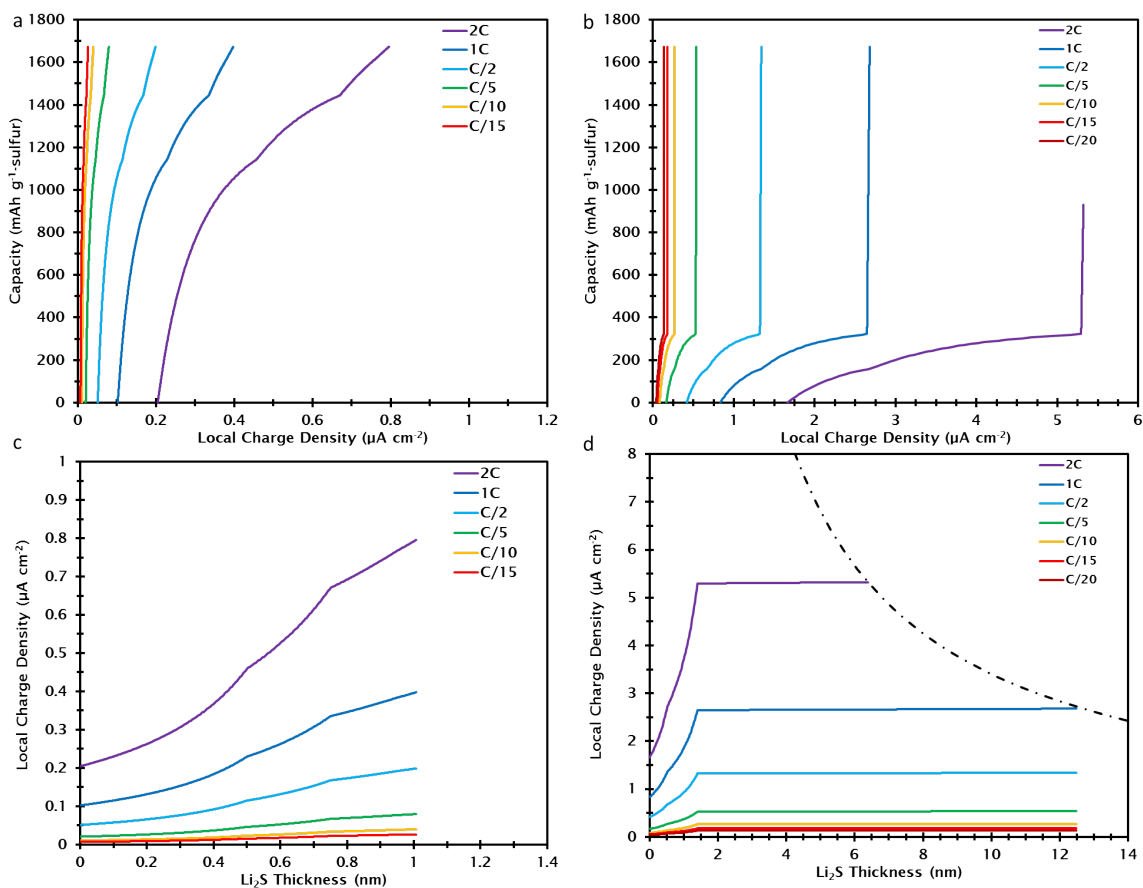


**Figure 6.11.** Calculated gravimetric charge capacity vs. local charge density as a function of charge rate for a model of the cathode structures in (a) Strubel *et al.*<sup>75</sup> and (b) Chung *et al.*<sup>171</sup> Calculated local charge density vs. Li<sub>2</sub>S thickness for a model of (c) Strubel *et al.*<sup>75</sup> and (d) Chung *et al.*<sup>171</sup> The dashed line in (d) indicates the charge/thickness envelope calculated from the experimental data in Figure 6.8.

### 6.3.6.2. Evaluation of pore-filling model assumptions

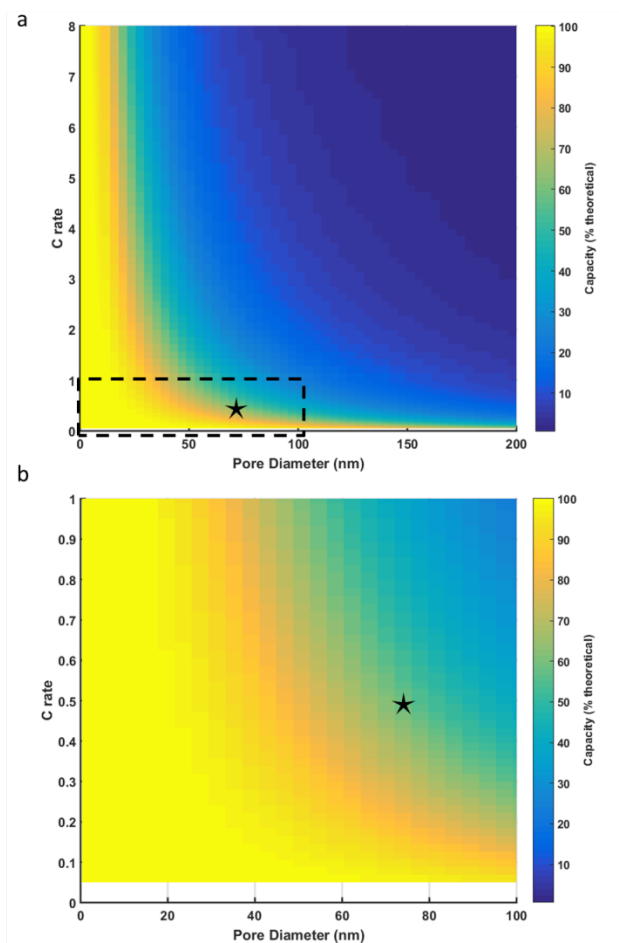


**Figure 6.12.** Surface plot of the charge capacity realizable by a regular array of close-packed cylindrical pores as a function of charge rate and pore diameter. (b) A magnified region of the dashed region in (a). The combination of charge rate and pore diameter from Moon *et al.*<sup>43</sup> is indicated by a star.

We can consider how several assumptions in the model are likely to influence its validity and applicability for a real system. The model assumes even, homogenous growth of a  $\text{Li}_2\text{S}$  film on all conductive surface area. In actuality, nucleation and growth of  $\text{Li}_2\text{S}$  particles can occur in large pores or on external surface areas. The distance from the conductive surface to the edge of the particle will be larger than for a film, which

would lead to worse performance than in the model. Similarly, while the conductivity of  $\text{Li}_2\text{S}_2$  should be substantially larger than  $\text{Li}_2\text{S}$ , only half of the theoretical capacity is realizable if the final discharge product of a Li-S battery is  $\text{Li}_2\text{S}_2$ . We have shown in the past that solid  $\text{Li}_2\text{S}_2$  only reduces to  $\text{Li}_2\text{S}$  when in intimate contact with the current collector,<sup>116</sup> so we expect that  $\text{Li}_2\text{S}$  thickness should still be limiting to cell-level capacity.

Our model assumes 100% accessibility of entirely cylindrical pores. A network of connected spherical pores could yield a higher specific surface area to volume ratio, which would improve the maximum thickness deposition, but any inaccessible pores would lead to capacity loss. Again, a model assuming no inaccessible pore volume is likely to overstate, rather than understate the realizable capacity. Likewise, our model assumes no binder is used, which would occupy pore volume and decrease performance in a realistic cell.

Our experimental results (and pore-filling model) are predicated on electrolyte- $\text{Li}_2\text{S}$  contact and lithium transport from the solid  $\text{Li}_2\text{S}$  to the electrolyte. A report of a fully-encapsulated Li-S battery within an anodic aluminum oxide (AAO)-templated carbon nanotube array<sup>43</sup> identified lithium transport through the (expandable) CNT wall to the electrolyte, as well as direct formation of a monoclinic metastable sulfur phase. The relevant diffusion limits in this scenario differ from our experiments, and the corresponding limiting thickness could differ. Indeed, their reported sulfur utilization (~90 %) at a C/2 rate would be slightly better than that predicted by our ideal pore array (though there was no specific surface area or pore volume reported to compare). This approach may be a promising means to stretch the limit of sulfur content without requiring excess electrolyte loading. It is worth noting, while they demonstrated remarkable discharge performance up to 8C, they did not charge above C/2, suggesting, in agreement with our work, that the cycling rate is dictated by fundamental limits on

Li<sub>2</sub>S thickness. If we match their results with our analysis of an ideal close-packed pore array, we see a charge rate of  $C/2$  for 75 nm pores lies right along the surface where a drastic decrease in realizable capacity occurs (Figure 6.12).

#### **6.4. CONCLUSION**

In this work we have demonstrated that the maximum thickness Li<sub>2</sub>S that can be utilized under realistic conditions in a Li-S battery is  $\sim 40$  nm, with a local charge density of  $1 \mu\text{A cm}^{-2}$ . The thickness of the Li<sub>2</sub>S formed is shown to be the limiting factor to determine sulfur content in a carbon/sulfur composite cathode. Finally, we have presented a set of design guidelines for the ideal pore structure of a conductive surface host to maximize the cell-level energy density of Li-S cathodes.

## Chapter 7: Summary

In this dissertation, considerable progress has been made toward understanding the role, reactions, and limitations of solid-state lithium sulfides in the lithium-sulfur battery system. Advances have been presented in the understanding of the  $\text{Li}_2\text{S}$  activation mechanism, the existence and electrochemical activity of  $\text{Li}_2\text{S}_2$ , and the limiting behavior of  $\text{Li}_2\text{S}$  thickness in determining the ideal composite cathode structure. Additional new insights are present throughout this work, including identification of a new solid-state sulfide structure, development of a new  $\text{Li}_2\text{S}$  surface reaction scheme, clarification of the spectroscopic and chemical properties of the lithium sulfides, and identification of complex plasma chemistry in the sputter deposition of lithium sulfides.

First, the role of  $\text{Mn}^{2+}$  as a facile *in situ*  $\text{Li}_2\text{S}$  surface modifier was identified, with substantial performance improvements demonstrated. This discovery was used as a basis to explore the mechanism by which  $\text{MnS}$  forms stably on the  $\text{Li}_2\text{S}$  surface, while many ostensibly similar transition-metal sulfides such as  $\text{FeS}$  do not. It is identified that the lack of electrochemical activity within the Li-S cycling window is key; else, lithiation of the surface layer causes rapid failure of the encapsulant with cycling. In this context, it is shown that the reduction in first charge activation overpotential, which is dependent on surface conductivity, is not a useful predictor of long-term cycle life. Indeed, these results demonstrated that poorly conducting surface layers can be a superior approach for encapsulating and activating  $\text{Li}_2\text{S}$  cathodes, provided they are stable and exhibit facile charge transfer behavior.

The role of sulfur-sulfur bonding in the solid, which is apparent when studying  $\text{Li}_2\text{S}$  activation via sulfide surface layers, motivated a more direct approach to evaluating the role of  $\text{Li}_2\text{S}_2$  in the Li-S reaction mechanism. Literature methods, which claimed

synthesis of  $\text{Li}_2\text{S}_2$  with limited chemical characterization, were duplicated and shown spectroscopically not to produce pure  $\text{Li}_2\text{S}_2$ . An initial solid product containing a mixture of  $\text{Li}_2\text{S}$ ,  $\text{Li}_2\text{S}_2$ , and higher-order polysulfides was generated. The initial product was used to develop a clearer understanding of the X-ray photoelectron spectra of lithium sulfides. The initial solid sulfide mixture was then sent through a tailored, electrochemically-monitored sequential filtration scheme to produce a solid sulfide containing approximately 9 mol% sulfur-sulfur bonded species, which was verified to be insoluble. This result confirmed that solid-state insoluble polysulfide species, *i.e.*  $\text{Li}_2\text{S}_2^-$  and  $\text{Li}_2\text{S}_3^-$ -type species, do exist as identifiable impurities. Furthermore, it is shown that they are almost invariably present in commercial samples of nominally pure  $\text{Li}_2\text{S}$ . Finally, it is shown that solid-state sulfur-sulfur bonds can be reduced in the absence of soluble polysulfides, though the reaction is strictly limited to sulfur-sulfur bonds in intimate contact with the conductive current collector. These results confirm that the formation of  $\text{Li}_2\text{S}_2$  is not inherently limiting to the capacity of lithium-sulfur batteries. However, great care must be taken to ensure sufficient conductive surface area is available when  $\text{Li}_2\text{S}_2$  electrodeposits during cell discharge.

Next, to better understand the fundamental performance limitation of solid lithium sulfide, a sputter deposition system for synthesis of air-sensitive sulfide films was built. The system was able to reliably grow films of  $\text{Li}_2\text{S}$  ranging in thickness from  $\sim 30$  nm to over  $3 \mu\text{m}$ . The plasma chemistry of the deposition was analyzed in depth, and shown to proceed as a complex hybrid process with low-energy thermalized deposition of a sulfide-rich surface film coupled with high-energy implantation of a lithium-rich flux. This process, driven by the large differences in size and surface energy between lithium and sulfur, yields a nonstoichiometric product shown to possess significant depth inhomogeneity. The as-synthesized product was characterized and shown to consist of a

novel metastable structure containing polymeric-type  $\text{Li}_2\text{S}$ . Potentially appealing solid-state electrochemistry was identified in this material. High-temperature annealing was used to produce a high-purity, homogenous crystalline  $\text{Li}_2\text{S}$  film. This was the first report of the synthesis of crystalline  $\text{Li}_2\text{S}$  films, and appears to be the first sample clearly characterized by XPS not to contain residual sulfur-sulfur bonding. A fully annealed thick film was shown to be functionally inactive electrochemically, confirming the role of sulfur-sulfur species in the charge mechanism of large  $\text{Li}_2\text{S}$  particles.

Finally, the sputter deposition technique was used to systematically approach the limiting charge capability of  $\text{Li}_2\text{S}$  down to 30 nm. The maximum thickness  $\text{Li}_2\text{S}$  film which could be charged at a practical rate, even given the presence of small amounts of sulfur-sulfur bonding, was estimated to be  $\sim 40$  nm at a local charge density of  $\sim 1 \mu\text{A cm}^{-2}$ . The activation overpotential was shown to appear in films above 70 nm as a result of the generation of a sufficient quantity of soluble polysulfides. However, it is shown that this activation effect cannot improve upon the limiting maximum average  $\text{Li}_2\text{S}$  thickness when considered over the total surface area of the cell. Finally, we use these results to develop a model for the charge capability of an arbitrary porous conductive host. This model is used to establish basic parameters for the rational design of sulfur composite cathodes with maximized cell-level energy density. Namely, the micropore volume should be closely matched to the total  $\text{Li}_2\text{S}$  volume to maximize rate capability, though any excess porosity should be avoided to minimize unnecessary electrolyte consumption. Macroporosity greater than 60 nm in diameter (at most) should be avoided to the extent possible at all costs, as it will lead to electrolyte consumption without possibly being utilized in a Li-S battery cycling stably at useful rates.

Overall, the results presented in this dissertation will enable the Li-S community to rationally design improved cathodes, with an eye toward lithium metal anode-free and

all-solid-state cells. The techniques developed, both facile  $\text{Li}_2\text{S}$  surface modification and thin-film  $\text{Li}_2\text{S}$  synthesis, will enable new battery architectures. Meanwhile, the fundamental performance limitations of solid-state sulfides identified will inform the future development of sulfur/carbon composites with minimized carbon and electrolyte requirements, and thus maximized cell-level energy density.

## Appendix

### A.1. MATLAB PORE-FILLING MODEL CODE

```
% poreFillingModel takes a finite distribution of pore sizes and volumes, a
% sulfur loading, a sulfur content, a charge rate, and a specific surface
% area and returns the charge density, total surface area, and charge
% capacity as a function of an increasing Li2S deposition thickness, as
% well as the E/S ratio based strictly on the pore filling. The thickness
% of Li2S deposited is limited by an envelope of local charge density and
% Li2S thickness as defined by the chargingEnvelope subroutine

function [thickness, chgDensity, totalSAs, capacities, ES] = ...
    poreFillingModel(pore_dist, loading, perc_S, Crate, SSA)

% pore_dist is an n-by-2 array with [avg_pore_size pore_volume] in units of
% [nm cm^3/g]
% tot_vol is the total pore volume; assumes that the excess pore volume is
% all larger
% loading is the areal sulfur density in mg_S/cm^2
% perc_S is the sulfur content in percent
% Crate is the C rate
% capacity is the capacity in mAh/g_S at the given rate
% SSA is the specific surface area of the carbon

%constants
densityLi2S = 1.66; % g/cm^3
molarStoLi2S = 45.94 / 32.06; % molar conversion for S to Li2S
nm2cm = 1 / 10 / 1000 / 1000; % convert nm to cm
sulfurCap = 1674; % mAh/g_sulfur

% calculate the raw rates, etc. based on the cell set-up
mass_S = loading / 1000; %mass sulfur in g per cm^2
max_Li2S = mass_S * molarStoLi2S; %maximum Li2S in g/cm^2 based on S loading
mass_C = (100 - perc_S) / perc_S * mass_S; %mass carbon in g per cm^2
rate = Crate * sulfurCap * mass_S; %rate per cm^2 in mA
muRate = rate * 1000; %rate per cm^2 in uA

% extract the number of distinct pore sizes
numPoreSizes = size(pore_dist,1);
% calculate the surface areas for all of the pores, the excess pore volume
% is assumed to exist as a flat surface (pore of infinite volume)
poreSAs = zeros(numPoreSizes+1,1); % m^2/g
[infiniteSA, poreSAs] = calcExcessSA(pore_dist,SSA,poreSAs); % m^2/g

% calculate, given the pore structure what the maximum possible thickness
% would be
max_thick = calcMaxThick(pore_dist,max_Li2S,infiniteSA,mass_C); %nm

thickness = linspace(0, max_thick,500); % nm
chgDensity = zeros(size(thickness)); % uA/cm^2
capacities = zeros(size(thickness)); % mAh/g S
totalSAs = zeros(size(thickness)); %m^2

% calculate the charge density at this rate
totalSA = sum(poreSAs) * mass_C; %m^2
totalSAs(1) = totalSA;
chgDensity(1) = muRate / (totalSA * 100 * 100); %uA/cm^2
```

```

capacities(1) = 0;

% iterate over increasing thickness of Li2S deposition
for j = 2:length(thickness)
    %iterate over all the pore sizes
    Li2S_vol = zeros(numPoreSizes+1,1); %cm^3/g
    for k = 1:numPoreSizes
        [poreSAs(k), Li2S_vol(k)] = poreSA(pore_dist(k,1), thickness(j),...
            pore_dist(k,2)); %[m^2/g, cm^3/g]
    end

    %calculate the Li2S volume on the excess SA
    infiniteSAcm = (infiniteSA * 100 * 100); % cm^2/g
    Li2S_vol(end) = infiniteSAcm * (thickness(j) * nm2cm); % cm^3/g

    % calculate the charge density under the new available surface area
    totalSA = sum(poreSAs) * mass_C; % m^2
    chgDensity(j) = muRate / (totalSA * 100 * 100); % uA/cm^2

    % calculate the total Li2S deposited
    depositedLi2S = sum(Li2S_vol) * mass_C * densityLi2S; % g
    cap = ((depositedLi2S / molarStoLi2S) * sulfurCap) / mass_S;
    capacities(j) = cap;
    totalSAs(j) = totalSA;
end

%end the deposition if the charging envelope is exceeded
final_thickness_index = length(thickness);
for n = 1:length(thickness)
    envelope = chargingEnvelope(thickness(n));
    if chgDensity(n) > envelope
        if n-1 < final_thickness_index
            final_thickness_index = n-1;
        end
    end
end
end

%limit the returned values to those within the charge envelope
thickness = thickness(1:final_thickness_index);
chgDensity = chgDensity(1:final_thickness_index);
totalSAs = totalSAs(1:final_thickness_index);
capacities = capacities(1:final_thickness_index);

%calculate ES ratio
elVol = calc_El(pore_dist, max_Li2S,mass_C); % uL
ES = elVol / loading; % uL/mg S

end

% function to calculate electrolyte volume required given a pore
% distribution and Li2S loading
function elVol = calc_El(pore_dist,max_Li2S,mass_C)
densityLi2S = 1.66; % g/cm^3
densityS = 2.07; %g/cm^3
molarStoLi2S = 45.94 / 32.06; % molar conversion for S to Li2S

Li2S_vol = max_Li2S / densityLi2S; %cm^3 or mL
total_pore_vol = sum(pore_dist(:,2))*mass_C; %cm^3 or mL

```

```

% calculate the volume compression when Li2S is deposited as sulfur
S_vol = max_Li2S / molarStoLi2S / densityS; % cm^3 or mL
vol_compression = (Li2S_vol - S_vol) / Li2S_vol; %fractional

if Li2S_vol < total_pore_vol
    %fill excess pore space + Li2S volume compression
    elVolmL = (total_pore_vol - Li2S_vol) + vol_compression * Li2S_vol; %mL
else
    %pores are full: Li2S volume compression
    elVolmL = vol_compression * Li2S_vol; %mL
end
elVol = elVolmL * 1000; %uL
end

% subroutine to calculate the pore size for a pore of given diameter with a
% given amount of Li2S deposited as well as the volume of Li2S in the pores
% vol is cm^3/g_carbon and SA is m^2/g_carbon
function [SA, vol] = poreSA(poreSize, thickness, poreVolume)

%calculate the total pore length and cross-sections
poreLength = calcPoreLength(poreSize, poreVolume); % cm/g
poreCS = pi * (poreSize/2)^2; % nm^2
poreCS = poreCS / (1000 * 1000 * 10)^2; % cm^2

% if the Li2S thickness is greater than the radius of the pore, the pore is
% filled and there is no surface area
if thickness >= poreSize/2
    SA = 0; % m^2/g
    vol = poreLength * poreCS; %cm^3/g
else
    %calculate the open circumference
    openDiam = poreSize - 2 * thickness; % nm
    openDiam = openDiam / 1000 / 1000 / 10; %convert to cm
    openCircum = pi * openDiam; % cm
    %calculate the open SA
    SA = openCircum * poreLength; % cm^2/g
    SA = SA / 100 / 100; %convert to m^2/g
    %calculate the open cross-section
    openRadius = poreSize/2 - thickness; % nm
    openRadius = openRadius / 1000 / 1000 / 10; %convert to cm
    openCS = pi * openRadius^2; % cm^2
    vol = poreLength * (poreCS - openCS); % cm^3/g
end
end

% subroutine that takes the poreSize (nm) and poreVolume (cm^3/g) and
% calculates the effective total length of the pore in cm/g
function poreLength = calcPoreLength(poreSize, poreVolume)
poreSize = poreSize / 1000 / 1000 / 10; %convert poreSize from nm to cm
poreLength = poreVolume / (pi * (poreSize / 2)^2); %cm/g
end

% function that takes the initial pore distribution and calculates what the
% excess surface area is
function [excess, poreSAsOut] = calcExcessSA(pore_dist, SSA, poreSAs)
numPoreSizes = size(pore_dist,1);
for i = 1:numPoreSizes
    [poreSAs(i), ~] = poreSA(pore_dist(i,1), 0, pore_dist(i,2)); % m^2/g

```

```

end

% calculate the infinite pore SA as the excess surface area beyond the pore
% distribution
if sum(poreSAs) > SSA
    ME = MException('PoreDist:TooLarge',...
        'Surface area of pore distribution exceeds total surface area');
    throw(ME);
else
    infiniteSA = SSA - sum(poreSAs(1:end-1)); %m^2/g
    poreSAs(end) = infiniteSA; % m^2/g
end
poreSAsOut = poreSAs; %m^2/g
excess = infiniteSA; %m^2/g
end

% function to calculate the total volume of Li2S deposited in a
% pore_distribution given a thickness (per g of carbon)
function Li2S_vol = calcTotalLi2S(pore_dist,thickness,infiniteSA)
Li2S_vol = 0; %cm^3/g
for m = 1:size(pore_dist,1)
    [~, poreLi2S_vol] = poreSA(pore_dist(m,1),thickness,pore_dist(m,2));
    Li2S_vol = Li2S_vol + poreLi2S_vol; %cm^3/g
end
infiniteVol = (thickness / 10 / 1000 / 1000) * (infiniteSA * 100^2); %cm^3/g
Li2S_vol = Li2S_vol + infiniteVol; %cm^3/g carbon
end

% function that takes a pore_distribution and the maximum Li2S and
% calculates at what thickness all the Li2S is deposited
function maxThick = calcMaxThick(pore_dist, max_Li2S, infiniteSA, mass_C)

densityLi2S = 1.66; % g/cm^3

numPoreSizes = size(pore_dist,1);
%volumeFilledPore = zeros(numPoreSizes,1);

maxPoreIndex = 0;
filledVolume = 0; %cm^3
max_vol = max_Li2S / densityLi2S; %cm^3
%calculate the volume of the filled pores
for n = 1:numPoreSizes
    % calculate the volume of Li2S, assuming the thickness just fills the
    % nth pore
    volume = calcTotalLi2S(pore_dist,pore_dist(n,1)/2,infiniteSA); %cm^3/g
    volumeFilledPore = volume * mass_C; %cm^3

    % if the volume of filling up to the nth thickness hole is less than
    % the max volume, then can save that value as the maxFilledVolume
    if volumeFilledPore < max_vol
        maxPoreIndex = n;
        %calculate the volume ONLY in the filled pores
        filledVolume = calcTotalLi2S(pore_dist(1:n,:),...
            pore_dist(n,1)/2,0); %cm^3/g
        filledVolume = filledVolume * mass_C; %cm^3
    end
end

maxThick = thkSolv(pore_dist, infiniteSA, filledVolume, max_vol,...

```

```

        maxPoreIndex, mass_C);
end

%function to use symbolic math toolbox to solve for thickness
function thickness = thkSolv(pore_dist, infiniteSA, filledVolume,...
    max_vol, maxPoreIndex, mass_C)
syms thk
%initialize equation
eqn = 0;
%iterate over the unfilled pore sizes and add to equation
for k = maxPoreIndex+1:size(pore_dist,1)
    pore_size = pore_dist(k,1);
    poreLength = calcPoreLength(pore_size,pore_dist(k,2)); %cm/g
    poreLength = poreLength * 10 * 1000 * 1000; % nm/g
    poreRadius = (pore_size / 2); % nm
    term = mass_C * poreLength * ...
        ((pi * poreRadius^2) - (pi * (poreRadius - thk)^2)); %nm^3
    eqn = eqn + term;
end
%add infinite volume to term
infiniteTerm = (infiniteSA * mass_C) * (1000 * 1000 * 1000)^2 * thk; % nm^3
eqn = eqn + infiniteTerm; %nm^3
%get left hand side in nm^3
lhs = (max_vol - filledVolume) * (10 * 1000 * 1000)^3; % nms

% solve for thickness
solution = solve(lhs==eqn,thk);
thickness = double(solution); %nm
% the thickness needs to be smaller than half the smallest unfilled pore
% diameter
if length(thickness) > 1
    index = find(thickness <= (pore_dist(maxPoreIndex+1,1)/2),1);
    thickness = thickness(index);
end
end

function chgDens = chargingEnvelope(thk)
% function to generate the envelope of charge density and Li2S thickness
% below which cell operation can be predicted to function
% takes an Li2S deposition thickness, thk, (in nm) and returns
% chgDens, the maximum local charge density (in uA/cm^2)

% Film conductivity based on least restrictive calculated conductivity for
% 30 nm film charged at 1 uA/cm^2: 3.4 x 10^9 S/m
conductivity = 3.4e-9; %S/m

% Calculate suitable charging current as one that generates 0.1 V of iR
% overpotential
eta = 0.1; %V overpotential

% Calculate resistance per unit area film
% thickness in m
thickness = thk / 1e9; %m

resistivity = 1 / conductivity; %ohm-m^2/m
resistance = resistivity * thickness; %ohm-m^2

% Calculate current density

```

```
i = eta/resistance; %A/m^2

% Convert to uA/cm^2
chgDens = i * 1e6 / (100^2); %uA/cm^2

end
```

## References

- 1 J. B. Goodenough and Y. Kim, *Chem. Mater.*, 2010, **22**, 587–603.
- 2 M. S. Whittingham, *Chem. Rev.*, 2004, **104**, 4271–4302.
- 3 M. Armand and J.-M. Tarascon, *Nature*, 2008, **451**, 652–657.
- 4 V. Etacheri, R. Marom, R. Elazari, G. Salitra and D. Aurbach, *Energy Environ. Sci.*, 2011, **4**, 3243–3262.
- 5 M. M. Thackeray, C. Wolverton and E. D. Isaacs, *Energy Environ. Sci.*, 2012, **5**, 7854–7863.
- 6 J. Liu, J.-G. Zhang, Z. Yang, J. P. Lemmon, C. Imhoff, G. L. Graff, L. Li, J. Hu, C. Wang, J. Xiao, G. Xia, V. V. Viswanathan, S. Baskaran, V. Sprenkle, X. Li, Y. Shao and B. Schwenzer, *Adv. Funct. Mater.*, 2013, **23**, 929–946.
- 7 A. Manthiram, Y. Fu and Y.-S. Su, *Acc. Chem. Res.*, 2013, **46**, 1125–1134.
- 8 H. Kim, D. A. Boysen, J. M. Newhouse, B. L. Spatocco, B. Chung, P. J. Burke, D. J. Bradwell, K. Jiang, A. A. Tomaszowska, K. Wang, W. Wei, L. A. Ortiz, S. A. Barriga, S. M. Poizeau and D. R. Sadoway, *Chem. Rev.*, 2013, **113**, 2075–2099.
- 9 M. Pasta, C. D. Wessells, R. A. Huggins and Y. Cui, *Nat. Commun.*, 2012, **3**, 1149.
- 10 A. Purvins and M. Sumner, *J. Power Sources*, 2013, **242**, 742–755.
- 11 T. Xu, W. Wang, M. L. Gordin, D. Wang and D. Choi, *JOM*, 2010, **62**, 24–30.
- 12 A. Manthiram, Y. Fu, S.-H. Chung, C. Zu and Y.-S. Su, *Chem. Rev.*, 2014, **114**, 11751–11787.
- 13 A. Manthiram, S.-H. Chung and C. Zu, *Adv. Mater.*, 2015, **27**, 1980–2006.
- 14 X. Ji and L. F. Nazar, *J. Mater. Chem.*, 2010, **20**, 9821–9826.
- 15 X. Ji, K. T. Lee and L. F. Nazar, *Nat. Mater.*, 2009, **8**, 500–506.
- 16 Y. Yang, G. Zheng and Y. Cui, *Chem. Soc. Rev.*, 2013, **42**, 3018–3032.
- 17 N. Nitta, F. Wu, J. T. Lee and G. Yushin, *Mater. Today*, 2015, **18**, 252–264.
- 18 J. Choi and A. Manthiram, *J. Electrochem. Soc.*, 2005, **152**, A1714–A1718.
- 19 N. Yabuuchi and T. Ohzuku, *Sel. Pap. Present. 11th Int. Meet. Lithium Batter.*, 2003, **119–121**, 171–174.
- 20 S. Dallek, D. W. Ernst and B. F. Larrick, *J. Electrochem. Soc.*, 1979, **126**, 866–870.
- 21 *J. Appl. Phys.*, 1966, **37**, 4292–4293.
- 22 B. Meyer, *Chem. Rev.*, 1976, **76**, 367–388.
- 23 P. T. Cunningham, S. A. Johnson and E. J. Cairns, *J. Electrochem. Soc.*, 1972, **119**, 1448–1450.
- 24 G. Yang, S. Shi, J. Yang and Y. Ma, *J Mater Chem A*, 2015, **3**, 8865–8869.
- 25 H. Park, H. S. Koh and D. J. Siegel, *J. Phys. Chem. C*, 2015, **119**, 4675–4683.
- 26 Y. Malozovsky, L. Franklin, C. Ekuma and D. Bagayoko, *Int. J. Mod. Phys. B*, 2015, **29**, 1542006.
- 27 B. S. D.-H. Kim, M. S. B. Lee, K.-Y. Park and K. Kang, *Chem. – Asian J.*, 2016, **11**, 1288–1292.

- 28 J. Scheers, S. Fantini and P. Johansson, *J. Power Sources*, 2014, **255**, 204–218.
- 29 D. Marmorstein, T. . Yu, K. . Striebel, F. . McLarnon, J. Hou and E. . Cairns, *J. Power Sources*, 2000, **89**, 219–226.
- 30 A. Hayashi, R. Ohtsubo, T. Ohtomo, F. Mizuno and M. Tatsumisago, *J. Power Sources*, 2008, **183**, 422–426.
- 31 T. Kobayashi, Y. Imade, D. Shishihara, K. Homma, M. Nagao, R. Watanabe, T. Yokoi, A. Yamada, R. Kanno and T. Tatsumi, *Sel. Pap. Int. Workshop Degrad. Issues Fuel Cells*, 2008, **182**, 621–625.
- 32 M. Cuisinier, P.-E. Cabelguen, S. Evers, G. He, M. Kolbeck, A. Garsuch, T. Bolin, M. Balasubramanian and L. F. Nazar, *J. Phys. Chem. Lett.*, 2013, **4**, 3227–3232.
- 33 C. Barchasz, F. Molton, C. Duboc, J.-C. Leprêtre, S. Patoux and F. Alloin, *Anal. Chem.*, 2012, **84**, 3973–3980.
- 34 F. Y. Fan, W. C. Carter and Y.-M. Chiang, *Adv. Mater.*, 2015, **27**, 5203–5209.
- 35 S. Waluś, C. Barchasz, R. Bouchet, J.-C. Leprêtre, J.-F. Colin, J.-F. Martin, E. Elkaim, C. Baetz and F. Alloin, *Adv. Energy Mater.*, 2015, **5**, 1500165.
- 36 Z. Feng, C. Kim, A. Vijn, M. Armand, K. H. Bevan and K. Zaghbi, *J. Power Sources*, 2014, **272**, 518–521.
- 37 M. Helen, M. A. Reddy, T. Diemant, U. Golla-Schindler, R. J. Behm, U. Kaiser and M. Fichtner, *Sci. Rep.*, 2015, **5**, 12146.
- 38 M.-K. Song, E. J. Cairns and Y. Zhang, *Nanoscale*, 2013, **5**, 2186–2204.
- 39 Z. Liu, D. Hubble, P. B. Balbuena and P. P. Mukherjee, *Phys Chem Chem Phys*, 2015, **17**, 9032–9039.
- 40 K. H. Wujcik, T. A. Pascal, C. D. Pemmaraju, D. Devaux, W. C. Stolte, N. P. Balsara and D. Prendergast, *Adv. Energy Mater.*, 2015, **5**, 1500285.
- 41 Y. V. Mikhaylik and J. R. Akridge, *J. Electrochem. Soc.*, 2003, **150**, A306–A311.
- 42 H.-S. Ryu, H.-J. Ahn, K.-W. Kim, J.-H. Ahn, K.-K. Cho, T.-H. Nam, J.-U. Kim and G.-B. Cho, *Spec. Issue Sel. Pap. Present. Second Int. Conf. Polym. Batter. Fuel Cells Together Regul. Pap.*, 2006, **163**, 201–206.
- 43 S. Moon, Y. H. Jung, W. K. Jung, D. S. Jung, J. W. Choi and D. K. Kim, *Adv. Mater.*, 2013, **25**, 6547–6553.
- 44 B. Dunn, H. Kamath and J.-M. Tarascon, *Science*, 2011, **334**, 928.
- 45 P. Rozier and J. M. Tarascon, *J. Electrochem. Soc.*, 2015, **162**, A2490–A2499.
- 46 L. Ma, S. Wei, H. L. Zhuang, K. E. Hendrickson, R. G. Hennig and L. A. Archer, *J. Mater. Chem. A*, 2015, **3**, 19857–19866.
- 47 C. Milroy and A. Manthiram, *Adv. Mater.*, 2016, **28**, 9744–9751.
- 48 J.-Z. Wang, L. Lu, M. Choucair, J. A. Stride, X. Xu and H.-K. Liu, *15th Int. Meet. Lithium Batter. IMLB*, 2011, **196**, 7030–7034.
- 49 Y. Cao, X. Li, I. A. Aksay, J. Lemmon, Z. Nie, Z. Yang and J. Liu, *Phys. Chem. Chem. Phys.*, 2011, **13**, 7660–7665.
- 50 L. Yin, J. Wang, F. Lin, J. Yang and Y. Nuli, *Energy Environ. Sci.*, 2012, **5**, 6966–6972.

- 51 L. Ji, M. Rao, H. Zheng, L. Zhang, Y. Li, W. Duan, J. Guo, E. J. Cairns and Y. Zhang, *J. Am. Chem. Soc.*, 2011, **133**, 18522–18525.
- 52 M.-K. Song, Y. Zhang and E. J. Cairns, *Nano Lett.*, 2013, **13**, 5891–5899.
- 53 H. Wang, Y. Yang, Y. Liang, J. T. Robinson, Y. Li, A. Jackson, Y. Cui and H. Dai, *Nano Lett.*, 2011, **11**, 2644–2647.
- 54 S. Evers and L. F. Nazar, *Chem. Commun.*, 2012, **48**, 1233–1235.
- 55 C. Zu and A. Manthiram, *Adv. Energy Mater.*, 2013, **3**, 1008–1012.
- 56 Y. Yang, G. Zheng and Y. Cui, *Energy Environ. Sci.*, 2013, **6**, 1552–1558.
- 57 J. Yan, X. Liu and B. Li, *Adv. Sci.*, 2016, **3**, 1600101–n/a.
- 58 J. Y. Koh, M.-S. Park, E. H. Kim, B. O. Jeong, S. Kim, K. J. Kim, J.-G. Kim, Y.-J. Kim and Y. Jung, *J. Electrochem. Soc.*, 2014, **161**, A2133–A2137.
- 59 D. Lin, Y. Liu and Y. Cui, *Nat Nano*, 2017, **12**, 194–206.
- 60 P. Bai, J. Li, F. R. Brushett and M. Z. Bazant, *Energy Environ. Sci.*, 2016, **9**, 3221–3229.
- 61 X.-B. Cheng, R. Zhang, C.-Z. Zhao, F. Wei, J.-G. Zhang and Q. Zhang, *Adv. Sci.*, 2016, **3**, 1500213–n/a.
- 62 Y. Yang, M. T. McDowell, A. Jackson, J. J. Cha, S. S. Hong and Y. Cui, *Nano Lett.*, 2010, **10**, 1486–1491.
- 63 Y. Yang, G. Zheng, S. Misra, J. Nelson, M. F. Toney and Y. Cui, *J. Am. Chem. Soc.*, 2012, **134**, 15387–15394.
- 64 C. Zu, M. Klein and A. Manthiram, *J. Phys. Chem. Lett.*, 2014, **5**, 3986–3991.
- 65 K. Cai, M.-K. Song, E. J. Cairns and Y. Zhang, *Nano Lett.*, 2012, **12**, 6474–6479.
- 66 Y. Son, J.-S. Lee, Y. Son, J.-H. Jang and J. Cho, *Adv. Energy Mater.*, 2015, **5**, 1500110–n/a.
- 67 Y. V. Mikhaylik and J. R. Akridge, *J. Electrochem. Soc.*, 2004, **151**, A1969–A1976.
- 68 S. S. Zhang, *Electrochimica Acta*, 2012, **70**, 344–348.
- 69 D. Aurbach, E. Pollak, R. Elazari, G. Salitra, C. S. Kelley and J. Affinito, *J. Electrochem. Soc.*, 2009, **156**, A694–A702.
- 70 M. Kazazi, M. R. Vaezi and A. Kazemzadeh, *Ionics*, 2014, **20**, 1291–1300.
- 71 Y.-S. Su, Y. Fu, T. Cochell and A. Manthiram, *Nat. Commun.*, 2013, **4**, 2985.
- 72 D.-W. Wang, Q. Zeng, G. Zhou, L. Yin, F. Li, H.-M. Cheng, I. R. Gentle and G. Q. M. Lu, *J. Mater. Chem. A*, 2013, **1**, 9382–9394.
- 73 Y.-S. Su and A. Manthiram, *Nat. Commun.*, 2012, **3**, 1166.
- 74 C. Zhao, L. Liu, H. Zhao, A. Krall, Z. Wen, J. Chen, P. Hurley, J. Jiang and Y. Li, *Nanoscale*, 2014, **6**, 882–888.
- 75 P. Strubel, H. Althues and S. Kaskel, *Carbon*, 2016, **107**, 705–710.
- 76 Z. Wang, Y. Dong, H. Li, Z. Zhao, H. Bin Wu, C. Hao, S. Liu, J. Qiu and X. W. (David) Lou, *Nat. Commun.*, 2014, **5**, 5002.
- 77 J. Song, M. L. Gordin, T. Xu, S. Chen, Z. Yu, H. Sohn, J. Lu, Y. Ren, Y. Duan and D. Wang, *Angew. Chem. Int. Ed.*, 2015, **54**, 4325–4329.
- 78 B. D. McCloskey, *J. Phys. Chem. Lett.*, 2015, **6**, 4581–4588.
- 79 Z. Lin, Z. Liu, N. J. Dudney and C. Liang, *ACS Nano*, 2013, **7**, 2829–2833.

- 80 P. Dubois, J. P. Lelieur and G. Lepoutre, *Inorg. Chem.*, 1988, **27**, 73–80.
- 81 P. Sigmund, *Nanofabrication Ion-Beam Sputtering Fundam. Appl.*, 2012, 1–40.
- 82 J. H. Keller and R. G. Simmons, *IBM J. Res. Dev.*, 1979, **23**, 24–32.
- 83 T. P. Drüsedau, *J. Vac. Sci. Technol. Vac. Surf. Films*, 2002, **20**, 459–466.
- 84 G. Sauerbrey, *Z. Für Phys.*, 1959, **155**, 206–222.
- 85 B. J. Lindberg, K. Hamrin, G. Johansson, U. Gelius, A. Fahlman, C. Nordling and K. Siegbahn, *Phys. Scr.*, 1970, **1**, 286.
- 86 U. Gelius, *Phys. Scr.*, 1974, **9**, 133–147.
- 87 J. B. Gilbert, M. F. Rubner and R. E. Cohen, *Proc. Natl. Acad. Sci.*, 2013, **110**, 6651–6656.
- 88 I. Lindau and W. E. Spicer, *J. Electron Spectrosc. Relat. Phenom.*, 1974, **3**, 409–413.
- 89 V. R. Koppolu, M. C. Gupta and L. Scudiero, *Sol. Energy Mater. Sol. Cells*, 2011, **95**, 1111–1118.
- 90 H. Chou, A. Ismach, R. Ghosh, R. S. Ruoff and A. Dolocan, *Nat. Commun.*, 2015, **6**, 7482.
- 91 D. A. Long and D. Long, *Raman spectroscopy*, McGraw-Hill New York, 1977.
- 92 W. G. Fateley, F. R. Dollish, N. T. McDevitt and F. F. Bentley, *Viley N. Y.*, 1972.
- 93 E. Barsoukov and J. R. Macdonald, *Impedance spectroscopy: theory, experiment, and applications*, John Wiley & Sons, 2005.
- 94 Z. Deng, Z. Zhang, Y. Lai, J. Liu, J. Li and Y. Liu, *J. Electrochem. Soc.*, 2013, **160**, A553–A558.
- 95 P. G. Bruce, B. Scrosati and J.-M. Tarascon, *Angew. Chem. Int. Ed.*, 2008, **47**, 2930–2946.
- 96 G. Ceder, Y.-M. Chiang, D. R. Sadoway, M. K. Aydinol, Y.-I. Jang and B. Huang, *Nature*, 1998, **392**, 694–696.
- 97 C.-X. Zu and H. Li, *Energy Environ. Sci.*, 2011, **4**, 2614–2624.
- 98 B. Scrosati, J. Hassoun and Y.-K. Sun, *Energy Environ. Sci.*, 2011, **4**, 3287–3295.
- 99 R. Xu, J. Lu and K. Amine, *Adv. Energy Mater.*, 2015, **5**, 1500408–n/a.
- 100 C. Zu, A. Dolocan, P. Xiao, S. Stauffer, G. Henkelman and A. Manthiram, *Adv. Energy Mater.*, 2016, **6**, 1501933–n/a.
- 101 Z. W. Seh, J. H. Yu, W. Li, P.-C. Hsu, H. Wang, Y. Sun, H. Yao, Q. Zhang and Y. Cui, *Nat. Commun.*, 2014, **5**, 5017.
- 102 F. Wu, J. T. Lee, N. Nitta, H. Kim, O. Borodin and G. Yushin, *Adv. Mater.*, 2015, **27**, 101–108.
- 103 Y. Hwa, J. Zhao and E. J. Cairns, *Nano Lett.*, 2015, **15**, 3479–3486.
- 104 Z. Cui, C. Zu, W. Zhou, A. Manthiram and J. B. Goodenough, *Adv. Mater.*, 2016, **28**, 6926–6931.
- 105 K. Yan, Z. Lu, H.-W. Lee, F. Xiong, P.-C. Hsu, Y. Li, J. Zhao, S. Chu and Y. Cui, *Nat. Energy*, 2016, **1**, 16010.
- 106 S. Meini, R. Elazari, A. Rosenman, A. Garsuch and D. Aurbach, *J. Phys. Chem. Lett.*, 2014, **5**, 915–918.

- 107 E. Peled, D. Golodnitsky, E. Strauss, J. Lang and Y. Lavi, *Electrochimica Acta*, 1998, **43**, 1593–1599.
- 108 D. Chen, H. Quan, G.-S. Wang and L. Guo, *ChemPlusChem*, 2013, **78**, 843–851.
- 109 S. S. Zhang and D. T. Tran, *Electrochimica Acta*, 2015, **176**, 784–789.
- 110 E. Strauss, D. Golodnitsky and E. Peled, *J. Solid State Electrochem.*, 2002, **6**, 468–474.
- 111 S. P. S. Badwal and R. J. Thorn, *J. Solid State Chem.*, 1982, **43**, 163–174.
- 112 L. Li, M. Caban-Acevedo, S. N. Girard and S. Jin, *Nanoscale*, 2014, **6**, 2112–2118.
- 113 C. D. Lokhande, A. Ennaoui, P. S. Patil, M. Giersig, M. Muller, K. Diesner and H. Tributsch, *Thin Solid Films*, 1998, **330**, 70–75.
- 114 A Schlegel and P Wachter, *J. Phys. C Solid State Phys.*, 1976, **9**, 3363.
- 115 N. Zhang, R. Yi, Z. Wang, R. Shi, H. Wang, G. Qiu and X. Liu, *Mater. Chem. Phys.*, 2008, **111**, 13–16.
- 116 M. J. Klein, K. Goossens, C. W. Bielawski and A. Manthiram, *J. Electrochem. Soc.*, 2016, **163**, A2109–A2116.
- 117 R. Okazaki, K. Takada, S. Oguro, S. Kondo and Y. Matsuda, *Denki Kagaku*, 1994, **62**, 1074–1080.
- 118 K. A. See, M. Leskes, J. M. Griffin, S. Britto, P. D. Matthews, A. Emly, A. V. der Ven, D. S. Wright, A. J. Morris, C. P. Grey and R. Seshadri, *J. Am. Chem. Soc.*, 2014, **136**, 16368–16377.
- 119 J.-M. Letoffe, J. Blanchard and J. Bousquet, *Bull. Soc. Chim. Fr.*, 1976, 395–398.
- 120 J. A. Gladysz, V. K. Wong and B. S. Jick, *Tetrahedron*, 1979, **35**, 2329–2335.
- 121 R. A. Sharma, *J. Electrochem. Soc.*, 1972, **119**, 1439–1443.
- 122 J. Letoffe, R. Joly, J. Thourey, G. Perachon and J. Bousquet, *J. Chim. Phys.*, 1974, **71**, 427–430.
- 123 J.-M. Letoffe, J.-M. Blanchard and J. Bousquet, *Bull. Soc. Chim. Fr.*, 1975, 485–489.
- 124 J. Letoffe, J. Thourey, G. Perachon and J. Bousquet, *Bull. Soc. Chim. Fr.*, 1976, 424–426.
- 125 K. Tatsumi, Y. Inoue, A. Nakamura, R. E. Cramer, W. VanDoorne and J. W. Gilje, *Angew. Chem. Int. Ed. Engl.*, 1990, **29**, 422–424.
- 126 K. Tatsumi, Y. Inoue, H. Kawaguchi, M. Kohsaka, A. Nakamura, R. E. Cramer, W. VanDoorne, G. J. Taogoshi and P. N. Richmann, *Organometallics*, 1993, **12**, 352–364.
- 127 K. Tatsumi, H. Kawaguchi, K. Inoue, K. Tani and R. E. Cramer, *Inorg. Chem.*, 1993, **32**, 4317–4323.
- 128 A. Demortier, P. Chieux and G. Lepoutre, *Bull. Soc. Chim. Fr.*, 1971, 3421–3424.
- 129 T. H. Elmer, I. D. Chapman and M. E. Nordberg, *J. Phys. Chem.*, 1963, **67**, 2219–2222.
- 130 D. Jackman and C. Keenan, *J. Inorg. Nucl. Chem.*, 1968, **30**, 2047–2057.
- 131 D. Lee and C. Jensen, *J. Chem. Educ.*, 2000, **77**, 629.
- 132 P. Swift, *Surf. Interface Anal.*, 1982, **4**, 47–51.

- 133 Z. Tian, M. W. C. Dharma-wardana, Z. H. Lu, R. Cao and L. J. Lewis, *Phys Rev B*, 1997, **55**, 5376–5383.
- 134 R. Steudel and Y. Steudel, *Chem. – Eur. J.*, 2013, **19**, 3162–3176.
- 135 C. D. Wagner, *J. Electron Spectrosc. Relat. Phenom.*, 1983, **32**, 99–102.
- 136 C. F. Bohren and D. R. Huffman, in *Absorption and Scattering of Light by Small Particles*, Wiley-VCH Verlag GmbH, 2007, pp. 286–324.
- 137 G. J. Coyle, T. Tsang, I. Adler and L. Yin, *J. Electron Spectrosc. Relat. Phenom.*, 1980, **20**, 169–182.
- 138 S. Wei, S. Xu, A. Agrawal, S. Choudhury, Y. Lu, Z. Tu, L. Ma and L. A. Archer, *Nat. Commun.*, 2016, **7**, 11722.
- 139 X. Meng, D. J. Comstock, T. T. Fister and J. W. Elam, *ACS Nano*, 2014, **8**, 10963–10972.
- 140 M. Yamashita, H. Yamanaka and H. Wakabayashi, *Solid State Ion.*, 1996, **89**, 299–304.
- 141 I. Seo and S. W. Martin, *Inorg. Chem.*, 2011, **50**, 2143–2150.
- 142 D. Chrisey, R. Johnson, J. Boring and J. Phipps, *Icarus*, 1988, **75**, 233–244.
- 143 A. P. M. Glassford, *J. Vac. Sci. Technol.*, 1978, **15**, 1836–1843.
- 144 B. J. Lindberg, K. Hamrin, G. Johansson, U. Gelius, A. Fahlman, C. Nordling and K. Siegbahn, *Phys. Scr.*, 1970, **1**, 286–298.
- 145 G. Yang, S. Shi, J. Yang and Y. Ma, *J Mater Chem A*, 2015, **3**, 8865–8869.
- 146 B Bertheville and H Bill and H Hagemann, *J. Phys. Condens. Matter*, 1998, **10**, 2155.
- 147 B. Eckert and R. Steudel, in *Elemental Sulfur und Sulfur-Rich Compounds II*, ed. R. Steudel, Springer Berlin Heidelberg, Berlin, Heidelberg, 2003, pp. 31–98.
- 148 B. A. Trofimov, L. M. Sinegovskaya and N. K. Gusarova, *J. Sulfur Chem.*, 2009, **30**, 518–554.
- 149 R. Steudel, in *Elemental Sulfur und Sulfur-Rich Compounds II*, ed. R. Steudel, Springer Berlin Heidelberg, Berlin, Heidelberg, 2003, pp. 99–126.
- 150 H. Wieser, P. J. Krueger, E. Muller and J. B. Hyne, *Can. J. Chem.*, 1969, **47**, 1633–1637.
- 151 O. El Jaroudi, E. Picquenard, A. Demortier, J.-P. Lelieur and J. Corset, *Inorg. Chem.*, 1999, **38**, 2394–2401.
- 152 O. El Jaroudi, E. Picquenard, A. Demortier, J.-P. Lelieur and J. Corset, *Inorg. Chem.*, 2000, **39**, 2593–2603.
- 153 R. Steudel, in *Elemental Sulfur und Sulfur-Rich Compounds II*, ed. R. Steudel, Springer Berlin Heidelberg, Berlin, Heidelberg, 2003, pp. 127–152.
- 154 G. J. Janz, J. R. Downey, E. Roduner, G. J. Wasilczyk, J. W. Coutts and A. Eluard, *Inorg. Chem.*, 1976, **15**, 1759–1763.
- 155 J. R. Mycroft, G. M. Bancroft, N. S. McIntyre, J. W. Lorimer and I. R. Hill, *J. Electroanal. Chem. Interfacial Electrochem.*, 1990, **292**, 139–152.
- 156 F. P. Daly and C. W. Brown, *J. Phys. Chem.*, 1975, **79**, 350–354.
- 157 A. V. Tobolsky, *J. Polym. Sci. Part C Polym. Symp.*, 1966, **12**, 71–78.
- 158 F. Cataldo, *Angew. Makromol. Chem.*, 1997, **249**, 137–149.

- 159 A. T. Ward, *J. Phys. Chem.*, 1968, **72**, 4133–4139.
- 160 L. A. Nimon, V. D. Neff, R. E. Cantley and R. O. Buttlar, *J. Mol. Spectrosc.*, 1967, **22**, 105–108.
- 161 H. Eysel, G. Wieghardt, H. Kleinschmager and G. Weddigen, *Z. Naturforschung Sect. B - J. Chem. Sci.*, 1976, **31**, 415–418.
- 162 H. Holleck, *Surf. Coat. Technol.*, 1988, **36**, 151–159.
- 163 C. Weissmantel, K. Bewilogua, D. Dietrich, H.-J. Erler, H.-J. Hinneberg, S. Klose, W. Nowick and G. Reisse, *Thin Solid Films*, 1980, **72**, 19–32.
- 164 J. B. Bates, N. J. Dudney, G. R. Gruzalski, R. A. Zuhr, A. Choudhury, C. F. Luck and J. D. Robertson, *This Vol. Contains Proc. 6th Int. Meet. Lithium Batter.*, 1993, **43**, 103–110.
- 165 G. M. Veith, A. R. Lupini, L. Baggetto, J. F. Browning, J. K. Keum, A. Villa, L. Prati, A. B. Papandrew, G. A. Goenaga, D. R. Mullins, S. E. Bullock and N. J. Dudney, *Chem. Mater.*, 2013, **25**, 4936–4945.
- 166 T. Fujimori, A. Morelos-Gómez, Z. Zhu, H. Muramatsu, R. Futamura, K. Urita, M. Terrones, T. Hayashi, M. Endo, S. Young Hong, Y. Chul Choi, D. Tománek and K. Kaneko, *Nat. Commun.*, 2013, **4**, 2162.
- 167 A. Kinbara, T. Nakano, A. Kobayashi, S. Baba and T. Kajiwara, *Appl. Surf. Sci.*, 1993, **70–71, Part 2**, 742–745.
- 168 S. M. Rossnagel, I. Yang and J. J. Cuomo, *Thin Solid Films*, 1991, **199**, 59–69.
- 169 J. R. Gavaler, J. Talvacchio, T. T. Braggins, M. G. Forrester and J. Gregg, *J. Appl. Phys.*, 1991, **70**, 4383–4391.
- 170 N. Ding, S. W. Chien, T. S. A. Hor, R. Lum, Y. Zong and Z. Liu, *J. Mater. Chem. A*, 2014, **2**, 12433–12441.
- 171 S.-H. Chung, C.-H. Chang and A. Manthiram, *ACS Nano*, 2016, **10**, 10462–10470.

## **Vita**

Michael Klein was born in Louisville, Kentucky. He attended the University of California, Berkeley and graduated with high honors in 2012 with a B.S. in chemical engineering. He then attended the University of Texas at Austin as an NSF Graduate Research Fellow, receiving a Ph.D. degree in Materials Science and Engineering in 2017. His graduate research focused on fundamental solid-state science related to lithium-sulfur batteries.

Email address: [klein.michael.james@gmail.com](mailto:klein.michael.james@gmail.com)

This dissertation was typed by the author.